HIGH ENERGY TWO-BODY DEUTERON PHOTODISINTEGRATION

BY

BART PAUL TERBURG

Ingenieur, Technische Universiteit Delft, 1992
M.S., University of Illinois, 1993

THESIS

Submitted in partial fulfillment of the requirements
for the degree of Doctor of Philosophy in Physics
in the Graduate College of the
University of Illinois at Urbana-Champaign, 1999

Urbana, Illinois

HIGH ENERGY TWO-BODY DEUTERON PHOTODISINTEGRATION

Bart Paul Terburg , Ph.D.
Department of Physics
University of Illinois at Urbana-Champaign, 1999
Douglas H. Beck, Advisor

The differential cross section for two-body deuteron photodisintegration was measured at photon energies between 0.8 and 4.0 GeV and center-of-mass angles θ_{cm}=37°,53°,70°, and 90° as part of CEBAF experiment E89-012. Constituent counting rules predict a scaling of this cross section at asymptotic energies. In previous experiments this scaling has surprisingly been observed at energies between 1.4 and 2.8 GeV at 90°. The results from this experiment are in reasonable agreement with previous measurements at lower energies. The data at 70° and 90° show a constituent counting rule behavior up to 4.0 GeV photon energy. The 37° and 53° data do not agree with the constituent counting rule prediction. The new data are compared with a variety of theoretical models inspired by quantum chromodynamics (QCD) and traditional hadronic nuclear physics.

Acknowledgements

Hidden behind my name on the title page of this thesis is a long list of names from people, without whose support, encouragement and friendship I could not have accomplished this work.

I would like to start by thanking my research advisor, Doug Beck, for his guidance and for giving me a great amount of freedom in the pursuit of my academic interests. I am grateful that he let me participate in the SAMPLE experiment, which gave me the opportunity to familiarize myself with the experimental nuclear physics environment early in my career, while tasting a different flavor of nuclear physics.

I was lucky for being in close proximity to Roy Holt and I am very grateful to him for teaching me the intricacies of his experiment, and for our discussions of the theoretical interpretations.

The experiences at CEBAF[1] were most valuable to the development of my skills as an experimental physicist. I admire Joe Mitchell for his leadership of the target group, with whom I spent a large share of my time working on the construction of the first high-power multiloop cryotarget for the lab. Many thanks go to Rolf Ent for being available for useful advice at times which overlap with graduate student's schedules.

I would like to acknowledge the rest of the Hall C staff members, Roger Carlini, Bill Vulcan, Dave Mack, Steve Wood, Chen Yan, Keith Baker, Dave Abbott, Kevin Baily, Cynthia Keppel and Hamlet Mkrtchyan and the postdocs Jim Dunne, Paul Guèye, and Kétévi Assamagan. They provided a thriving experimental and academic

[1] It has been argued that I took that name with me when I left the lab.

environment. Thanks also to Paul Brindza, Jim Takacs, Steve Lassiter, Mike Fowler, and Joe Beaufait for their technical support and to Jim Rohrbach who has been helpful for machining many of the difficult target parts. Thanks to my friends, the "Bobos" Steve Knight, Paul Hood, and Mark Hoegerl for spending the most enjoyable time during the target construction.

Fraser Duncan, Mike "Computer-Bobo" Johnson, David Beatty, Bruce Rayner, Johnny Tang, David Wetherholt, and Bonnie Madre were instrumental in the development and testing of the cryotarget control system. I am thankful to Don Geesaman and Hal Jackson for choosing me to upgrade the system for the helium experiments.

I owe a great deal to my fellow graduate students for their dedication to the experiment. I thank Chris Bochna for a fruitful partnership, in which we succeeded in getting the most out of our data. I have gained many wonderful friends in Derek van Westrum, David Meekins, Dipangkar Dutta, John Arrington, and Kenneth Gustafsson. I would also like to acknowledge Chris Armstrong, Jin Seok Cha, Chris Cothran, Valera Frolov, Doug Koltenuk, Rick Mohring, Gabriel Niculescu, and Ioana Niculescu. Your hard work is greatly appreciated.

I would like to thank the postdocs Mike Miller and Haiyan Gao for managing the daily running of experiment and for their helpful comments. I convey a large thanks to the E89-012 collaboration, and in particular to the long time photodisintegraters, Ed Kinney, Jim Napolitano and my predecessor Eric Belz, for sharing their experience in the experiment and data analysis. My thanks also go to Misak Sargsian and Sergey Nagornyĭ for communicating their results for inclusion in the figures in Chapter 6.

Penny Sigler and Gaylon Reeves, who manage the Nuclear Physics business office, deserve many thanks for arranging over a dozen smooth experimental run and conference travels.

I owe Nathan Yanasak and Dan McLaughlin for teaching me a great deal about the "American Way" during my first months in the New World. I have also greatly enjoyed the friendship of my class mates Benoît Vanderheyden and Brian Bunker. I am thankful to my friends Dan, Jim, Alan, Joey, Lee, Darla, Eric, Mosheh, Tanya, Heejung, Hye-yun, and others for many happy times.

The Knight, Hoegerl, Meekins and Fontanares families welcomed me during my CEBAF residency with a warmth and hospitality, for which I would like to express my appreciation.

A special thanks goes to my better half Giovanna for creating a nourishing environment to complete this work.

My mother, my brother, and my grandmother gave me the love and support that has been essential to complete my research. I am particularly grateful to my mother for giving me the freedom to travel across the world to pursue my goals.

This material is based on work supported by the National Science Foundation under Grants NSF PHY 89-21146, NSF PHY 92-57057, NSF PHY 93-10871, and NSF PHY 94-20787. I also wish to acknowledge the University of Illinois Felix T. Adler Fellowship in April, 1999.

Contents

Chapter 1

Introduction

With the discovery of the neutron by Chadwick [1] in 1932, and the mass-2 isotope of hydrogen, deuterium, later that year [2], nuclear physicists obtained the deuteron, the simplest nucleus, and therefore a system that is as important to the development of nuclear theory, as the hydrogen atom is to atomic theory. Following the first observation of deuteron photodisintegration by Chadwick and Goldhaber [3] in a cloud chamber, the process of the electromagnetic interaction of deuterons with γ-radiation, has been the subject of many experimental and theoretical studies. A well known example is that deuteron photodisintegration, ^{2}H(n,γ)^{1}H, or the inverse capture reaction, ^{1}H(n,γ)^{2}H, can be used as means to study the binding energy of the deuteron, thus establishing the deuteron's mass [4].

After the discovery of the strongly interacting π-meson [5] in 1947, which as Yukawa [6] had conjected in 1935 should be responsible for the strong nuclear binding forces through the exchange of a bosonic particle with a mass midway between the electron and nucleon, a large effort was made to understand the binding between two nucleons in the deuteron, through extensive modeling using potentials that describe the NN-interaction in terms of meson and baryon degrees of freedom, constrained by an abundance of data at low and moderate energy. This approach was very successful at moderate energies, but as the energy of experimentally available electromagnetic probes increased, new substructure in the nucleons was resolved and it became necessary to describe nuclear processes at high energies in terms of the quark and gluon degrees of freedom of quantum chromodynamics[1] (QCD), the new theory of strong interactions under development since the early 1970's. Figure 1.1 is an illustration

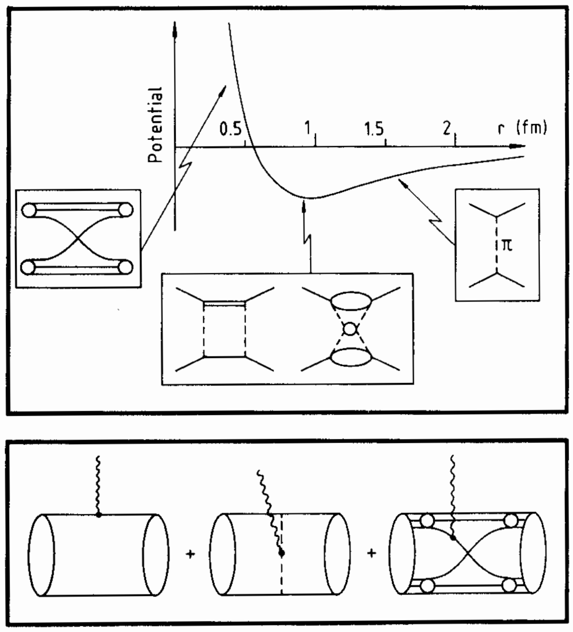

Figure 1.1: The upper frame shows a general form of the nucleon-nucleon potential, and the dominant processes that drive the NN-interaction. At long distance the pion exchange mechanism dominates. At intermediate distance a nuclear resonance (e.g. a Δ-resonance) can be created between the exchange of two pions. Short distances can be characterized by the exchange of heavy mesons, but ultimately the subnuclear degrees of freedom come into play, as shown for example by the quark-interchange mechanism. In the lower panel, the coupling of the electromagnetic probe to the particle which is being exchanged is shown, as the energy increases from left to right. Figure taken from Reference [8].

of how the new degrees of freedom enter in the description of the nucleon-nucleon potential, when the energy increases (i.e. when the range becomes shorter).

For the $\gamma d \to pn$ reaction the break-up has been well described at low energies with the traditional meson-exchange models. At very high (asymptotic) energies the reaction cross section is expected to show a simple scaling behavior which is directly related to the number of elementary constituents in the process. This scaling behavior

[1]A review of the early developments of QCD is given in Reference [7].

can be constructed with perturbative QCD. Surprisingly it has been observed in the intermediate energy (few GeV) regime, where a pQCD description is not a priori warranted. Yet this intermediate energy regime is of particular interest since it is there where the transition from a description in terms of meson-baryon to a description in terms of quark-gluon degrees of freedom is expected to take place. A measurement of the deuteron photodisintegration cross section can provide new insights on how the two different descriptions are connected.

The cross section for the photodisintegration reaction has a strong energy dependence, with a fall-off of many decades when the the photon energy is doubled. The Continuous Electron Beam Accelerator Facility (CEBAF), a new facility dedicated to nuclear physics research in the intermediate energy region, provides a high luminosity continuous electron beam with low accidental background, which enables the accurate measurements of small scattering cross sections in a greatly reduced time. Moreover, the available beam energies up to 4 GeV give access to a new region of the intermediate energy regime which has not yet been explored.

In this work the results are presented of measurements of the deuteron photodisintegration reaction, $\gamma d \rightarrow pn$, which were carried out as part of CEBAF experiment E89-012. This experiment, which was the first [9] to use the CEBAF beam in combination with high power cryogenic targets, is designed to study the energy and angular dependence of the $\gamma d \rightarrow pn$ cross section. The primary goal of the experiment is to investigate whether the simple scaling behavior of the cross section, which was first observed in SLAC experiment NE8 [10] at proton center-of-mass angle of 90°, and confirmed by SLAC experiment NE17 [11] up to photon energies of 2.7 GeV, continues at higher photon energies, and whether an onset of scaling will be observed for other, smaller center-of-mass angles.

The motivation behind this experiment, and an overview of the theoretical approaches to model the reaction are discussed in the next chapter, followed by a description of the experimental apparatus in Chapter 3. Chapter 4 discusses the calibration of the apparatus and the first stage in the extraction of the experimental data. The determination of the photodisintegration cross section and a discussion of the accuracy of the experimental procedure is covered in Chapter 5. In Chapter 6 the results are presented, along with data from previous experiments and an interpretation of the data in terms of the available theoretical models. A summary and concluding remarks are given in the last chapter.

Chapter 2

Exclusive Deuteron Photodisintegration

2.1 Overview and Physics Motivation

After providing successful descriptions for numerous high energy hadronic phenomena over the past two decades quantum chromodynamics (QCD) is widely accepted as the correct fundamental theory of strong interactions [12]. The successes in the high energy regime can be attributed to the QCD property of asymptotic freedom, which warrants the use of perturbative calculations in a system of weakly bound quarks and gluons.

If QCD is indeed the correct theory of strong interactions, then by extension it must also provide a fundamental description of the nuclear force and nuclear physics in terms of quarks and gluons [13]. This conjecture can be made, because the characteristic length scale of QCD is the size of the nucleon (~1 fm), which is of the same order as the size of nuclear systems. The implication is that nuclear phenomena which are explained in a traditional meson-nucleon approach, must have an alternative explanation in terms of quarks and gluons. At this level the understanding and application of QCD is still in its infancy.

Bound states of quarks and gluons, like mesons and baryons, are not well understood in QCD, and it is difficult to make quantitative predictions about them. In the description of bound states generally techniques are used which isolate the "soft" not well understood (low-energy) part of the theory, from the "hard" (high energy) part, which can be modeled with perturbative QCD. For the description of the high energy part a set of empirically justified relations [14], dimensional scaling laws (also referred to as constituent-counting rules), makes it possible to deal with bound states, even though they are difficult to describe in QCD. The constituent counting rules characterize the asymptotic behavior (scaling at high energies) of scattering cross sections of bound states, in terms of the number of elementary point-like constituents (e.g. photons, electrons, quarks) involved in the reaction.

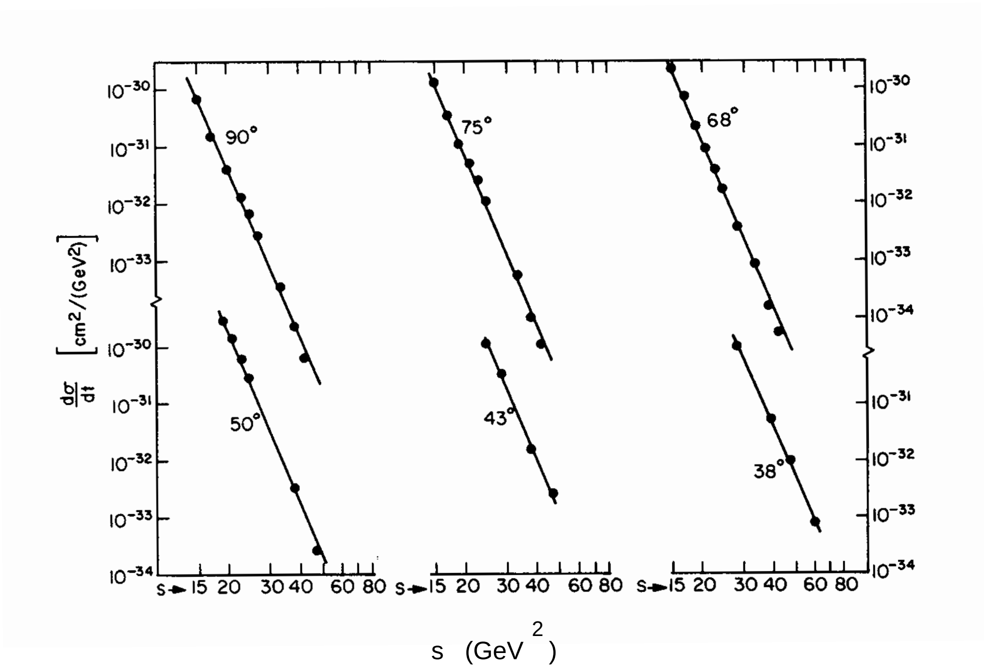

Figure 2.1: Scaling of the invariant cross section for fixed center-of-mass angle for elastic *pp* scattering. The data compilation is from Landshoff and Polkinghorne [15]. The Figure is taken from [16].

A classic example of a successful application of constituent counting rules to the description of fixed angle exclusive[1] scattering processes at high energies is the agreement between predicted and measured energy dependence of proton-proton scattering, $p + p \to p + p$. The four-proton system has a total of 12 constituents (3 quarks for each proton), for which the scaling laws predict an energy dependence[2] of the invariant cross section according to $\frac{d\sigma}{dt} \sim s^{-10}$, where s is the square of the center-of-mass

[1]In an exclusive hard scattering process the kinematics of all final state hadrons are fixed.

[2]See Section 2.2 for a derivation of this result.

energy. Experimental data from the reaction are in excellent agreement with the scaling law prediction, for $s > 15$ GeV^2, as shown in Figure 2.1.

Since the asymptotic scaling behavior is believed to be true for reactions involving nuclei as well [17], a study using the deuteron[3] would be the most suitable. In the search for quark degrees of freedom in bound systems, experiments with high energy electromagnetic probes provide a valuable tool. Holt [18] has argued that for the same beam energy, a photodisintegration reaction may start to show scaling at lower energy than an elastic electron-deuteron scattering reaction, because of the larger momentum transfer per constituent in the former reaction. Hence the exclusive deuteron photodisintegration reaction ($\gamma d \to pn$) is the most suitable reaction to study the scaling behavior of a nuclear system at beam energies that are currently available. Figure 2.2 shows a schematic of the reaction in the center-of-mass frame, including the definition of center-of-mass scattering angle (In this work natural units, $\hbar = c = 1$, are used).

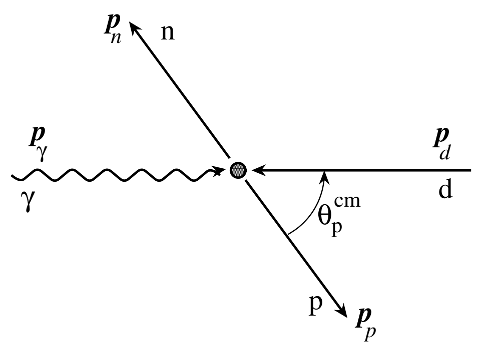

Figure 2.2: Schematic of the two-body deuteron photodisintegration reaction $\gamma d \to pn$ in the center-of-mass frame, including the definition of kinematics quantities.

Thus, even though the quarks and gluons are not observed as physical states in the laboratory, a quark-gluon description of nuclear physics processes has become of tremendous importance. In the following section the application of QCD to nuclear

[3] The deuteron is the bound state of a proton and a neutron and therefore the simplest nucleus.

physics is further discussed with the emphasis on the intermediate energy region, where the photodisintegration measurements take place. This is the regime where a transition in the number of degrees of freedom that describe the process is supposed to take place, and where the onset of the scaling behavior is expected.

2.1.1 QCD and Nuclear Interactions

Quantum chromodynamics (QCD) is a renormalized Lagrangian field theory, which describes the strong interactions in terms of fundamental quark and gluon degrees of freedom, which are expected to obey an exact SU(3) color symmetry [19]. The quarks are point-like spin-1/2 fermions which carry both a fractional electric charge and a color charge, the latter producing the color field that enables binding in hadronic matter. The gluons are bicolored spin-1 vector bosons, which interact with the quarks, and with themselves.

QCD is modeled after quantum electrodynamics (QED), the theory of electromagnetic interactions between electrons and photons. The color interactions are assumed to be a copy of the electromagnetic interactions, and the (qg) vertex has the same structure as the $(e\gamma)$ vertex, where the effective strength is given by the strong coupling constant α_s in analogy with the electromagnetic coupling constant α. The major difference between QED and QCD, however, is that the gluons carry charge, so that three-gluon (ggg) and four-gluon $(gggg)$ couplings are allowed. Unlike QED, where vacuum polarization can lead to screening, thereby reducing the strength of the coupling at *large* distances, certain gluon-gluon couplings in QCD can spread the color charge, causing an effective *anti-screening*, which reduces the strength of the coupling at *short* distances. The effective strength of the quark-gluon interaction includes the anti-screening effect, and is given by the so-called running coupling constant

$$\alpha_s(Q^2) = \frac{4\pi}{(11 - \frac{2}{3}n_f)\log(Q^2/\Lambda^2_{QCD})}\ , \tag{2.1}$$

where Q^2 is the square of the four-momentum transfer at the vertex (a measure for range at which the coupling strength is evaluated), and n_f the number of types or "flavors" of quarks with effective mass much smaller than Q. The parameter Λ_{QCD} sets the basic mass scale for QCD, and is determined from experiment, with a current value $\Lambda_{QCD} \approx$ 100–300 MeV [20] .

The coupling constant decreases with increasing Q^2 and therefore becomes small for short distance interactions. This phenomenon is referred to as the asymptotic freedom of QCD, and makes perturbative calculations of hadronic processes in terms of an expansion in the coupling constant possible. However, since a general probability amplitude for a process is a combination of short- and long-distance behavior, asymptotic freedom may not always provide the solution, and the use of factorization theorems [16], enables one to separate the non-perturbative from the perturbative part of the amplitude. Using a factorization formula for an exclusive hard scattering process, the Q^2 dependence of the hard scattering probability amplitude, which describes the dynamics of the scattering process, and the Q^2 dependence of the probability amplitude that describes the bound state dynamics of each incoming or outgoing hadron, can be separately calculated. Through the combination of asymptotic freedom and the factorization theorems perturbative (i.e. calculable) QCD (pQCD) is created, which has been successfully tested in high momentum transfer inclusive reactions [12].

The relatively low mass scales of QCD ($\Lambda_{QCD} \approx 200\pm100$ MeV, and the mean transverse momentum in high energy collisions, $\langle k_\perp^2 \rangle^{\frac{1}{2}} \sim 300$ MeV) suggest that the most critical test of the theory's description of strong interactions will take place in the intermediate (1–5 GeV) energy regime, where the perturbative and non-perturbative domain meet. This is the regime dominated by nuclear processes, in which the nucleon structure plays a prominent role. An effort to perform an explicit evaluation of such a nuclear process using pQCD would require the evaluation of millions of Feynman diagrams [21], even at leading order in α_s, and is consequently cumbersome if feasible at all. In addition, for any prediction beyond leading order one would have to include contributions of non-valence Fock states, wave functions and binding corrections. Moreover, the validity of the perturbation expansion becomes questionable, since the coupling constant can no longer be considered a small expansion parameter at momentum transfers of the order of a few GeV. On the other hand, perturbative QCD provides predictions for the leading fixed angle power-law scaling behavior of hadronic and nuclear scattering reactions at large momentum transfer, which should be applicable to the intermediate energy range, when requirements on the momentum transfer are met. The power-law behavior enables one to study bound states [14].

At the low end of the intermediate energy regime, nuclear physics phenomena are traditionally described in terms of meson-baryon degrees of freedom, using meson-exchange mechanisms, an approach which has proved to be very effective [8]. In this picture the assumption that mesons and baryons are made of quarks and gluons is still a valid one, if one assumes that nucleon-nucleon or nucleon-meson interactions take place through coherent interactions of their constituents. However, a proof that the meson-nucleon interactions are indeed obtained in the low-energy limit of QCD is not available at this time. In an effort to increase the range of validity of the meson-exchange models, calculations that are valid at low energies are often extended to the intermediate regime, while the model is being constrained by experimental data at low energy. Several authors (e.g. [22]) have also attempted to construct models to incorporate QCD in the description of nucleon-nucleon and nucleon-meson interactions. But it has been pointed out that even if a description of nuclear dynamics in terms of nucleon, isobar and meson degrees of freedom corresponds to the low-energy limit of QCD, that these hadronic bound states do not constitute a complete basis for calculations in QCD [23]. In addition to the standard color singlet quark-antiquark ($q\bar{q}$) and three quark (qqq) states, which physically manifest themselves as the mesons and baryons of nuclear physics at low momentum transfers, QCD has not disproved the existence of a (qqq) color octet, and there has been speculation of 6-quark color singlets [21]. The possible existence of these hidden-color Fock states suggests that a duality between hadrons and quark-gluon states is likely not completely correct. Nevertheless, the success of the meson-exchange theory in describing the interactions in terms of colorless objects at long distances and small momenta is indisputable, which indicates that the hidden-color Fock components of the wave function must be negligible at low momentum transfer.

It is evident that nuclear reactions in the intermediate energy region (1–5 GeV) aid significantly to the understanding of the transition in behavior of form factors, structure functions and exclusive scattering amplitudes from a description in terms of meson-exchange mechanisms to a description using QCD asymptotic scaling rules. It is expected that the short distance behavior of the nucleon-nucleon interaction which is well-described by QCD, joins smoothly and analytically with the large distance constraints of hadronic nuclear physics, but an explicit description of the connection requires thorough theoretical considerations, and a large body of experimental data for verification. The deuteron photodisintegration reaction is a powerful tool to acquire new information about nuclear structure in the few GeV energy range. The onset of perturbative QCD is strongly related to the amount of momentum transferred to the constituents in a reaction, and the photon imparts all its energy and momentum to the nucleon, so that the pQCD region comes within reach of the experimenter for the currently available beam energies. From a theoretical point of view the deuteron is also a preferred system to study since it can be considered as either a bound state of two nucleons or as a (relatively simple) six-quark system. Results from this experiment may aid in the determination of whether a description in terms of the QCD quark-gluon degrees of freedom is applicable in the intermediate energy range, or whether a description using the traditional hadronic nuclear physics picture is more appropriate.

2.1.2 Theoretical Approaches

There is a collection of theoretical models that attempt to describe the $\gamma d \rightarrow pn$ reaction in the energy range of this experiment. The models that are discussed in this chapter each have different assumptions about the degrees of freedom present in the bound state, as well as in the details of the reaction mechanism. The dimensional scaling model [24] describes the deuteron as a bound state of 6 free quarks.

This model is valid in the asymptotic region, where the total center of mass energy is much larger than deuteron mass, $s \gg m_d^2$. The same scaling result can also be obtained using perturbative QCD as shown by Brodsky and Lepage [17] and others. In Brodsky and Hiller's reduced nuclear amplitude (RNA) model [21] the deuteron is modeled as a bound state of two constituent nucleons, which each have asymptotic quark properties. The two nucleons are bound in the deuteron through the quark interchange mechanism. The quark interchange mechanism is also used by Frankfurt *et al.* [25] who treat the reaction as a hard scattering but include strong final state interactions between the outgoing nucleons. Kondratyuk *et al.* [26] undertake a vastly different approach, but still utilize the quark-gluon degrees of freedom. They combine the quark-gluon string (QGS) model with Regge phenomenology to obtain a prediction of the energy behavior of the cross section at moderate momentum transfer. Three models use the traditional nuclear physics approach, of describing the reaction in baryon-meson degrees of freedom. Lee [27] and Laget [28] both calculate the reaction cross section in the traditional meson-exchange scheme. Nagornyĭ *et al.* [29] developed the asymptotic amplitudes model, a gauge-invariant, covariant formulation using baryon degrees of freedom, with allowance for the internal structure of the deuteron.

2.2 Dimensional Scaling

The dimensional scaling laws (also known as constituent counting rules) were developed by Brodsky and Farrar [24], and independently by Matveev *et al.* [30], to understand the energy dependence of high-energy scattering processes at fixed center-of-mass angles. For an exclusive two-body reaction $AB \to CD$ as depicted in Figure 2.3 the scaling laws predict the asymptotic (large s) behavior of the invariant cross section at fixed center-of-mass angle as

$$\frac{d\sigma}{dt}(AB \to CD) \quad \overset{s\to\infty}{\longrightarrow} \quad s^{-(n-2)} f(t/s), \tag{2.2}$$

where the integer $n = n_A + n_B + n_C + n_D$ is the (minimum) total number of elementary fields (lepton, photon and quark components, collectively referred to as *constituents*) carrying a finite fraction of the momentum in the particles A, B, C, D. The variables s, t are the invariant Mandelstam variables defined in terms of the four-momenta p_i $(i = A, B, C, D)$ of the particles involved:

$$s = (p_A + p_B)^2, \tag{2.3}$$

$$t = (p_A - p_C)^2. \tag{2.4}$$

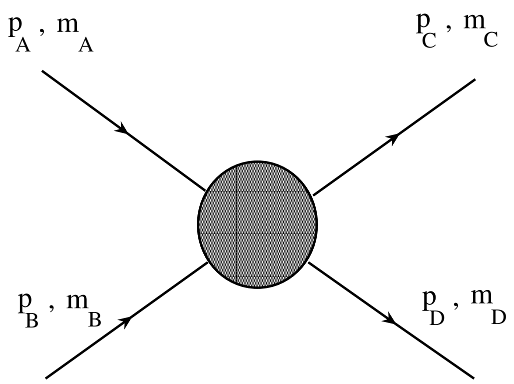

Figure 2.3: Generic scattering reaction $AB \to CD$. The particles i $(i = A, B, C, D)$ have masses m_i and four-momenta p_i.

Brodsky and Farrar arrive at this result starting with a dimensional analysis and some basic assumptions. They picture a hadron as a collection of n_H constituents in a bound state, where each constituent carries a fraction of the total hadron momentum. The scattering amplitude for the hadronic process, $M_{AB \to CD}$ is then related to the amplitude for scattering of their constituents, integrated over possible constituent momenta with the constraint that the constituent momenta sum to the hadron momenta. If the scattering process has a total number of n elementary fields in initial and final state combined, the Feynman amplitude M_n for the constituent scattering process has dimension[4] $[\text{length}]^{n-4}$. At large energy and fixed center-of-mass angle (fixed t/s) the only length scale available for the amplitude M_n is $1/\sqrt{s}$, so that the dependence becomes

$$M_n \sim (\sqrt{s})^{4-n} f(t/s) \ , \tag{2.5}$$

where the function $f(t/s)$ contains the angle dependence. If the momentum fraction of each of the constituents is finite, integration over the possible momenta cannot produce additional s-dependence, and the amplitude for the hadronic process has the same asymptotic s-dependence as M_n. The large-s behavior of the cross section is obtained from the generic expression for the invariant cross section (see Appendix A, Equation A.10),

$$\frac{d\sigma}{dt} = \frac{|M|^2}{64\pi s |\boldsymbol{p_A}|^2} \ , \tag{2.6}$$

where $\boldsymbol{p_A}$ is the center-of-mass three-momentum of the incident particle. In the large-s limit the invariant cross section simplifies to

$$\frac{d\sigma}{dt} \sim \frac{1}{s^2} |M|^2 \ , \tag{2.7}$$

since $\boldsymbol{p_A^2} \to s$ for $s \to \infty$ (see Appendix A.) In this equation, substitution of Equation 2.5 for M directly results in Equation 2.2.

The above heuristically derived scaling law is correct (except for logarithms) in any renormalizable field theory, if the following three assumptions hold:

1. The physical hadrons have ground state wave functions which are finite when the quark separation in coordinate space is zero, and vanish for large quark coordinate separation.

2. The large-momentum-transfer interactions of the constituents in the hadrons are asymptotically scale-invariant.

3. Multiple scale-invariant interactions between the constituents of different hadrons can be neglected.

[4]The conventional normalization $\langle p|p'\rangle = 2E\delta^3(\vec{p} - \vec{p}\,')$ is chosen.

The first assumption limits the binding corrections and implies that there are no elementary fields with quantum numbers of the hadrons so that the scattering amplitude for the hadronic process $M_{AB \to CD}$ can be related to the Feynman amplitude M_n for the collection of constituents. The scaling behavior at fixed angle of $M_{AB \to CD}$ is then given by the scaling behavior of M_n.

The second and third assumption form the basis for the $(\sqrt{s})^{4-n}$ scaling dependence of M_n. In particular the third assumption is needed to eliminate contributions to M_n due to disconnected or Landshoff [31] diagrams, which would violate dimensional scaling. Figure 2.4 shows a Landshoff diagram and a hard scattering diagram for the same meson-baryon process. The Landshoff diagram is characterized by fewer

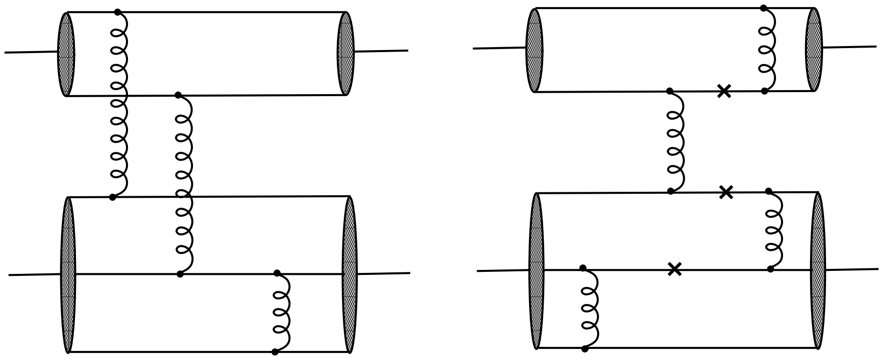

(a) (b)

Figure 2.4: Meson-baryon scattering diagram in (a) Landshoff description and (b) hard scattering gluon exchange description. In figure (a) all quarks and the gluon inside the baryon are near-mass-shell. In figure (b) the crosses label quark lines which are far off the mass shell. The gluons are far off the mass shell as well. Figure after Reference [32].

off-shell fermions and gluons than the standard diagram. Physically the diagram corresponds to a mechanism in which hadrons scatter at large angles, by successive independent, near-mass-shell elastic scatterings of each constituent of one hadron, off a constituent of the other, such that the final momenta are properly aligned. In, for example, the case of pion-pion scattering, two spatially separated scatterings occur, each between a quark (antiquark) from one pion and a quark (antiquark) of the other pion. In the Landshoff case, the constituent scattering amplitude then scales as $M_n \sim (\sqrt{s})^{4-n}(\sqrt{s})^{L-1}$, where L is the number of pairs of constituents from different hadrons, which have a large-angle scale-invariant interaction. Thus the "Landshoff" cross section would have a $1/Q^2$ dependence with less powers and dominate the constituent counting rule prediction. As opposed to hard scattering, which takes place in a small volume of 3-dimensional space ($|\Delta\vec{x}| < 1/\sqrt{s}$), the Landshoff scatterings are confined in only two dimensions, whereas the spatial separation in the 3rd dimension can amount to as much as the hadron diameter (1 fm) [33]. This variation in spatial separation (dependent on virtuality of the quark and gluon propagators) is believed to allow for a smooth connection between the Landshoff and hard scattering regions.

At the high energies of interest here, the Landshoff mechanism is shown to be not physically important. This can be understood by examining the pion-pion case again [33]. Because the hard scattering occurs within a small region of space-time, the wave functions are compact, and no additional gluons are present, making the pions color neutral down to distances $1/\sqrt{s}$. In the Landshoff picture the quark and antiquark in each of the incoming pions are separated in one direction by 1 fm. Thus the pion is globally color neutral, but not locally, since the separated quarks have a virtual gluon cloud around them. An isolated, nearly on-shell quark will radiate gluons when it scatters and the amount of gluon radiation increases as the change of the quark's state of motion becomes larger. In an exclusive process such gluon bremsstrahlung is prohibited, and as a result the amplitude for the Landshoff process is suppressed. This suppression is known as Sudakov suppression [16].

Since their conception, the scaling laws have successfully described the energy dependence at fixed angle of a large number of processes. A comparison between a number of hadronic processes is made in Table 2.1. Indeed the scaling laws provide an accurate description of the energy dependence of the hadronic processes shown. In particular the elastic pp scattering data are in excellent agreement with the dimensional counting prediction over a large energy and wide angular range, as was already shown in Figure 2.1. However, the other requirement for asymptotic scaling behavior of fixed-angle cross sections, namely that helicity is conserved (see Section 2.4.1) has not been met for this reaction [35].

Reaction	Energy Range (GeV^2)	θ_{cm}	s-dependence (predicted)	s-dependence (measured)	Ref.
$\gamma p \to \pi^+ n$	$8< s <15$	$90°$	7	7.3 ± 0.4	[34]
$\gamma p \to \pi^0 p$	$8< s <10$	$90°$	7	7.6 ± 0.7	[34]
$\gamma d \to pn$	$7.5< s <13.5$	$90°$	11	11.2 ± 0.2	[11]
$pp \to pp$	$15< s <60$	$38°< \theta_{cm} <90°$	10	9.7 ± 0.5	[15]

Table 2.1: For a number of hadronic processes the s-dependence as measured and as predicted by dimensional scaling laws is listed. The last column shows the reference for each reaction.

Table 2.1 also lists the deuteron photodisintegration reaction, $\gamma d \to pn$, which is the only fixed angle hadronic scattering process involving a nucleus, in which scaling (at θ_{cm}=90°) has been observed so far [10, 11]. Applying the scaling model to this reaction, the constituents are identified as follows: $n_d = 6$, $n_p = n_n = 3$, $n_\gamma = 1$. Then using Equation 2.2, their sum $n = n_d+n_\gamma+n_p+n_n = 13$ predicts an energy dependence of the invariant cross section for fixed center-of-mass angle in the asymptotic regime

$$\frac{d\sigma}{dt}(\gamma d \to pn) \quad \stackrel{s\to\infty}{\longrightarrow} \quad s^{-11} f(\theta_{cm}). \tag{2.8}$$

This result is valid in the limit of large $\boldsymbol{p_A} = (s - m_d^2)/(2\sqrt{s})$, which implies that $s \gg m_d^2$.

Figure 2.5 shows the most recent deuteron photodisintegration data from SLAC experiment NE17 [11] for three center-of-mass angles, 37°, 53°, and 90°. Since s^{11} ranges over several orders of magnitude (the s-range for this experiment is $6.59 < s < 18.6$ GeV^2) it is customary to plot the quantity $s^{11} d\sigma/dt$ versus the photon energy for a best observation of the energy dependence. The exponent of s was fitted and the results are n=11.2 ± 0.2, n=10.6 ± 0.6 and n=9.5 ± 0.4 for θ_{cm} = 90°, 53°, and 37° respectively [11]. The 90° data exhibits scaling starting at $E_\gamma \geq$1 GeV,

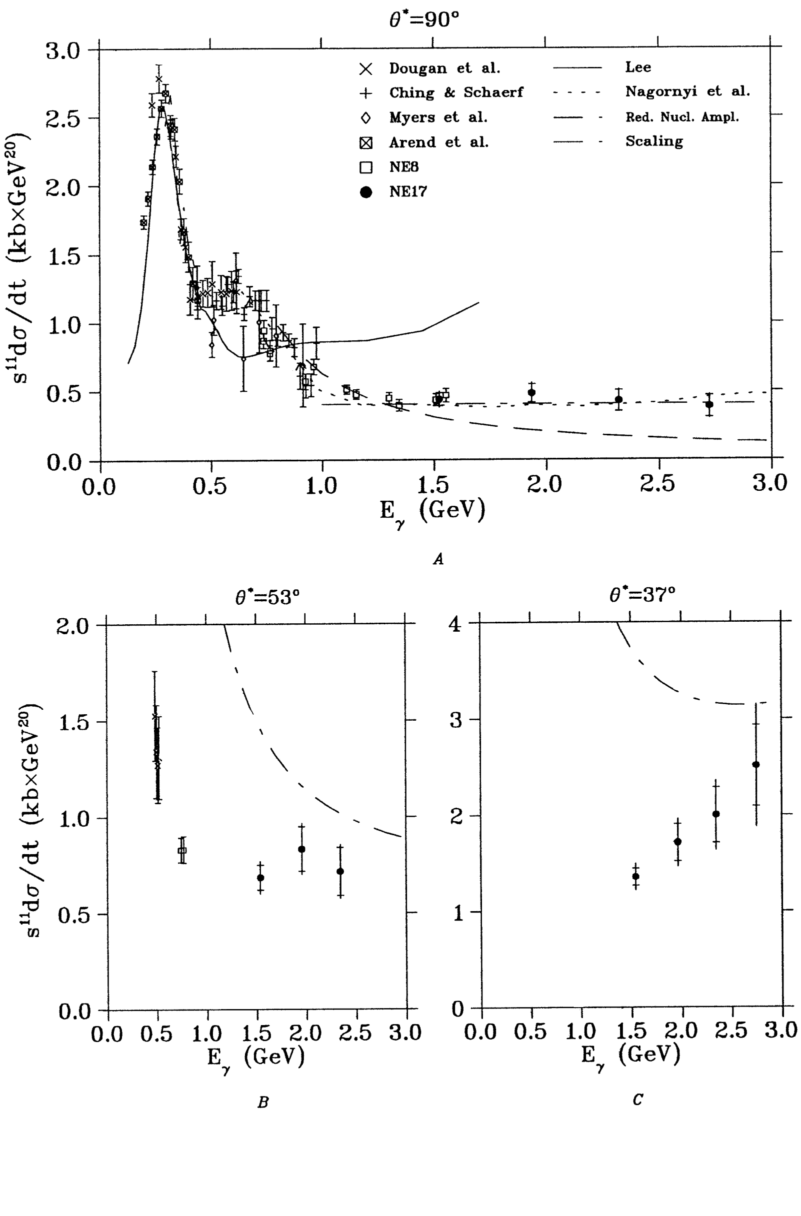

Figure 2.5: Deuteron photodisintegration data for center-of-mass angles 90°(A), 53°(B), and 37°(C). References for the data: Dougan, *et al.* [36], Ching and Schaerf [37], Myers, *et al.* [38], Arend, *et al.* [39], SLAC NE8 [10,40] and SLAC NE17 [11]. The curves are theoretical predictions, which are discussed in the text. Figure adapted from [41].

where the horizontal dashed line is drawn to guide the eye. Consistency of the 53° data with constituent counting rules, is inconclusive and the 37° do not exhibit any scaling. Asymptotic scaling of the deuteron photodisintegration reaction has also been investigated for a different reaction channel, $\gamma d \to d\pi^0$, which is expected to scale as $\sim s^{-13}$. Recent measurements at deuteron center-of-mass angles of 90° and 136° at photon energies up to 4 GeV have provided data which are inconsistent with dimensional scaling rules [42].

The dimensional scaling laws can also be used to describe the large-momentum transfer Q^2 behavior of hadronic electromagnetic form factors. In fact, the invariant cross section for electron-hadron scattering in terms of the spin-averaged electromagnetic form factor [43],

$$\frac{d\sigma}{dt}(eH \to eH') = \frac{4\pi\alpha^2}{t^2} F_H^2(t) f(t/s), \tag{2.9}$$

is a special case of Equation 2.2 in the large energy limit ($Q^2 \gg M^2$, with M the mass of the hadron). In the $eH \to eH$ scattering process, the ingoing and outgoing electrons are counted as one elementary field each, and the hadron has n_H elementary fields in both the initial and final state. In the asymptotic regime, where $s \sim t$, the dimensional scaling law predicts

$$\frac{d\sigma}{dt}(eH \to eH) \sim t^{-2n_H} f(t/s). \tag{2.10}$$

Because $s \sim t$, the ratio t/s is independent of energy, and the function $f(t/s)$ dependents on the θ_{cm} only. Combination of Equations 2.9 and 2.10 then yields the scaling behavior for the spin-averaged electromagnetic form factor:

$$|F_H(t)| \sim |t|^{1-n_H}. \tag{2.11}$$

Thus at large Q^2 the spin-averaged hadronic elastic form factor $F_H(Q^2)$ $(1/Q^2 = 1/|t|)$ has a power law dependence $\sim (Q^2)^{1-n}$. A comparison between the predicted power law behavior and experimental data is shown for a variety of hadron electromagnetic form factors in Figure 2.6 (note that $(Q^2)^{n-1}\sqrt{\sigma/\sigma_M} = (Q^2)^{n-1} F_H(Q^2)$ at small angles, where σ_M is the Mott cross section).

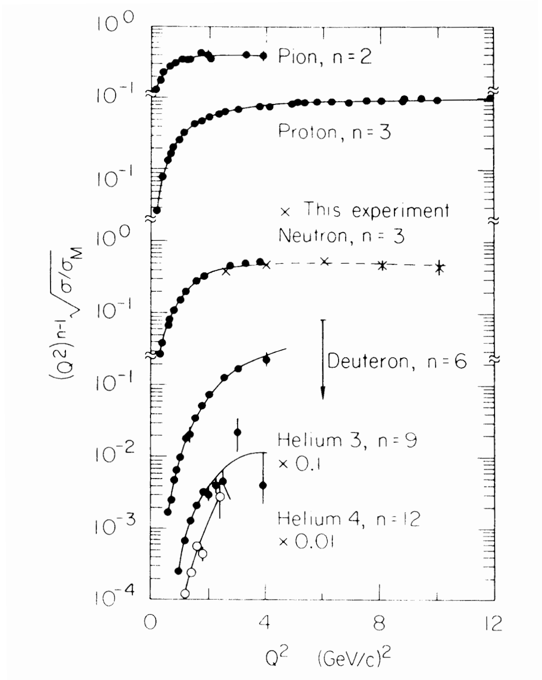

Figure 2.6: Measured spin-averaged electromagnetic form factors of elastic electron-hadron scattering compared with predictions from dimensional scaling laws. The figure is taken from Reference [44].

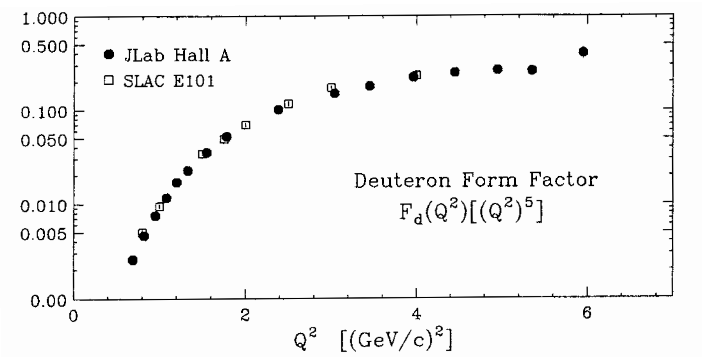

Figure 2.7: The deuteron form factor $F_d(Q^2)$ multiplied by $(Q^2)^5$ as function of the momentum transfer Q^2. Solid dots are recent measurements described in Reference [45]. The open squares are from [46]. The data show a behavior consistent with dimensional scaling rules. The figure is taken from Reference [45].

The dimensional scaling laws appear to explain the monopole behavior of the pion form factor ($F_\pi \sim |t|^{-1}$) and the dipole behavior of the nucleon form factor ($F_N \sim |t|^{-2}$) well at momentum transfers $Q^2 \approx$ few $(\mathrm{GeV/c})^2$. For the deuteron, which is a 6-quark system, $|t|^{-5}$-scaling is expected, which had not previously been observed due to the absence of high-Q^2 data. However, in very recent data [45] scaling of the deuteron form factor has been observed, as shown in Figure 2.7. There have been questions about the validity of dimensional scaling laws at these momentum transfers [47, 48] (in particular in their perturbative QCD interpretation, see Section 2.4.1) and the onset of scaling of the deuteron form factor appears to premature when compared with the empirical lower limit suggested by Holt [18]. This lower limit can be understood by considering the average momentum transfer to the nucleons in the deuteron,

$$|\hat{t}_N^{eN}| \approx m_d T_d/2, \tag{2.12}$$

where T_d is the laboratory kinetic energy of the scattered deuteron. At a momentum transfers $\sim Q^2 = 4$ $(\mathrm{GeV/c})^2$ in elastic ed scattering, the momentum transferred to each nucleon in the deuteron is only $|\hat{t}_N^{eN}| \approx 1$ $(\mathrm{GeV/c})^2$. The nucleon form factor starts to exhibit scaling behavior at $|\hat{t}_N^{eN}| = Q^2 \approx 2$ $(\mathrm{GeV/c})^2$, which would correspond to a deuteron momentum transfer $Q^2 \approx 8$ $(\mathrm{GeV/c})^2$. The absence of scaling of the deuteron form factor prior to the most recent data prompted Brodsky and Chertok [49] to develop their theory of the reduced deuteron form factor in an attempt to obtain a scaling behavior at lower momentum transfer. This theory is described in Section 2.3

2.3 Reduced Nuclear Amplitudes

The reduced nuclear amplitudes (RNA) model [21] originated in the failure of constituent counting rules to describe elastic electron-deuteron scattering up to 4 GeV. In an effort to understand the scaling of the deuteron form factor Brodsky and Chertok [49] developed the concept of a reduced deuteron form factor, which was found to exhibit scaling starting at Q^2 of a few $(\mathrm{GeV/c})^2$.

Their starting point is an interpretation of the deuteron form factor $F_d(Q^2 = -q^2)$ as the probability that the composite deuteron system remains intact after absorbing a four-momentum q. Then, under the assumption that the nuclear binding energy can be neglected, the deuteron can be viewed as two nucleons, which each absorb one-half of the momentum imparted to the deuteron. The probability that each nucleon stays intact after absorbing one-half of the momentum transfer to the deuteron is thus contained in nucleon form factors, and can be factored out. This leads to the definition of the reduced deuteron form factor:

$$f_d(Q^2) = \frac{F_d(Q^2)}{F_n(Q^2/4)F_p(Q^2/4)} \,, \tag{2.13}$$

where the $F_N(Q^2)$, $(N = p, n)$ are the nucleon form factors, which describe the internal degrees of freedom of the nucleons and have a well known scaling behavior. The $F_N(Q^2)$ are given by the dipole formula [19]

$$F_N(Q^2) \sim \frac{1}{(1 + Q^2/0.71 \text{ GeV}^2)^2}. \tag{2.14}$$

By dividing out the asymptotic scaling behavior of the nucleons the nucleus can be considered as a bound state of reduced nucleons, which can be treated as point-like spin-1/2 fermions. The reduced deuteron form factor, now describing the bound state of two point-nucleons, is interpreted as the probability amplitude that the binary system reforms in the ground state after scattering, and is therefore expected to be a decreasing function of Q^2. In fact, since the reduced deuteron effectively has two "constituents", perturbative QCD predicts a $1/Q^2$ dependence for $f_d(Q^2)$ similar to that of the meson form factor:

$$f_d(Q^2) \sim \frac{1}{Q^2 + m_0^2} \longrightarrow \frac{1}{Q^2} \,, \tag{2.15}$$

where m_0^2=0.28 GeV^2 comes from a parameterization of pion form factor data, but is irrelevant at the Q^2 range of interest [21]. Consequently the quantity $Q^2 f_d(Q^2)$ is expected to show asymptotic scaling. Scaling behavior is indeed observed (see Figure 2.8) and extends down to $Q^2 \sim 1$ (GeV/c)^2.

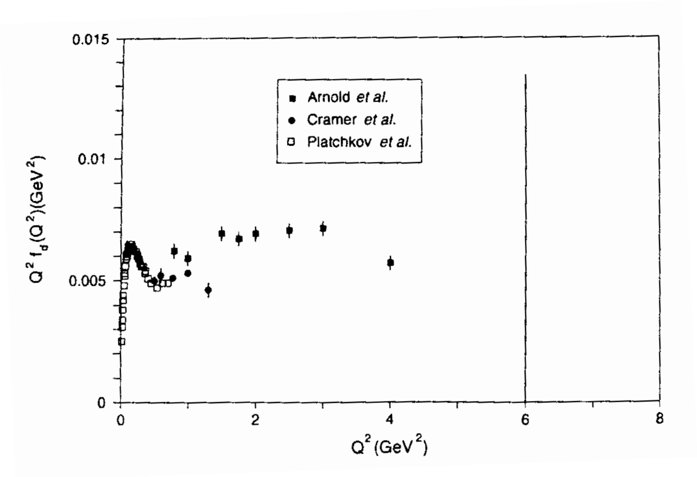

Figure 2.8: Scaling of the reduced deuteron form factor. The figure is from Reference [50]. The data are from Reference [51].

The reduced form factor description draws its power from the premise that the nucleons are allowed to retain their identity in the composite deuteron. This is in contrast with the six-quark bag picture of asymptotic scaling, depicted in Figure 2.9.(a), in which binding of the constituent quarks inside the nucleons is ignored. However, in color SU(3) where the gluon is a color octet, a single gluon exchange between color-singlet nucleons is forbidden, and a color-singlet quark-interchange between the nucleons is necessary to satisfy color selection rules. An example of this interaction is shown in Figure 2.9.(b) . Since the mass scale for the quark-quark interaction inside the nucleon is different from the mass scale of the quark-interchange reaction between the nucleons, and the mass scales can be interpreted as effective binding strengths, a simplification can be made by separating the two interactions according to their mass scales [23]. This separation provides the justification for the reduced form factor approach.

Based on the success of the description of *ed* elastic scattering using reduced nuclear form factors, Brodsky and Hiller [21] introduce a more general theory of reduced nuclear scattering amplitudes. For a nuclear process with amplitude $\mathcal{M}(s,t)$ that involves A ingoing and outgoing nucleons, the reduced nuclear amplitude is

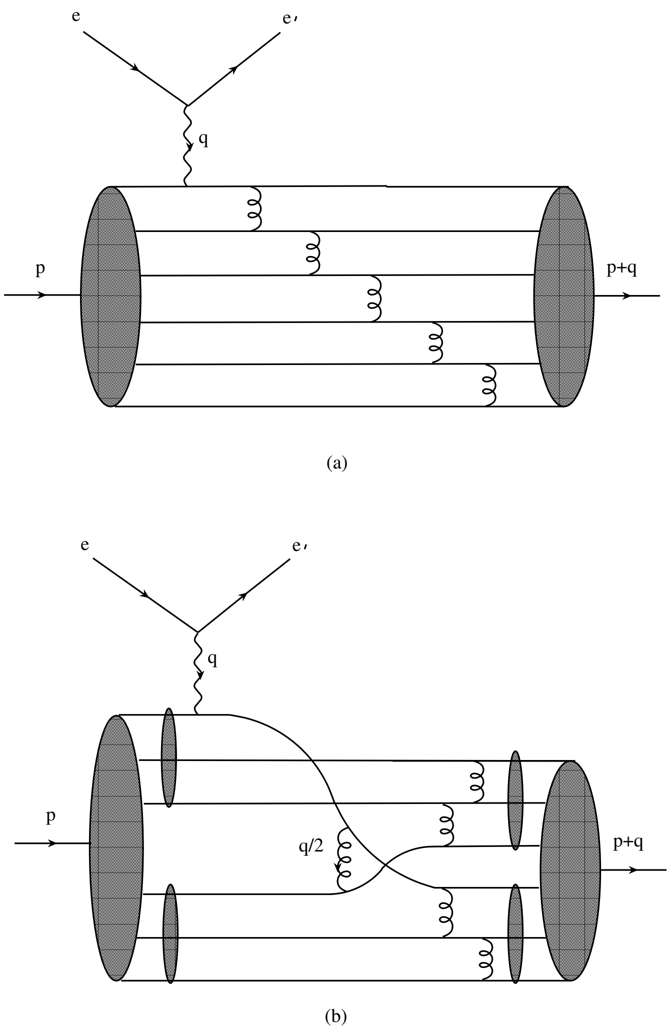

Figure 2.9: Two views of elastic electron deuteron scattering: (a) shows the democratic chain model; (b) shows the quark-interchange model. Figure after Brodsky and Chertok [49].

defined as

$$m(s,t) = \mathcal{M}(s,t)\left[\prod_{i=1}^{A} F_N(\hat{t}_i = q_i^2)\right]^{-1}, \tag{2.16}$$

where q_i is the four-momentum transfer to nucleon i. Hence, for the exclusive deuteron photodisintegration reaction, the reduced nuclear amplitude is expressed in terms of the true amplitude $\mathcal{M}_{\gamma d\to pn}$ as

$$m_{\gamma d\to pn} = \frac{\mathcal{M}_{\gamma d\to pn}}{F_n(\hat{t}_n)F_p(\hat{t}_p)}. \tag{2.17}$$

Because the binding energy of the deuteron is neglected in this description, both nucleons receive an equal portion of the nuclear momentum, and the momentum transfer to each of the two nucleons (N=p,n) in the deuteron, expressed in terms of the initial four-momentum of the deuteron (p_d) and the four-momentum of the recoiling nucleon (p_N) is given by:

$$\hat{t}_N = (p_N - \frac{1}{2}p_d)^2 \ . \tag{2.18}$$

The fixed center-of-mass angle scaling behavior of the reduced nuclear amplitude is predicted by dimensional scaling [24, 30]:

$$m \sim {p_T}^{4-n} f(t/s) \ , \tag{2.19}$$

where p_T is the transverse momentum given by

$$p_T^2 = tu/s \ . \tag{2.20}$$

The factor n in the exponent of p_T is the total number of ingoing and outgoing photons, leptons, gluons, quarks and *reduced* nucleons. For the deuteron photodisintegration reaction where n=5 (one photon and 4 reduced nucleons), the reduced nuclear amplitude scales as:

$$m_{\gamma d\to pn} \sim {p_T}^{-1} f(\theta_{cm}), \tag{2.21}$$

with $p_T^2 = \frac{1}{2} m_d E_\gamma \sin^2(\theta_{cm})$, and θ_{cm} the angle of direction of the outgoing proton with the beam direction in the center-of-mass frame. Examining equation (2.21), Brodsky and Hiller express the hope that simple scaling $m_{\gamma d\to pn}p_T \simeq$ constant will occur for fixed θ_{cm} at $p_T^2 \geq 1$ (GeV/c)^2, since the deuteron form factor begins to scale in that regime. The differential cross section is proportional to $|\mathcal{M}_{\gamma d\to pn}|^2$ and a kinematical factor. Combining Equation (2.17) and Equation (2.21) gives

$$\left(\frac{d\sigma}{d\Omega}\right)_{cm} \propto \frac{1}{\sqrt{s(s-m_d^2)}} F_p^2(\hat{t}_p) F_n^2(\hat{t}_n) \frac{1}{p_T^2} f^2(\theta_{cm}). \tag{2.22}$$

In comparison with data they suggest that $f^2(\theta_{cm})$ must be independent of energy at any fixed angle to obtain the predicted scaling, and peaked in the forward or backward direction at energies approaching the scaling limit. The long dashed line in Figure 2.5 shows the prediction according to Equation (2.22). The calculations for the three center-of-mass angles have a common normalization to the 0.8 GeV data point at θ_{cm}=90°. At 90° the calculation is lower than the previous data and does not reach the predicted asymptotic limit. For the other two angles shown, the calculation predicts too high a cross section.

2.4 QCD Descriptions of Deuteron Photodisintegration

The theoretical models which have been discussed so far did allow for a compositeness of the deuteron (in case of the RNA in terms of nucleons with a substructure), but did not include a description of the dynamics of the substructure. In the following sections three models are presented that attempt to describe the deuteron photodisintegration process and other asymptotic exclusive reactions using quantum chromodynamics (QCD), which describes the fundamental degrees of freedom of hadrons in terms of constituent quarks and gluon fields.

2.4.1 Dimensional Scaling in the Perturbative QCD Picture

Even though the dimensional scaling laws can be readily derived from perturbative quantum chromodynamics (QCD, calculated using perturbation theory, pQCD) it is often overlooked that the original scaling laws discussed in Section 2.2 were developed before the existence of QCD. In their paper on QCD and nuclear physics [17], Brodsky and Lepage state that the power law behavior of the QCD predictions for exclusive processes at large momentum transfer is characterized by simple counting and helicity rules. To leading order in $1/Q$ the following two criteria have to be met:

1. The total hadron helicity is conserved.

2. Dimensional scaling laws (Equation 2.2) predict the power law scaling of the cross section of fixed center-of-mass angle scattering processes.

The first criterion was not present in the original "dimensional" derivation of the scaling laws, and has its origin in the QCD coupling of gluons to quarks. Helicity, usually denoted by λ, is spin along the direction of motion. Under the assumptions that the quark mass and binding effects are small, and that the valence quarks dominate the dynamics of the hadrons, one can view a hadron, moving rapidly in one direction, as a collection of quarks, moving in the same direction, where the hadron helicity is the sum of the quarks helicities. Thus criterion 1 implies that electromagnetic form factors are helicity conserving and independent of total spin to leading order in $1/Q$. An illustration of how the dimensional scaling results can be understood in terms quark-rescattering is shown in Figure 2.10, which is a lowest order pQCD diagram for elastic electron-nucleon scattering. In the pQCD description of elastic electron-

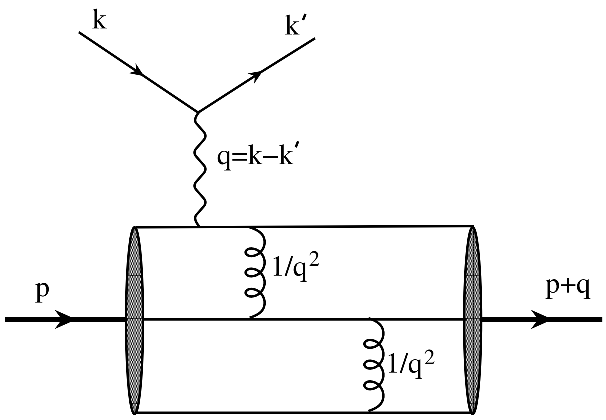

Figure 2.10: Diagram of the perturbative QCD quark rescattering description of elastic electron-nucleon scattering.

nucleon scattering the electron exchanges a virtual photon carrying four-momentum q with a quark in the nucleon. To rebind the nucleon, the four momentum is distributed to the remaining two quarks via the exchange of two hard gluons. Each of the gluons carries a momentum factor $1/q^2 = 1/|t|$, so that the total t-dependence goes

$\sim 1/|t|^2$ which is the familiar dipole form factor dependence. Similarly, for the elastic electron-deuteron scattering depicted in Figure 2.9.a the pQCD quark re-scattering picture gives a $\sim 1/|t|^5$ dependence. Thus, in this simple picture, the form factor of a hadron with n_h constituents is obtained by multiplication of the $n_h - 1$ gluon propagators and Equation 2.11 is obtained.

More rigorous prescriptions to obtain the scaling behavior in a pQCD description are given by Carlson [52] and in References [53, 54], where the latter authors include a set of rules to treat the quark helicity at the quark-gluon vertex. In Carlson's [52] description Figure 2.10 represents the lowest order diagram for the helicity amplitude G_+ (a positive helicity virtual photon hitting a quark inside the nucleon), which for elastic scattering is related to the magnetic nucleon form factor $G_M \propto F_N(Q^2)$ through $G_+ \sim QG_M$. Scaling with Q of a diagram for G_+ as depicted in Figure 2.10 is obtained by:

- counting each internal fermion propagator as $1/Q$.
- counting each internal gluon propagator as $1/Q^2$.
- considering the Dirac spinor for each external quark line; if helicity is conserved a scaling factor of Q is assigned to that line.

For the leading amplitude the hadronic helicity is conserved, and the amplitude scales as

$$G_+ \propto Q^3 \left(\frac{1}{Q}\right)^2 \left(\frac{1}{Q^2}\right)^2 = \frac{1}{Q^3} , \tag{2.23}$$

so that $G_M \sim Q^{-4}$ which is in agreement with the nucleon dipole form factor.

Carlson and Gross [54] provide three simple rules to determine the Q^2 and spin dependence of hadronic form factors. In order to formulate the rules, a diagram like the one shown in Figure 2.10 is divided into subgraphs, which are depicted in Figure 2.11. The three rules are then formulated as follows:

- *The one-gluon rule* (see Figure 2.11.(a)). The amplitude of this subgraph is proportional to Q for a transverse (T) gluon, or proportional to m (a mass

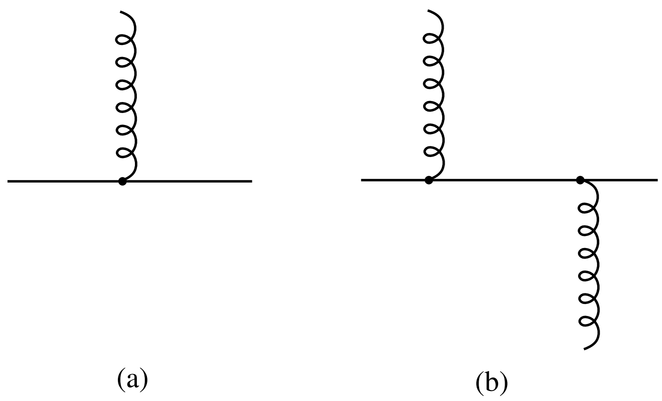

Figure 2.11: Subgraphs of the the scattering diagram shown in Figure 2.10.

scale) for a longitudinal (L) gluon. The quark helicity is conserved in the case of the T-gluon and flipped for the L-gluon.

- *The two-gluon (or gluon-photon) rule* (see Figure 2.11.(b)). In this subgraph one gluon is absorbed, and one emitted. In the case that one gluon is transverse and the other longitudinal, the helicity is conserved and the amplitude of the subgraph does not depend on Q^2 (this includes the quark propagator, but not the gluon propagators). When both gluons are longitudinal the helicity is flipped, and the amplitude is of $\mathcal{O}(m/Q)$. If both gluons are transverse, the amplitude is zero.

- *The transverse gluon rule.* Two quark lines connected by a transverse gluon have opposite helicities. Helicities of quark lines connected by a longitudinal gluon have no correlation.

By applying these rules to the helicity $+1/2$ –helicity $+1/2$ leading order diagram for elastic electron-nucleon scattering, where the virtual photon is transversely polarized (see Figure 2.12) one can readily show that the amplitude falls as $1/Q^4$ (again using the relationship $G_+ \propto QG_M$) as was seen above. The added information in this picture is the insight into the helicity conservation. Thus, pQCD provides a mechanism

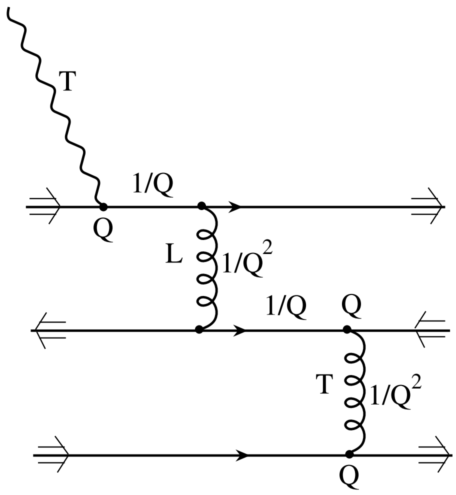

Figure 2.12: Leading order helicity $+1/2$ –helicity $+1/2$ diagram of elastic electron-nucleon scattering. The large arrows indicate the helicity of the quarks.

to describe asymptotic scaling in form factors and exclusive reactions, but the validity of the application of these mechanisms at momentum transfers $Q^2 \approx$ few $(\mathrm{GeV/c})^2$ remains a controversial topic [47, 48, 55].

The picture outlined above where each gluon propagator contributes a factor $1/Q^2$ to the form factor or exclusive fixed-angle scattering amplitude yields the correct Q^2 dependence of the form factors and cross sections, but leaves out important information about the strong interactions. For a more correct description, the coupling constant $\alpha_s(Q^2)$ which describes the strength of the quark-gluon interaction, has to be included at each quark-gluon vertex. Then, each gluon contributes a factor $\alpha_s(Q^2)/Q^2$ to the scattering amplitude. Therefore, if the constituent counting rules are a result of pQCD, one not only has to include the $1/Q^2$ dependence from the gluon propagators, but also factors $\sqrt{\alpha_s}$ at each gluon-quark vertex. Then scaling violations are expected, especially when many hard gluon transfers are present in the reaction.

As an example consider the deuteron form factor. The hard scattering diagram in Figure 2.9.(a) shows the leading order diagram in which five hard gluons are exchanged. When the factors of $\sqrt{\alpha_s(Q^2)}$ at each vertex are included, (but neglecting any logarithmic dependences) the deuteron form factor becomes [17]

$$F_d(Q^2) \sim \left(\frac{\alpha_s(Q^2)}{Q^2}\right)^5 . \tag{2.24}$$

The factor $\alpha_s(Q^2)^5$ could give rise to strong scaling violations. However, scaling of the deuteron form factor is traditionally described in terms of the reduced deuteron form factor (see Section 2.3), which is obtained by dividing two factors $F_N(Q^2) \sim (\alpha_s(Q^2)/Q^2)^2$ out, so that only one power of $\alpha_s(Q^2)$ remains, $f_d(Q^2) \sim \frac{\alpha_s(Q^2)}{F_d(Q^2)}$. With this reduction (division) the scaling violations, or soft gluon processes, which are contained in the nuclear form factors, are removed.

It is instructive to estimate the size of possible scaling violations for the deuteron photodisintegration reaction, which observes the dimensional scaling behavior at θ_{cm}=90° over an energy region $1 < E_\gamma < 3$ GeV. In this energy region the momentum transfer per quark in the deuteron, Q^2/quark, varies from 1/36 to 9/36 (GeV/c)^2, which is well below the ~1 GeV^2 where Bjorken scaling sets in, making the observed scaling behavior at such a low energy surprising. Following the above reasoning, the deuteron photodisintegration cross section is expected to have a $[\alpha_s(Q^2)/Q^2]^{10}$ dependence in leading order.

An estimate of the $\alpha_s(Q^2)^{10}$ Q^2-dependence over the energy range over which scaling is observed was made using the running coupling constant (Equation 2.1) and Λ_{QCD}=200 MeV. Since $Q^2/\Lambda^2_{QCD} \gg 1$ for the running coupling constant to be valid, the lower limit on E_γ is 1.3 GeV. Over this range a predicted fall-off due to the ten powers of the strong coupling constant of $\sim 10^{10}$ is expected. This fall-off is not observed, and a possible explanation is that the coupling $\alpha_s(Q^2)/Q^2$ which enters the hard scattering amplitude is effectively frozen at the low virtualities involved, resulting in minimal scaling violations [56]. Several authors have proposed models in which the coupling constant is modified for the soft region. In one approach, Cornwall [57] proposes a formula for $\alpha_s(Q^2)$ in the form of

$$\alpha_s(Q^2) = \frac{4\pi}{(11 - \frac{2}{3}n_f)\log[(Q^2 + m_g^2)/\Lambda_{QCD}^2]}. \tag{2.25}$$

which introduces a cut-off by means of the mass-parameter m_g. This parameter is interpreted as a dynamical gluon mass, and has a typical value of 0.5 GeV^2. For momentum transfers $Q^2 \gg m_g^2$ the familiar running coupling constant from Equation 2.1 is obtained, but at very low momentum transfers, Equation 2.25 "freezes" the coupling constant to some finite value. In an effort to obtain finite values for $\alpha_s(Q^2)$ in the soft regime, Capstick and Isgur [58] assume that $\alpha_s(Q^2)$ saturates at some critical value when $Q^2 \to 0$. They construct the following parameterization (Q^2 is in (GeV/c)^2):

$$\alpha_s(Q^2) = 0.25e^{-Q^2} + 0.15e^{-Q^2/10} + 0.20e^{-Q^2/1000}\,. \tag{2.26}$$

For these two models $\alpha_s(Q^2)^{10}$ was also evaluated and the ratio

$$R_\alpha = \alpha_s(Q^2_{low})^{10}/\alpha_s(Q^2_{high})^{10} \tag{2.27}$$

was computed, where Q_{low} and Q_{high} are the values of the momentum transfer corresponding to the limits of the energy interval. The ratio is expected to be an indication of expected scaling violations. The results for R_α are shown in Table 2.2. A comparison of the results for R_α with the experimental observed scaling behavior in this Q^2-range suggests that perhaps the coupling constant reaches a finite value in the soft region for exclusive reactions.

2.4.2 QCD Rescattering with Final State Interactions

Frankfurt *et al.* [25] investigate a description of the deuteron photodisintegration process in which a quark in one nucleon absorbs the real photon, and has a high momentum transfer (hard) scattering with a quark in the other nucleon, creating a final state with two nucleons with high relative momentum. A diagram of this process is shown in Figure 2.13. A brief outline of the theory is presented in this section.

Model and Reference	Q^2-range $(\mathrm{GeV/c})^2$	R_α
Running Coupling Constant [19]	0.028–0.25	$\sim 10^{10}$
Frozen Coupling Constant (Cornwall) [57]	0.028–0.25	1.7
Capstick-Isgur Parameterization [58]	0.028–0.25	2.3

Table 2.2: Comparison of the $\alpha_s(Q^2)$-dependence of the pQCD scaling result for leading order deuteron photodisintegration over the energy range $1.3 < E_\gamma < 3$ GeV for three models of the coupling constant. In the models Λ_{QCD}=200 MeV is used.

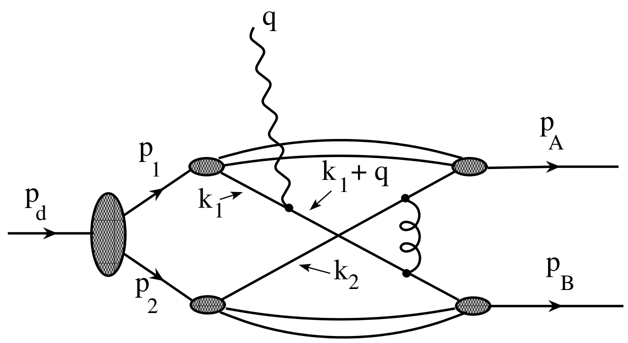

Figure 2.13: Quark rescattering diagram, after Reference [25].

The detailed formulae and justification can be found in [25].

Frankfurt *et al.* start with the hypothesis that the size of the photodisintegration reaction is determined by the physics of high-momentum transfer contained in the hard scattering NN amplitude. They suppose that, since the deuteron is a loosely bound system, the contribution coming from the low relative momentum (<300 MeV/c) two-nucleon component of the deuteron wave function is dominant, and that the short-range behavior of the deuteron wave function is not important. They show that the scattering amplitude for the process in Figure 2.13, with a deuteron (four-momentum p_d, mass m_d) in the initial state and two nucleons of momenta p_A and p_B in the final state is a convolution between the large angle pn scattering amplitude, the hard photon-quark interaction vertex, and the soft component of deuteron wave function.

In this particular process, the scattering amplitude depends on the quark-interchange mechanism contribution to the wide-angle nucleon-nucleon scattering amplitude, A_{pn}^{QIM}, and all other quark interactions are included in the wave functions of the nucleon. The amplitude A_{pn}^{QIM} represents a sum of all leading quark interchange diagrams. In these diagrams, the spectator quark-gluon systems are represented with a general structure, so that A_{pn}^{QIM} absorbs the non-perturbative part of the calculation. Frankfurt *et al.* further make use of the observation that quark-interchange is the dominant topology for (non strange) baryon-baryon and meson-baryon scattering at θ_{cm}=90° and high momentum transfer [59], and in fact replace A_{pn}^{QIM} by experimental cross section data for $pn \to pn$ scattering, $\frac{d\sigma^{pn\to pn}}{dt}$ at $t_N = (p_B - p_d/2)^2$. Through the above prescription they arrive at a formulation of the $\gamma d \to pn$ invariant cross section:

$$\frac{d\sigma^{\gamma d\to pn}}{dt} = \frac{4\alpha}{9}\pi^4 \cdot \frac{1}{s'}C(t_N/s)\frac{d\sigma^{pn\to pn}(s,t_N)}{dt} \times \left| \int \Psi_d^{NR}(p_z = 0, p_\perp)\sqrt{m_N}\frac{d^2 p_\perp}{(2\pi)^2} \right|^2 , \tag{2.28}$$

where $s' = s - m_d^2$ and $\alpha = \frac{p_{1+}}{p_{d+}}$[5]. Thus the cross section depends on the soft component of the wave function, the measured high momentum transfer $pn \to pn$ cross section, and the function $C(\frac{t_N}{s})$, which accounts for the difference between the hard propagators in $\gamma d \to pn$, and those in wide angle pn scattering. The function $C(\frac{t_N}{s})$ is a slowly varying function of θ_{cm} and approximately equal to unity at $\theta_{cm} \sim 90°$. In their calculations Frankfurt *et al.* use $C(\frac{t_N}{s})$=1. Furthermore they use a non-relativistic Paris potential [60] model of the deuteron wave function, Ψ_d^{NR}, since the scattering amplitude depends on only small relative momenta of target nucleons. Experimental data are used for $\frac{d\sigma^{pn\to pn}}{dt}$, but since the $pn \to pn$ data are not measured at t_N, the model is calculated using existing pn data at $t_N^{min,max}$ with $-t_N^{min} < -t_N < -t_N^{max}$ so that the predicted cross sections form a band.

[5] The light cone four-momentum is defined as $p = (p_+, p_-, p_\perp)$, where $p_\pm = E \pm p_z$. The z-axis is defined to point in the direction opposite to the photon.

For their hard scattering mechanism to be valid a number of kinematic conditions must be met. First, because the partonic picture is chosen over a description of intermediate baryon resonances, the mass of the intermediate (between the photon absorption and quark rescattering) virtual state, $m_{int} \sim \sqrt{2E_\gamma m_N}$, has to be larger than the continuum threshold ($\approx$ 2.2 GeV), which implies that $E_\gamma \geq 2.4$ GeV. Next, the struck quark in nucleon 1 should be energetic enough to reach the quark in nucleon 2 without radiating soft bremsstrahlung gluons. The radiation of bremsstrahlung gluons by a scattered quark is governed by the regeneration length $l_{regen} \approx E_\gamma R^2$ [33], where R is identified with the confinement radius ($R \approx 0.3$ fm). A quark traveling in excess of the regeneration length is likely to radiate bremsstrahlung gluons. Therefore in order to prevent the radiation of bremsstrahlung gluons, the regeneration length has to be larger than or at best comparable to the nucleon radius and typical inter-nucleon distances in the loosely bound deuteron. A typical distance is 1.1 fm, which restricts the applicability of this method to photon energies $E_\gamma \geq 2.5$ GeV. The final requirement is on the transverse momentum of the final nucleons, which should be large enough to ensure that hard quark rescattering occurred. This is the case for final state nucleons with $p_T \geq 1$ GeV/c, giving $-t \geq 2$ GeV^2. Thus the model is applicable for $E_\gamma \geq$ 2.4–2.5 GeV and $-t \geq 2$ GeV^2, and able to make a prediction for cross sections measured in this experiment at all angles. This model is compared with the present data in Section 6.2.3.

2.4.3 The Quark Gluon String Model

Kondratyuk *et al.* [26] apply the quark-gluon string (QGS) model [61] and Regge phenomenology to obtain a description of the $\gamma d \to pn$ cross section in the region of small momentum transfers t and u. A comprehensive discussion of Regge theory is given in Reference [62]. In Appendix B an overview of the fundamentals of Regge theory pertaining to the discussion in this section is presented.

Regge phenomenology requires absence of resonances in the cross section, so the deuteron photodisintegration reaction is a very suitable reaction to study, since it has no resonances above the Δ peak ($\sim$280 MeV), and a theory can be formulated starting at energies above a few hundred MeV. The kinematic region of interest is at higher energies, but different from the one where dimensional scaling rules are valid (large s, t/s fixed, i.e. $t \gg 1$ (GeV/c)^2), namely the region where s is large, but t and u are still small ($t \leq 1$ (GeV/c)^2). In this region Kondratyuk *et al.* suppose that the photodisintegration amplitude is dominated by the exchange of three valence quarks in t or u channels, and that any number of gluons can be exchanged between the valence quarks. They then proceed by describing the reaction dynamics using the quark-gluon string model [61] for binary hadronic reactions at high energy. In the QGS model hadrons are pictured as "bubbles" in a "liquid" vacuum and a high energy collision between hadrons is described in terms of interactions between these bubbles. In these interactions only slow quarks will annihilate or have interactions, while the fast "spectator" quarks move and penetrate the liquid, stretching the strong field lines, so that a color tube is formed. For large enough separation the color tube splits into smaller $q\bar{q}$ fragments. Thus in space time representation, the deuteron photodisintegration reaction can be described by the formation of a quark-gluon string in the intermediate state. One of the diagrams describing this process for deuteron photodisintegration is depicted in Figure 2.14.(a) , where the intermediate state is denoted by a dashed line. In Regge theory, this quark-gluon string can be identified with a Regge trajectory. The fermion Regge pole is responsible for the dominant contribution to the deuteron photodisintegration reaction. In this description, a Reggeon, an assembly of three quarks and several gluons, with angular momentum $\alpha_N(t)$ is exchanged, as depicted in Figure 2.14.(b) .

By combining the Regge phenomenology and QGS model Kondratyuk *et al.* obtain a parameterization for the cross section of the deuteron photodisintegration reaction in the form

$$\frac{d\sigma_R}{dt} = \frac{1}{64\pi s}\frac{1}{p_{c.m.}^2}\left[|T(s,t)|^2 + \frac{1}{R}|T(s,u)|^2\right] , \tag{2.29}$$

where $p_{c.m.}$ is the photon momentum in the center-of-mass frame, $T(s,t)$ and $T(s,u)$ the photodisintegration amplitudes, and R the forward-backward ratio of the cross

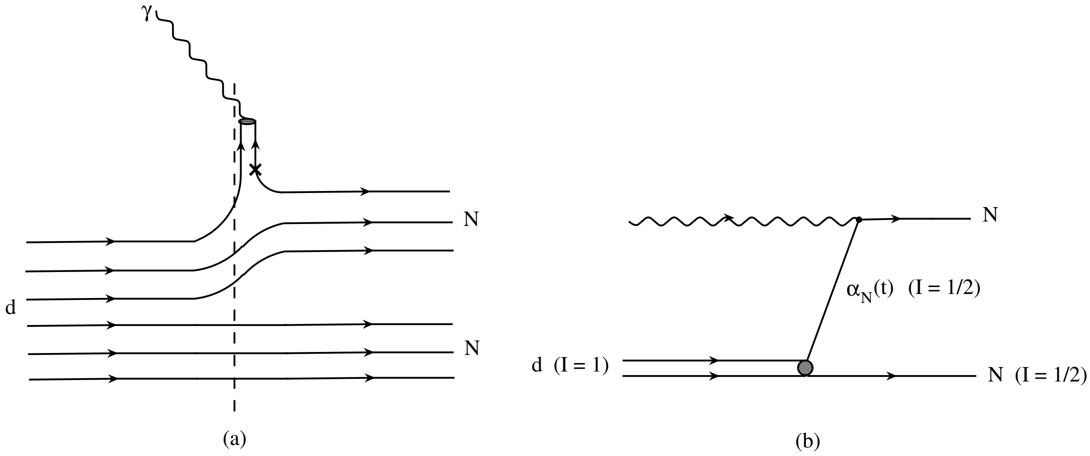

Figure 2.14: Diagrams of deuteron photodisintegration in the QGS and Regge description. In the space-time picture figure (a) corresponds to the creation of a string in the intermediate state (denoted by the dashed line) with at one end a fast quark. At the point "×" the string breaks up via the creation of $q\bar{q}$ pairs from vacuum. Finally the pieces of string form a proton and neutron. Figure (b) shows the same process in Regge language, where the quark-gluon string is identified with the exchange of a Reggeon $\alpha_N(t)$.

section values. The forward-to-backward ratio R is obtained from the naive quark model [63], where it is related to the charges z_u and z_d of the u and d quarks in the nucleons:

$$R = \frac{(d\sigma/d\Omega)_{0^\circ}}{(d\sigma/d\Omega)_{180^\circ}} = \frac{2z_u^2 + z_d^2}{2z_d^2 + z_u^2} = 1.5 \ . \tag{2.30}$$

The fermion Regge-pole exchange governs the energy behavior of the amplitude $T(s,t)$. For fixed t the energy behavior is given by [61, 62]

$$T(s,t) \approx F(t) \left(\frac{s}{s_0}\right)^{\alpha_N(t)} \cdot \exp\left[-i\frac{\pi}{2}\left[\alpha_N(t) - \frac{1}{2}\right]\right] \ , \tag{2.31}$$

where $\alpha_N(t)$ is the trajectory of the N Regge pole, and $F(t)$ the residue of the pole. The parameter s_0 is equal to the square of the deuteron mass, and the exponential represents a phase factor. The $\alpha(t)$ dependence of the scattering amplitude, as in Equation B.3 is evident. The photodisintegration amplitude $T(s,u)$ is obtained from Equation 2.31 by substituting t with u. The baryon Regge trajectory $\alpha_N(t)$ is deduced from data on πN backward scattering, and includes a known non-linearity, compared to the more standard linear form, Equation B.2. The trajectory $\alpha_N(t)$ is parameterized as

$$\alpha_N(t) = \alpha_N(0) + \alpha'_N(0)t + \frac{1}{2}\alpha''_N t^2 \ . \tag{2.32}$$

The coefficients have values $\alpha'_N(0)$=0.9 GeV^{-2}, α''_N=0.25 GeV^{-4}, and $\alpha_N(0)$=−0.5, where the latter is the intercept for the nucleon Regge trajectory N_α, which is the relevant choice of Regge trajectory for this case. When Equations 2.31 and 2.32 are combined with Equation 2.29, the deuteron photodisintegration reaction at small t and high photon energy has a predicted energy dependence

$$\frac{d\sigma_R}{dt} \sim \frac{|T(s,t)|^2}{s^2} \sim \left(\frac{s}{s_0}\right)^{2\alpha_N(t)-2} . \tag{2.33}$$

The residue of the pole depends on t, and is given by

$$F(t) = B(\theta_{cm}) \left[\frac{1}{m_N^2 - t} \exp\left(-R_1^2 t\right) + C \exp\left(-R_2^2 t\right)\right] \ , \tag{2.34}$$

where the first term is due to the nucleon pole in the t channel, and the second term accounts for the contribution of non-nucleon degrees of freedom in the deuteron. The coefficients in this equation are obtained from fits to data. The following values are used: C=0.7 GeV^{-2}, R_1 =1.0 GeV^2, R_2 =−0.1 GeV^{-2}, and $B(\theta_{cm}) = (C_1 + C_2 \sin^2\theta_{cm})$, with C_1=6.99 μb$^{1/2}$GeV^3 and C_2=7.12 μb$^{1/2}$GeV^3. The parameterization of B in terms of θ_{cm} is necessary to ensure gauge invariance, analyticity and conservation of angular momentum, which is obtained in Regge phenomenology by considering all possible helicity amplitudes. The actual form of B corresponds to the differential cross section, averaged over the initial and summed over the final helicities.

A few remarks of the validity of this approach are in place. Even though the Regge pole analysis of exclusive hadronic reactions was formulated before the development of quantum chromodynamics, this phenomenological application remains valid, since the theory is based on fundamental properties of the scattering amplitude, such as analyticity, unitarity and crossing symmetry. In a quantum mechanical approach, high energy implies that the wavelength of photon must be smaller than radius of the target, $\lambda \sim 1/E_\gamma \ll R_0$. In QCD R_0 is the radius of confinement, $R_0 \sim 1$ fm, and this requirement is reasonably satisfied for $1/E_\gamma \geq 1$ GeV. In Regge phenomenology, the requirement on s is that it has to be much in excess of a characteristic value of t, which is around 1 (GeV/c)^2. The values of $|t|$ and $|u|$ are generally limited to ≤ 1 (GeV/c)^2 to avoid having secondary singularities in the complex angular momentum plane come into play.

With the definitions and parameter values in place, a comparison to the data can be made. The predicted energy dependence of the cross section at fixed θ_{cm} comes from Equation 2.29:

$$\frac{d\sigma}{dt} \sim F^2(t) s^{2\alpha-2} \ . \tag{2.35}$$

In this form no power law of energy can be obtained, but in a limited energy region the parameterization $\frac{d\sigma}{dt} \sim s^{-n}$ can be approximately made, where the power n depends on the center-of-mass angle. This parameterization of the cross section has been plotted in Figure 2.15 for three center-of-mass angles, θ_{cm}=37°,53°, and 90°. Experimental data from SLAC experiment NE17 [11] have been included in this figure. For the powers of s in the parameterization, L.A. Kondratyuk *et al.* find n=9.1 for θ_{cm}=37°, n=10.3 for θ_{cm}=53°, and n=11.8 for θ_{cm}=90°. A comparison of the values of n at these angles with exponents of s, fitted from the SLAC NE17 results (see Section 2.2, Figure 2.5 or Reference [11], $n=11.2 \pm 0.2$, $n=10.6 \pm 0.6$ and $n=9.5 \pm 0.4$ for θ_{cm}=90°, 53°, and 37° respectively) shows that the experimentally fit values are in good agreement with the QGS-model prediction. However, the parameterized and fit values of n are only in agreement with the prediction of the dimensional scaling rules (Equation 2.8) for θ_{cm}=90°. For the angles θ_{cm}=37° and 53° $|u|$ is considerably larger than $|t|$, so that the term proportional to $1/R$ in Equation 2.29 can be neglected. The data at these two angles falls within the t-region where the model is valid. At θ_{cm}=90° $t = u$, and both T-amplitudes contribute, the second one with a factor $1/R$=2/3. The data at this angle has larger t and falls outside the region of validity of the theory, and the agreement is not as good, as shown in the figure.

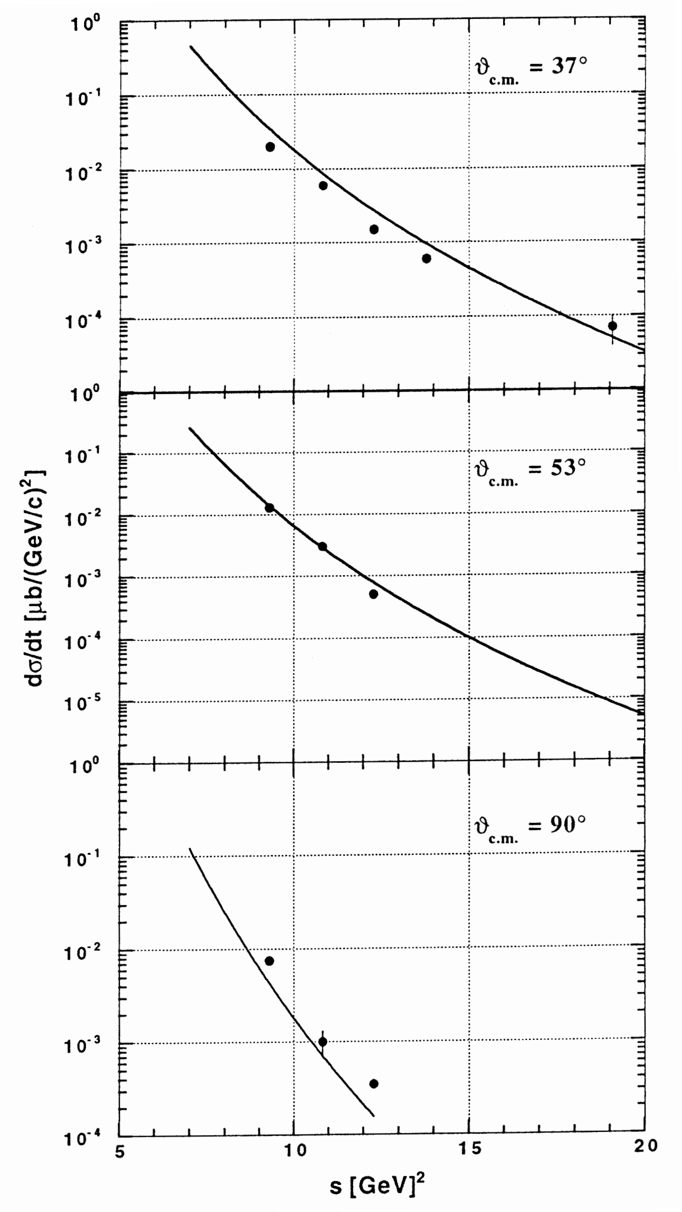

Figure 2.15: Invariant differential cross sections as function of s for two-body deuteron photodisintegration at center-of-mass angles θ_{cm}=37°,53°, and 90°. The curves are theoretical predictions using the formalism described in the text. The data is from Reference [11]. The figure is taken from Reference [26].

2.5 Meson-Exchange Models

Traditionally the meson is considered to be the mediator of the nuclear force. Meson-exchange models have been successful in describing nuclear physics reactions at low energies and momentum transfers, using hadronic degrees of freedom, in terms of nucleons that interact by exchanging mesons [8]. A variety of meson-exchange models exist, which often use different potentials for the nucleon-nucleon (NN) interaction. The NN interaction has been well studied, and many descriptions of the NN-potential exists, see for example Reference [64], in which a discussion of the Paris potential is presented.

In this framework the mechanism of the photodisintegration reaction is essentially described as follows: the incident photon is absorbed by one of the nucleons in the deuteron forming an excited state, which decays, creating one or more mesons which in turn are absorbed by the other nucleon. The exchanged meson is generally a pion (the lightest meson), but heavier mesons like the ρ or ω are included in some of the models. Some calculations are also extended to included a two-pion exchange through a strong s-wave $\pi\pi$ interaction, which is often represented by a fictitious σ "meson". Other refinements of the theory include the inclusion of resonant states of the nucleon, such as the $\Delta(1236)$[6] or N*(Roper) resonances. Many models include so-called final state interactions (FSI) which describe the interactions of the outgoing nucleons with each other through the exchange of mesons. The calculations are constrained by a range of experimental data such as elastic and inelastic nucleon-nucleon scattering, and use a set of adjustable parameters. Figure 2.16 shows generic diagrams of the predominant processes that contribute to deuteron photodisintegration, described in hadronic degrees of freedom.

The many different approaches in modeling of the deuteron photodisintegration reaction using meson-exchange models, have been reasonably successful in describing the low and intermediate [8, 65] energy dependence of the process, but most models

[6] The number in parentheses represents the mass of the resonance in MeV.

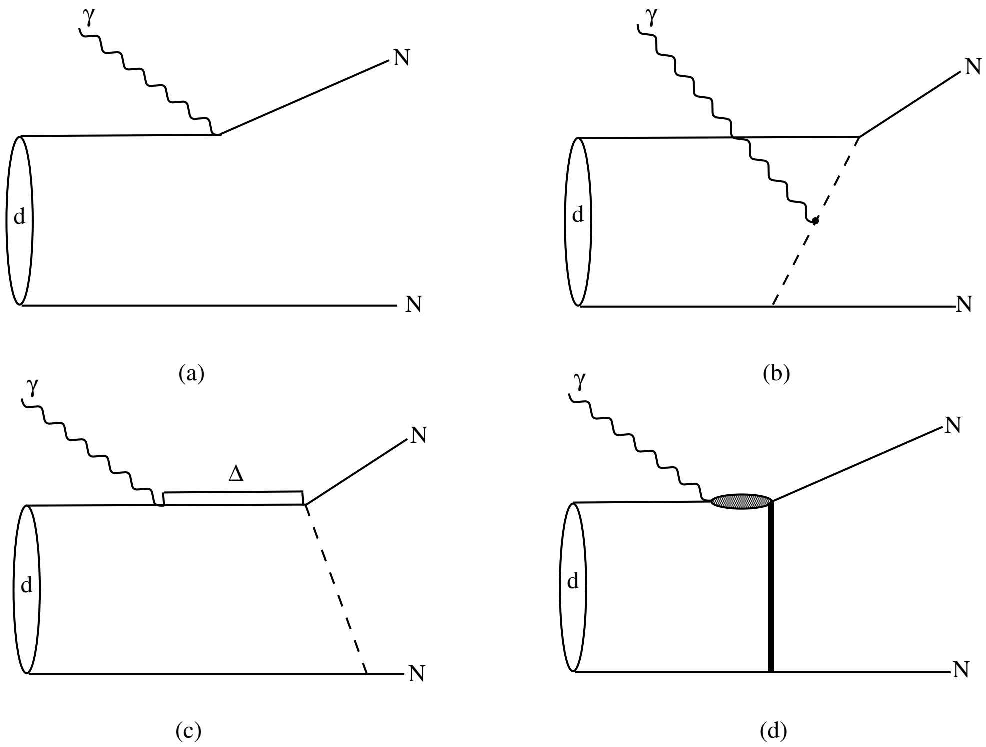

Figure 2.16: Diagrams of the predominant processes contributing to deuteron photodisintegration in a hadronic description. The Born term (one photon couples to a nucleon) is depicted in (a). Figures (b) and (c) show typical meson exchange contributions, where in (c) the meson is exchanged after an isobar excitation. Figure (d) is included as a more general diagram, where the blob and the black bar represent complex interactions. Figure after Reference [36].

start to show a disagreement with the data at energies above $\sim$ 500 MeV. Here the discussion will be limited to two models, Lee's coupled-channel model [27], and a model by Laget [28], which both predict the cross section behavior for $\theta_{cm} = 90°$. A summary of the the characteristics of the two models is given in Table 2.3.

Figure 2.17 shows the coupled-channel meson exchange model of the $\gamma d \to pn$ reaction as developed by Lee [27]. The model is a conventional model which includes final state interactions. The coupled-channel approach takes it name from the mathematical approach, where a set of coupled differential equations have to be solved. For example in the case of coupled NN and NΔ channels in the Δ resonance region [65] of the deuteron photodisintegration reaction the following pair of coupled Schrödinger

Model	Potential	Excitations	Mesons	FSI	Range
Lee	Paris	Δ, N*(1470)	π, 2π	Yes	500 MeV
Laget	Reid soft core	Δ	π, ρ	Yes	800 MeV

Table 2.3: Characteristics of the meson-exchange models by Lee [27] and Laget [28]. For both models the table lists the potential used for the NN-interaction, the excited states of the nucleon that absorbs the photon, which mesons are included in the meson exchange current, whether the model includes final state interactions (FSI), and over what range the model is in agreement with experimental data.

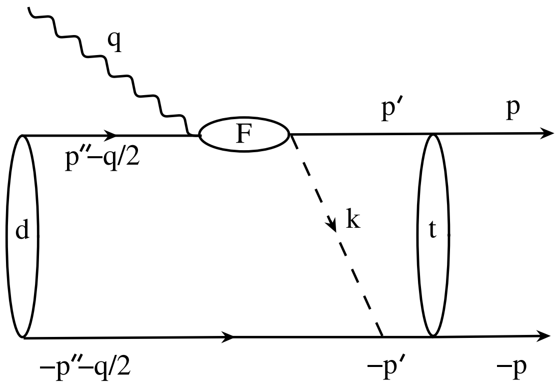

Figure 2.17: Center-of-mass kinematics of Lee's meson-exchange model of the $\gamma d \to pn$ reaction. The incident photon is absorbed by the nucleon creating an excited state. Here F corresponds to the off-shell amplitude for γ+N$\to$N+mesons. The excited state decays, and the meson(s) are absorbed by the other nucleon. The final state interaction is described through t, the half-off-shell matrix for the NN interaction.

equations have to be solved

$$\left[\frac{p^2}{2\mu_{NN}} + V_{NN} - E\right] \Psi_{NN} = -V_{NN,N\Delta}\Psi_{N\Delta} \ , \tag{2.36}$$

$$\left[\frac{p^2}{2\mu_{N\Delta}} + (m_\Delta - m) + V_{N\Delta} - E\right] \Psi_{N\Delta} = -V_{N\Delta,NN}\Psi_{NN} \ . \tag{2.37}$$

Here $V_{NN,N\Delta}$ is the transition potential, V_{NN} and $V_{N\Delta}$ the diagonal potentials for the NN and NΔ channels, m and m_Δ the masses of the nucleon and the delta, and μ_{NN} and $\mu_{N\Delta}$ the reduced masses for the NN and NΔ configurations respectively.

The process in Figure 2.17 can be broken down into three parts. The amplitude that describes the creation of a meson from absorption of a photon by a nucleon, the part that describes the absorption of the meson by the other nucleon, and the final state interactions. Lee starts by basing the FSI on a previously formulated coupled-channel meson-exchange model for NN-scattering [66]. The NN-scattering model was obtained by extending the Paris potential [64] to include coupling to two resonances, the Δ and N*(1470 MeV) Roper resonance. The associated one-pion and two-pion (σ) production mechanisms are described by the standard isobar model with the vertices $\Delta \leftrightarrow \pi$N, $N^* \leftrightarrow \pi$N and $N^* \leftrightarrow \pi\Delta$. The NN-model provides a reasonable description of the NN phase shifts and various NN total cross sections up to 2 GeV. Therefore it is suitable to generate the half-off-shell t (transition) matrix for the final state interactions, as is shown in Figure 2.17.

Next, the photo-meson production amplitude F is described by a Born term, which is borrowed from [8]. The Born term is extended with the isobar model for $\gamma N \rightarrow \Delta \rightarrow \pi N$ from [67] to include the $\gamma N \rightarrow N^* \rightarrow \pi N$ and $\gamma N \rightarrow N^* \rightarrow \pi\Delta \rightarrow \pi\pi N$ amplitudes. In the latter amplitude the two-pion channel is approximated with the fictitious scalar-isoscalar σ-meson. The third and last input to the calculation are the πNN and σNN vertices that describe the absorption of the π and σ by the second nucleon. The vertices are taken to be of a dipole form. The detailed formulae can be found in Reference [27].

Experimental measurements of the NN phase shifts and photo-meson production provide constraints for the calculation in the construction of F and t. The model is further constrained by deuteron photodisintegration data at 90° and below 1 GeV so that a prediction of the energy dependence in the energy region above 1 GeV can be made. The calculated prediction is shown in Figure 2.18, where Lee's coupled-channel model is represented by the solid line. Note that quantity on the vertical axis is the same quantity as used in Figure 2.5. The model describes the data well up to about 500 MeV, but above 500 MeV the model shows too little strength up to 1 GeV and then too much above 1 GeV. In a further effort, Lee examined the model dependence of his calculation on the description of the final state interactions, as well as on the choice of the deuteron wave function. It was concluded that the results are significantly sensitive to the choice of wave function and FSI, but that none of the combinations are able to describe the behavior of the data at energies above 1 GeV in the current coupled-channel formalism [66, 68].

More recently Lee has also performed a relativistic calculation [69] using the existing meson-exchange model, including Paris potential and the coupled-channel model. The predicted energy dependence from this "front-form" calculation does not differ much from earlier non-relativistic calculations, which suggests that the failure of the meson-exchange calculations to describe the data at high energies is not due to the neglect of relativistic effects.

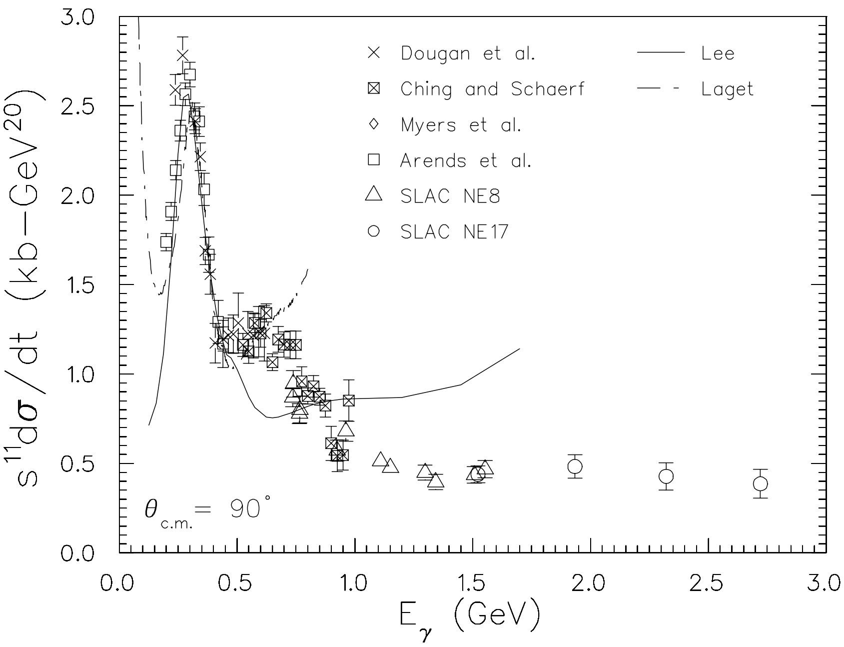

Figure 2.18: Comparison of the meson-exchange calculations by Lee and Laget with the deuteron photodisintegration data [10,11,36–39] at θ_{cm}=90° available before this experiment.

In the approach by Laget [28] the deuteron photodisintegration amplitude is calculated in an expansion of the leading diagrams. Above the pion threshold and in the

$\Delta(1236)$ resonance region, the cross section is dominated by the pion re-absorption amplitude. This is the amplitude for a process where a virtual pion is created at one nucleon, and re-absorbed by the other. The re-absorption amplitude is expanded in terms of the elementary $\gamma N \rightarrow N\pi$ amplitude, which in turn is expanded in terms of the Born terms, the nucleon exchange terms, the Δ formation terms, and an ω^0 exchange term. The detailed formulae and diagrammatic expansion can be found in Reference [28]. The exchanged meson is far from its mass shell, therefore form factors are needed at each meson-nucleon vertex. Assuming that the $\pi\Delta N$ and πNN form factors are the same, they are both modeled with the same monopole form

$$F_\pi(q^2) = \frac{\Lambda_\pi^2 - m_\pi^2}{\Lambda_\pi^2 - q^2} \,, \tag{2.38}$$

where q^2 is the four-momentum squared of the pion, and Λ_π=1.2 GeV . Moreover, since the exchanged meson is as far from the pion pole as from the ρ-meson pole (the squared four momentum of the pion ranges from $-16m_\pi \leq q^2 \leq -4m_\pi$ in the Δ resonance region), the ρ meson is included as well. The $\rho\Delta N$ and ρNN form factors are again assumed to be the same, and parameterized in a dipole form:

$$F_\rho(q^2) = \left[\frac{\Lambda_\rho^2 - m_\rho^2}{\Lambda_\rho^2 - q^2}\right]^2 \,, \tag{2.39}$$

where Λ_ρ=$2m_N$. Final state interactions are taken into account by computing the neutron-proton rescattering diagram in the S- and P-waves of the neutron-proton final state system. A Reid [70] soft core NN wave function is used. Figure 2.18 shows the calculation by Laget as a dashed line. The calculation agrees well with the data beyond the Δ-resonance and extends further than Lee's calculation, up to about 800 MeV, where it starts to show a large deviation as well.

2.5.1 Scaling in the Traditional Meson-Nucleon Description

Carlson [52] provides an interesting comment regarding the relation between results from a pQCD description of deuteron photodisintegration behavior at high energy and those from traditional meson-nucleon nuclear physics. Under certain common conditions (which will not and should not be realized in the most general calculation) the same high energy scaling law is obtained from meson-nucleon nuclear physics as from pQCD. Scaling with energy of the process which is shown in its traditional

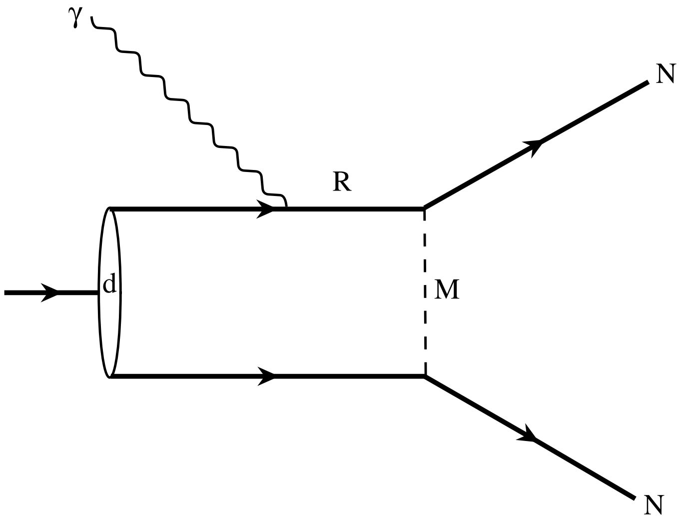

Figure 2.19: Diagram for a traditional description of deuteron photo-disintegration. Figure after Reference [52].

description in Figure 2.19 is calculated using the following three conditions, common to meson-nucleon theories [27]

1. Only a finite number of different baryon resonances R will be included.

2. Only a finite number of mesons M will be exchanged.

3. In each vertex, "standard" form factors are used. In the γNN vertex the dipole form factor is used and in the MNN vertices the monopole form factors are are used.

In this description there are two fermion lines (the nucleons), one internal fermion propagator (the resonance), one internal boson propagator (the meson), one γNN-vertex, and two MNN-vertices. Using the rules of scaling with Q given in Section 2.4.1

the following Q dependence is found for the amplitude:

$$\mathcal{M} \propto Q^2 \frac{1}{Q}\frac{1}{Q^2}\frac{1}{Q^4}\left(\frac{1}{Q^2}\right)^2 \propto \frac{1}{Q^9} . \tag{2.40}$$

After recognizing again that at the momentum scale of interest $\sqrt{s}$ is the only scale, a substitution for Q can be made. If the resulting amplitude is then substituted in Equation 2.7, the pQCD (or dimensional scaling law) for fixed center-of-mass angle exclusive deuteron photodisintegration is obtained:

$$\frac{d\sigma}{dt} \sim \frac{1}{s^{11}}. \tag{2.41}$$

This scaling is obtained for one intermediate resonance and one meson, but the same scaling is obtained by summing the results over any finite number of resonances and mesons. However, there are three caveats [52]. Both the sums over the intermediate resonances and mesons should not be truncated, and the scaling behavior of the MNN vertex in pQCD does not behave as a monopole, but has a $1/Q^6$ behavior at large momentum transfers.

2.6 Asymptotic Amplitudes

Nagornyĭ *et al.* [29] argue that the unsuccessful attempts to describe deuteron photodisintegration with conventional meson-theories above energies $E_\gamma >$1 GeV can be attributed to the use of realistic (phenomenological) deuteron potentials, which are not adequate to describe the deuteron-core at the characteristic distances corresponding to $E_\gamma > 1$ GeV ($r_{eff} \sim (mq_0)^{\frac{1}{2}} \simeq 0.2$ fm). To overcome the lack of knowledge of the deuteron wave function at short distances, they consider an approach in terms of a Lorentz- and gauge-invariant field theory, allowing the deuteron to have an hadronic internal structure [29, 71].

Assuming that in the asymptotic energy region only tree diagrams survive, the deuteron photodisintegration matrix element is calculated from the gauge-invariant covariant diagrams depicted in Figure 2.20 in terms of the masses, charges, magnetic and quadrupole moments of the particles using a covariant parameterization for the deuteron vertex in terms of a hard component. In Figure 2.20 diagrams 1–3 correspond to s, t, and u channel break-up of the deuteron, with an off-shell deuteron, proton and neutron in the intermediate state, respectively. The fourth diagram represents the contact term, which is required for gauge invariance. The amplitude of contact diagram doesn't vanish [72], and is of particular importance in hard processes, which take place at small inter-nucleon distances, where the realistic deuteron wave function deviates from the asymptotic Yukawa form that describes larger distances.

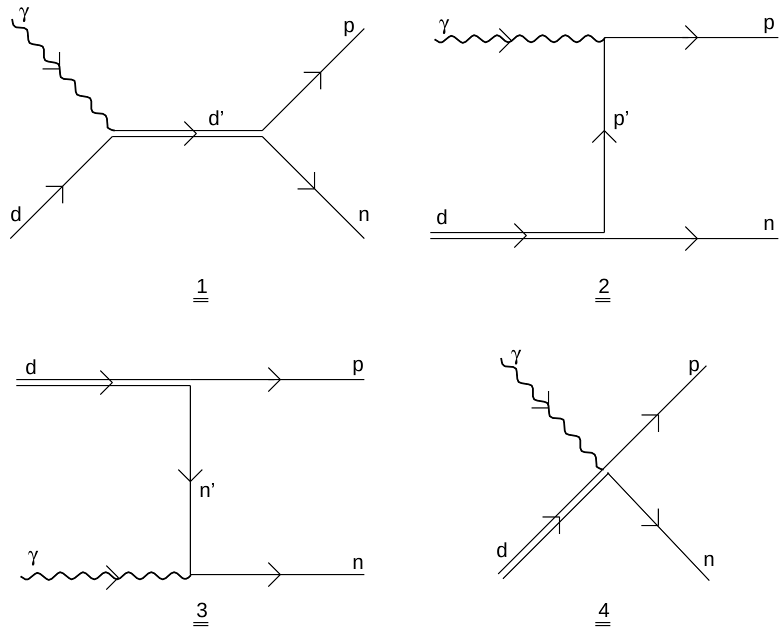

Figure 2.20: Gauge-invariant covariant diagrams for deuteron photodisintegration at asymptotic energies. Diagrams 1–3 correspond to the s, t, and u channel break-up respectively. Diagram 4 is the contact diagram. Figure after [29].

In this description, the d-np vertex is assumed to consist of two parts, a soft part corresponding to conventional meson exchange theory, and a hard component describing the processes at short distances. It is furthermore assumed the nucleon-nucleon interaction is fully contained in the initial deuteron vertex, and that no short range interactions occur in final np state. In the asymptotic region the hard component dominates and the covariant half-off shell d-pn vertex with one virtual nucleon is expressed as a sum of 4 invariant form factors. Only the vector form factors $G\gamma_\nu$ in the d-np vertex contribute to the amplitudes of the diagrams in Figure 2.20. Since the wave function at short distances is poorly known, an effective counting rule prescription [73] is used for the form factor G:

$$G(p^2) = \frac{C}{(\Lambda^2/2 + m^2 - p^2)^g} \, , \tag{2.42}$$

where p is the momentum of the off-shell nucleon, C a normalization constant, and Λ is related to the inverse of the range. The parameter g determines the rate of decrease of the d-pn vertex function.

In the asymptotic region where relativistic effects play an important role, the form factor G from Equation 2.42 is evaluated using the instant form (if) and light-cone (lc) relativistic approach. In the covariant approach, using instant form kinematics, the vertex function is expressed in terms of the four momentum difference between the outgoing proton and neutron. The vertex form factor then takes the form ($i = s, t, u$):

$$G^{\text{if}}(-k_i^2) = \frac{C}{(\beta^2 - k_i^2)^g} \, , \tag{2.43}$$

where $k_s^2 = -\vec{k}^2$, $k_t^2 = -\alpha\vec{k}^2$, $k_u^2 = -(2-\alpha)\vec{k}^2$, and $\vec{k}^2 = s/4 - m^2$. The quantity $\alpha = 2pq/(dq) = 1 - \frac{k}{E_k}\cos\theta$. The parameter $\beta^2 = \Lambda^2/4 + \alpha_0^2$, with $\alpha_0^2 = m^2 - m_d^2/4$. In the case g=3 where Equation 2.43 becomes the triple-pole vertex function, known from scalar meson-nucleon theory, β can be identified with the mass of the pion, $\beta^2 \simeq m_\pi^2 \simeq 0.02m^2$. The constant C is fixed by a fit to data.

In the light-cone approach, the angle dependence (through α) is factored out, and the form factor becomes:

$$G^{\text{lc}}(\alpha, \vec{k}^2) = \frac{C}{(\beta^2 - \vec{k}^2)^g}\phi(\alpha), \text{ with } \phi(\alpha) = \alpha^{-\kappa}, \qquad \kappa{=}1/2, \tag{2.44}$$

This form factor has the same functional dependence on $\vec{k}^2$ as the instant form form factor, but the angular dependence is now present in the function $\phi(\alpha)$. In the non-relativistic limit $\phi(\alpha) \to 1$. The constant C is again fixed by a fit to data. In this description the light-front variable α is identified with the longitudinal momentum fraction carried by the nucleon in the deuteron.

After the matrix element has been calculated by summing the individual amplitudes of the diagrams in Figure 2.20 using the model (2.43) or (2.44) for the d-pn vertex function, the invariant cross section for large (but finite) s becomes

$$\frac{d\sigma}{dt} = \frac{Cm_d}{\sqrt{s}(s-m_d^2)^{2g-1}(s-m_d^2)^{3/2}} f(\theta_{cm}, s) \ , \tag{2.45}$$

where the angle dependence is now contained in the function $f(\theta_{cm}, s)$. For θ_{cm}=90° the kinematic variable α=1 which gives $f(\theta_{cm}, s) = 1$. In the s-region of interest(s=8–20 GeV), m_d^2 is still non-negligible. For g=3 a "prescaling" behavior that resembles that of the dimensional counting rules is seen. The behavior is approximated by $\frac{d\sigma}{dt} \approx s^{-n+2}$, with $n-2=10$. At other center-of-mass angles, the s dependence in $f(\theta_{cm}, s)$ originates from $\alpha(\theta, s)$, which gives the function a different s-dependence at different angles, except when $s \to \infty$, where α no longer depends on s and angular independent scaling is expected. For finite s in the range of interest, this model predicts a cross section s-dependence with a power ranging from $n-2 \approx 10$ at θ_{cm}=90° to $n-2 \approx 8$ at θ_{cm}=10°. This s-dependence can also be interpreted as an angular dependence on the light-front variable α, namely $\frac{d\sigma}{dt} \approx \alpha^{-2}$ ($\alpha > 1$) or $\approx (1-\alpha)^{-2}$ ($\alpha < 1$).

The angular dependence of the cross section is governed by the variable α which is one of the arguments of G, and depends on the choice of vertex form factor. The instant form description depends on α for the t and u channels, and correspondingly shows a strong angular dependence at forward and backward angles. Moreover, the vertex depends on one covariant variable e.g. $k_t(s,\theta)$ so that the angle and s-dependence are coupled by the parameter g. In the light-cone description the vertex depends on two in principle independent parameters, α and $\vec{k}^2$, so that the s- and θ-dependence are de-coupled, and a flat angular dependence can go together with a steep s-dependence.

A calculation of the cross section in Equation 2.45 based on the covariant vertex form factor description was performed for θ_{cm}=90° and g=3. The result is shown in Figure 2.5 and agrees well with the scaling of the data at θ_{cm}=90° up to 3.0 GeV. In this calculation the parameter C is fitted by data at E_γ=1 GeV. The original asymptotic amplitudes calculation in Reference [29] also contained contributions from the d-pN* vertex (N* is the Roper resonance (1440 MeV)). They are represented with two diagrams similar to diagram 2 and 3 in Figure 2.20, but with the off-shell proton and neutron replaced by R^+ and $R^{(0)}$ respectively. It is unclear whether the d-pN* vertex was used in the calculation shown in Figure 2.5. The d-pN* vertex is not included in the latest calculations presented in [71].

2.7 Summary

This chapter has presented the central role that the deuteron photodisintegration reaction ($\gamma d \rightarrow pn$) plays in the search for the onset of asymptotic scaling in exclusive nuclear reactions. The resolution of quark degrees of freedom in exclusive nuclear reactions is believed to be strongly governed by the size of momentum transfer to the nucleons. The $\gamma d \rightarrow pn$ reaction is a particularly suitable candidate for the search of quark degrees of freedom, since the photon transfers *all* of its momentum and energy to the outgoing proton and neutron. Because of the deuteron's simplicity the reaction has received tremendous theoretical attention. Models that describe the reaction in terms of quark-gluon degrees of freedom, as well as models that use the hadronic degrees of freedom familiar from low energy nuclear physics have been reviewed.

Chapter 3

Experiment

3.1 Overview

The deuteron photodisintegration experiment (E89-012) was run in experimental Hall C at the Continuous Electron Beam Accelerator Facility (CEBAF) in Newport News, Virginia in the Spring of 1996 with an additional short run in the Fall of 1997. A high current 100% duty factor (i.e. continuous) beam of electrons with energies up to 4.0 GeV impinged on a 6% radiation length copper foil, producing a continuous spectrum of bremsstrahlung photons. The beam of bremsstrahlung photons (as well as the remainder of the electron beam) is incident on a 15 liquid deuterium (LD_2) target, contained in an aluminum cylindrical flask. The photons induce the deuteron photodisintegration reaction $\gamma d \to pn$, and the final state photoprotons are detected in the HMS spectrometer. Figure 3.1 shows a schematic diagram of the experiment.

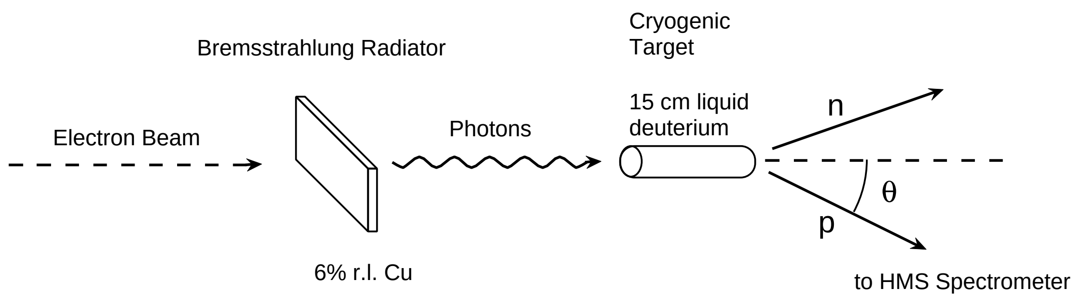

Figure 3.1: Schematic of the experiment.

Figure 3.2 shows a plan view of the experimental set-up with some of the components

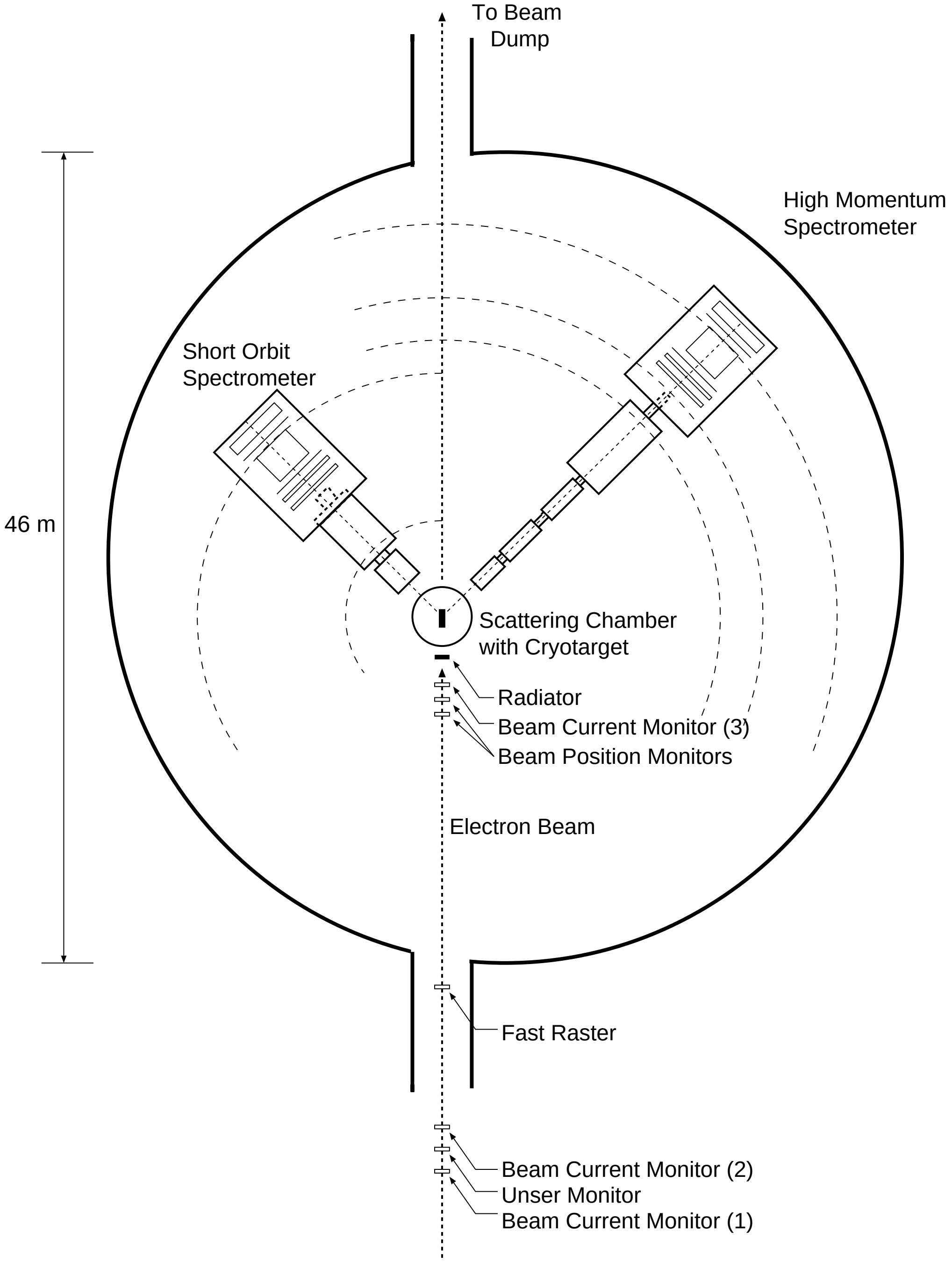

Figure 3.2: Plan view of the experimental set-up in Hall C.

that will be discussed in subsequent sections.

Table 3.1 gives a summary of the kinematic settings at which data were taken during this experiment. The entries in brackets next to the beam energy, correspond to the estimated statistical errors in the final invariant cross sections. The statistical errors were estimated assuming that the cross section has the energy dependence of Equation (2.8), using results from SLAC experiment NE17 and the proposed experimental parameters and total beam time. Measurements over a large angular range were made and the table shows all E89-012 kinematics which had a proton in the final state. The backward angle SOS data taking in this experiment will not be discussed in this work. Data were taken at all settings during the 1996 run, and additional data were taken for E_{beam} = 4.045 GeV, θ_{cm}=53° and 70° in the Fall of 1997.

Run Plan						
θ_{cm} nom.	Beam Energy (GeV)					Spec.
37°	0.845(5%)	1.645(5%)	2.445(5%)	3.245(5%)	4.045(5%)	HMS
53°	–	1.645(5%)	2.445(5%)	3.245(7%)	4.045(10%)	HMS
70°	–	1.645(5%)	2.445(5%)	3.245(7%)	4.045(15%)	HMS
90°	0.845(5%)	1.645(5%)	2.445(5%)	3.245(7%)	4.045(15%)	HMS
114°	0.845(5%)	1.645(5%)	2.445(7%)	3.245(10%)	–	SOS
130°	0.845(5%)	1.645(5%)	2.445(10%)	–	–	SOS
143°	0.845(5%)	1.645(5%)	2.445(10%)	–	–	SOS

Table 3.1: Kinematic settings (θ_{cm}, E_{beam}) for the experiment. The number in brackets next to the beam energy is the estimated statistical accuracy for that setting. The last column lists the spectrometer used for data taking at that setting.

3.2 Electron Beam

The electron beam needed to create the photon beam for the photodisintegration experiment was delivered by the CEBAF accelerator. Figure 3.3 shows a schematic layout of the accelerator and the three end stations. The accelerator is capable of

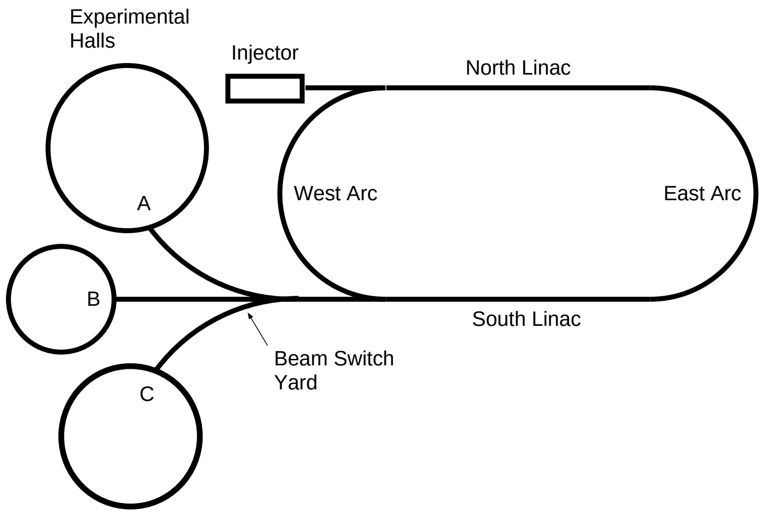

Figure 3.3: Schematic top view of the CEBAF accelerator and experimental halls. Not to scale.

delivering a continuous wave electron beam with energy in multiples of 0.8 GeV up to 4.0 GeV to each of its three end stations.

At the injector a thermionic gun emits electrons which undergo an initial acceleration up to 45 MeV, after which they enter into the North linear accelerator (linac). In the North linac the beam is accelerated in superconducting radio frequency cavities, where it gains 400 MeV. At the end it passes through a 180° degree bend (the East arc) and enters an identical linac where it gains another 400 MeV. At the end of the South linac the beam can either be extracted and sent to one of the ends stations, or recirculated by passing it through another 180° bend so that the beam can undergo another acceleration in the North linac. Up to 4 recirculations are possible giving a total of 5 passes through the accelerator, corresponding to beam energies $45 + n \times 800$ MeV, where n=1,. . .,5 , the number of passes through the accelerator. When the beams are recirculated electrons with different energies pass together through the linacs, but they cannot be transported through the same string of arc magnets because different field strengths are necessary to provide the 180° bend. For this purpose each arc consists of a vertical stack of separate arcs, each with different bending fields (five for the East arc and four for the West arc). Beams with different energies are separated at the end of each linac, travel through the designated arc and are re-combined to travel through the next linac. After the beam has made the number of circulations corresponding to the desired energy for the experiment, it is extracted just before the West arc, where it is transported to the beam switchyard (BSY). At the BSY it can sent to the experimental hall of choice. At CEBAF beams with different energy can be delivered simultaneously to all three end stations.

The RF cavities in the linacs operate at 1497 MHz, creating a beam of 1.67 ps long bunches at the same frequency. At the BSY the extractor directs one third of the bunches to each of the end stations, providing a beam with a 499 MHz structure in Hall C. From the BSY to Hall C the beam is transported through the Hall C arc, which contains magnets to steer the beam into the hall and instrumentation for beam diagnostics, including beam current monitors, beam position monitors and superharps (for beam position and profile measurement).

Hall C can receive electron beams from the accelerator with beam currents in excess of 100 μA. Because of the small beam spot ($\sim$ 200 μm FWHM) and the CW character of the beam, it can deposit a large amount of power in the target. To prevent damage to the radiator or local boiling in the cryotargets the beam is rastered before striking the target. Two steering magnets (one bends horizontally, the other vertically), installed about 20 meters upstream from target are driven by currents that vary sinusoidally at different frequencies [74]. As a result the beam moves within a square area with a side of about 2 mm and the power deposited is spread. In this experiment moderate beam currents were used (up to about 25 μA), where local boiling in the target is of no concern (see Section 3.4). Moreover, the radiator caused a beam spread as well, so even though beam rastering was turned on, it was not a necessity.

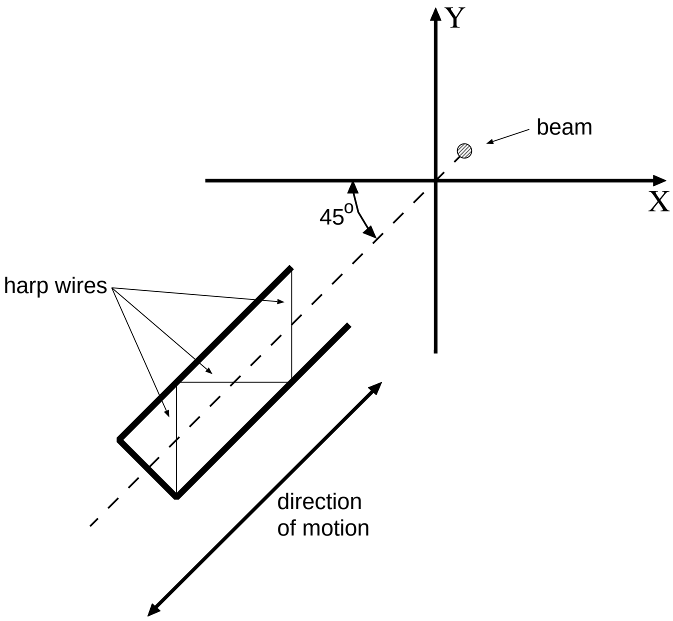

Figure 3.4: Superharp beam position and profile monitor.

3.2.1 Beam Position Measurement

The beam position is measured at a number of locations in the arc and beam line upstream of the target scattering chamber. The most accurate measurement of the beam position is carried out with a superharp [75], of which several are present in the beam line. A superharp consists of three tungsten wires mounted in a frame which is connected to an arm that can be moved in and out of the beam with a stepper motor. An encoder records the absolute position of the arm. In a beam position/profile measurement the arm is extended and retracted, so the wires in the frame sweep through the beam. Figure 3.4 shows the device and the method of operation. The angle of the arm with the beam line and the orientation of the wires in the frame are chosen so that a measurement provides a horizontal-vertical-horizontal position and profile measurement of the beam. With this measurement an absolute beam position measured of better than $\pm$ 10μm can be achieved. Superharps are also used in the arc beam energy measurement (see Section 3.2.2).

The superharp beam position measurement is an intrusive measurement, because the electrons in the beam scatter of the wires when they pass through the beam. Hence superharp beam position measurements are only performed at set times, while data are not being taken. To make continuous measurements of the beam position during data taking, beam position monitors (BPMs) are installed which provide a non-disruptive measurement of the position of the beam. A BPM is a cylindrical cavity containing two pairs of antennae, perpendicular to each other at $\pm 45°$ with respect to the horizontal and vertical, see Figure 3.5. The beam passes through the cavity parallel to the symmetry axis and both pairs of antennae pick up the frequency of the bunch structure of the beam. Each antenna gives off a signal proportional to the distance that the antenna is removed from the beam. The beam position is derived from the difference over the sum of the signals from antennae on opposite sides of the beam. This method provides a position measurement independent of beam current.

Moving downstream along the Hall C beam line, the last BPM is located about

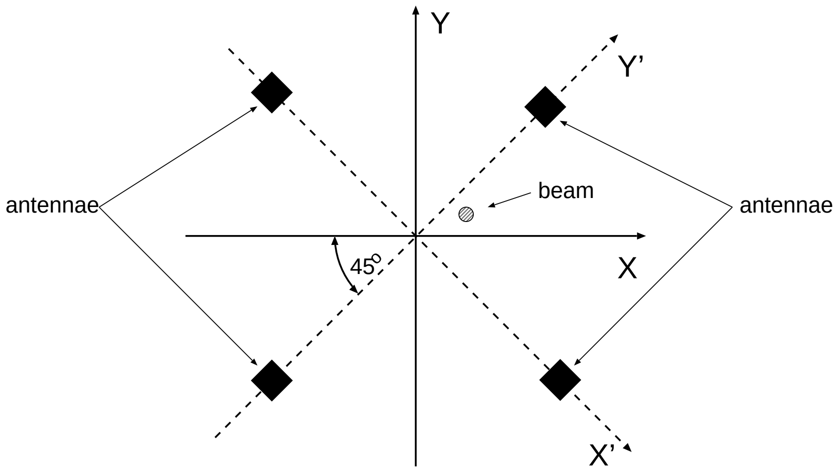

Figure 3.5: Diagram of the orientation of the BPM antennae.

1.60 m in front of the entrance to the scattering chamber. During the experiment, the position at this BPM was recorded as the beam position on target. This enabled the accelerator control system to retune the beam in a same spot on the target, after a period of beam loss. A detailed description of the BPMs can be found in [76]. Using the BPMs the final accuracy in the absolute beam position is ± 1.0 mm with a relative uncertainty <0.2 mm.

3.2.2 Beam Energy Measurement

The electron beam energy is measured using well-known field settings of magnets in the Hall C arc. The method relies on accurate determination of the magnet fields and the beam trajectory through the arc. For this measurement the focusing magnets in the arc are turned off, and the dipoles are set to the nominal central path through the arc. Using superharps (see Section 3.2.1) the beam position is measured at the beginning, in the middle and at the end of the arc, and the position information is used to steer the beam to the central path. For one of the dipoles in the arc the field has been precisely mapped (the golden dipole). The other magnets in the arc are the same, and assuming their fields are similar, the field integral $\int \vec{B} \cdot \vec{dl}$ can be determined accurately for a beam passing through the central path. Using this method the the beam energy was determined to 0.2% [77]. Details of the measurement and a break-down of the effects that contribute to the uncertainty in the beam energy are presented in this reference.

3.2.3 Beam Current Measurement

The Hall C beam line has four devices installed to measure the beam current, three microwave cavity beam current monitors (BCMs), and a parametric DC current transformer (Unser monitor [78]). The BCMs measure the integrated beam current in two second intervals and their output voltage, as well as the output voltage of the Unser, is converted into frequency using a voltage-to-frequency converter, and read out in a scaler.

The BCM is a cylindrical wave guide, mounted in the beam line so that the beam travels on the symmetry axis of the cylinder. The dimensions of the cylinder are selected so that the 499 MHz structure of the beam excites the 1497 MHz TM_{010} mode in the wave guide. The resonance frequency is picked up by wire loop antennae, and converted to a DC voltage through a rms-to-DC converter (Analog Devices AD367). The cavities and associated read-out electronics are described in [79, 80]. The cavities have a stable gain and offset, and a high signal/noise ratio, but cannot measure the absolute current, because the output power as function of the measured beam current depends on the cavity impedance, quality factor, and signal cable attenuation. The absolute calibration is done with the Unser monitor.

The Unser monitor is installed between BCM1 and BCM2 well upstream of the target. It cannot be used for charge measurements because it is very sensitive to thermal fluctuations, resulting in large drifts in its zero-offset (an offset change of 1 μA in a 24 hr period with no beam has been observed [81]). However, the gain of the Unser is very stable and well measured, which makes the device suitable for calibration of the BCMs.

Calibration of the BCMs using the Unser monitor is carried out once every eight hour shift period. During a calibration run the accelerator delivers beam to the hall in current steps lasting 2 minutes, first increasing up to the current at which data is taken, then decreasing, with equal time intervals of no beam in between the steps. During the beam-off intervals the zero offsets of the Unser and the BCMs are measured. During the beam-on intervals the gains of the BCMs and Unser are measured. Then the BCM gains are calibrated using the offset and well known gain of the Unser monitor.

The experiment was run with beam currents ranging 10–25 μA, with majority of the data taken at 20 μA. Some of the 1997 data was taken at 25 μA. For data taken at the start of the experiment (settings at $E_{beam} = 2.445$ GeV), the integrated charge is determined from the BCM3 current measurements. BCM1 is used to determine the charges for all other settings, except for the 1997 data, which also have the integrated charge determined from BCM3. The systematic error from the calibration procedure due to the 0.2 μA noise of the Unser PCT signal, amounts to 1% for average 20 μA running. An additional 1% systematic error due to the uncertainty of the gain of the power meter used to measure the beam current signal from the BCM brings the overall uncertainty in the beam current measurement to 1.4% [82].

3.3 Bremsstrahlung Radiator

The beam of real photons used in this experiment is generated with a bremsstrahlung radiator, which can be inserted in the electron beam just in front of the target. Half the opening angle of the bremsstrahlung cone emerging from the radiator is approximated by [83]

$$\theta_\gamma \approx m_e/E_{beam}, \tag{3.1}$$

and is of the order of a few milliradians for high energy electrons ($E_{beam} \gg m_e$). Because of the small opening angle and radiator-target distance (the radiator is installed 1.21 m upstream from the target), the entire photon beam is assumed to pass through the target. Consequently, a high photon flux is obtained, and the correct bremsstrahlung flux can be accurately evaluated. The latter is important, because the experiment does not use a tagged photon beam. The photon flux per unit photon energy and per incident electron is calculated with the thick-target bremsstrahlung formulae from Matthews and Owens [84], which are discussed in Section 5.5.

The radiator assembly is a vertical stack of thin copper foils mounted in a ladder which can be inserted in the beam using a remotely controlled stepping motor. The ladder has five nominal foil thicknesses mounted, 2%, 4%, 6%, 7%, and 8% radiation lengths. Each radiator foil is in fact stacked from extruded thin copper foils, with standard thicknesses, 0.0005, 0.001, 0.010, and 0.025 inches, combined in a way that the total radiation length matches the nominally desired radiation length for that ladder-position. In this experiment data were taken with the 6% radiator foil, except at the lowest energy (E_{beam}=0.845 GeV), where the 4% foil was used. The other foils in the ladder are used for calibration purposes. The nominal 4% and 6% foils have thicknesses 0.4487 g/cm^2 and 0.7742 g/cm^2 respectively. Using the radiation length for copper (X_0(Cu)=12.86 g/cm^2) the two foils have radiation lengths 3.489 $\pm$ 0.003 % and 6.021 $\pm$ 0.003 %. The thicknesses of the foils are known to better than 0.1%. A detailed description of the radiator assembly and the foil thickness measurements is given in [42].

3.4 Targets

At the common center of rotation of the spectrometers in Hall C (the pivot point), a cylindrical vacuum chamber (the scattering chamber) is installed in which the targets used for experiments are contained. Both solid targets (thin metallic foils) and cryogenic targets are available. The latter targets are used for experiments on hydrogen, and deuterium, which, in the gas phase at room temperature, do not provide enough luminosity to measure small cross sections in a reasonable time. By liquefying the target gas a density increase of order 10^3 is obtained, providing a similar increase in luminosity. In order to accommodate and utilize the continuous wave nature and the available high currents of the CEBAF beam, a high-power multiloop cryogenic target was constructed which can dissipate in excess of 500 W of power deposited by the electron beam. In this target deuterium and hydrogen are in liquid phase simultaneously in separate loops, to facilitate fast target changes. A detailed description of the cryotarget and scattering chamber is given in Appendix C and also in Reference [85]. No data were taken with solid targets in this experiment but a beryllium oxide (BeO) solid target was used for optics studies (see Section 4.3.1).

In essence, a cryotarget[1] is a cell containing a volume of cryogen. The cell is constructed so that an electron or photon beam can pass through and induce a nuclear reaction with the nuclei of the cryogen without undergoing significant multiple scattering in the cell walls. Figure 3.6 shows a drawing of the cell-block assembly used in the cryogenic target. The cell block is assembled from an aluminum base,

[1] often the term cryotarget is also used to refer to the complete installation (mechanical system, gas panels and instrumentation/controls) that the cell is hooked up to.

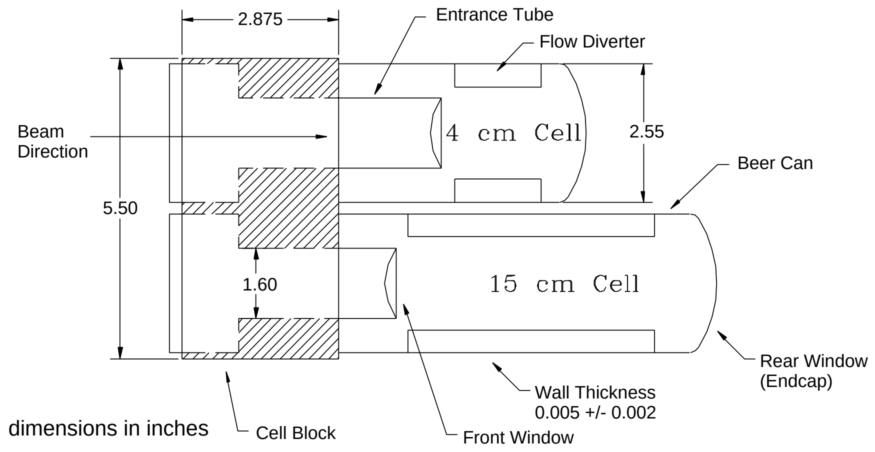

Figure 3.6: A cell block with a pair of target cells, a 4 cm and 15 cm cell is shown. The main parts of the cell block are the aluminium base, aluminum beer can flasks and the upstream window tubes with upstream windows, where the beam enters through. Figure courtesy of D. Meekins.

which has two thin cylindrical aluminum flasks connected to the front. The rear of the block is open, and an aluminum beam tube is inserted (the upstream window tube), which is sealed at the front with a convex thin aluminum window (0.028 inch thick). Thus a contained volume of cryogen with thin entrance and exit windows is obtained. The aluminum flasks are made from beer can blanks supplied by Coors Brewing Company, Golden Co. The beer can blanks are produced by extrusion and have thin walls (0.005 ± 0.002 inch) with uniform wall thickness. The cell walls have to be thin, not only to reduce multiple scattering and energy loss of the beam, but also to reduce multiple scattering and absorption of reaction products in the cell walls. Therefore the endcaps are chemically etched to reduce the wall thickness. A detailed description of the construction of the cell block including dimensions and parameters of the cells is given in Appendix C, Section C.1.3. The block contains cells with two different nominal lengths, 4 cm and 15 cm, to match extended target acceptance of the SOS and HMS spectrometers, respectively. Two stainless steel pipes connect the cell block to a heat exchanger, forming a closed loop. The heat exchanger has an axial circulation fan inside that forces the target liquid to flow through the cells in the closed loop, and provides refrigeration to remove the power deposited by the beam in the cryogen, so that the cells are kept at a constant temperature. Refrigeration is provided by 2 MPa, 15 K helium gas, which flows through the primary side of the heat exchanger. The secondary side of the heat exchanger is connected to a gas handling system, which supplies the target gas from a storage tank.

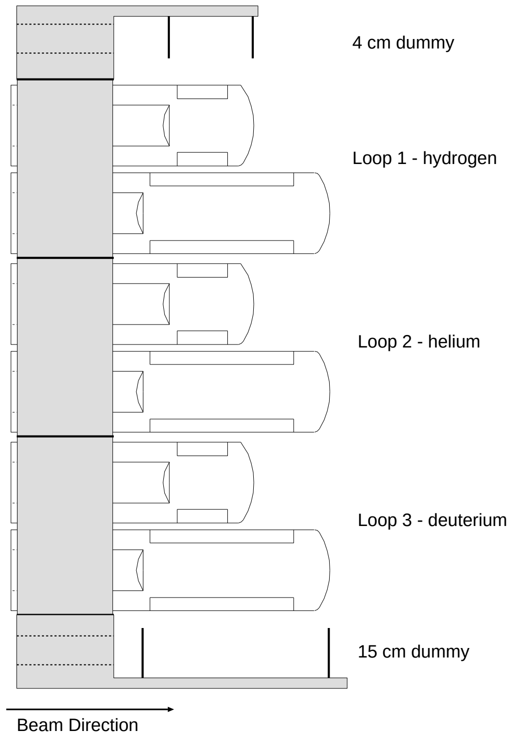

Figure 3.7: Schematic of the cryo-stack. The cryo stack is a vertical stack of three cell blocks which each have a nominal 4 cm and 15 cm cell. At the top and bottom 4 and 15 cm aluminum dummy targets are installed.

Experiments often require background measurements with targets that have well-known cross sections (e.g. hydrogen). To avoid lengthy target warm-up and re-liquefication times for measurements with different cryogens, a system was developed that is able to contain three different cryogens simultaneously, by combining three of the closed loop systems, and mounting the three cell blocks in a vertical stack. Figure 3.7 shows the stack of cells (the cryo-stack) that is part of the multiloop cryogenic target. The loops are numbered in vertical order, where loop 1 is nominally loaded with hydrogen, loop 2 with helium (gas) and loop 3 with deuterium. The three loops with cryo-stack are mounted to a vertical lifting mechanism (the target lifter), which can lift the desired cell into the beam line. In addition, the entire three-loop assembly can be rotated out of the beam by 90° to enable the insertion of solid targets through a separate port. Target motion (lift/rotation) is controlled remotely from the Hall C counting house through the cryotarget control system. At the top and bottom of the stack two dummy targets are mounted to measure the background from the target cell windows. The dummy targets have flat aluminum strips at the same position as the endcaps of the 4 cm and 15 cm targets, but about 10 times thicker, to have a radiation length comparable to that of a filled cell. The dummy targets were not used in this experiment.

The cryo-stack was surveyed both at room temperature and with the cells cooled down, so that the thermal contraction could be calculated. The cold cell length and target center for each cell were estimated. The endcap wall thicknesses were measured on a Coordinate Measuring Machine. The results of the measurements are listed in Table C.1 and References [86, 87]. The target lengths in these references have been corrected for the thermal contraction (about 0.4% at 20 K). The error in the cell length measurement is negligible and the thermal contraction has an estimated relative error $\sim$0.2%. To accurately determine the target length, knowledge of where the beam travels through the target is also required. However, in the analysis of the data, accurate knowledge of the cell length is of little importance, since the effective target length used in the cross section calculation is calculated from software cuts that exclude the aluminum cell windows (see Section 5.8.1), rather than from the full target length.

All data for the photodisintegration reaction were taken with 15 cm targets, except for the 1997 runs. Those runs were taken with nominal 12.5 cm cells, which had replaced the 15 cm cells in a target overhaul. The main run of the experiment started immediately after the installation and commissioning of the cryotarget, during which a leak was discovered in loop 1. Since the layout of the refrigeration plumbing

E_{beam}, θ_{cm}	D_2	H_2	empty
0.845 GeV, all angles	Loop 2	–	Loop 1
1.645 GeV, all angles	Loop 2	–	Loop 1
2.445 GeV, all angles	Loop 3	–	Loop 1
3.245 GeV, all angles	Loop 3	–	Loop 1
3.245 GeV, $\theta_{cm} = 90°$	Loop 2	–	Loop 1
4.045 GeV, all angles	Loop 2	–	Loop 1
4.045 GeV, $\theta_{cm} = 53°$,70° (1997)	Loop 3	Loop 1	–

Table 3.2: Target–Loop configurations for all kinematics.

in the target does not allow for loop 2 to be filled with hydrogen, while loop 3 is filled with deuterium, the experiment was run with deuterium in loop 3, while the background measurements (see Section 5.2) were carried out with loop 1 empty. Later in the run loop 3 developed a leak as well, and the experiment was completed with deuterium in loop 2. During the 1997 runs the cryotarget was fully operational, and backgrounds were measured with hydrogen in loop 1. Table 3.2 shows the target–loop configurations for all kinematics.

The hydrogen target is operated at a pressure of 24 psiA and a temperature of 19 K (in this state the boiling temperature of hydrogen is 22.80 K). The deuterium target is operated in a similar subcooled fashion. The operating parameters and corresponding target densities [86] are listed in Table 3.3. For hydrogen, the relative fluctuation

Cryogen	Temperature (K)	Pressure (psiA)	Value (g/cm^3)
H_2	19	24	0.07230 $\pm$ 0.00036
D_2	22	20	0.1670 $\pm$ 0.0008

Table 3.3: Operating parameters and densities of the cryogens used in the cryogenic target.

in the density of the liquid, ρ_L, with temperature T and pressure P (at 20 K and 0.2 MPa) is given by $\frac{1}{\rho_L}\frac{d\rho_L}{dT} = -1.25$ % K^{-1} and $\frac{1}{\rho_L}\frac{d\rho_L}{dP} = 0.01$ % PSIA^{-1}. Besides errors in the temperature and pressure that propagate to errors in the density, the uncertainty in the density also has contributions due to target boiling, uncertainties in the equation of state and the target purity.

Each target loop is instrumented with two radiation resistant Lakeshore Cernox semiconductor resistors and two vapor pressure bulb to enable accurate temperature measurements. The Cernox resistors are calibrated at Lakeshore, and the calibration curves are loaded into an Oxford ITC502 temperature controller, which converts a resistance measurement to a temperature. With the Cernox resistors the absolute temperature can be measured to 100 mK and temperature changes to 50 mK. The relative error in the temperature measurement corresponds to a relative uncertainty of less than 0.1% in the density for D2 and H2. The target loop is instrumented with two heaters (resembling a hair dryer heater element) to control the temperature. Small temperature fluctuations are stabilized by means of a low power heater (max. output $\sim$80 W), which is controlled in a feedback loop, slaved off of one of the Cernox resistors. A high power heater (max. output $\sim$800 W) replaces the beam energy deposit when the beam is turned off. The pressure transducers used to measure the target pressure have an absolute error of 0.25 psi. Since the relative fluctuation of the density with the pressure is very small, pressure-related uncertainties in the density are negligible.

The electron beam deposits a significant amount of power in the target ($\sim$ 100 W @ 20 μA, for a 15 cm cell) and experiments were done to determine at which beam currents passage of the beam through the cell causes local boiling in the vicinity of the beam. Local boiling causes a reduction in the density and hence the luminosity. To prevent local boiling, the fluid flow in the target cell is made turbulent by adding flow diverters (see Figure 3.6), and the beam spot is enlarged through rastering. Experiments were carried out to study target density dependence on the beam current [88] and showed that no measurable density changes occur at the beam currents < 25 μA used in this experiment.

A chemical analysis of gas samples from the deuterium and hydrogen target gases was carried out by Lawrence Livermore National Laboratory. A detailed description of the sampling and analysis method is given in Appendix C, Section C.2.1. One hydrogen sample was taken, which was found to contain 99.8% hydrogen (by volume), with contaminations of nitrogen and oxygen. Three deuterium samples were taken, containing on average 99.5% deuterium (by volume), with the largest contamination hydrogen-deuteride (HD), in addition to nitrogen and oxygen. In both samples the nitrogen and oxygen contaminations are of no concern, since both N_2 and O_2 will freeze to the refrigerant tubing in the heat exchanger. The average HD contamination was 0.4%, therefore the target gas contained 99.8% deuterium nuclei (by volume), and a 0.2% correction to the target thickness was made.

The errors in the density listings in Table 3.3 were calculated for a stationary target (no beam) and reflect the uncertainty in the temperature measurement and the uncertainty in the equation of state. The equation of state for para-hydrogen was used to calculate the density, and the main contribution to the $\sim 0.5\%$ relative error is from the uncertainty in the relative amounts of ortho- and para-hydrogen in the target gas.

The operation of a target system with explosive hydrogen and deuterium gas in a sub-cooled fashion requires many safety features. An extensive target control system is in use. The target control system is built around an input/output controller (IOC), a Motorola microprocessor, housed in a VME crate. An EPICS [89] database is loaded on the IOC, which monitors target parameters such as temperature, pressure and fan speed. The front end is provided by a Tcl/Tk [90] graphical user interface (GUI), which connects to the EPICS database, and runs on a PC running the Linux operating system. A detailed layout of the target instrumentation and control system is given in Appendix C.

3.5 HMS Spectrometer

In the $\gamma d \to pn$ reaction, the proton is the only detected final state particle. Therefore the experiment is run as a single arm experiment, and both Hall C spectrometers (see Figure 3.2) can be used to take data simultaneously at different angles. The run plan for this experiment was designed to fully utilize the Hall C set-up, with the High Momentum Spectrometer (HMS) detecting photoprotons at forward angles, and the Short Orbit Spectrometer (SOS) at backward angles. Since data taken with the HMS is the focus of this work, the description of the spectrometers in Hall C will be limited to the HMS.

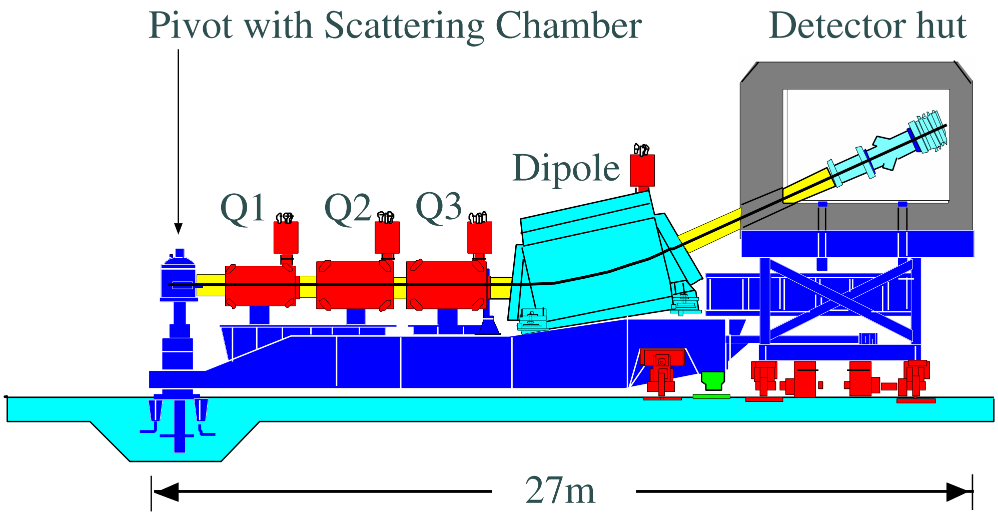

Figure 3.8: Side view of the HMS spectrometer showing the carriage supporting the three superconducting quadrupoles Q1, Q2, Q3, the superconducting dipole, and the detector hut with detector package.

Figure 3.8 shows a side view of the HMS. The HMS is a vertical bend spectrometer with three quadrupoles and a dipole in a QQQD configuration. Particles enter the spectrometer through a series of focusing quadrupoles, after which the dipole transports the particles to a detector package (housed in a lead-lined concrete shielding hut) by bending them in a vertical plane (the bend angle is 25° for the central ray).

The quadrupoles and dipoles are superconducting magnets, cooled with 4 K liquid helium from the CEBAF Central Helium Liquefier (CHL). The magnets are supported by a carriage, which has an extension to mount the detector supports, to minimize the relative motion of detectors and magnets in the system. A separate carriage supports the concrete detector hut. Both carriages are coupled together and rotate around the pivot point common to HMS and SOS, which supports the scattering chamber that houses the target.

For this experiment the spectrometer was used in a point-to-point tune. In this tune particles with same momentum and position at a target vertex are focused to same point in the focal plane (located between the two drift chambers in the detector package, see Section 4.3.1). To achieve this tune, Q1 and Q3 are set to focus in the dispersive direction and Q2 in the non-dispersive direction, providing a large momentum bite, solid angle and extended target acceptance. A summary of the HMS performance characteristics for the point-to-point tune is given in Table 3.4.

Quantity	Definition	Value
Maximum Central Momentum	–	7.4 GeV/c
Momentum Bite	$(p_{max} - p_{min})/p_c$	18%
Momentum Resolution	$\delta p/p$	<0.1%
Solid Angle	–	8.1 msr
Angular Acceptance (in plane)	–	$\pm$32 mr
Angular Acceptance (out of plane)	–	$\pm$85 mr
Angular Reconstruction (in plane)	–	0.5 mr
Angular Reconstruction (out of plane)	–	0.8 mr
Extended Target Acceptance	–	$\sim$ 10 cm

Table 3.4: HMS performance characteristics.

During the experimental running magnet currents and fields are calculated with a script that requires the central momentum as input. For the quadrupoles which are set by current, a field map relating power supply current to the magnet field was made. The dipole power supply is connected to a NMR-probe feedback loop that measures the field in the magnet. It can be set using field values directly. Magnet field/current and polarity settings and spectrometer rotation are all accomplished remotely from the Hall C counting house.

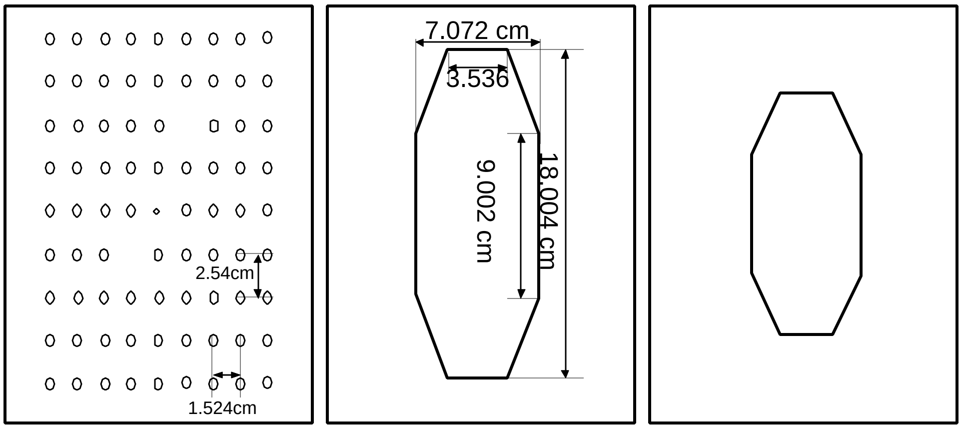

Figure 3.9: The HMS collimators and sieve slit. In the sieve slit two holes are missing to provide information for the optics data analysis. Both collimators are 2.5 inch thick, the sieve slit is 1.0 inch thick. Only the large collimator and the sieve slit were used in this experiment. Figure courtesy of J. Arrington.

At the entrance of the spectrometer, in front of the first quadrupole, a system with three collimator slits on a vertical ladder is installed. Figure 3.9 shows the two octagonal collimators and a sieve slit. The desired collimator is inserted remotely from the counting house. The collimators and sieve slit are constructed from sheets of Hevimet [91], a machinable tungsten alloy (90% tungsten, 10% CuNi). During normal data taking one of the two octagonal collimators is used. In this experiment the large collimator was used, which defines a rough spectrometer acceptance of 6.8 msr, but a more precise extended target acceptance is calculated with a Monte Carlo model (see Section 5.9). The sieve slit is a special collimator designed for optics and acceptance studies. It is an array of small holes (diameter 0.508 cm) with a smaller diameter hole in the center and two missing holes which provide information for the correct orientation during the analysis of optics data. The HMS optics studies will be discussed in Section 4.3.1

3.5.1 HMS Detectors

In the HMS detector hut an array of four separate detector systems is installed. Information from the four systems is combined to determine the momentum (from the trajectory) and identity (from velocity, mass and energy) of a particle that passes through the package. A schematic of the HMS detector package is shown in Figure 3.10.

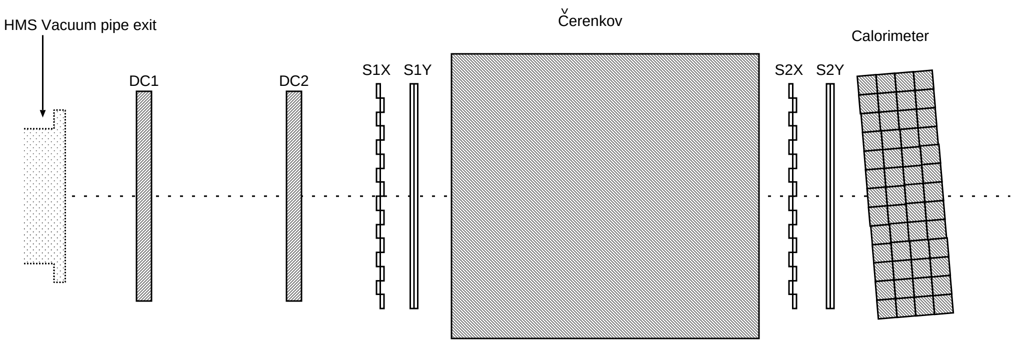

Figure 3.10: Schematic of the HMS detector package.

A particle that enters the detector package first enters one of a pair argon-ethane drift chambers. The drift chambers provide position information, which is used by tracking algorithm to calculate the trajectory of particle in the detector package. After passing through the second drift chamber the particle encounters a crossed pair of scintillator hodoscopes, a gas Čerenkov detector, another pair of crossed scintillator hodoscopes, and a lead glass calorimeter. The scintillator hodoscopes provide the trigger for detector read-out. In addition, they provide means of particle identification for heavy particles, through time-of-flight. The gas Čerenkov detector also provides particle identification as it can provide signals to separate electrons from pions or, as used in this experiment, protons from pions. Finally, the lead glass shower counter provides particle identification to enable electron-pion separation.

In order to combine the information from different detectors in the data analysis all spatial detector components and their position information must be expressed in a single coordinate system. The coordinate system in use in the detector stack is defined following the TRANSPORT [92] convention. In this convention the x coordinate is in the dispersive direction with $\hat{x}$ pointing downwards in the direction of particles with higher momentum. The z coordinate is on the central ray (z=0 in the focal plane), with $\hat{z}$ pointing in the direction of the incoming particles. The y coordinate is along the non-dispersive direction, with $\hat{y}$ pointing towards smaller scattering angles, so that a correct right-handed coordinate system is formed. Figure 3.11 shows the definition of the spectrometer coordinate system.

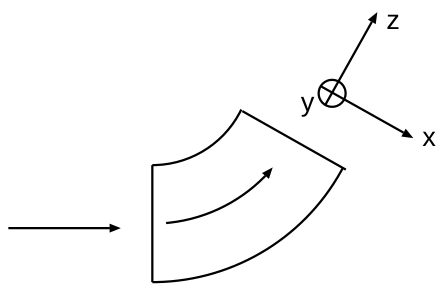

Figure 3.11: Definition of the spectrometer coordinate system for vertical bend spectrometers. This definition follows the TRANSPORT convention, see the text.

The particle trajectory reconstruction in the HMS detector package relies on the use of drift chambers. A drift chamber consists of an array of thin sense wires in a volume filled with a gas, susceptible to ionization. When a charged particle enters the drift chamber it ionizes the gas, and ionization electrons drift to the nearest sense wires. The generated charge creates a pulse on the wire, which indicates that a particle was somewhere in the vicinity of the wire. Wires in one direction do not provide enough position information, and planes with wires in different orientations are added. Then a combination of wires from different planes determines a point in space where the particle must have passed. However, an ambiguity remains, as to whether the particle passed a wire on the left or on the right. To solve the left-right ambiguity a second plane with parallel "like" wires is added to each plane present in the original set. The wires in the added planes are offset with respect to the wires in the original set, which provides the additional information to solve the left-right ambiguity.

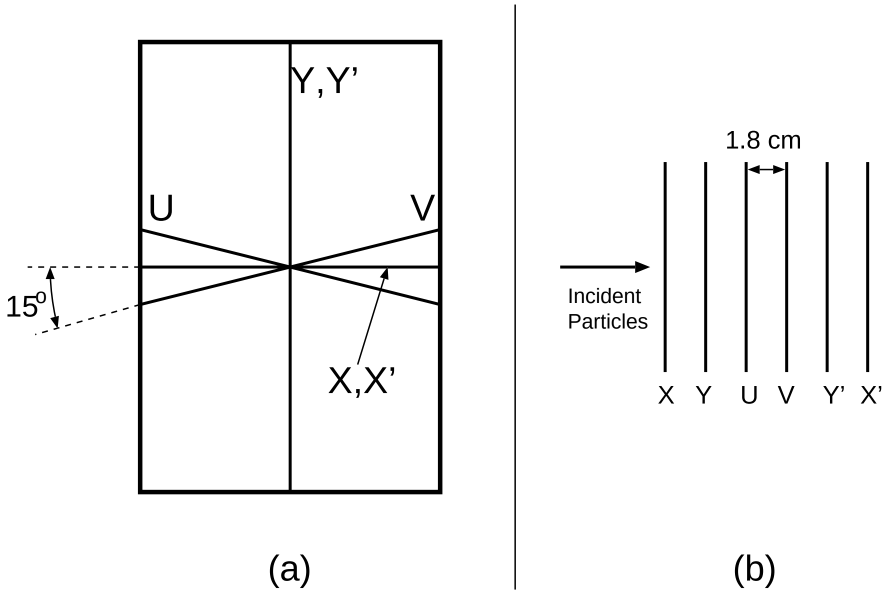

Figure 3.12: (a):View of an HMS drift chamber showing the wire orientation in the planes as seen by a particle entering the detector package; (b): The drift chamber planes and the order in which they are traversed by an incident particle.

The HMS detector package has two drift chambers separated by 81.2 cm, with the first one located directly behind the dipole vacuum pipe exit. Each chamber has 6 planes, separated by 1.8 cm, the horizontal X and X′ planes, both measuring the dispersive x direction, the vertical Y and Y′ planes, measuring the non-dispersive y direction, and U and V planes which make angles of $-15°$ and $+15°$ respectively, with the X plane. Figure 3.12.(a) shows a view of an HMS drift chamber as seen by a particle entering the detector package. The order in which the planes in a chamber are traversed by an incoming particle is X,Y,U,V,X′,Y′ as shown in Figure 3.12.(b) . The X and X′ plane each have 113 wires, the Y and Y′ plane each 52 and the U and V planes each 107 wires. The sense wire spacing in each plane is 1 cm so that an active area of 113 cm in x (vertically) by 52 cm in y (horizontally) is defined for each drift chamber.

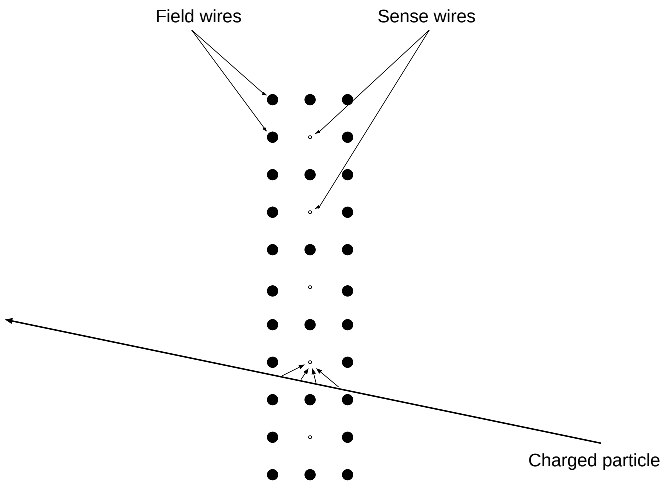

Figure 3.13: Cross section of a typical HMS drift chamber, showing the cell structure with field wires and sense wires. A trajectory of a charged particle passing through the chamber is shown, ionizing the chamber gas with the electrons being collected by the sense wire.

In addition to sense wires, the drift chambers also contain field wires. In each of the active planes the sense wires are spaced at 1 cm intervals with field wires in between. The active planes are separated by a plane with only field wires, so that each sense wire is isolated in a cell surrounded by field (guard) wires which create the electric field, that cause the ionization electrons to drift to the sense wire. The field wires are kept at a negative potential ranging between -1800 to -2500 V. The exact value is defined by the distance to the nearest sense wire, in a way that the equipotential lines in a cell are approximately circular. In the HMS drift chambers 25 μm diameter gold-plated tungsten wire is used for the sense wires (anodes). The field wires (cathodes) are 150 μm diameter gold-plated beryllium wires. Figure 3.13 shows the cross section of a typical HMS drift chamber, showing the cell structure with field wires and sense wires. The figure is not to scale. A trajectory of a charged particle passing through the chamber and ionizing the chamber gas is also shown. The planes V,X$'$,Y$'$ have the sense wires offset by one half cell-width (0.5 cm) with respect to the X,Y,U planes, to aid in the solution of the left-right ambiguity. The 6 planes are mounted in an aluminum frame, which has a thin mylar entrance and exit window attached to it. An argon-ethane gas mixture (50/50 by weight) flows through the chamber at a flow rate of about 200 cm^3/minute. A gas system was in place to monitor the gas mixture and flow rate, since variations in the gas mixture have an effect on the chamber efficiency, and consequently can influence the particle tracking efficiency. The sense wires are read out in groups of 16 by a pre-amplifier/discriminator card (either LeCroy 2735DC or Nanometrics N-277-L). The signals from the discriminator cards are sent to LeCroy 1877 multihit Fastbus time-to-digital converters (TDCs). The TDCs receive a common stop signal from the trigger. At that time all hits that came within 32 μs from the stop signal are stored (up to 16 hits per wire).

The time measured by a drift chamber TDC in combination with other trigger timing is used to calculate the time it takes the ionization electron to drift from the point of creation to the sense wire (the "drift time"). In turn, the drift times are used to create a drift-time-distance relationship, which allows for a conversion between measured drift times and the distance from the wire where the particle passing through causes the ionization. The drift time-distance relationship is determined from data. Using a high statistics run with >20000 events a histogram is created of the drift times for all wires. The distribution in time is then mapped to a uniform distribution over the ± 5 mm cell width, and stored for use by the tracking algorithm. A complete description of the drift chambers and their performance is presented in Reference [93].

The HMS hodoscopes perform two central tasks in the detector package. First and foremost they provide the signals to form the trigger, which prompts the the data acquisition to start and read out all detector information. Secondly, they provide means of separating protons from other positively charged hadrons like pions and deuterons, using time-of-flight.

The HMS hodoscopes are built from strips (paddles) of BC404 plastic scintillator. On both ends UVT lucite light guides form the interface between the paddle and Philips XP82282B photomultiplier tubes (PMTs). When charged particles pass through the scintillator material, they ionize the atoms in the material, and leave free electrons from the scintillator molecules in an excited state as well. As these excited states decay, light is emitted. The emitted light either travels directly to the PMT, or reaches the PMT as it undergoes total internal reflection of the walls of the paddle (provided the angle of incidence on the scintillator surface is greater than the critical angle). To increase reflectivity the paddles are wrapped in one layer of aluminum foil. The scintillator is finished by wrapping it in two layers of Tedlar to make the entire assembly light tight. Most plastics used for scintillator material offer an extremely fast signal decay constant of 2–3 ns, and high light output [94]. As the light is produced and collected quickly, the scintillators provide a very accurate timing of the charged particle passing through. Thus, the hodoscopes meet the requirements to form the trigger which prompts the fast electronics to accept an event. The trigger for this experiment is set up so that hodoscopes firing in coincidence (a predefined combination of planes "fires" when a particle passes through) form the trigger to read out rest of the detectors.

The HMS detector package has 4 hodoscopes, with are paired in two horizontal-vertical X–Y sets. S1X and S1Y form a pair hodoscopes located in front of the Čerenkov detector, and S2X and S2Y directly behind it. The sets are separated by 220 cm. The X(Y) hodoscopes each consist of 16(10) horizontally (vertically) oriented paddles. The paddles that make up the X and Y hodoscopes are all 1 cm thick and 8 cm wide, however they differ in length, with the X-paddles measuring a length of 75.5 cm and the Y-paddles a length of 120.5 cm .Thus the total active area of each hodoscope pair is 120.5 cm vertically by 75.5 cm horizontally. In each of the 4 planes, the paddles are staggered in z with a 0.5 cm overlap between the paddles to avoid gaps between the elements. Each element is read by PMTs on both ends. The signals are sent to the counting house, where they are split, to be read out by ADCs, TDCs, scalers, and prepared for input to the hadron trigger. The hodoscope electronics and its connection to the hadron trigger is discussed in Section 3.6. Timing calibrations to correct for pulse height variation and offsets of the individual PMTs are carried out using experimental data. The procedure is described in detail in Section 4.4.1. The final timing resolution per plane is $\sim$ 100 ps, which results in a β resolution of 0.018 for electrons (β=1) [95], making these hodoscopes very suitable for proton particle identification through time-of-flight.

Time-of-flight particle identification is based on measurement of the particle momentum and velocity, which uniquely define the particle's mass, in turn identifying the particle. The particle momentum is known from the HMS central momentum setting and the velocity can be calculated using hodoscope timing information. In the HMS the hodoscope planes are separated by an adequate distance, and the velocity is calculated from the distance between the first and last hodoscope plane and the difference in response times between those planes. Since pions, protons and deuterons have the same momentum, but different velocities as they enter the detector package, time-of-flight provides means to identify and select the protons from all other events. Time-of-flight particle identification is described in more detail in Section 4.4. Figure 3.14 shows a view of an HMS X–Y pair of hodoscopes, including an incident particle, which causes a crossed pair of two scintillators to fire.

At high momenta ($p \geq 2.5$ GeV/c), where time-of-flight separation between protons and pions becomes increasingly difficult, the gas Čerenkov detector aids in proton/pion separation. Čerenkov detection of particles is based on the principle that a particle that moves through a medium at a velocity greater than the speed of light in that medium emits Čerenkov radiation. A threshold Čerenkov detector contains a medium that has an index of refraction which is chosen so that the faster of the two particles to be distinguished emits radiation, and the slower does not. The emitted Čerenkov light is detected and provides means to discriminate against the particle type that produced the light. Because the detector has to be applicable to e/π as well as p/π separation a medium with gaseous phase is very suitable, since the index of refraction can be easily modified by changing its pressure. In addition, a gas has a small effect on the attenuation of particles passing through. For a medium with index

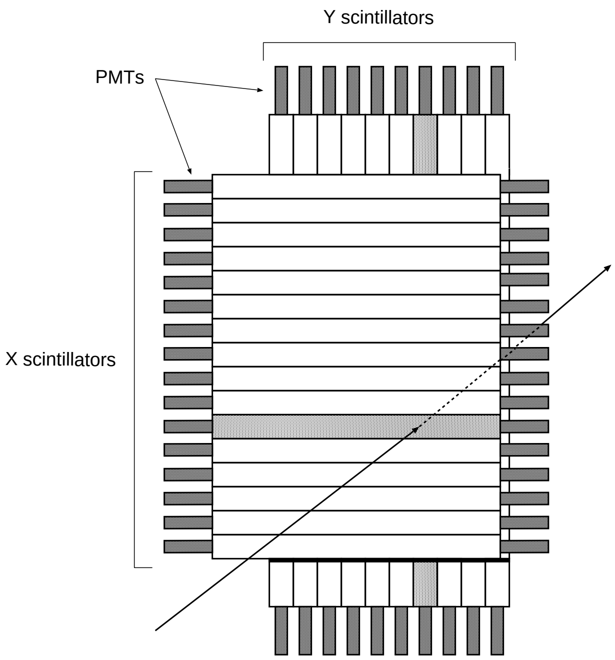

Figure 3.14: View of an HMS hodoscope pair. The X-plane is made from 16 paddles, the Y-plane from 10 paddles. In reality the paddles are staggered with a 5 mm overlap. Also shown is the track of a particle firing a crossed pair of two scintillators (indicated by shading).

of refraction n, the Čerenkov threshold velocity is defined by $\beta_{th} = 1/n$ [20]. In the case of pion/proton separation, as desired for this experiment, the pion momentum threshold becomes:

$$p_{\pi,thres} = \frac{m_\pi}{\sqrt{n^2 - 1}}. \tag{3.2}$$

Thus, when a vessel is filled with an appropriate gas at a pressure corresponding to the threshold index of refraction, pions with momentum greater than $p_{\pi,thres}$ will emit Čerenkov light, and protons will not.

The HMS Čerenkov detector is an aluminum cylindrical tank with large concave entrance and exit windows. The tank has a diameter ~ 150 cm and length ~ 165 cm and is located between the two pairs of hodoscope planes. The tank was designed to run at pressures up to 3 atmospheres, as well as below atmosphere, the latter by reversing the 0.040 inch thick aluminum entrance and exit windows. During this experiment the tank was filled with perfluorobutane (C_4F_{10}, n=1.00143 at 1 atm. and 300 K) at a pressure p =14.2 psiA (0.966 atm.), corresponding to an index of refraction n=1.00138. At this pressure, the pion momentum threshold is equal to 2.65 GeV/c. Two spherical mirrors at the back of the tank focus the Čerenkov light to two Burle 8854 photomultiplier tubes. The signals from both PMTs are sent to the Counting House, where they are split in a 50/50 splitter. One half of each signal goes to a Fastbus ADC (LeCroy LRS1881M), the other half is summed in a linear fan-in module and passed to a discriminator. From the discriminator the signals are sent to TDCs, scalers, and the trigger, where they can serve as an input for the trigger logic. In the hadron trigger used in this experiment, no Čerenkov signals were used in the trigger. The Čerenkov detector was used in the data analysis, to establish a clean proton particle identification. It was observed that the pions were located at a PMT signal >3 photoelectrons for the majority of the kinematical settings. A detailed description of the Čerenkov detector, its performance and associated electronics can be found in reference [95].

The last detector that a particle encounters in the stack is the lead glass calorimeter (shower counter). The calorimeter provides particle ID of electrons, and pions, facilitating pion rejection. The shower counter is an electromagnetic calorimeter, measuring the energy deposited by a particle (in particular an electron) that enters the lead glass. As a high energy electron enters the lead glass it decelerates in the field of lead glass nuclei and emits bremsstrahlung photons. When the bremsstrahlung photons are energetic enough, they cause pair-production, creating e^+/e^- pairs. In turn the generated electrons and positrons radiate more photons, and a shower occurs. The calorimeter is built from blocks of lead glass, which each have a photomultiplier tube (PMT) connected to them. The PMTs detect Čerenkov light emitted by the charged particles passing through the lead glass blocks. The amount of light measured by a PMT is proportional to the amount of energy deposited in the block it is mounted to. By summing the light contribution from all blocks a signal proportional to the energy of the initial electron is obtained. Even though the primary objective of the calorimeter is to measure the electron energy, hadrons (pions, protons etc.) also leave a signature. In contrast with electrons, which deposit their entire energy in the calorimeter, hadrons typically deposit about 300 MeV. The calorimeter energy deposit is expressed as an energy fraction, the ratio of the energy detected in the calorimeter to the particle momentum (from tracking), which is 1 for electrons, and shows up as a distribution around E_{cal}/p=0.3 GeV/p for hadrons in the calorimeter energy fraction distribution.

The shower counter is an array of TF1 lead glass blocks, stacked in 4 layers of 13 blocks each. Each block measures 10 cm$\times$10 cm$\times$70 cm and has a Philips XP3462B PMT attached to one end. In total the detector has an active area of 130$\times$70 cm, with a depth corresponding to roughly 16 radiation lengths (X_0=2.54 cm). As shown in Figure 3.10 the detector is rotated 5° with respect to the HMS optical axis to prevent particles from passing through cracks. Each lead glass block is wrapped in one 25 μm layer aluminized mylar which reflects the light and two 38 μm layers of Tedlar film to make the block light tight. A detailed description of the design and performance of the calorimeter is given by [96]. Signals from the PMTs are run to counting house where they are split 50/50. One half of the signal is passed to a LeCroy 1881M ADC, the other half is sent to fan-ins for summation. Two sums are generated, a sum of the first layer of blocks (the pre-shower sum, PRSUM) and a sum of the entire calorimeter (SHSUM). The summed signals can serve as a particle ID input to the trigger, but were of no use in the HMS hadron trigger used in this experiment. However, the calorimeter signal was used in combination with proton time-of-flight to obtain a clean proton sample for the tracking efficiency analysis (see Section 4.1.1).

3.6 HMS Hadron Trigger

Hall C trigger electronics can generate triggers for both HMS and SOS in single arm mode, as well as coincidence triggers, when both spectrometers are used in coincidence. At the start of each data taking run the Trigger Supervisor (TS) is programmed to accept, reject or prescale (i.e. read only every n^{th} event) each of the trigger types. Prescaling is often done to achieve a more manageable data rate and to reduce the dead time. Since the photoproton was the only final state particle of interest, only single spectrometer triggers were taken and coincidence triggers were prescaled away. For a few beam energies, data was taken with HMS and SOS spectrometers simultaneously in single arm mode. In this set-up it is conceivable that both HMS and SOS receive a single arm trigger within the time interval that would create a coincidence trigger. Even though the COIN triggers are ignored, the TS will accidentally treat this event as a coincidence trigger. Due to the very small occurrence of these false coincidence events (about 1 in every 10^5 events), the effect is negligible. Moreover, the false coincidences were only observed for very high SOS trigger rates, and prescaling of the SOS triggers further reduced the effect.

For the detection of photoprotons in this experiment the HMS single arm hadron trigger was used, which is based on the HMS single arm electron trigger, described in great detail in [95]. The main difference is that since the particle identification of protons relies primarily on time-of-flight, other particle ID signals like the shower counter signal for electrons, or the Čerenkov veto signal for charged pions, are removed from the trigger, and the trigger is formed by the hodoscope trigger (SCIN) only. The SCIN trigger is produced by combination of signals from the scinitillator planes, which fire as any charged particle (not just a photoproton) passes through them.

The X(Y) hodoscope planes in the HMS are built from 16(10) individual paddles, each of which have a photomultiplier tube (PMT) on both sides. To be able to distinguish the sides, one side is designated as the "positive" side and the other as the "negative" side. Figure 3.15 shows a diagram of the hodoscope electronics. As they

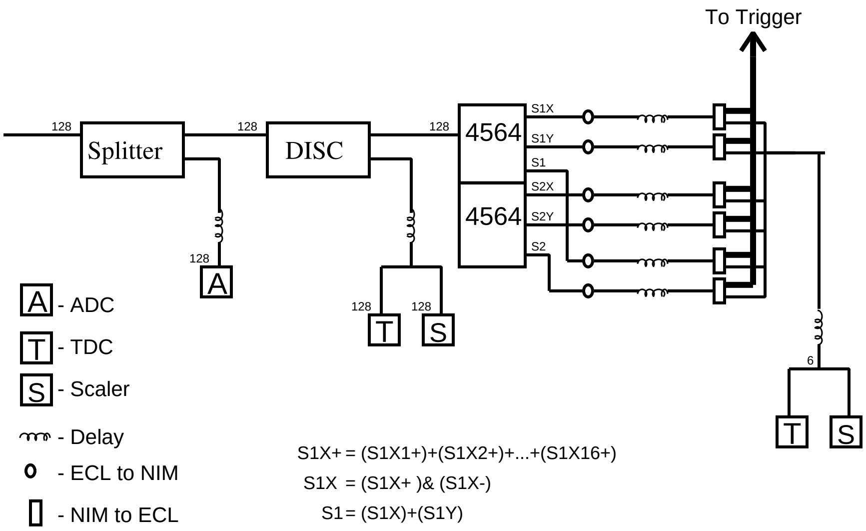

Figure 3.15: Schematic of the HMS hodoscope electronics. The numbers next to the modules indicate the number of channels used.

arrive in the counting house, the signals from the PMTs are split in a splitter, where 1/3 of the amplitude of the signal is passed through a delay and fed into a LeCroy Fastbus (LRS1881M) Analog-to-Digital Converter (ADC), which measures the integral of the signal. The other 2/3 of the signal is passed to a leading edge discriminator (Philips PS7106). The discriminator has two outputs, one that passes the discriminated signal through a delay to VME scalers and to LeCroy Fastbus (LC1872A) high resolution Time-to-Digital Converters (TDC). The other discriminator output is passed to a LeCroy 4564 logic module, which takes the logical OR of the signals from a given side of the hodoscope, and forms a signal S1X+ (S1X−), in case of the S1X plane. A hit in a given plane is then defined as a logical AND of S1X+ and S1X−, S1X, i.e. for a hit at least one tube on each side has to fire, but the tubes do not have to belong to the same paddle. The latter was done to reduce the amount of electronics, without causing significant random signals [95].

The scintillator trigger SCIN is formed by combining the signals S1X, S1Y, S2X, and S2Y corresponding to hits in each of the 4 planes in a LeCroy logical unit (LRS365AL), as shown in Figure 3.16. For SCIN to be true either 3 out of 4, or

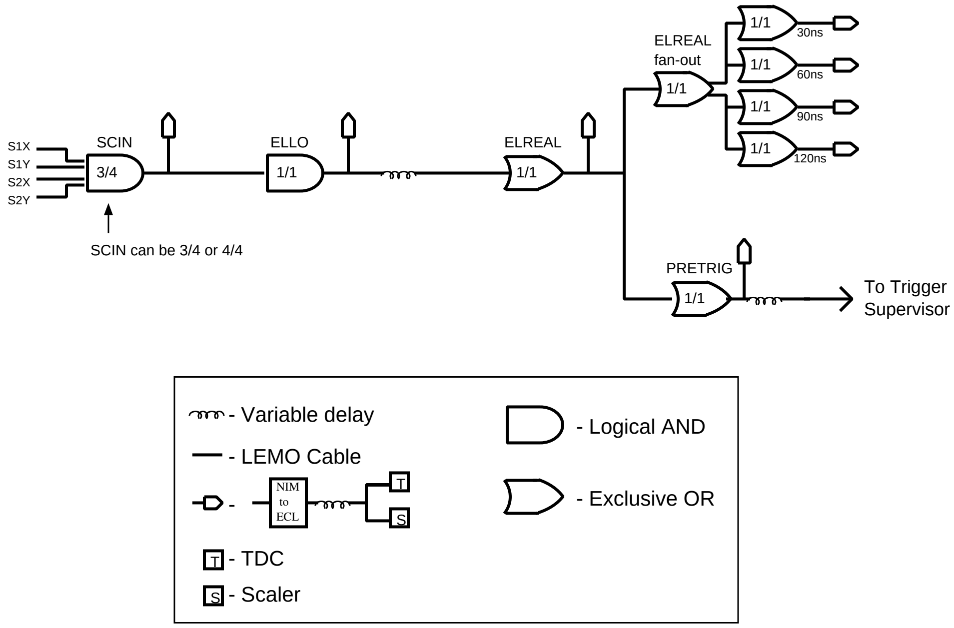

Figure 3.16: HMS single arm hadron trigger electronics.

4 out of 4 hodoscope planes need to have a valid hit. The 4/4 trigger provides the tightest scintillator trigger. When SCIN is formed, the ELLO trigger automatically fires as does ELREAL, which generates the raw spectrometer trigger, the so-called "pretrigger". The trigger diagram also shows that many intermediate signals are sent to scalers and TDCs. From the TDCs it can be determined which signals were present during the run, and the scalers provide information about raw data rates and the performance of the electronics.

The pretriggers generated in ELREAL have a 30 ns gate width and are passed to the LeCroy 8LM programmable logic module (LC2365), which is part of the Trigger Supervisor electronics (see Figure 3.17). The 8LM has six inputs, the HMS, SOS and COIN pretriggers and the signals TS GO, TS EN1, and TS BUSY from the Trigger Supervisor, and provides eight outputs, four pretriggers and four triggers, which are logical combinations of the six inputs (see Table 3.5). When a data run is started the TS GO signal is enabled, and random pedestal (PED) triggers are generated to read the pedestal information from the ADCs (see Section 3.7). After 1000 pedestal

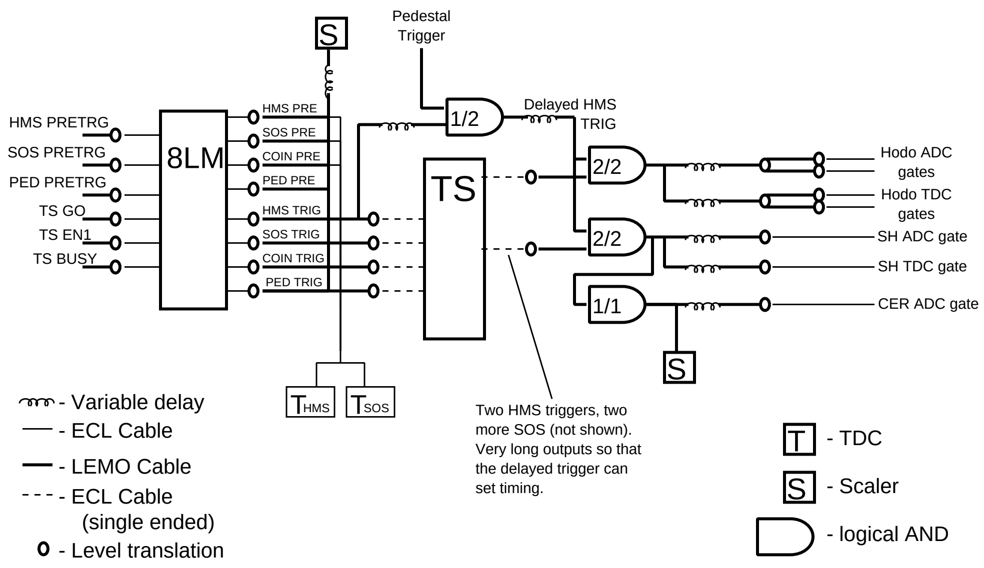

Figure 3.17: Schematic of the Hall C Trigger Supervisor electronics.

events the signal TS EN1 is enabled for physics data taking. When the TS is busy processing an event incoming event, the signal TS BUSY is enabled, and triggers generated at the 8LM are not passed on to the TS. However, the pretrigger type is still read by a scaler, for use in dead time calculations (see Section 4.6). When the TS is not busy, the 8LM trigger is split in two parts, one of which bypasses the TS and is delayed. The other is passed to the TS, which creates two HMS gates, which are long enough that the Fastbus crate reports are included in the gate. When the TS trigger and the bypassed trigger are combined, ADC gates and TDC common start and stop signals for the event are generated, where the actual timing of the ADCs and TDCs is determined by the bypassed delayed HMS trigger.

3.7 Data Acquisition

The data files from physics experiments in Hall C are generated with a data acquisition system that is controlled by CODA (the CEBAF Online Data Acquisition system) [97] which runs a Hewlett-Packard 9000/735 Unix workstation. When the

Output Signal	Definition in Logic
HMS PRE	HMS & $EN1$
SOS PRE	SOS & $EN1$
COIN PRE	$COIN$ & $EN1$
PED PRE	PED & GO & $\overline{EN1}$
HMS TRIG	HMS & $EN1$ & $\overline{BUSY}$
SOS TRIG	SOS & $EN1$ & $\overline{BUSY}$
COIN TRIG	$COIN$ & $EN1$ & $\overline{BUSY}$
PED TRIG	PED & GO & $\overline{EN1}$ & $\overline{BUSY}$

Table 3.5: LeCroy 8LM trigger logic. Triggers are pretriggers which have a non-active $BUSY$ signal from the TS. The signal GO is active when a run is started. The $EN1$ signal is used to block physics triggers during pedestal running and block pedestal triggers during physics data taking. In this table the logical AND operation is denoted by '&', and the logical negation by a horizontal bar above the variable.

Trigger Supervisor generates a trigger, the control system reads the data through a fiber optic link from Read-Out Controllers (ROCs), which are CPUs in the Fastbus and VME crates that contain the ADCs, TDCs and scalers that log the event information. The CODA event builder then builds the events from the fragments read from the ROCs and writes the complete physics events directly to a hard disk.

To limit the raw event size to a minimum amount of bytes and improve the data acquisition rate, the TDCs and ADCs are operated in a sparsified ("zero-suppression") mode. For the TDCs this means that only channels with stops are read out. Sparsified read-out of the ADCs is achieved by means of a programmable threshold, which is typically set at 15 channels above the pedestal (zero reading). A separate measurement of the ADC pedestals is carried out at the beginning of each run, by generating 1000 pedestal with random triggers (with a pulser) and sparsification turned off. These are written to disk in the same data file as the physics data. After the pedestal running, sparsification is turned on and physics events containing only non-zero data from the ADCs and TDCs are written to disk.

In addition to the physics events CODA also reads out the hardware scalers every two seconds. Values of parameters of experimental equipment which is not directly related to the data acquisition is read into the data stream every 30 seconds. Among these so-called slow control parameters are the target pressure and temperature read-back, detector high voltages, and magnet current settings. The target and magnet controls also have separate data acquisition that logs a larger subset of the control parameters and status variables.

Chapter 4

Data Analysis

The E89-012 analysis code is based on the standard Hall C analysis package [95] to which subroutines for experiment specific physics were added. In the standard package events are decoded from the raw CODA run-files. After detector calibration, subsequent data reduction generates a track in the detector stack, timing information, and particle identification information for each event. From position and angle of the track at the focal plane the momentum, vertex position, and angles at the target are reconstructed. Histograms to check detector performance are generated and saved in PAW [98] HBOOK files. Physical parameters including the reconstructed quantities, focal plane coordinates, and particle identification are saved on an event by event basis in PAW ntuples. Scalars, calculated tracking efficiencies, and dead times are saved in text form in scalar report files

4.1 Particle Tracking

For each event the two drift chambers in the HMS detector stack are used to construct a track, which defines hit coordinates and slopes in the focal plane. Using matrix elements to describe the transport through the spectrometer, the vertex at the target is reconstructed from the focal plane coordinates.

The tracking algorithm starts by converting the TDC timing information of the wire hits to drift distances of the ionization electrons that reached the sense wires. The drift distance defines a radial distance from the sense wire, where the ionising particle passed through the drift chamber. The individual planes in each chamber are calibrated by generating a drift-time-to-distance map. This ensures that the distribution of drift distances is uniform over the cell around the sense wire, and minimizes the effects of rate variation with run type.

The hit position along the wire is determined by combining information from planes with non-parallel wires, e.g. a hit on an X and Y wire. Since in the HMS the U(V) wires are at $+(-)\ 15°$ relative to the X-wires, the combinations X−U, X−V, and U−V are considered too parallel to give reliable position information. Combinations of non-parallel wires that lie within a defined radius (the space-point-criterion) are grouped into a space point. At this time the particle could have passed the wire in the space point on the left or on the right. To solve this left-right ambiguity, stubs (short tracks inside the chamber) are fitted through the space points in the chamber, and the stub with the best χ^2 is chosen. Since this results in a time consuming algorithm, the physical layout of the drift chambers is used to reduce the number of left-right combinations for the stubs. In the HMS wire chambers the Y and Y′ planes, which are offset by 0.5 cm, are close together, enabling the use of a small angle approximation. This eliminates the left-right ambiguity for these planes since a particle that caused a hit in both Y and Y′ planes is assumed to have passed between the wires. After the best stubs have been selected in both chambers, stubs in both chambers that roughly point at each other and have consistent slopes are linked to form a track. In case multiple tracks are formed, the track with the best χ^2 is selected.

Standard Hall C software requires that 5 out of 6 planes in each chamber are hit by a particle passing through to find a track for that event. Therefore, always at least one plane with Y-like information is present. In experiment E89-012 it was observed that there were a considerable number of events for which scintillator hits showed that the particle passed through the center of the acceptance, but only 4 planes fired, in one (or both) of the chambers. To include these potentially good photoprotons in the analysis, the tracking algorithm was changed to find a track with at least 4 planes out of 6 firing, subject to the restriction that sufficient Y-like position information is present for the event.

Whereas for 5 out of 6 tracking the left-right ambiguity is solved by fitting the stubs and selecting the one with the best χ^2, for 4 out of 6 the ambiguity often remains, and is solved by selecting the stub with the minimum slope [99, 100]. Because tracks cannot be found for events with missing Y and Y′ information, 4 out 6 tracking cannot recover all "good" events. Therefore the procedure will not be 100% efficient, but generally more efficient than 5 out of 6 tracking [101]. The use of 4 out of 6 tracking to recover "lost" events can only be justified if the tracking-efficiency corrected yields are consistent for both the 4 out of 6 and 5 out of 6 case. A comparison has been been made and is presented in Section 4.1.1

Once the track for the particle is selected, the focal plane quantities are known. The set of focal plane quantities is made up of x_{fp} and y_{fp}, the vertical and horizontal coordinates, respectively, and $x'_{fp} = \frac{dx_{fp}}{dz}$ and $y'_{fp} = \frac{dy_{fp}}{dz}$, the vertical and horizontal tangents to the track in the point (x_{fp},y_{fp}).

4.1.1 Tracking Efficiency

Even though each particle has a well-defined track through the detector package, the reconstruction of that track fails a small percentage of the time. Events that fail to meet the requirements on the minimum number of firing planes per chamber, the maximum number of hits in each chamber, as well as noisy wires can prevent the tracking algorithm from finding a track. The tracking efficiency quantifies how well the drift chambers work as well as the ability of the tracking algorithm to find a track for a given event.

The tracking efficiency is calculated with a method that utilizes a fiducial area in the hodoscope planes in combination with loose particle identification cuts. The particle ID cuts are important because the protons have to be singled out to find the correct tracking efficiency. In each scintillator plane a group of paddles is chosen to mask an area (the fiducial area) corresponding to the central acceptance as shown in Figure 4.1. A particle that produces a signal in the scintillators within the fiducial

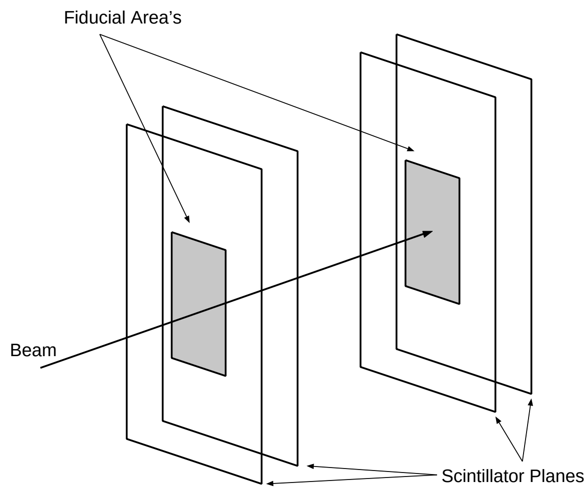

Figure 4.1: Location of the fiducial areas in the HMS hodoscope planes.

area had to pass through both wire chambers. A binary variable is assigned to the fiducial area, which turns to 1 if any of the scintillator paddles inside the fiducial area fires, and none outside. As a "trigger" for a track through the fiducial volume, a hit in either 3 of 4, or all 4 scintillator planes is required. The case of 4 of 4 scintillator planes generates the highest quality tracks and was used exclusively for the E89-012 tracking efficiency analysis.

In this experiment the fiducial area is made up of paddles 5–12 for the X-scintillator planes and paddles 3–8 for the Y planes. The area chosen is slightly larger than the standard fiducial area (X:6–11, Y:5–6) to increase statistics, without losing accuracy on the calculated tracking efficiency. For run 7400 (E_{beam}=1.645 GeV, θ_{cm}=37°), tracking efficiencies were calculated for all fiducial area combinations. As compared to the standard fiducial area a maximum variation of 5% in the calculated tracking efficiency was observed for the most extreme combinations of fiducial areas (i.e. all paddles used as fiducial area). An average variation of about 1% in the calculated tracking efficiency is observed when the value for the E89-012 fiducial area is compared with those for directly adjacent areas. This is part of the systematic uncertainty in the tracking efficiency.

Since the tracking efficiency analysis is done prior to the definition of the track with the lowest χ^2, particle ID cuts have to be applied to variables that do not depend on reconstructed quantities. The energy along the track in the calorimeter and β_{TOF} do not depend on reconstructed quantities and are used for these particle ID cuts.

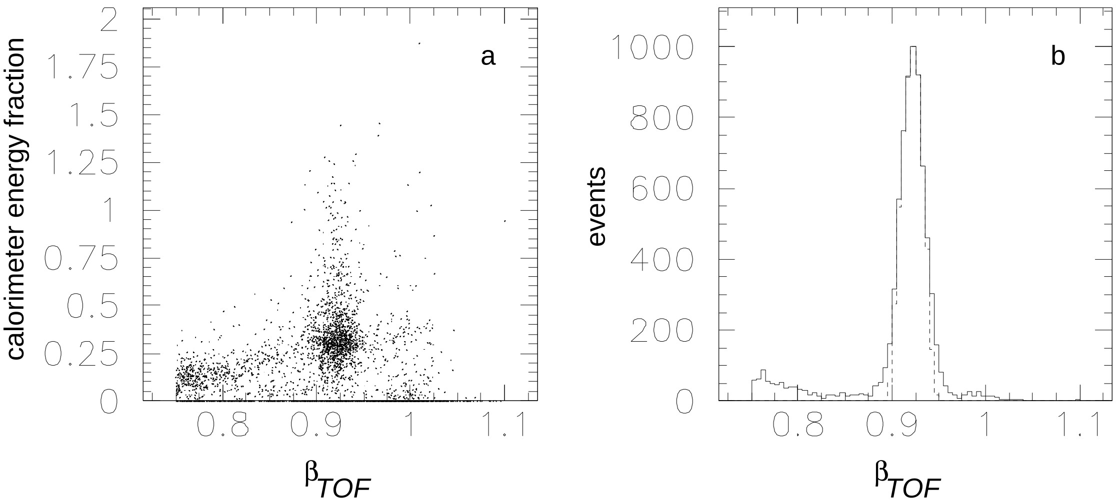

Figure 4.2: (a): Distribution of the calorimeter energy fraction as function of the particle velocity β_{TOF}. (b): Clean β_{TOF} distribution (solid) and part of the β-spectrum included in the tracking PID cut (dashed). Both figures are for E_{beam}=3.245 GeV, θ_{cm}=90°.

Figure 4.2.(a) shows the distribution of the energy fraction $E_{cal-track}/p$, which is a measure for total energy deposited in the calorimeter along the track, versus β_{TOF} for E_{beam}=3.245 GeV, θ_{cm}=90° kinematics. The figure shows that a *clean* sample of protons can be obtained by taking the protons with $E_{cal-track}/p > 0.45$. This limit is determined using the total calorimeter energy deposited *after* the track is found, which includes a cluster-correction. However this correction is only a few percent, which justifies the use of this value for a cut on the calorimeter energy deposited *before* the track was found. In addition to the lower limit on energy deposited in the calorimeter, a mass-squared cut on the clean β-spectrum generates a β-interval that

the protons have to fall within. Figure 4.2.(b) shows the clean beta spectrum as a solid line. The dashed line represents the protons that fall within the mass-squared cut. For most kinematics the cut on $E_{cal-track}/p$ is placed at 0.50–0.60, for the lower energies the cut varies from 0.05 to 0.30. Table 4.1 lists the lower and upper limits on β and the lower limit on $E_{cal-track}$/p.

E_{beam} (GeV)	θ_{cm} (nominal)	$E_{cal-track}/p$	β_{low}	β_{high}	
0.845	37°	0.060	0.739	0.825	
	90°	0.055	0.640	0.755	
1.645	37°	0.450	0.850	0.950	
	53°	0.350	0.850	0.909	
	70°	0.400	0.820	0.900	
	90°	0.200	0.779	0.861	
2.445	37°	0.350	0.909	0.969	
	53°	0.500	0.910	0.954	
	70°	0.400	0.884	0.950	
	90°	0.400	0.854	0.920	
3.245	37°	0.550	0.935	0.989	
	53°	0.500	0.924	0.979	
	70°	0.500	0.910	0.978	
	90°	0.450	0.894	0.945	
4.045	37°	0.600	0.950	1.000	
	53°	0.500	0.940	1.000	
	53°	0.500	0.940	1.000	1997 dataset
	70°	0.550	0.925	0.990	
	70°	0.400	0.920	0.990	1997 dataset
	90°	0.500	0.909	0.970	

Table 4.1: Particle identification cuts used in the tracking efficiency analysis, for all kinematics. The table lists the lower limit on the calorimeter energy fraction $E_{cal-track}/p$, and the lower (upper) limits on the particle velocity, β_{low} (β_{high}).

With the proper PID cuts the tracking efficiency is defined as

$$T_{eff} = \frac{N_{tracks}}{N_{fid\_hits}}, \tag{4.1}$$

where N_{fid_hits} is the number of "triggers" in the fiducial area that meet the criteria on number of planes, number of hits, and PID, and N_{tracks} the number of those for which the tracking algorithm found a track at the focal plane. Each run was corrected with its corresponding tracking efficiency, calculated using this method. For the 4 different run types (radiator in with and without deuterium, LDI & MTI, and radiator in with and without deuterium, LDO & MTO, see Section 5.2) the charge-weighted tracking efficiencies and standard deviations were calculated. The results are listed in Table 4.2. A "–" in the σ columns of the table corresponds to a kinematic setting where only one run was taken, and no standard deviation could be calculated. The table shows that on average, tracking efficiencies of better than 90% for protons only were obtained with this method, which is in agreement with the observed performance for electrons [95]. The values found here are slightly lower due to the presence of the gate valve. The tracking efficiency analysis is carried out before tracks and reconstructed quantities are known, so the gate valve cut (see Section 5.6.2) could not be applied. The increase in the standard deviations seen at the higher energy kinematics is largely due to low statistics at these settings. An untimely gas-bottle change at the E_{beam}=4.045 GeV, θ_{cm}=37° and 53° setting resulted in lower than average tracking efficiencies at these kinematics. The low tracking efficiencies at E_{beam}=2.445 GeV, θ_{cm}=37° and 53° is most likely attributed to the chambers being out of equilibrium, caused by a drift chamber threshold sensitivity experiment that was carried out just prior to those runs. Moreover, insufficient HMS dipole shielding during the early 2.445 GeV data taking, caused a high level of accidental background, which greatly reduced the available statistics for empty target runs.

To determine the systematic uncertainty in the tracking efficiency, a set of runs was analyzed using the 4-out-of-6 as well as the 5-out-of-6 tracking algorithms. The endpoint yields obtained with both algorithms were corrected with their respective tracking efficiencies, and then compared. Table 4.3 shows the corrected endpoint yields $N^c_{4/6}$ and $N^c_{5/6}$ for 4/6 and 5/6 tracking respectively. As expected, the yields are in excellent statistical agreement. Also shown is the percentage difference between

E_{beam} (GeV)	θ_{cm} (nominal)	T_Q^{LDI}	σ_{LDI}	T_Q^{LDO}	σ_{LDO}	T_Q^{MTI}	σ_{MTI}	T_Q^{MTO}	σ_{MTO}
0.845	37°	0.958	0.009	0.962	0.005	0.964	0.066	0.967	0.008
	90°	0.971	0.009	0.971	–	0.973	–	0.972	0.007
1.645	37°	0.808	0.022	0.832	–	0.826	-	0.840	–
	53°	0.835	–	0.831	0.018	0.837	–	0.844	–
	70°	0.862	0.006	0.859	0.028	0.859	0.013	0.901	–
	90°	0.967	0.001	0.970	0.008	0.967	–	0.963	–
2.445	37°	0.764	0.140	0.832	–	0.877	0.009	0.859	–
	53°	0.959	0.009	0.963	0.007	0.290	–	0.305	–
	70°	0.884	0.021	0.472	–	0.697	–	0.616	0.099
	90°	0.960	0.016	0.974	0.008	0.969	0.018	1.000	0.000
3.245	37°	0.931	0.008	0.954	–	0.885	0.026	0.857	–
	53°	0.943	0.011	0.946	0.026	0.898	0.041	0.912	–
	70°	0.946	0.010	0.953	0.025	0.939	0.036	0.933	0.059
	90°	0.957	0.017	0.969	0.016	0.964	0.024	0.973	0.006
4.045	37°	0.921	0.009	0.925	0.017	0.803	0.013	0.681	–
	53°	0.907	0.015	0.896	0.058	0.728	0.059	0.648	0.109
	53°†	0.904	0.022	0.949	0.013	0.880	0.116	0.864	–
	70°	0.918	0.025	0.915	0.050	0.909	0.037	0.888	0.093
	70°†	0.918	0.034	0.921	–	0.918	–	1.000	–
	90°	0.923	0.039	0.908	0.044	0.973	0.024	0.847	0.192

Table 4.2: Charge weighted tracking efficiencies and standard deviations for all kinematics. A "–" in the σ columns of the table corresponds to a setting where only one run was taken, and no standard deviation could be calculated. Kinematics labeled with † were measured in 1997.

the yields of both methods, as compared to the 5/6 case. This number is assumed to be a measure of how well the tracking efficiency correction works, since both yields should theoretically be identical. The weighted mean of the percentage difference was determined to be $3.3 \pm 0.2\%$. This result was taken as the systematic uncertainty due to tracking algorithm. The overall systematic uncertainty in the tracking efficiency is obtained by adding the algorithm and fiducial area contributions in quadrature, and comes to 3.4%.

run	E_{beam}, θ_{cm} (nominal)	$N^c_{5/6}$ (# counts)	$N^c_{4/6}$ (# counts)	$(\frac{N^c_{4/6}}{N^c_{5/6}} - 1)$ (%)
7393	1.645 GeV, 37°	839.9	846.9	0.8
7400	1.645 GeV, 37°	8250.9	8155.6	−1.2
6379	2.445 GeV, 37°	1015.0	1053.0	3.7
6747	4.045 GeV, 37°	237.0	243.3	2.7
6567	3.245 GeV, 53°	333.3	344.8	3.5
6397	2.445 GeV, 90°	118.2	127.1	7.5
6421	2.445 GeV, 90°	384.4	383.9	−0.1
6500	4.045 GeV, 90°	70.7	76.6	8.3

Table 4.3: Endpoint yields, corrected for tracking efficiency, as measured with the 4/6 ($N^c_{4/6}$) and 5/6 ($N^c_{5/6}$) tracking algorithm for a variety of runs and kinematics. The last column shows the relative difference between the yields, expressed in a percentage.

4.2 Event Reconstruction

The four focal plane quantities x_{fp}, y_{fp}, x'_{fp}, y'_{fp} in combination with knowledge about the spectrometer optics define a particle trajectory through the spectrometer, which can be traced back to the reaction vertex in the target. The target quantities at the reaction vertex are reconstructed from the focal plane quantities through transformations of the form

$$y_{tar} = \sum_{i,j,k,l} R^y_{ijkl} \cdot x^i_{fp} y^j_{fp} (x'_{fp})^k (y'_{fp})^l \quad (1 \leq i+j+k+l \leq N), \tag{4.2}$$

where R^y_{ijkl} is the column of the reconstruction matrix corresponding to y_{tar}, and N the order of the expansion. The quantity $y_{tar} = z_{target}\sin(\theta_{HMS})$, where z_{target} is the z-coordinate of the vertex on the beam axis, and θ_{HMS} the central angle of the HMS. Identical transformations are used for the other target quantities, each time using the corresponding column of the reconstruction matrix R. Since four focal plane quantities are available, only four target quantities can be reconstructed. In addition to y_{tar}, the tangents to the ray at the vertex in the target, x'_{tar}, y'_{tar}, are reconstructed, and the the quantity δ which expresses the particle momentum relative to the central momentum setting of the spectrometer, p_{HMS}:

$$\delta = \frac{p - p_{HMS}}{p_{HMS}}. \tag{4.3}$$

Note that since only four variables can be reconstructed, knowledge of the momentum through δ is chosen over knowledge of x_{tar}, and it is assumed that all events have a vertex with $x_{tar} = 0$. This is a reasonable assumption since the beam is located close to $x_{tar} = 0$, and it has a small transverse size.

Two methods exist to determine the matrix R. In the first method the matrix is generated using the computer program COSY Infinity [102] which models the magnetic part of the spectrometer, using magnet positions, internal dimensions and magnet field maps. With this method a set of matrix elements was calculated up to order N=5. In the second method, matrix elements are fitted from calibration data taken with well-defined spectrometer-target configurations. Data are taken with a point target placed at known positions in the beam, while the HMS collimator has been replaced by the sieve slit (see Figure 3.9). The fitting procedure uses a set of COSY generated matrix elements for the initial description of the the optical transport through the spectrometer. Starting with the COSY matrix elements, y_{tar} and the angles at the target are reconstructed. Using these reconstructed target quantities the data are projected to the sieve slit. At the sieve location, the slit hole closest to the particle position is determined, which imposes constraints on the target angles because the sieve slit hole positions are well known. The matrix elements are then varied in an iterative process to produce target angles that cause the tracks to pass through the center of the holes in the sieve, until a convergent set of matrix elements is obtained. The matrix elements for δ are obtained from calibrations with elastic data at different field settings, and y_{tar} is reconstructed using sieve slit data from targets at different positions along the beam. A complete description of the fitting procedure is given in [103].

For this experiment data were analyzed with COSY 5th order matrix elements. Data were also analyzed with 5th order fitted matrix elements, but final results were not obtained because of complications that occurred extracting physics quantities from the reconstructed target quantities. The complications that were encountered are discussed in further detail in Section 5.10.

4.3 HMS Calibration and Modeling

The HMS spectrometer serves as the instrument to measure physical variables, like the momentum and scattering angle which are used in cross section calculations. A good understanding of how these quantities are measured and knowledge of the propagation of their associated uncertainties to the uncertainty in the final cross section result is essential. In addition, a model to study the behavior of the HMS and its magnet optics provides valuable means to make a comparison with data taken. In this section the HMS momentum and angle calibration and their associated uncertainties are presented, and an introduction to the Monte Carlo model of the spectrometer is given.

4.3.1 HMS Calibration

The result of the tracking algorithm is a particle trajectory that passes through both drift chambers, and intersects with the detection plane of the spectrometer. The "detection" focal plane (hereafter referred to as focal plane), is a plane perpendicular to the central ray, located roughly halfway between the two drift chambers. In the analysis, coordinates and slopes of the track at the intersection with this plane are used to calculate physical quantities. The detection focal plane is different from the true focal plane, which is the surface where initial rays, coming from the target with different angles and momenta, converge. The true focal plane has slight curvature, and is tilted at an angle $\sim 85°$ from the detection focal plane, intersecting it in a point, located on the central ray. The coordinate system in the focal plane is defined following the TRANSPORT [92] convention. In this convention $\hat{x}$ points downwards in the dispersive direction of the spectrometer, $\hat{y}$ points towards smaller scattering angles and $\hat{z} = \hat{x} \times \hat{y}$ is parallel to the central ray (z=0 in the focal plane). Using a calibration procedure with a thin BeO solid target, the focus is adjusted in the dispersive (x) direction, so that rays belonging to the central momentum ($\delta = (p - p_{HMS})/p_{HMS} = 0$), are projected to the point (0,0) in the focal plane. This is accomplished using an iterative procedure where each time first the Q1 field (displaces rays in the x direction) and then the Q2 field (displaces rays in the y direction) is adjusted, until the best focus is obtained.

Figure 4.3 shows an event distribution in the focal plane for calibration data. The data for this calibration run was taken with a thin BeO solid target, and the sieve slit in front of the first quadrupole of the HMS. The ray-like particle distributions are caused by the sieve slit. The sieve slit, a dedicated collimator designed for HMS optics calibrations, is part of the HMS collimation system depicted in Figure 3.9. Particles entering the spectrometer can only pass through the array of holes in the sieve slit, thus causing the observed focal plane distribution. The two missing holes provide information for the correct orientation during the analysis of optics data. A focus, centered at the correct position, (x_{fp},y_{fp})=(0,0) is observed.

The HMS absolute momentum was calibrated in two ways. In a measurement using elastic H(e,e$'$)p scattering the momentum calibration was determined to $\sim$0.2%. Contributions to the uncertainty come from the uncertainties in spectrometer angle and beam energy, the latter causing the main contribution. A fractional momentum spread, $\delta p/p$=0.03% was obtained by taking an angular scan of H(e,e$'$)p at the same beam energy, thereby reducing the contribution of the uncertainty in the beam energy to the uncertainty in p [95]. Based on the results from these two techniques a 0.1% uncertainty in the HMS momentum was used in the data analysis.

To measure the central angle of the HMS, an array of surveyed marks were scribed into the Hall C floor, placed on a section of a circle with the pivot as center. The central angle of the HMS is determined by lining a needle at the back of the spectrometer carriage up with the desired scribe. The uncertainty in the angle due to positioning of the carriage in this is manner is better than 0.1 mrad. A larger contribution in

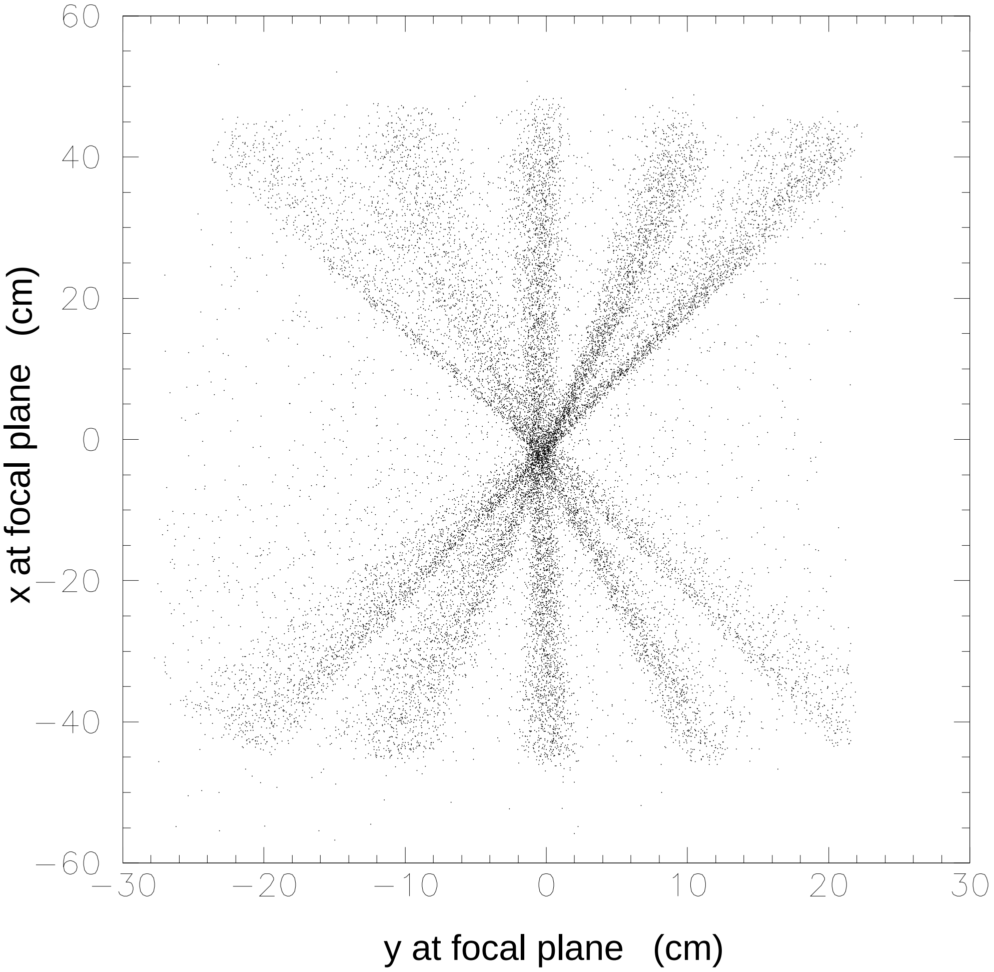

Figure 4.3: HMS focal plane distribution for a calibration run with BeO target and sieve slit. Shown is the distribution of x_{fp} versus y_{fp} in the detection focal plane. The ray-like particle distributions are caused by the sieve slit, since particles can only pass through certain holes. The focus is located at (x_{fp},y_{fp})=(0,0).

the angular uncertainty is caused by the motion of magnets on the carriage as it is rotated. At forward angles ($\theta_{HMS} < 70°$) magnet motion contributes to the uncertainty of the angle at the 1.0 mrad level. The angular uncertainty can be checked by performing inclusive elastic H(e,e′) scattering. Using this method, and assuming that spectrometer momentum is well-known, the r.m.s. uncertainty in the HMS angle was determined to 0.5 mrad. The out-of-plane angle reconstruction is determined to 0.8 mrad. Arrington [95] provides a detailed description of the momentum and angle calibration procedures.

4.3.2 HMS Monte Carlo Model

The HMS accepts particles within a limited spread around the central values for momentum and scattering angle of a given kinematic setting. To simulate the transport of charged particles through the spectrometer, a Monte Carlo model has been developed [95]. The model is available in a software package that records the results in PAW histograms and n-tuples [98]. The model consists of three main components. The event generator creates events with initial conditions randomly distributed over uniform distributions in the target coordinates, x, y, x', y' and particle momentum $\delta = \frac{p-p_0}{p_0}$, where p_0 is the central momentum. Limits on the distributions of the target coordinates are defined by the user and serve as an input to the simulation. Generally the limits are based on the experimental target configuration and values of cuts used in the data analysis.

The coordinates at the target, which are in a frame with $\hat{z}$ along the direction of the beam and $\hat{y}$ pointing vertically upward are transformed to spectrometer TRANSPORT coordinates (see Section 3.5.1). The resulting TRANSPORT target coordinates $x_{tar}, y_{tar}, x'_{tar}, y'_{tar}$, and δ can be projected forward through the spectrometer past apertures of the various components in the system. In the HMS model apertures are defined at the collimator, the entrance and exit of each of the magnets and a position 2/3 of the way through Q1 and Q2 to determine if events hit the inside of the magnets. At these locations particles can undergo multiple scattering, or get totally stopped. To be registered as a valid event, particles that have passed all magnetic components need to pass a fiducial area of the drift chambers and hit at least three out of four of the scintillator planes, to satisfy the minimum trigger requirement. Events which do not meet the above criteria are rejected, and a summary of the rejected events and the positions where they were rejected is included in the output as well.

The transport of the particles through the magnetic section of the spectrometer is modeled using the computer program COSY Infinity [102]. Using magnet positions, internal dimensions and their field maps, COSY generates a forward matrix that converts target coordinates to coordinates in the focal plane. The focal plane coordinates and angles are obtained from the target quantities using the COSY Matrix in expansions like:

$$x_{fp} = \sum_{i,j,k,l,m} F^{x}_{ijklm} \cdot x^{i}_{tar} y^{j}_{tar} (x'_{tar})^{k} (y'_{tar})^{l} \delta^{m} \quad (1 \leq i+j+k+l+m \leq N) \qquad (4.4)$$

where N is the order of the expansion and F^{x}_{ijkl} the column of the forward transport matrix corresponding to x_{fp}. Similar expansions exist for y_{fp}, x'_{fp} and y'_{fp}. For E89-012 the matrix F_{ijklm} was calculated to 5th order. The above description is known as the *forward* transport of the particles through the spectrometer, because focal plane quantities are calculated using initial coordinates at the target, in the same way as a particle would travel through the spectrometer. To calculate initial conditions from known focal plane quantities The Monte Carlo uses the same transformation as used in the event reconstruction (see Equation 4.2 and the discussion in Section 4.2).

The Monte Carlo package includes a standard model that was developed for all experiments in Hall C, and does not include any experiment specific information like the physics processes that created the event. For E89-012 the model was customized by calculating an initial momentum distribution which was weighted with a bremsstrahlung spectrum that was folded with the s^{-11} cross section dependence as predicted by the dimensional scaling model (see Section 2.2). Further experiment specific changes that were made include the HMS gate valve as an additional 'aperture' (see Section 5.6) and the estimation of multiple scattering and energy loss from events striking the collimator and/or gate valve.

4.4 Particle Identification

Since only photoprotons are of interest for the deuteron photodisintegration cross section, the protons need to be distinguished from other particles that pass through the detector stack. The HMS detector package provides three means of particle identification, of which time-of-flight is suitable to select the protons of interest. In a time-of-flight measurement the particle velocity is determined from the path length traversed between two spatially separated detectors at distance d, and the time elapsed between hits in these detectors, Δt:

$$\beta_{TOF} \;=\; \frac{d}{\Delta t} \quad . \tag{4.5}$$

In the HMS detector package the time-of-flight is measured with the 4 hodoscope planes, of which the first and fourth are approximately 220 cm apart. The exact path length is calculated from the reconstructed track of the particle in the detector package. The time difference is calculated from the scintillator hit times, which are recorded with a time-to-digital converter (TDC). Difference in cable lengths, signal pulse height variation, timing offsets between individual tubes, and the propagation time of scintillation light in the paddle, cause variations in timing, which need to be corrected for. The correction procedure is discussed in Section 4.4.1

A combination of β_{TOF} and the particle momentum p provides the most accurate particle identification. Hence the protons are selected using a cut on the reconstructed mass

$$m^2 \;=\; p^2(\frac{1}{\beta_{TOF}^2} - 1) \;, \tag{4.6}$$

with $p = p_c(1 + \delta/100)$, where p_c is the central momentum setting of the HMS. Figure 4.4 shows mass-squared distributions for 3 selected kinematic settings. The distributions in Figures 4.4.(a)–(c), represent the normalized total number of events, after acceptance and focal plane cuts. The figures show that protons and deuterons are well distinguishable by their respective mass squared distributions around $m_p^2 = 0.88$ GeV^2 and $m_d^2 = 3.524$ GeV^2.

For each kinematic setting the proton mass-squared distribution was fitted with a Gaussian. The final cross section is calculated using the photoprotons that fall within $\pm 2.5\ \sigma$ of the mean of the fitted distribution. Assuming a Gaussian shape, this choice of the cut includes all but 1.2% of the photoprotons. The mass-squared

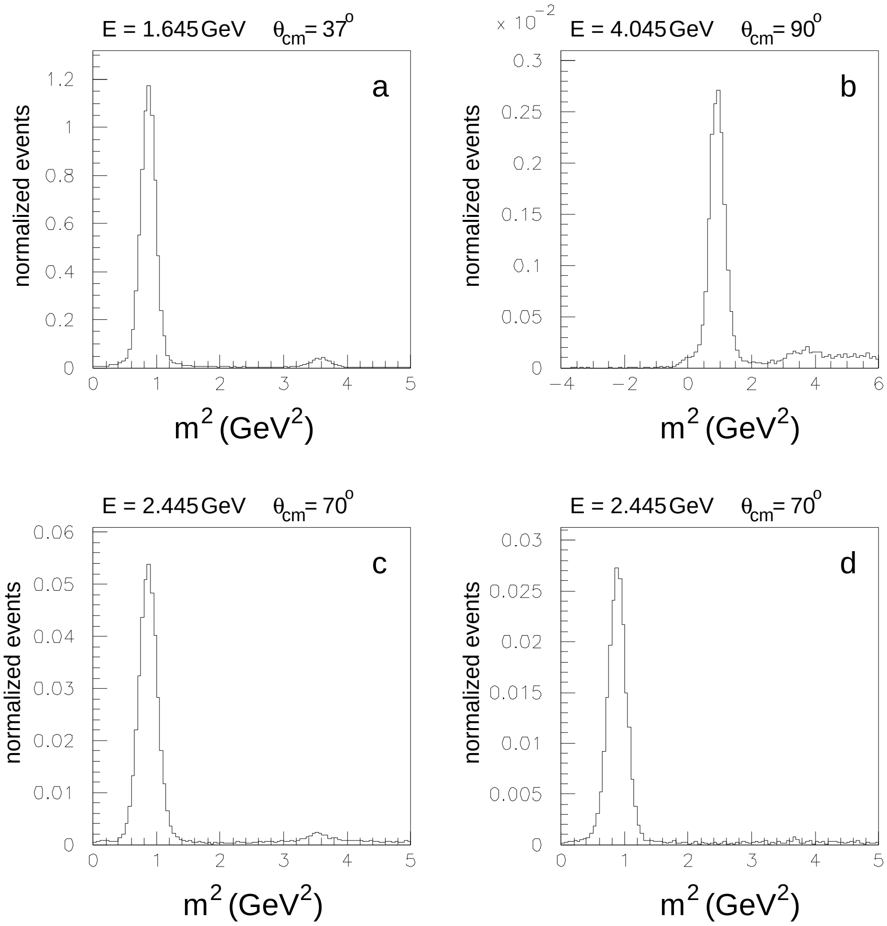

Figure 4.4: Reconstructed clean mass squared spectra for 3 kinematics (a)–(c): Summed normalized events; (d): Normalized events after physics background.

cuts corresponding to $\pm 2.5\ \sigma$ limits on the fitted distributions are summarized in Table 4.4 for all kinematics.

Figure 4.4.(d) shows the mass-squared distribution after the physics background subtraction (discussed in Section 5.3) is applied. The subtraction removes the majority of the deuterons from the mass-squared spectrum but a small signal remains.

At high energies and small angles, where the mass-squared distribution broadens and tails of the proton and deuteron distributions start to overlap, deuterons remaining after the subtraction could overflow into the proton mass-squared cut, thereby being misidentified as photoprotons. In addition, a small effect from the accidental

E_{beam} (GeV)	θ (nominal)	m^2_{low} (GeV^2)	m^2_{high} (GeV^2)	
0.845	37°	0.65	1.20	
	90°	0.70	1.30	
1.645	37°	0.30	1.30	
	53°	0.50	1.30	
	70°	0.50	1.30	
	90°	0.50	1.30	
2.445	37°	0.03	1.52	
	53°	0.17	1.50	
	70°	0.32	1.30	
	90°	0.45	1.30	
3.245	37°	−0.60	1.91	
	53°	−0.22	1.78	
	70°	0.09	1.55	
	90°	0.31	1.36	
4.045	37°	−1.56	2.44	
	53°	−0.59	2.00	
	53°	−0.46	2.03	1997 dataset
	70°	−0.20	2.10	
	70°	−0.40	1.80	1997 dataset
	90°	−0.04	1.70	

Table 4.4: Mass-squared cut limits for all kinematics. The table shows the low (m^2_{low}) and high (m^2_{high}) limits corresponding to a $\pm$ 2.5 σ cut-off of the assumed Gaussian photoproton mass-squared distribution.

background is also expected. For the data taken at beam energies of 3.245 GeV and 4.045 GeV, where overlap of the proton and deuteron mass-squared distributions becomes most apparent, the systematic uncertainty due to background and undesired deuterons was estimated. Laboratory cross sections (see Section 5.4) were calculated for mass-squared cuts at $\pm 1.0\ \sigma$, $\pm 1.5\ \sigma$, $\pm 2.0\ \sigma$ from the mean of the fitted distribution, in addition to the standard $\pm 2.5\ \sigma$ calculation. For the purpose of this analysis raw cross sections were used, that did not include any corrections for e.g. proton absorption, but the tracking efficiency correction had been applied. Expected cross sections were calculated from the raw cross sections by dividing them by a factor equal to the enclosed area under a normalized Gaussian with $\pm 1.0\ \sigma$, $\pm 1.5\ \sigma$, $\pm 2.0\ \sigma$, and $\pm 2.5\ \sigma$ cut-off, respectively,

$$\left(\frac{d\sigma}{d\Omega}\right)_{lab}^{expect} = \frac{1}{C_{Gauss}} \cdot \left(\frac{d\sigma}{d\Omega}\right)_{lab}^{raw} . \tag{4.7}$$

This enables a proper comparison.

The expected cross sections for the 4 cut-offs are in excellent agreement with each other for each of the four angles at 3.245 GeV and 4.045 GeV. Table 4.5 shows the comparison for $\theta_{cm} = 37°$ and $E_{beam} = 3.245$ GeV. For each kinematic setting the

σ_{cut}	m^2 (GeV^2)	$(\frac{d\sigma}{d\Omega})_{lab}^{raw}$ (nb/sr)	$(\frac{d\sigma}{d\Omega})_{lab}^{expect}$ (nb/sr)	C_{Gauss}
± 1.0	$0.153 < m^2 < 1.157$	0.6575 ± 0.0654	0.9631 ± 0.0960	0.6827
± 1.5	$-0.098 < m^2 < 1.408$	0.8054 ± 0.0713	0.9296 ± 0.0823	0.8664
± 2.0	$-0.349 < m^2 < 1.659$	0.8880 ± 0.0750	0.9303 ± 0.0786	0.9545
± 2.5	$-0.600 < m^2 < 1.910$	0.9160 ± 0.0766	0.9275 ± 0.0776	0.9876

Table 4.5: Comparison of laboratory cross sections for $\gamma d \to pn$ at $\theta_{cm} = 37°$ and $E_{beam} = 3.245$ GeV for four different cuts on the Gaussian mass-squared distribution. In order to make the proper comparison each raw cross section, $(\frac{d\sigma}{d\Omega})_{lab}^{raw}$, is converted to the expected cross section $(\frac{d\sigma}{d\Omega})_{lab}^{expect}$ using a factor equal to the enclosed area under a normalized Gaussian, C_{Gauss}.

cross section calculated at $\pm 2.5\ \sigma$ (for this purpose corrected for the 1.2% left-out photo-protons) was then compared with the mean of the 4 expected cross sections at $\sigma = \pm 1.0, \pm 1.5, \pm 2.0, \pm 2.5$, giving a systematic uncertainty for each kinematic setting. In the case of the 37° and 3.245 GeV shown in the table the mean expected cross section was 0.9376 ± 0.017 nb/sr, and the systematic uncertainty 1.1%. The overall systematic uncertainty in the background due to the chosen σ cut-off of the mass-squared cut is obtained by averaging over the systematic uncertainties for each of the kinematic settings at a given energy. For kinematics with two data runs, like 53° and 70° at 4.045 GeV, the weighted average of these results was taken before the mean of all angles was calculated. Using this method, the systematic uncertainty in the background due to particle ID is 1.3% at E_{beam}=3.245 GeV, and 2.6% at E_{beam}=4.045 GeV. At lower beam energies the mass-squared distributions are well separated, and the systematic uncertainty was estimated to be less than 1%.

4.4.1 Hodoscope Timing Corrections

Timing information for the time-of-flight calculation in Equation 4.5 is provided by TDCs which measure the times at which photomultiplier tubes (PMT) in the hodoscope planes fire, due a charged particle passing through. Between the scintillator hit and the TDC time measurement a number of delays occur which cause variations in the recorded time. Light propagation time in the scintillator paddles, different cable lengths, individual offsets between the PMTs, as well as signal pulse height variations have to be corrected for. A detailed description of the TDC calibrations, which were carried out as part of the Hall C electronics commissioning, can be found in [95]. Other timing calibrations are experiment specific and a procedure including dedicated software has been developed [104]. This procedure was used in E89-012.

The first step in the procedure is to calculate the pulse height corrections. The timing signal from the PMT comes from a fixed threshold discriminator, hence the height of the signal will determine how soon after the start of the signal the threshold is exceeded. For each PMT the time measured with the TDC is adjusted based on the ADC value of the PMT. An empirical correction of the form

$$\Delta t \;=\; PHC\,\sqrt{max(0,(ADC/PHOFF-1))}\;+t_0 \tag{4.8}$$

is used, where ADC is the raw ADC value of the fitted tube, PHC and $PHOFF$ are timing parameters, and t_0 an arbitrary offset between two scintillators. In essence the correction is fit by comparing the mean times of the two PMTs on each end of a scintillator with the mean time of those on a crossed reference scintillator, limiting the region to avoid velocity corrections (see below). Taking the mean eliminates the dependence on position along the scintillator. Then 3 of the 4 PMTs are corrected for pulse height walk and the timing correction is fitted using the ADC value of the remaining tube. The final correction is taken as the weighted average of fit values from fits with different reference elements. This procedure is repeated for all scintillators. Since particles with different velocities and masses create signals with different pulse heights in the tubes, a particle ID cut was applied to calculate the proper pulse height correction with a clean sample of protons from high statistics runs.

After determination of the pulse height correction, the velocity correction is measured. When a particle creates light in the scintillator, the light bounces of the sides of the scintillator, rather than traveling directly to the PMT. Thus the time at which the PMT registers the light is different from the time calculated by dividing the distance to the hit by the speed of light in the plastic scintillator. When the difference in PMT times on two opposite ends of a paddle is plotted versus the hit-position along the element, the true velocity of propagation is given by the slope. In this way a velocity correction was measured for each scintillator plane, and the average correction was used for each paddle.

The last correction accounts for timing offsets in the individual tubes, which is caused by variations in cable length or different response times of the PMTs. These timing offsets are fit by comparison of element times of crossed pairs of scintillators in a way similar to the pulse height correction method. After accounting for pulse height and velocity corrections, the mean time for a pair of scintillators is calculated. Then the offsets are adjusted so that the time between scintillator hits agrees with the well known velocity of the particle, which is calculated from the momentum, β_p. As with the pulse height correction the fits were carried out with proton samples obtained by placing particle identification cuts on large statistics runs.

Figure 4.5.(a) shows the distribution of measured proton velocities ($\beta = v/c$) for E=3.245 GeV, θ_{cm}=70° after application of the above timing correction procedure. For each hodoscope element on a track a corresponding time at the focal plane is calculated. Next, the standard deviation is calculated from the 3 (or 4, dependent on the trigger) scintillator focal plane time measurements. A distribution of the standard deviations of focal plane time measurements from the different planes is

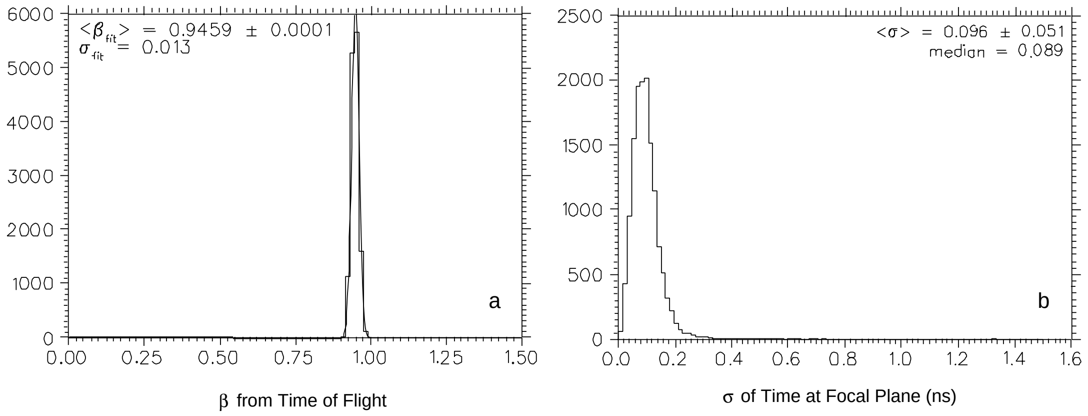

Figure 4.5: HMS time-of-flight and timing resolution for E_{beam}=3.245 GeV, θ_{cm}=70°. (a): Distribution of measured proton velocities, $\beta = v/c$. (b): Distribution of the standard deviation of the focal plane time measurements from the different hodoscope planes.

shown in Figure 4.5.(b) . The timing resolution is the mean of this distribution, and is in good agreement with the ~70-100 ps resolution obtained in bench tests [95].

4.5 Photoproton Absorption

While traversing the flight path between target and detector stack, protons encounter various materials of the target, scattering chamber, spectrometer and detector components. A proton can undergo both elastic and inelastic collisions with the nuclei in these materials, thereby removing it from the acceptance before a trigger is produced, and reducing the 'true' photoproton yield

Proton absorption can be estimated from the nuclear interaction length (mean free path between nuclear interactions) of the materials. The elastic cross section is very peaked in the forward direction, so that only a small fraction of the photoprotons undergoing elastic scattering will be removed from the acceptance. On the other hand, protons that undergo inelastic reactions are assumed to be lost and cannot be detected. The mean free path between nuclear collisions, λ_C, and the mean free path between inelastic nuclear interactions, λ_I are calculated from $\lambda_i = \frac{A}{N_A \sigma_i}$, where N_A is

Avogadro's number, and σ_i the cross section corresponding to the interaction. Values for λ_C and λ_I are listed in Reference [20]. To estimate the photoproton absorption, the mean free path between nuclear interactions, $\bar{\lambda}$ is taken as the average of λ_C and λ_I, corresponding to the two extreme cases. With the definition of $\bar{\lambda}$, the absorption for a photoproton traversing the target-HMS system becomes

$$A = 1 \; - \; e^{-\sum_i X_i/\bar{\lambda}_i}, \tag{4.9}$$

where X_i is the thickness of absorber i, and the summation is carried out over all the materials in the path of the proton. Table 4.6 gives a full listing of all materials that the photoproton encounters in the target-HMS system, with for each material the density, thickness, mean free path $\bar{\lambda}$, and its contribution to the overall absorption. A summary of the major contributions to the absorption is given in Table 4.7.

The amount of the liquid deuterium traversed by the proton depends on the scattering angle of the proton, and varies from 3.6 cm at θ_{lab}=65.6° to 11.8 cm at θ_{lab}=15.9°. Thus the absorption is angle dependent, and the contribution due to LD_2 varies from 1.2% to 3.9%. Since photoprotons can exit the target through the front window, as well as through the sides (especially at very forward angle kinematics) an average target length of 6 cm was chosen to calculate the absorption for the final analysis. Assuming that a proton traversing one quarter of the third scintillator plane is adequate to produce a trigger, the absorption for a 3/4 trigger is equal to 9.5%. For a 4/4 trigger extra scintillator material is added, and the absorption amounts to 10.9%.

A measurement of proton absorption in the cryotarget-HMS system was carried out using the H(e,e′,p) reaction [105]. For the target-spectrometer configuration in that experiment an absorption of 6.5% was calculated. The measurement yielded an absorption 5.5 ± 2.0 %, which is in agreement with the theoretical prediction, but has a large statistical error.

The photodisintegration cross sections have been corrected with a transmission (transmission = 1 − absorption) of 89.1%, taking deuterium path length variations

Absorber	Density (g/cm^3)	Thickness (cm)	$\bar{\lambda}$ (g/cm^2)	X (g/cm^2)	$X/\bar{\lambda}$ (10^{-3})
LD_2 target (after scattering)	0.167	~ 6	50.2	1.0	19.9
0.005 in. Al target window	2.70	0.0127	88	0.0343	0.39
0.016 in. Al chamber window	2.70	0.0406	88	0.1096	1.24
Air	0.00121	~ 15	75	0.0182	0.24
Kevlar	0.74	0.0381	~ 70	0.0282	0.40
Mylar	1.39	0.0127	72	0.0177	0.25
Kevlar	0.74	0.0381	~ 70	0.0282	0.40
Mylar	1.39	0.0127	72	0.0177	0.25
Air (exit pipe through S2)	0.00121	~ 256	75	0.310	4.13
0.004 in. Mylar (entrance/exit)	1.39	0.0102	72	0.0142	0.20
Sense Wires (effective) 25μm W, 12 planes	19.3	0.000076	147.7	0.00146	0.010
Field Wires (effective) 150μm Al/Au (99/1) 18 planes	2.70	0.0068	89.1	0.0184	0.21
Ar/Ethane (50/50 weight)	0.00154	16.6	~ 70	0.0256	0.36
Field Wires (effective) 150μm Cu/Be (50/50) 18 planes	5.40	0.0068	87.9	0.0368	0.42
Polystyrene (1.067 overlap)	1.03	2(1.067)(1.0)	70	2.198	31.40
Čerenkov windows 0.040 in. Al (entrance/exit)	2.70	2(0.102)	88.5	2(0.275)	6.22
Čerenkov gas C_4F_{10}	0.0106	150	78.8	1.59	20.18
Rohacell Mirror support	~ 0.05	~ 1.8	~ 70	0.09	1.3
Mirror SiO_2	2.20	0.3	83.1	0.66	7.94
Polystyrene (1.067 overlap)	1.03	$\frac{1}{4}$(1.067)(1.0)	70	0.275	3.93
Total					99.4

Table 4.6: Materials in the HMS and their absorption properties. The amount of LD_2 depends on the scattering angle.

Absorber	Density (g/cm^3)	Thickness (cm)	λ (g/cm^2)	X (g/cm^2)	X/λ (10^{-3})
LD_2 target	0.167	~ 6	50.2	1.0	19.9
Air (det. hut)	0.00121	~ 256	75	0.310	4.13
Polystyrene (S1)	1.03	2.134	70	2.198	31.40
Al Čerenkov windows	2.70	0.204	88.5	0.55	6.22
Čerenkov gas C_4F_{10}	0.0106	150	78.8	1.59	20.18
Čerenkov Mirror SiO_2	2.20	0.3	83.1	0.66	7.94
Polystyrene (S2)	1.03	0.267	70	0.275	3.93

Table 4.7: Summary of the materials that make major contributions to the photo-proton absorption. A comprehensive listing is provided in Table 4.6.

into account, as well as the fact that within certain kinematics, some runs were taken with a 3/4 and others with a 4/4 trigger. Since the aforementioned experiment provided a realistic statistical uncertainty on the absorption measurement, the systematic uncertainty in the absorption estimation for E89-012 was taken to 2.0%.

4.6 Dead Time Correction

During data taking both the data acquisition electronics and computers are unavailable to accept new events for small time intervals, during which they are processing the acquired events. In the determination of the cross section, a correction has to be applied to account for the events that were "lost", because they arrived during these so-called "dead time" intervals. Two sources of dead time can be identified, the electronic dead time which causes events to be missed because the logic modules in the trigger are processing previous events, and the computer dead time, which includes delays due to transfer of data from the trigger electronics to the data acquisition computer and event processing.

The trigger system is a non-paralyzable system (except for the hodoscope discriminators [95]), therefore being unable to accept new triggers for duration of the 30 ns gate width, causing the electronic dead time. If the average event rate is R, the probability of finding n events occurring in a time interval t is given by the Poisson distribution [94]

$$P(n) = \frac{(Rt)^n e^{-Rt}}{n!}, \tag{4.10}$$

Only events which arrive at the trigger at time intervals greater than the gate width are accepted. The distribution of time intervals between events arriving at average rate R is given by [106]

$$P(t) = Re^{-Rt}. \tag{4.11}$$

The fraction of time intervals which are larger than the gate width is obtained by integrating the distribution (4.11) from the gate width τ to ∞

$$P(t > \tau) = R\int_{\tau}^{\infty} e^{-Rt}dt = e^{-R\tau}. \tag{4.12}$$

The measured event rate, R_{meas} is a fraction of the true event rate, R, defined by the distribution of available time intervals with $t > \tau$

$$R_{meas} = Re^{-Rt} \approx 1 - Rt. \tag{4.13}$$

The approximation can be made because the event rate is small enough compared to the gate width.

To measure the counts lost in the 30 ns gate width, four versions of the final trigger were generated, each with a different gate width (τ = 30,60,90, and 120 ns) and the rates were measured with each of the gate widths and read into a scaler. An approximation of the true event rate is then made by extrapolating the linear form (Equation 4.13) back to zero gate width, τ=0. The ratio of the measured rate to the true rate is the electronic live time (live time=1 $-$ dead time). At all kinematic settings live times $>$ 99.9% were measured for the 30 ns gate width, giving a dead time $<$ 0.1%. The electronic dead time is sufficiently small compared to other corrections that no correction to the data was applied.

The dominant contribution to the dead time comes from the data acquisition computers. They handle, among other things, network transfers and processing of the incoming data and are unavailable for a more sizeable fraction of the time than the trigger modules. The live time of the data acquisition computers is calculated directly from the the number of scalar pretriggers, (events presented to the trigger supervisor, *HMSPRE*) and triggers, (events passed by the trigger supervisor, *HMSTRIG*), see Section 3.6. The true yield Y_{true}, is obtained from the measured yield, Y_{meas}, according to the following relationship,

$$Y_{true} = \frac{HMSPRE}{HMSTRIG} \times PS1 \times Y_{meas} \;, \tag{4.14}$$

where $PS1$ is the HMS prescale factor. The prescale factor is an input variable which instructs the data acquisition algorithm to process 1 out of every $PS1$ HMS events in case of very high data rates. This reduces the actual dead time of the data-acquisition computers, so that more events can be accepted. Generally the computer dead time corrections are between 10 and 25%, except for the data taken at low energy with radiator in, where prescale factors higher than 1 were used. It is assumed that the uncertainty in the computer dead time is negligible, since the correction is obtained through the division of two accurate scalers.

Chapter 5

Measurement of the Photodisintegration Cross Section

To carry out a precise measurement of the $\gamma d \to pn$ cross section, the flux of the photons entering the target and the yield of photoprotons emerging from the target have to be well known. Corrections for background due to the presence of the radiator and aluminum target cell in the electron beam have to be made. This section presents the procedure used to extract the cross section after photoprotons have been identified. Methods to calculate the bremsstrahlung flux and spectrometer acceptance, the other main quantities needed for the cross section calculation, are described. Special attention is given to the estimation and subtraction of the sources of background. The section concludes with a discussion of the systematic errors that can be attributed to the various facets of the cross section measurement.

5.1 Extraction of Photoprotons from Spectrometer Observables

For exclusive deuteron photodisintegration with a proton and neutron in the final state ($\gamma d \to pn$), the initial photon energy in the laboratory frame is determined from the proton momentum p_p and scattering angle θ_p, using two-body kinematics (see Appendix A):

$$E_\gamma = \frac{E_p m_d - \frac{1}{2}(m_d^2 + m_p^2 - m_n^2)}{m_d - E_p + p_p cos(\theta_p)}. \tag{5.1}$$

where $E_p = \sqrt{p_p^2 + m_p^2}$. The quantities p_p and θ_p are measured by the spectrometer. It is important to note that θ_p, is the true scattering angle of the event, defined in terms target coordinates, x'_{tar}, y'_{tar} and the central angle of the spectrometer, θ_c. Using small angle approximations the relationship is:

$$\cos(\theta_p) = \frac{\cos(\theta_c) + y'_{tar}\sin(\theta_c)}{\sqrt{1 + x'^2_{tar} + y'^2_{tar}}}. \tag{5.2}$$

A histogram of E_γ has a characteristic shape in which the photoproton yield falls off very rapidly with increasing photon energy, showing a steep decline (the "endpoint") near the beam energy. This shape depends in essence on the sum of the cross sections of production processes of the photoprotons, convolved with the bremsstrahlung spectrum of the incident photons, and the spectrometer acceptance. The steep fall-off near the beam energy is due to the fact that the maximum possible energy of the photons produced in the radiator is approximately equal to the beam energy. When Equation 5.1 is applied, all protons are treated as if they originated from deuteron photodisintegration, even though in reality, they could be have created by another (background) process. In the yield determination, only photoprotons with the highest energies, very near to the endpoint in the E_γ spectrum are included, to ensure that the cross section is solely based on the reaction with a proton-neutron two-body final state.

Figure 5.1 shows photoproton distributions as function of E_γ for θ_{cm}=90°, and the five available beam energies, 0.845, 1.645, 2.445, 3.245, and 4.045 GeV. At each kinematic setting spectra are shown for the liquid deuterium measurement (labeled LD_2^{IN}, as well as for three background run types (LD_2^{OUT}, MT^{IN}, MT^{OUT}) which are discussed in more detail in the next section. The characteristic bremsstrahlung shape, with yield steeply rising at energies below the endpoint is clearly visible. The figures also show that the continuous CEBAF beam enables the measurement of beautiful high statistics endpoint spectra, even at the highest energies (and in a reasonable amount of time). Furthermore, the accidental background above the endpoint is low. The next section will focus on the measurement of the known sources of background and a detailed discussion of other backgrounds follows in Section 5.7

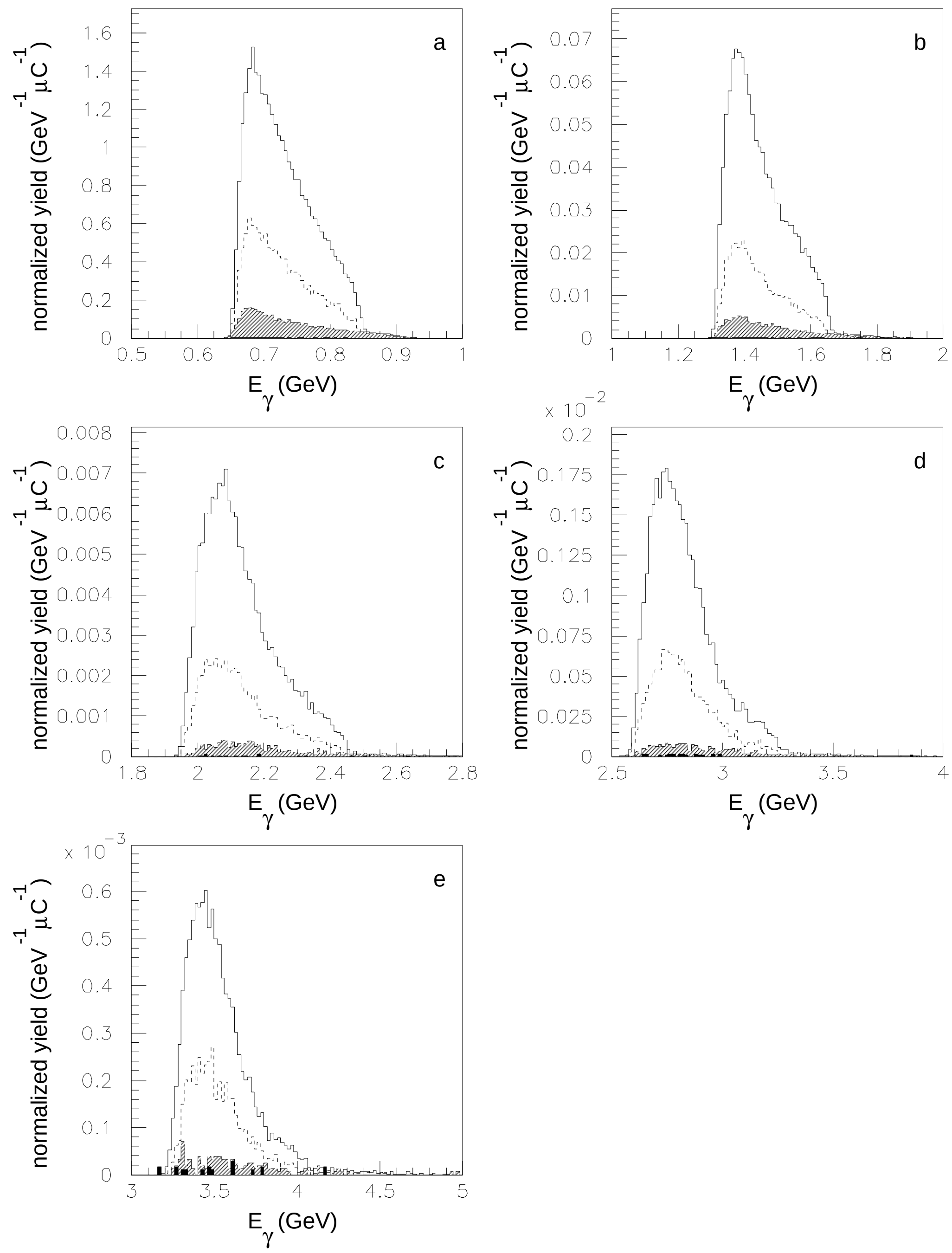

Figure 5.1: Normalized endpoint spectra for θ_{cm}=90°, E_{beam} = 0.845 GeV (a), 1.645 GeV (b), 2.445 GeV (c), 3.245 GeV (d), and 4.045 GeV (e). Each of the figures shows the yields for LD_2^{IN} (solid line), LD_2^{OUT} (dashed line), MT^{IN} (hatched) and MT^{OUT} (solid black filled). Plotted on the vertical axis is the yield, normalized to the integrated charge, per bin of E_{bin} GeV, where E_{bin}=0.005 GeV (a), 0.010 GeV (b,c), 0.015 GeV (d), and 0.020 GeV (e).

5.2 Measurement and Subtraction of the Known Background

During the experiment the deuterium is contained in an aluminum target cell. The electron beam which is used to create the photon beam in the bremsstrahlung radiator passes through the target cell together with the photon beam. Interactions of the photon and electron beam with the target materials create identifiable sources of background, which must be measured and corrected for.

The dominant proton background is caused by reactions like $^{27}\mathrm{Al}(\gamma,p)X$ in the up- and downstream aluminum end-caps of the cryotarget, as well as by reactions induced by virtual photons and real bremsstrahlung produced in the bulk of the target. The yield from these processes is measured separately and subtracted afterwards. In addition to this subtraction, a correction is made for accidental background protons that originate from places other than the target volume.

The known background processes are measured by making three measurements in addition to the measurement with liquid deuterium and radiator in the beam (hereafter denoted by LD_2^{IN} for "liquid deuterium, radiator in"). The largest source of background photoprotons is created by the electron beam itself interacting with the deuterium. Mixed with the photon beam created in the radiator, is the remainder of the original electron beam, which also passes through the target and consists of electrons that have energies on average >99% of their original energy. These electrons can create photoprotons through two processes. The first interaction involves electrodisintegration of the deuterium by virtual photons. In the second process, the upstream part of the deuterium volume serves as a bremsstrahlung radiator for the downstream part, and photodisintegration takes place with real photons created inside the target volume. The yield from this background is measured with radiator removed from the beam, and will be denoted by LD_2^{OUT}.

A measurement with an identical liquid hydrogen and radiator can be used to subtract the photoproton yield due to photoproton production in the up- and downstream aluminum end-caps in the cryotarget. A 15 cm target cell filled with liquid hydrogen has a radiation length equivalent to a 15 cm cell with liquid deuterium, however photoprotons from hydrogen are kinematically forbidden at the deuterium setting. During the February 1996 running of E89-012 technical problems with the cryotarget prevented simultaneous use of hydrogen and deuterium targets, and a helium-filled ("empty") target was used to measure the effects of the cell windows. A correction for the absence of liquid hydrogen as radiator has been applied, see Section 5.3. In 1997 a fully operable cryotarget was available and background measurements were done with liquid hydrogen. For simplicity the measurements with empty or hydrogen target and radiator in, will be denoted by MT^{IN}.

The third and last background measurement, a measurement with hydrogen (or empty) target and radiator removed from the beam, is carried out to subtract the photoproton yield originating from the target end-caps in the LD_2^{OUT} measurement. This measurement will be denoted by MT^{OUT}.

Photoproton energy distributions as function of E_γ for the three types of background measurements are shown in Figure 5.1 for θ_{cm}=90° at the five available beam energies. The figure confirms that the LD_2^{OUT} measurement accounts for the largest source of background, followed by MT^{IN}, whereas the MT^{OUT} measurement contributes virtually nothing, especially at the lowest energies.

5.3 Extraction of the Yield

Calculation of the the deuteron photodisintegration cross section requires the determination of the photoproton yield. The yield of interest is located under bremsstrahlung curve, close to the endpoint. For each liquid deuterium run with radiator in and its three corresponding background runs, the net yield corrected for efficiencies and normalized to the integrated charge, but before background subtraction, is given by

$$Y_{net} = (Y_{LD_2^{IN}} - c_r Y_{MT^{IN}}) - f(E_\gamma)(Y_{LD_2^{OUT}} - c_r Y_{MT^{OUT}}). \tag{5.3}$$

Here Y_k, $k = LD_2^{IN}, LD_2^{OUT}, MT^{IN}, MT^{OUT}$ are the normalized yields of the deuterium run and the three background runs, and $f(E_\gamma)$ an energy dependent correction factor to account for the radiative straggling of the electron beam in the radiator. The grouping of the yields in Equation 5.3 reflects the contributions of the different physics processes in the cross section measurement. The first term corresponds to the yield due to photons and electrons interacting in the deuterium, and the second term corresponds to the yield due to electrons only. The subtraction ensures that only the yield due to real photons is counted.

The factor c_r corrects the empty target yields for fact that there was no hydrogen present for empty target runs during the 1996 running. A 15 cm liquid hydrogen target has a 2% radiation length which results in an effective radiation length (taken at the center of the target) of 1%. Including the 6% radiation length of the copper radiator, the total effective radiation length with hydrogen target present would be 7%, with it absent 6%, thus defining c_r=7/6. In the analysis of the data taken in 1997, c_r=1.

The a given kinematic setting the normalized yields Y_k ($k = LD_2^{IN}$, LD_2^{OUT}, MT^{IN}, MT^{OUT}) are obtained by taking the weighted sum of the individual normalized yields of all the runs j ($j = 1...N_k$) of type k. For each run j the normalized yield is obtained by integrating the photoproton yield per bin under the bremsstrahlung curve within the energy interval. The yield per bin, $(y_i)_j$ for run j is given by

$$(y_i)_j = \left(\frac{dN_i}{dE_\gamma}\right)_j = \frac{N_{E_\gamma}}{Q_j\ T_j\ d_j\ \delta E_{\gamma,bin}}, \tag{5.4}$$

where N_{E_γ} is the number of photoprotons in bin i, Q_j the integrated charge for run j, T_j the tracking efficiency, d_j the dead time, and $\delta E_{\gamma,bin}$ the bin size. The integration interval is divided in N_{kin} 5 MeV energy bins (see Table 5.2). Using the normalized yields of the individual runs, the integrated normalized yield for run type k is

$$Y_k = \frac{\sum_{j=1}^{N_k}(\sum_i^{N_{kin}} y_i)_j\ w_j^2}{\sum_{j=1}^{N_k}\ w_j^2}, \tag{5.5}$$

with the weight $w_j = \frac{1}{Q_j\ T_j\ d_j}$, where Q_j, T_j and d_j are the same as in Equation 5.4. This choice of weights was prompted by very low counting statistics at the highest en-

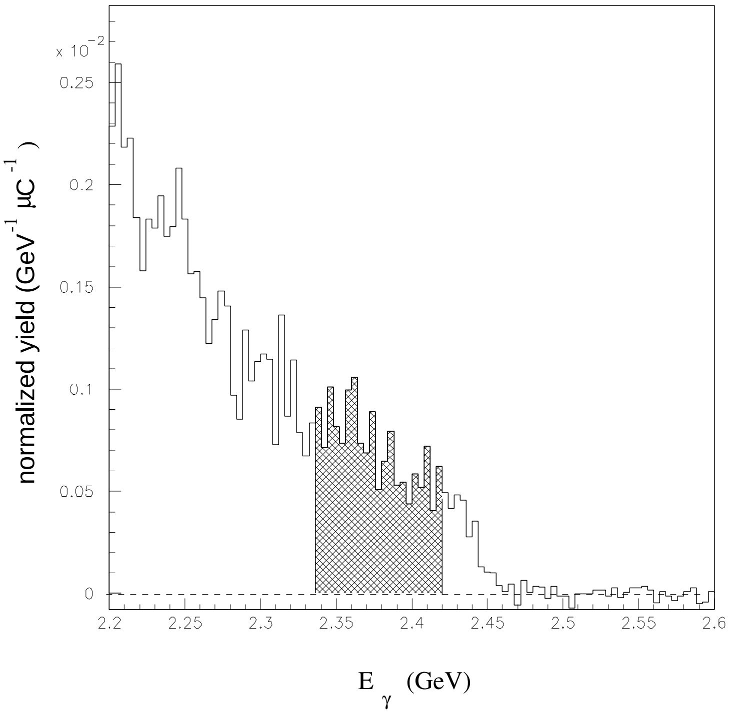

Figure 5.2: Normalized photoproton yield near the endpoint as function of E_γ for E_{beam}=2.445 GeV, θ_{cm}=70°. Shown is the spectrum after background subtraction (Equation 5.3). The yield plotted on the vertical axis is for 4 MeV bins, corrected for tracking efficiency, dead time and normalized to the integrated charge. The shaded region is the area from which the yield for the exclusive two-body reaction is extracted.

ergy kinematics which precluded the otherwise customary use of weights proportional to the errors in the count rate as determined from Poisson statistics [107].

Figure 5.2 shows the normalized photoproton yield that results after the above described background subtraction procedure is applied to data for E_{beam}=2.445 GeV, θ_{cm}=70°. The photoprotons of interest for this kinematic setting are in the shaded area. The determination of the energy limits that define the integration area will be discussed in Section 5.3.1.

When the electron beam passes through the radiator, radiative and ionization processes take place, which change the energy distribution of the beam. Since part of the photoproton background is generated by real and virtual photons which are produced in the target by the electron beam that passes through, a correction has to be made to account for the difference in energy distribution of the electron beam that did not pass through the radiator. The correction is energy dependent and defined as the ratio of the photon spectra produced in the *target*, with radiator in, and out:

$$f(E_\gamma) = \frac{dN^{IN}_{\gamma,target}}{dE_\gamma} \Big/ \frac{dN^{OUT}_{\gamma,target}}{dE_\gamma}. \tag{5.6}$$

The photon spectrum produced in the target consists of two parts, a contribution due to real photons and one due to virtual photons. With the radiator out, the total spectrum is calculated as the integral over the cross sections for real and virtual photon production:

$$\frac{dN^{OUT}_{\gamma,target}}{dE_\gamma} = N_0 \int dE' \delta(E_0 - E') \left[\frac{d\sigma_{brem}}{dE_\gamma}(E', E_\gamma) + \frac{d\sigma^{eff}_{virtual}}{dE_\gamma}(E', E_\gamma) \right] \tag{5.7}$$

$$= N_0 \left[\frac{d\sigma_{brem}}{dE_\gamma}(E_0, E_\gamma) + \frac{d\sigma^{eff}_{virtual}}{dE_\gamma}(E_0, E_\gamma) \right], \tag{5.8}$$

where the delta-function represents the electron beam energy distribution approximated as a spike centered around E_0, and N_0 is a normalization constant. The first term in square brackets, $\frac{d\sigma_{brem}}{dE_\gamma}(E', E_\gamma)$ represents the cross section for the production of a real photon with energy E_γ by an electron of energy E' in the target materials (upstream aluminum end-cap and deuterium volume). The effective virtual photon spectrum, represented $\frac{d\sigma^{eff}_{virtual}}{dE_\gamma}(E', E_\gamma)$, is given by Wright and Tiator [108], who obtain it by relating the electro-disintegration cross section to the virtual photon spectrum and photodisintegration cross section. The photon spectrum produced in the target by an electron beam that passed through the radiator is calculated in the same way as Equation 5.7, but the delta-function has to be replaced with the true energy distribution of the electrons after passing through the radiator, $I(E_0, E', Z, t_{rad})$:

$$\frac{dN^{IN}_{\gamma,target}}{dE_\gamma} = N_0 \int dE' I(E_0, E', Z, t_{rad}) \left[\frac{d\sigma_{brem}}{dE_\gamma}(E', E_\gamma) + \frac{d\sigma^{eff}_{virtual}}{dE_\gamma}(E', E_\gamma) \right]. \tag{5.9}$$

The electron energy distribution at depth t_{rad} (in radiation lengths) in a radiator with atomic number Z, $I(E_0, E', Z, t_{rad})$, is the solution of the electron "energy-loss" or "straggling" equation, which describes the probability that an electron penetrating the radiator undergoes an energy reduction from E_0 to $E' < E_0$ due to radiative energy loss. Using the correct bremsstrahlung shape, an analytical expression for $I(E_0, E', Z, t_{rad})$ cannot be obtained, but numerical and analytic approximations are discussed in [109]. For experiment E89-012, $f(E_\gamma)$ was calculated with algorithm that was developed by Belz [41]. The algorithm calculates the correction factor for a 200 MeV interval starting at the bremsstrahlung endpoint, in 1 MeV bins. The deuterium and aluminum entrance window are treated as *thin* radiators, i.e. radiative straggling and the finite energy spread of the electron beam are neglected, as they do not change $f(E_\gamma)$ by a significant amount.

Figure 5.3 shows the correction function for an electron beam energy of 3.245 GeV, a 15 cm deuterium target and 6.02% radiator. In the analysis, the $f(E_\gamma)$ correction was carried out bin-by-bin. The correction at the center of each 5 MeV analysis bin was obtained by averaging the $f(E_\gamma)$ spectrum over an interval (−5 MeV, 5 MeV) centered around the analysis bin.

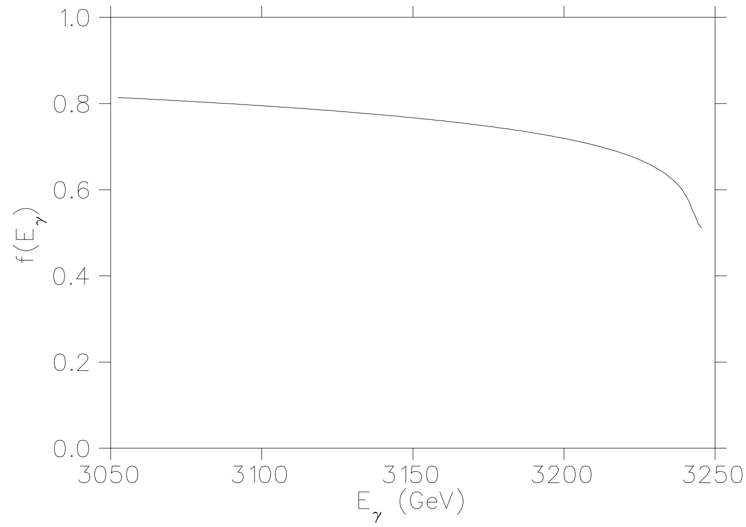

Figure 5.3: Energy dependent correction function $f(E_\gamma)$ for electrons with E_{beam} = 3.245 GeV impinging on a 6.02% copper radiator. The correction factor is applied to the photoproton spectra that are measured with the radiator removed from the beam to account for the radiative straggling of the electron beam in the radiator.

5.3.1 The E_γ Energy Interval

To ensure that only photoprotons originating from the two-body final state are included in the cross section calculation, the photoproton yield is integrated in a small region directly below the endpoint of the E_γ spectrum. Since there is an uncertainty in the exact location of the endpoint of the bremsstrahlung spectrum, the energy interval for which photoprotons are integrated starts 25 MeV below the beam energy.

For photon energies reconstructed using Equation 5.1 and about 100 MeV or more below the beam energy, reaction channels with one or multiple pions are possible. In the first available pion production channel one pion is created in addition to the final state proton and neutron, $\gamma d \to pn\pi^o$. Straightforward application of Equation 5.1 using the momentum of the slow proton produced at threshold pion production will result in an E_γ-value that is too low compared to the actual photon energy, which was near the beam energy. To ensure that only events originating from the $\gamma d \to pn$ two-body reaction are included in the photoproton yield, the energy interval for the yield integration is terminated at the energy corresponding to the highest possible proton momentum for a photoproton in a three-body final state, i.e. at pion production threshold. The energy threshold depends on the scattering angle, hence the width of the integration interval varies with scattering angle.

At threshold pion production the proton momentum is maximum when, in the center of mass frame, the pion and neutron have parallel momenta, and move in the opposite direction to the proton with equal velocities (see Appendix A). This maximum proton energy in the center of mass frame is given by:

$$E^{cm}_{p,max} = \frac{E^2_{cm} + m^2_p - (m_n + m_{\pi^0})^2}{2E_{cm}}, \tag{5.10}$$

After boosting the proton energy into the lab frame, the reconstructed photon energy at which pion production occurs is calculated using Equation 5.1 and the proton lab-momentum. Pion production first occurs at the most forward angle, so the proton scattering angle in Equation 5.1 is taken at the downstream edge of the collimator, $\theta_p = \theta_{HMS} - 1.6^\circ$.

E_{beam} (GeV)	θ_{cm} (nominal)	$E_\gamma(\gamma d \to pn) - E_\gamma(\gamma d \to pn\pi^0)$ (MeV)
0.845	37°	93.4
	90°	138.2
1.645	37°	87.6
	53°	96.2
	70°	110.7
	90°	138.8
2.445	37°	85.1
	53°	93.8
	70°	108.9
	90°	138.7
3.245	37°	83.7
	53°	92.5
	70°	107.8
	90°	138.7
4.045	37°	82.8
	53°	91.6
	70°	107.1
	90°	138.6

Table 5.1: Pion thresholds, expressed as the difference between the true photon energy $E_\gamma(\gamma d \to pn)$ and the apparent photon energy $E_\gamma(\gamma d \to pn\pi^0)$. $E_\gamma(\gamma d \to pn)$ is close to the electron beam energy.

Table 5.1 shows the calculated pion production thresholds for all kinematic settings, expressed as the difference between the true photon energy $E_\gamma(\gamma d \to pn)$ and the apparent photon energy $E_\gamma(\gamma d \to pn\pi^0)$. The lower limit of the energy integration interval is determined by the highest threshold-energy for a given angle, the upper limit is 25 MeV below the beam energy for all angles, defining the width of the interval to $E_{beam} - 0.025 - \Delta E < E_\gamma < E_{beam} - 0.025$ GeV. Table 5.2 list the widths, ΔE, and the number of 5 MeV energy bins N_{kin} per interval used for the analysis of the HMS angles $\theta = 37°, 53°, 70°$, and $90°$.

Previous experiments [10, 11] showed that the energy dependence at E_{beam}= 0.845 GeV, $\theta_{cm} = 90°$ is very strong. Because of this strong energy dependence, the size of

θ_{cm} (nominal)		ΔE (MeV)	N_{kin}
37°	all energies	55	11
53°	all energies	65	13
70°	all energies	80	16
90°	E=0.845 GeV only	100	2 × 10
90°	except E=0.845 GeV	110	22

Table 5.2: Energy interval widths for yield integration in the photoproton distribution for all kinematics. For E_{beam}=0.845 GeV, θ_{cm}=90° the interval is divided in two 50 MeV intervals to better represent the strong energy dependence. The entries for N_{kin} correspond to the number of 5 MeV bins used in Equation 5.5.

the integration interval was reduced to 100 MeV. To give a better representation of the energy dependence it was split up into two equal bins of 50 MeV.

5.4 Determination of the Cross Section

Once the photoproton yield in the E_γ spectrum has been integrated, the cross section can be calculated. In the laboratory system, where the deuteron is at rest, the photodisintegration cross section is given by

$$\frac{d\sigma}{d\Omega} = \frac{Y_{tot}}{n_{nucl} N_\gamma \Delta\Omega A}, \tag{5.11}$$

where Y_{tot} is the total yield, N_γ the photon flux produced in the radiator per incident electron, $\Delta\Omega$ the effective solid angle, n_{nucl} the number of deuterium nuclei per unit area, and A a factor in which global corrections to the yield are accumulated. The total yield is the net yield from Equation 5.3 after background subtraction. The determination of N_γ, n_{nucl}, and $\Delta\Omega$ will be discussed in subsequent sections.

Though not explicitly shown in Equation 5.11 the photodisintegration cross section $\frac{d\sigma}{d\Omega}(E_\gamma)$ has a strong dependence on the photon energy E_γ, through the energy dependence of $Y_{tot}(E_\gamma)$ and $N_\gamma(E_\gamma)$. The energy at which the cross section is properly normalized, E_γ^{true}, is defined by the following relationship:

$$\frac{d\sigma}{d\Omega}(E_\gamma^{true}) = \frac{\int \frac{dN_\gamma}{dE'_\gamma}\frac{d\sigma}{d\Omega}(E'_\gamma)dE'_\gamma}{\int \frac{dN_\gamma}{dE'_\gamma}dE'_\gamma}, \tag{5.12}$$

where $\frac{d\sigma}{d\Omega}(E_\gamma^{true})$ is the average cross section, measured in the experiment. The expression on the right hand side represents the actual energy dependent cross section. Without prior knowledge of $\frac{d\sigma}{d\Omega}(E_\gamma)$ Equation 5.12 cannot be exactly solved for E_γ^{true}, but it can be numerically evaluated when an approximate dependence $\frac{d\sigma}{d\Omega}(E_\gamma) \sim s^{-10}$ is substituted on the right hand side. It was shown by Belz [41] that the value of E_γ^{true} calculated in this way is $\approx$0.5 MeV smaller than the average energy of the photons created in the radiator,

$$\bar{E}_\gamma = \frac{\int E'_\gamma \frac{dN_\gamma}{dE'_\gamma}dE'_\gamma}{\int \frac{dN_\gamma}{dE'_\gamma}dE'_\gamma} \ . \tag{5.13}$$

Since the difference is negligible, the latter simpler equation was used to calculate the average photon energy for the settings in this experiment.

The center-of-mass (CM) cross section is obtained from the lab cross section through a coordinate transformation:

$$\frac{d\sigma}{d\Omega_{cm}} = \left(\frac{d\sigma}{d\Omega}\right)_{lab}\frac{d\Omega_{lab}}{d\Omega_{cm}}, \tag{5.14}$$

with $\frac{d\Omega_{lab}}{d\Omega_{cm}}$ the Jacobian of the coordinate transformation,

$$\frac{d\Omega_{lab}}{d\Omega_{cm}} = \frac{\sin^2\theta_{lab}}{\sin^2\theta_{cm}}\left[\cos\theta_{cm}\cos\theta_{lab} + \gamma_{cm}\sin\theta_{cm}\sin\theta_{lab}\right], \tag{5.15}$$

where

$$\gamma_{cm} = \frac{\bar{E}_\gamma + m_d}{[m_d(2\bar{E}_\gamma + m_d)]^{\frac{1}{2}}}. \tag{5.16}$$

5.4.1 The Invariant Cross Section: $d\sigma/dt$

To study the scaling properties of the cross section, it is customary to observe the energy dependence of the invariant cross section $d\sigma/dt$, where t is the Mandelstam variable. The invariant cross section and the center-of-mass cross section are related by a coordinate transformation:

$$\frac{d\sigma}{dt} = \frac{d\sigma}{d\Omega_{cm}} \frac{d\Omega_{cm}}{dt}, \tag{5.17}$$

$$\frac{d\Omega_{cm}}{dt} = \frac{\pi}{\bar{E}_{\gamma,cm} p_{p,cm}}, \tag{5.18}$$

with $\bar{E}_{\gamma,cm}$ the average photon energy and $p_{p,cm}$ the proton momentum in the center-of-mass frame.

5.5 Calculation of the Bremsstrahlung Flux

In addition to the photoproton yield, the incident photon flux must be accurately known to calculate the photodisintegration cross section. Since the experiment makes use of an untagged photon beam, the photon yield is calculated using the bremsstrahlung cross section. Using the procedure of Matthews and Owens [84] the bremsstrahlung spectrum is calculated and the flux integrated in the same energy region of the spectrum where the photoproton yield is extracted from the E_γ spectrum.

When the electron beam strikes the radiator, a forward peaked cone of bremsstrahlung photons with a continuous spectrum is produced. The electrons undergo multiple scattering in the radiator, with a r.m.s. deflection [20]

$$\theta^{rms}_{m.s.} = \sqrt{2}\theta_{m.s.}, \tag{5.19}$$

where $\theta_{m.s.}$ is the width of a Gaussian angular distribution for multiple scattering:

$$\theta^{rms}_{m.s.} \approx \frac{13.6 \text{ MeV}}{\beta p} z \sqrt{\frac{l}{l_r}} [1 + 0.038 \ln(l/l_r)] \ . \tag{5.20}$$

Here p, β, and z are the momentum, velocity and charge of the electron, and l/l_r the thickness of the radiator measured in radiation lengths. Since high energy electrons are used ($E_0 \gg m_e$) half the opening angle of the bremsstrahlung cone is approximated by [83]

$$\theta_\gamma \approx m_e/E_0. \tag{5.21}$$

For high energy photons the angles $\theta_{m.s.}^{rms}$ and θ_γ are of the order of a few milliradians. In combination with a radiator-target distance ~1 m this implies that the entire bremsstrahlung cone impinges on the target, which facilitates the use of the over angle integrated bremsstrahlung cross section for the calculation of the flux.

For an infinitely thin radiator with foil thickness $d\tau$ the number of photons per incident electron per MeV is given by [41]

$$\frac{dN_\gamma}{dk} = \frac{X_0 N_A d\tau}{A} \frac{d\sigma_{brem}}{dk}(E_0, k), \tag{5.22}$$

where E_0 is the energy of the electrons impinging on the foil, A the atomic weight and X_0 (g/cm^2) the radiation length of the radiator material. Equation 5.22 represents the integrated-over-angle spectrum, which is only valid for an un-collimated photon beam, as was used in this experiment. The total integrated-over-angle bremsstrahlung cross section $\frac{d\sigma_{brem}}{dk}(E_0, k)$ is the sum of electron-nuclear and electron-electron contributions [84]:

$$\frac{d\sigma_{brem}}{dk}(E_0, k) = \frac{\alpha r_0^2}{k}[Z^2 \Phi_n(Z, E_0, k) + Z\Phi_e(Z, E_0, k)], \tag{5.23}$$

where $\alpha = \frac{1}{137}$, r_0 the classical electron radius (2.82×10^{-13} cm), k the photon energy, Z the atomic number of the radiator, and Φ_n and Φ_e the electron-nuclear and electron-electron bremsstrahlung fluxes respectively. The electron-nuclear spectrum is calculated with Bethe-Heitler extreme relativistic theory including intermediate screening and Coulomb correction. For high-Z radiator materials the electron-electron contribution is small and accounts for roughly $1/(1+Z)$ ($=\frac{1}{30}$ for Cu) of the total yield in the region of interest just below the endpoint.

With the above formulation the *thin-target* bremsstrahlung spectrum is calculated, which results in a yield that is ~15% too high in region near the tip. A more sophisticated calculation to evaluate the actual photon flux is carried out using the *thick-target* bremsstrahlung spectrum, which includes corrections for the finite thickness of the radiator. Among the corrections made, are corrections for the energy spread of the electron beam, multiple scattering and straggling of the electrons in the radiator and absorption of the photons in the radiator and target. A detailed description of the thick-target approach is provided in [84]. Inclusion of the corrections in the calculation introduces a 3% uncertainty in the flux for the energy region below the endpoint.

The photon yields corresponding to the kinematic settings of this experiment are calculated using a computer code developed by Belz [41]. Starting with a user supplied beam energy and estimated beam energy width, the code calculates thin-target and thick-target bremsstrahlung spectra for an energy region of 200 MeV below the endpoint. The output is a photon spectrum with the photon yield per unit charge as function of photon energy, binned in 1 MeV bins. The energy dependent correction factor $f(E_\gamma)$ used to correct the proton yields measured with the radiator removed (see Section 5.3) is also calculated with this code.

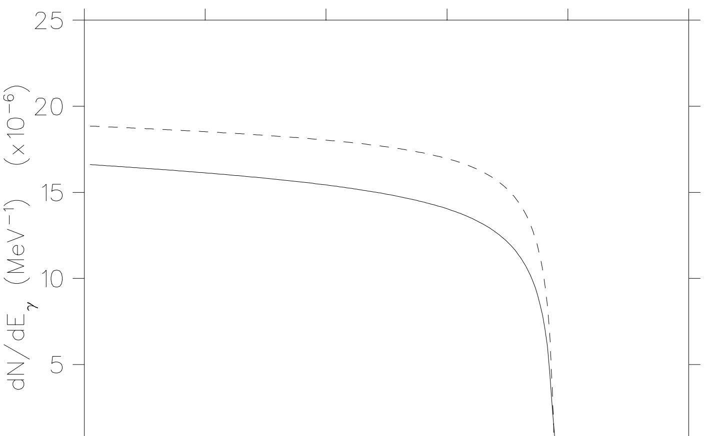

Figure 5.4: Bremsstrahlung spectra calculated with the computer code from Belz. The dashed line corresponds to the spectrum calculated with the thin-target cross section, the solid line shows the spectrum including corrections for finite radiator thickness. Both calculations are for electrons with energy E_0=3.245 GeV and $\Delta E/E = \pm 0.2\%$, striking a 6.02% radiation length copper foil.

An example of spectra calculated with the bremsstrahlung code is given in Figure 5.4. The figure shows spectra for thin-target bremsstrahlung (dashed) and thick-target bremsstrahlung (solid) for the case when electrons with initial energy E_0=3.245 GeV strike a copper foil with radiation length 6.02%.

To calculate the cross section (cf. Equation 5.11), the yield under the thick-target bremsstrahlung spectrum is integrated over the same energy range where the photoproton yield is integrated. The resulting integrated yields, N_γ, are listed in Appendix D, in Table D.1 for the half acceptance cross sections, and Table D.2 for the full acceptance cross sections.

5.6 The HMS Vacuum System Gate Valve

The particle flight path through the HMS magnets is kept under vacuum, and sealed off by kevlar vacuum windows at the entrance and exit. A stainless steel gate valve is added at the entrance of this vacuum system for additional protection during periods when no experiments are being run. This pneumatic valve, which is located about 145 cm downstream of the target between the collimator and the first quadrupole, is open under normal operating conditions(=data taking). During the E89-012 data taking a failure in the operating pressure caused it to move and partially obstruct the spectrometer acceptance. Because the obstruction became apparent after the experiment had ended, the consequences of the presence of this valve in the acceptance had to be accounted for in the analysis.

Figure 5.5 shows a schematic of the gate valve assembly blocking the spectrometer acceptance, in a view looking from the target to the spectrometer entrance. The moving part of the valve is a circular disk (the shutter), which is mounted on a carriage that slides in and out. A distribution of measured events over a plane at the position of the gate valve (z_{HMS}=145 cm) is shown in Figure 5.6. The data were taken at E_{beam}=1.645 GeV, θ_{cm}=90°. An arc is drawn to mark the approximate edge of the gate valve, which causes an eclipse-like attenuation of the data. Inspection of the data showed that all kinematics were affected by the presence of the valve, except the settings at the start of the experiment, E_{beam}=2.445 GeV, θ_{cm}=37°, 53°,

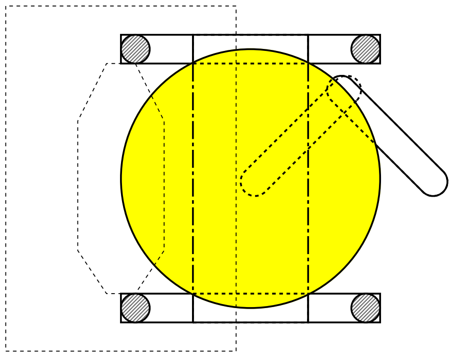

Figure 5.5: Schematic of the HMS gate valve shutter (disk) blocking part of the acceptance, as seen looking from the target to the spectrometer. The acceptance is defined by the octagon shape of the collimator, which is represented by dashed lines in this figure. This figure is not to scale.

and 70°. Further inspection made it clear that only the shutter (a stainless steel SST-316 disk with diameter 37.58 cm and thickness 1.33 cm) of the valve was obstructing the acceptance. Figure 5.5 shows the shutter positioned so that only the upstream half of the collimator was covered. The position of the valve remained unchanged for the duration of the experiment, and enables a division of the acceptance into an upstream, "bad" (covered) part and a downstream, "good" part.

A cross section calculation with a divided acceptance and data set provides a straightforward way to separate the events that are arguably corrupt because they struck the shutter, from the good events. However, the consequences of such a division go beyond the obvious loss of accuracy due to the reduction of logged events, and the application of this division-method has to be validated. The next section will discuss modeling of the HMS behavior when the gate valve is included in the Monte Carlo simulation. Results of the simulation validate the use of a divided acceptance, rejecting the corrupted data set. The section thereafter will present a description of the data analysis where the so-called "gate-valve-cut" was applied, including a study of the systematic uncertainties incurred by applying this method.

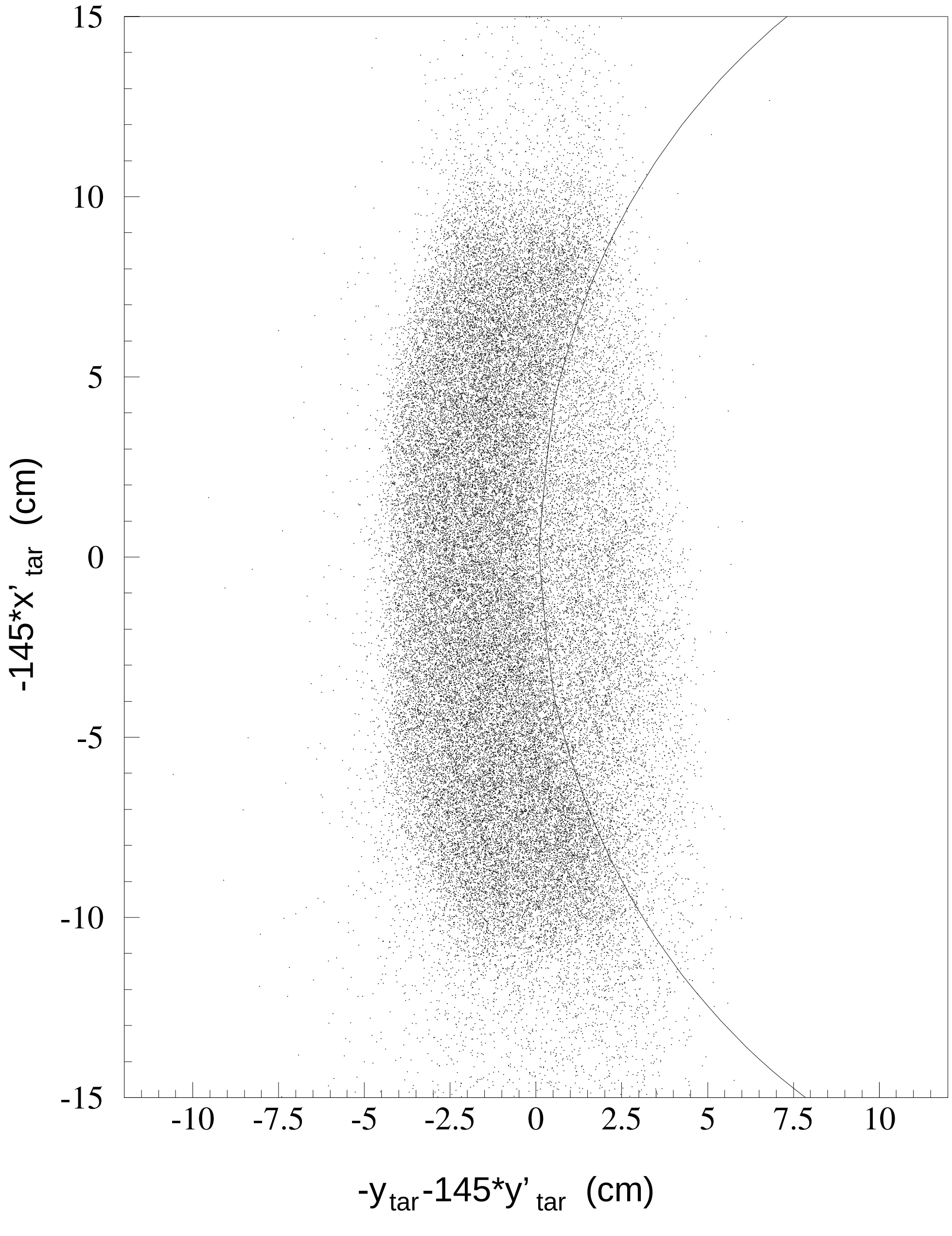

Figure 5.6: This figure shows a two dimensional scatter plot of the measured particle positions in the plane of the gate valve (z_{HMS} =145 cm) as seen looking from the target to the HMS for data taken at E_{beam}=1.645 GeV. An arc is drawn to mark the approximate edge of the gate valve shutter. Attenuation due to the presence of the shutter is considerable, as shown.

5.6.1 Modeling of the Gate Valve Shutter

Even though the position of the valve allowed for a well defined division of the acceptance of the spectrometer into a "good" and "bad" part, one cannot a priori assume that the two data sets created in this way obey the division. An estimate must be made of protons striking the shutter and multiple scattering into the "good" data set. The HMS Monte Carlo (Section 4.3.2) was used to make this estimate. The added feature to the standard Monte Carlo model was a new aperture at the location of the gate valve, which could be modeled by a stainless steel disk of uniform thickness. For an event that crossed this position, new event parameters are calculated based on multiple scattering and energy loss estimates for the shutter. The particle is then transported forward through the spectrometer starting from these new "initial conditions".

Using the composition and thickness of the shutter, the multiple scattering is added to the model by assuming a Gaussian angular distribution with width given by [20]

$$\theta_0 = \frac{13.6 \text{ MeV}}{\beta p} z \sqrt{\frac{x}{X_0}} \left[1 + 0.038 \ln\left(\frac{x}{X_0}\right)\right]. \tag{5.24}$$

Here p, β, and z are the momentum, velocity and charge of the particle, and $\frac{x}{X_0}$ the thickness of the shutter expressed in its radiation length X_0. To find the scattered angle $\delta\theta_{plane}$ and and linear offset δy_{plane}, two random variables, z_1 and z_2 are chosen over a Gaussian distribution [82]

$$\delta y_{plane} = \frac{z_1 x \theta_0}{\sqrt{12}} + \frac{z_2 x \theta_0}{2}, \tag{5.25}$$

$$\delta\theta_{plane} = z_2 x \theta_0. \tag{5.26}$$

To calculate the mean energy loss of a proton due to ionization of materials it strikes, the familiar Bethe-Bloch formula is used, to which a density effect correction δ and shell correction C are added [94]:

$$-\frac{dE}{dx} = (0.1535 \text{ MeV cm}^2/\text{g})\rho \frac{Z}{A}\frac{z^2}{\beta^2}\left[\ln\left(\frac{2m_e\gamma^2\beta^2 W_{max}}{I^2}\right) - 2\beta^2 - \delta - 2\frac{C}{Z}\right] \tag{5.27}$$

where m_e is the electron mass, β and γ the usual relativistic quantities, and I the mean excitation potential. Material properties of the gate valve shutter are substituted for the atomic number Z, the atomic weight A and density ρ (Z=26.36, A=56.72, ρ=7.94 g/cm^3). For a heavy particle like the proton, the maximum energy that can be transferred in a collision W_{max} is approximated as $W_{max} \approx 2m_e c^2 \beta^2 \gamma^2$. In Equation 5.27 dE is measured in MeV and dx in g/cm^2 .

In addition to small angle scattering and energy loss effects that will not remove the protons from the acceptance, a proton can also undergo nuclear reactions in the shutter causing it to be removed from the acceptance, or ultimately stopped in the shutter. An estimate of the fraction of photoprotons absorbed by the shutter, was modeled in the Monte Carlo using the probability of absorption given in Equation 4.9.

The success of the Monte Carlo modeling of the gate valve is evident when a simulation for E_{beam}=1.645 GeV, θ_{cm}=90° presented in Figure 5.7 is compared with the actual experimental data at the same setting from Figure 5.6 . A clear outline of the valve-shutter is discernible in the Monte Carlo result, which was obtained by modeling small angle multiple scattering only. The change in reconstructed target quantities due to events passing through the valve can be investigated with the Monte Carlo as well. Figure 5.8 shows the difference between the initial and reconstructed quantities for respectively δ, y_{target} and E_γ for protons that passed through the good side of the acceptance and protons that entered the HMS after penetrating the valve shutter. The Monte Carlo result shows that multiple scattering and energy loss in the gate valve cause a broadening in the difference between reconstructed and initial target quantities and photon energy that greatly exceeds the spectrometer resolution. Based on this simulation the reconstructed target quantities were found to be unreliable for events that passed through the valve, i.e. the simulation justifies the division of the acceptance into two parts to recover the good events, since no correction can be applied to recover the original values of the target quantities for the events that crossed the gate valve.

Accepting only events that pass the good half of the acceptance removes the

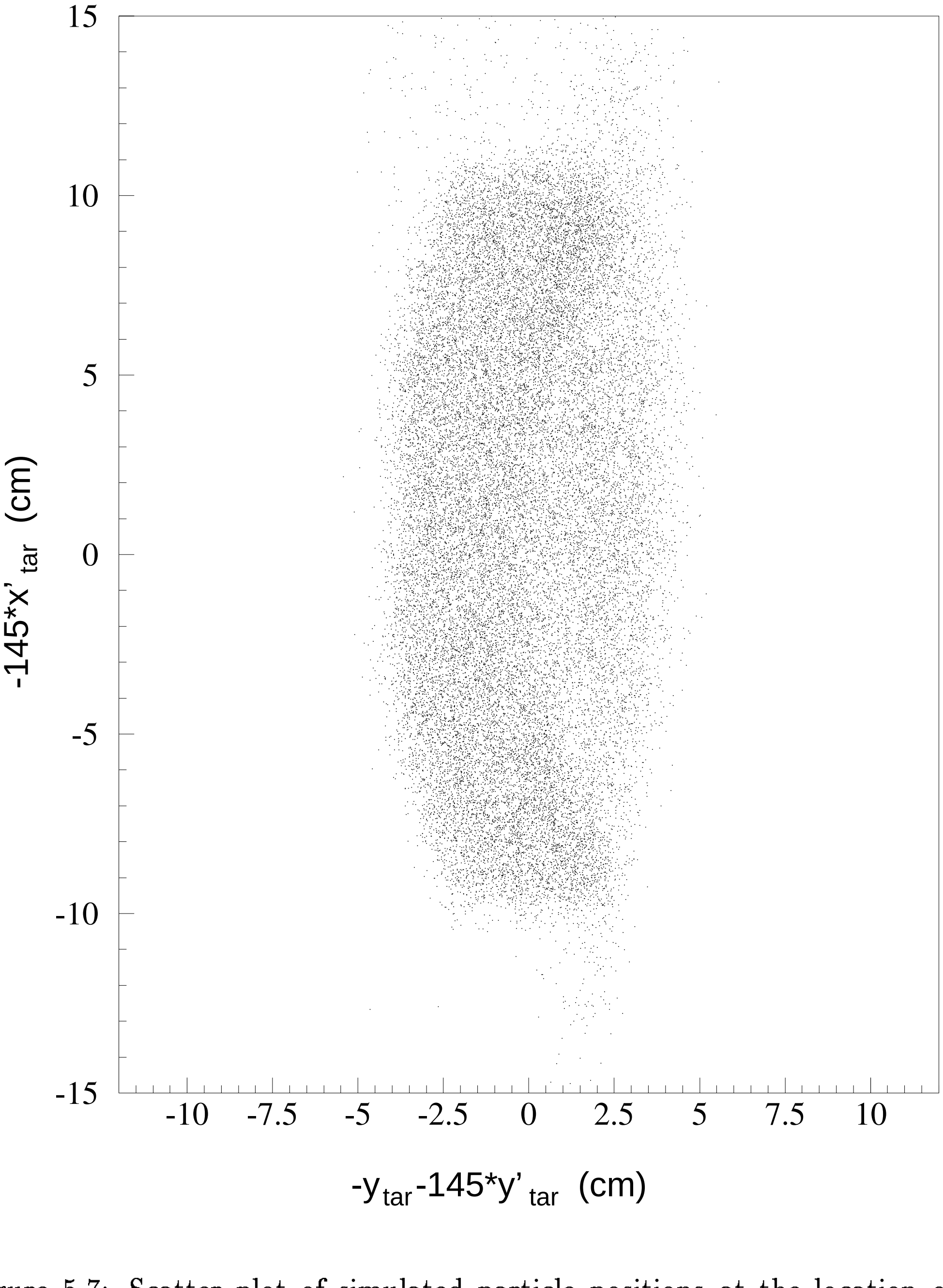

Figure 5.7: Scatter plot of simulated particle positions at the location of the gate valve (z_{HMS} =145 cm), as seen looking from the target to the HMS collimator. Data shown is for E_{beam}=1.645 GeV, θ_{cm}=90°. Figure courtesy of C.W. Bochna.

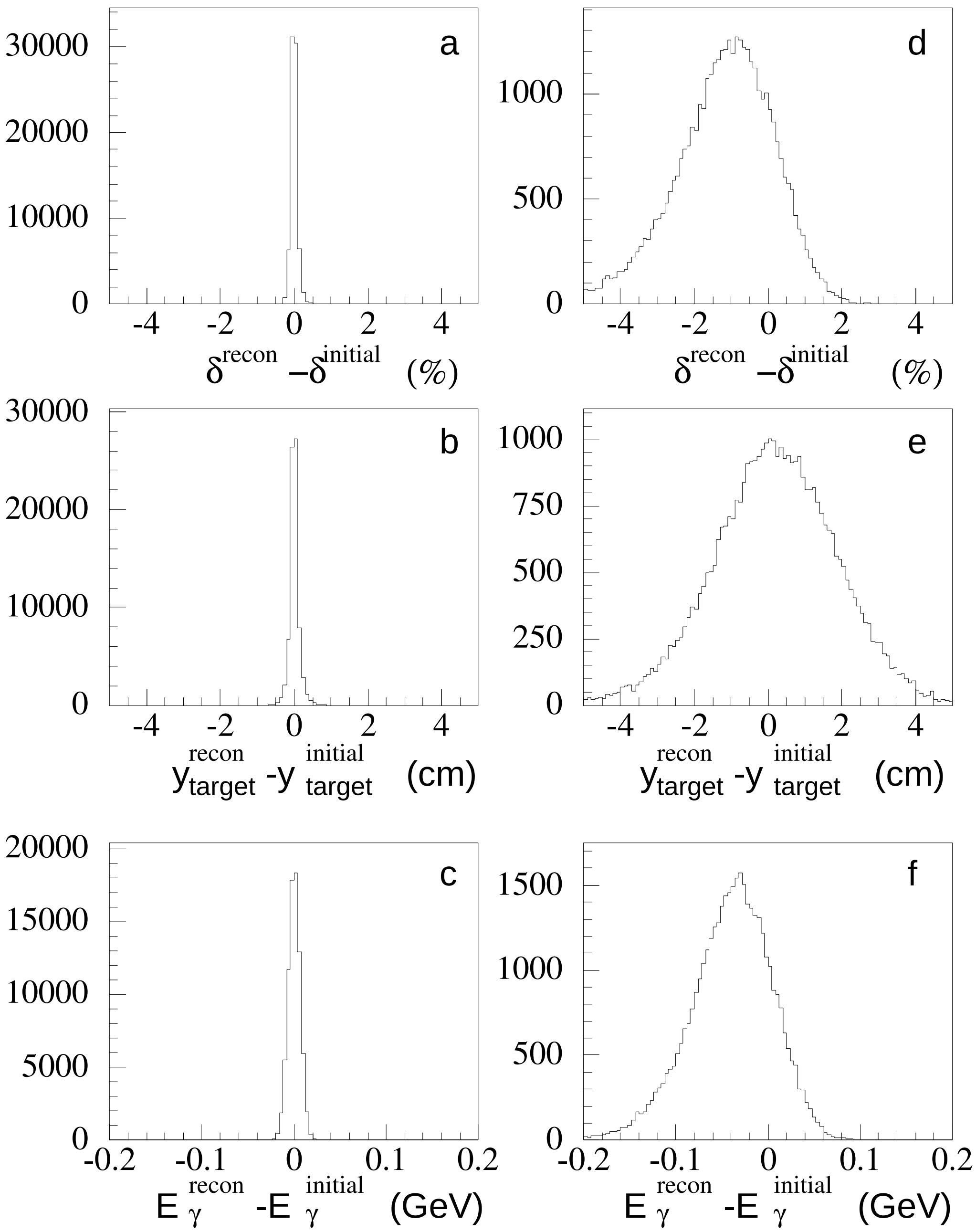

Figure 5.8: Monte Carlo simulation results for θ_{cm}=90°, E_{beam} = 1.645 GeV. The figures show the difference between reconstructed and initial quantities for δ, y_{target} and E_{γ}. Figures *a-c* on the left show the difference for events that did not have the gate valve in their path. Figures *d-f* on the right show the difference for events that entered the spectrometer by passing through the gate valve shutter. Figure courtesy of C.W. Bochna.

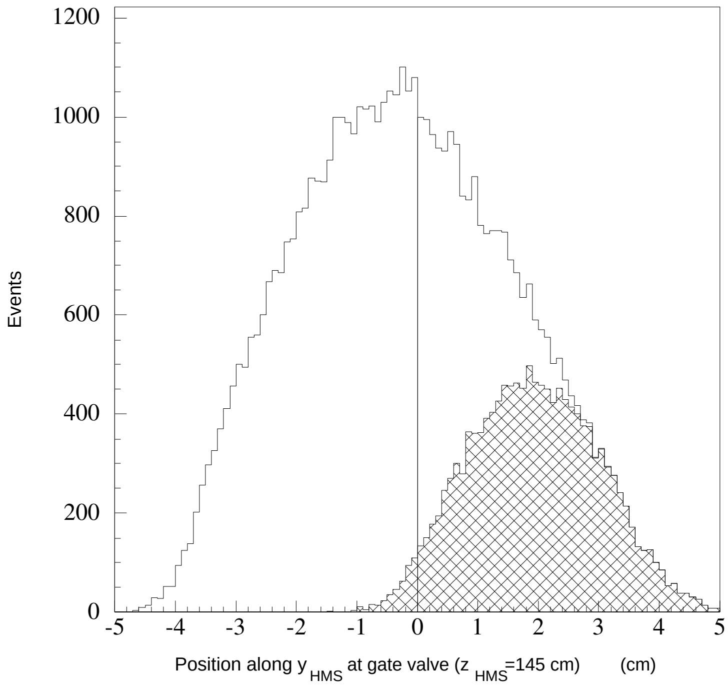

Figure 5.9: Monte Carlo simulation of the reconstructed position along y_{HMS} at the location of the gate valve (z_{HMS}=145 cm) for E_{beam}=1.645 GeV, θ_{cm}=90°. The solid line shows y_{HMS} for all events that enter the HMS acceptance. Events that were scattered by the gate valve shutter are shown in the cross hatched area. The events in the cross hatched area that fall left of the line at $y_{HMS} = 0$ represent protons scattered into the good part of the acceptance, applied to the data-analysis of the 1996 data. Figure courtesy of C.W. Bochna.

vast majority of the events with unreliable reconstructed quantities, but a small remaining contribution due to events striking the shutter, thereby being scattered into the good half of the acceptance, is expected. A Monte Carlo simulation was carried out to estimate the fraction of events that undergo a scattering ending up in the 'wrong' part of the acceptance. Figure 5.9 illustrates the effect. The solid line shows the total distribution of the event position along y_{HMS} in the the plane of the gate valve (z_{HMS}=145 cm). The vertical line at y_{HMS}=0 marks the division between the good part (left) and bad part (right) of the acceptance. The cross hatched distribution corresponds to events that passed through the gate valve shutter. The events in the cross hatched area that fall left of the line at y_{HMS}=0 represent protons scattered into the good part of the acceptance. In this case an estimated 1.5% of the events in the good part originated from gate valve scattering. At higher proton momenta the "inscattering" effect is expected to become smaller because the average multiple scattering angle is reduced. As a conservative estimate an overall inscattering correction of 1.5% was applied to all 1996 data. The systematic uncertainty in the inscattering correction was estimated at 0.5% [82].

5.6.2 Gate Valve Constraints on the Data Analysis

The results of the Monte Carlo simulation support the suggested method of cross section calculation with divided acceptance and data sets. For all kinematic settings the cross section was calculated using only the downstream (good) part of the acceptance. The most important implication of using this method is the need to redefine the lab scattering angle, since it does not coincide with the central setting of the HMS. Solid angles corresponding to the correct collimator opening must also be calculated. The sensitivity of the cross section to the placement of the gate valve cut was investigated as well, and a systematic uncertainty is assigned. At those settings where the valve shutter was not present, the cross section with the full acceptance was calculated in addition to the half-acceptance cross section.

The correct scattering angle is defined using the geometry of the HMS collimator in combination with the HMS central scattering angle. Figure 5.10 shows a diagram of the scattering plane including a horizontal cross section of the collimator. The HMS is located at θ_{HMS}, which corresponds to particle ray through the center of the acceptance. When only the downstream part of the acceptance is used, the new "central" ray is moved forward to θ^{good}_{HMS}. The collimator aperture accepts particles with scattering angles $\pm 1.6°$ from the central ray. The new central ray is in the center of the forward half-acceptance, hence θ^{good}_{HMS}=$\theta_{HMS} - 0.8°$. The corresponding new center-of-mass scattering angles were calculated by boosting the lab angles to

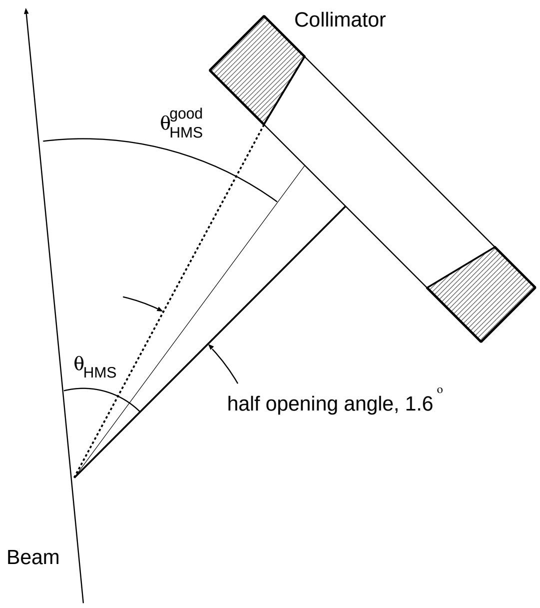

Figure 5.10: Diagram of the scattering plane including a horizontal cross section of the collimator (opening angle is slightly exaggerated). The figure shows the definition of the scattering angles for analysis including the gate valve cut. θ_{HMS} is the central angle in the lab at which the HMS is positioned. θ_{HMS}^{good} is the central lab scattering angle for the analysis using the downstream part of the acceptance. For all lab angles that define the central ray of the "good" part of the acceptance, $\theta_{HMS}^{good}=\theta_{HMS}-0.8°$, where the 0.8° is half of the half opening angle of the collimator.

the CM-frame. The central settings and the new lab- and CM-angles are listed in Table 5.3.

In the yield extraction a box cut is applied in the plane of the collimator (z_{HMS}=126 cm) to remove most of the accidental background events from collimator punch-through and other sources that fall outside the aperture of the collimator. Then, in the plane of the gate valve shutter (z_{HMS}=145 cm) the data set is divided into two parts, theoretically at y_{HMS}=0. For all kinematic settings the box cuts were defined as loosely applied rectangular "envelope" cuts around the shape of the collimator, based on the event distribution in figures similar to Figure 5.6. It was found that the reconstructed collimator position has a small offset in y_{HMS}, thereby precluding a straightforward acceptance division at y_{HMS}=0. Instead, the location of the accep-

θ_{cm} (nominal)	E_{beam} (GeV)	$\theta_{lab,central}$	$\theta_{lab,good}$	$\theta_{cm,good}$
37°	0.845	25.13°	24.33°	36.17°
	1.645	21.31°	20.51°	35.82°
	2.445	18.89°	18.09°	35.57°
	3.245	17.20°	16.40°	35.46°
	4.045	15.92°	15.12°	35.40°
53°	1.645	31.13°	30.33°	51.90°
	2.445	27.68°	26.88°	51.64°
	3.245	25.30°	24.50°	51.64°
	4.045	23.40°	22.60°	51.50°
70°	1.645	42.30°	41.50°	68°.87
	2.445	37.90°	37.10°	68.80°
	3.245	34.66°	33.86°	68.68°
	4.045	32.22°	31.42°	68.70°
90°	0.845, low bin	65.61°	64.81°	88.68°
	0.845, high bin	65.61°	64.81°	89.46°
	1.645	57.14°	56.34°	88.97°
	2.445	51.50°	50.70°	88.83°
	3.245	47.40°	46.60°	88.79°
	4.045	44.20°	43.40°	88.77°

Table 5.3: Nominal experiment settings and the corresponding central HMS angles for the full acceptance, $\theta_{lab,central}$, and usable (good) part of the acceptance, $\theta_{lab,good}$. For the latter case the corresponding center-of-mass angle, $\theta_{cm,good}$ is also listed.

tance partition cut was also determined by visual inspection from these figures. Since the accuracy of this procedure is subject to the precision with which the observer can determine the dimensions of the collimated data set from a figure, an estimation of the systematic uncertainty in the location of the cut must be made.

An estimate of the systematic uncertainty in the placement of the valve cut is made by studying the dependence of the cross section on the location in y_{HMS} of the cut. Center-of-mass cross sections (normalized to the integrated charge and corrected for dead time and tracking efficiency) were calculated for different acceptance partition cuts, starting at y_{HMS}=0 and going up to y_{HMS}=0.5 cm in steps of 0.1 cm. Cross sections were calculated for both sides of the divided acceptance. For the purpose of comparison between the sides, data E_{beam}=4.045 GeV, θ_{cm}=53° from 1997 was taken, which had not been compromised by the gate valve. The cross section dependence as function of the location of the valve cut is shown in Figure 5.11. Figure 5.11.(a) shows the trends for both the "good" side of the acceptance (open circles) and "bad" side of the acceptance (solid triangles). The cross section for the full acceptance was also calculated and is represented by the solid circle. Only statistical error bars are shown. Both sets of cross sections were fit with a linear fit. The coefficients that were found for the slopes are in good agreement. In addition, the full acceptance is in agreement with the mean of the two half-acceptances for each of the cut positions.

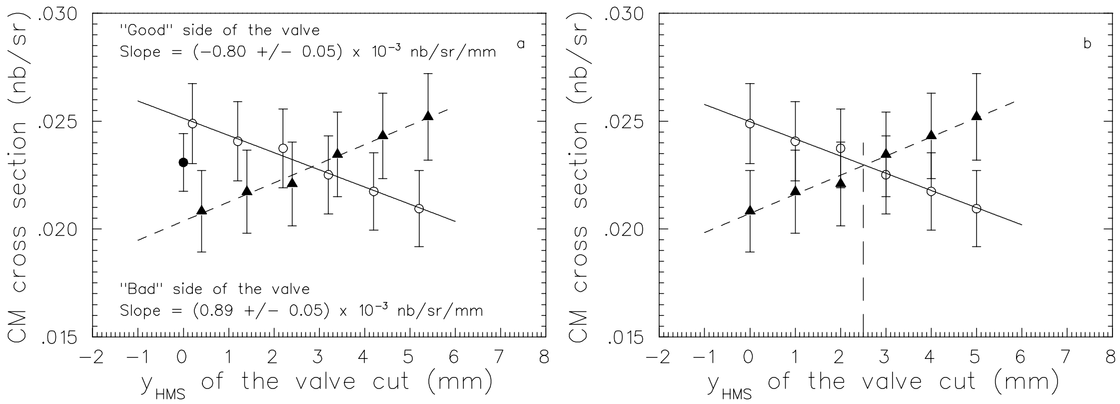

Figure 5.11: Dependence of the center-of-mass cross section on the placement of the valve cut for E_{beam}=4.045 GeV, θ_{cm}=53° data from 1997. Three data sets are shown: the cross section for the full acceptance (solid circles), for the downstream ("good") part of the acceptance (open circles), and the upstream ("bad") part (solid triangles). The cross sections shown are normalized to the integrated charge and corrected for tracking efficiency and dead time. For both half-acceptances data is shown for 6 different y_{HMS} locations of the valve cut. The solid and dashed lines are linear fits to the data. In Figure (a) both half-acceptance data sets are plotted at an offset of their true y_{HMS} for better comparison. In Figure (b) the data sets are plotted at their correct value of y_{HMS} to determine the intersection of the two fits, which coincides with the chosen valve cut position for this setting, 2.5 mm.

The angular dependence of the cross section causes the distribution over the face of the collimator to be non-uniform, with a larger contribution at more forward angles. This effect is the strongest at the most forward scattering angles. Thus the intersection point of the two linear fits should theoretically be close to the optimal position for the valve cut. This is observed for the 1997 data, where the intersection point agrees well with the cut location from observation at 0.25 cm, marked by the vertical dashed line in Figure 5.11.(b) . For the data taken in 1996 the offset from y_{HMS}=0 was visually determined to be 0.2 cm. The slope of the cross section in Figure 5.11 is 3%/mm. Since the average observer can place the valve cut to $\pm$1 mm by visual inspection of the figures, the systematic uncertainty in the cross section due to the valve cut placement was taken to be 3%.

5.7 Sources of Background

Background photoprotons arising from physics processes where the photon or electron beam interacts with the target cell windows are measured and corrected for with the scheme outlined in Section 5.2. After applying this scheme, background events remain in the E_γ spectrum, which cannot be identified as protons without further investigation. A known source of background are positive pions (π^+), which are created through various reaction channels, including deuteron photodisintegration. But the largest remaining source of background are accidentals, which are not necessarily associated with deuteron photodisintegration, but create an event with the fingerprint of a photoproton. In this section these sources of background are identified, and a scheme is presented to enable a proper subtraction and correction.

5.7.1 Pion Background

In the mass-squared distribution a small pion distribution can be discerned for most of the kinematics. Figure 5.12 shows mass-squared distributions for E=4.045 GeV, θ_{cm}=90° (a), and θ_{cm}=37° (b). In both distributions a pion mass-squared distribution centered around m^2=0.018 GeV^2 is clearly visible (marked by cross hatching). Even at momentum settings below $\simeq$2.3 GeV/c the pions have a velocity very close to c (β >0.99), so that they can be separated from the protons using time-of-flight. For the higher momentum settings, the gas Čerenkov detector provides means to reject the pions. During experiment E89-012 the gas Čerenkov counter was configured so that the the pion momentum threshold is equal to 2.65 GeV/c (see Section 3.5.1).

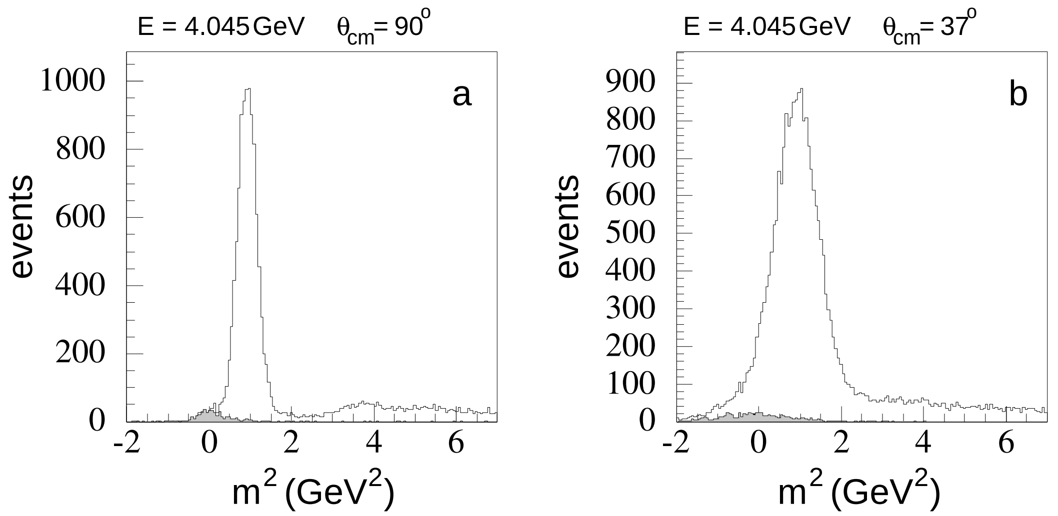

Figure 5.12: Clean mass-squared distributions for E=4.045 GeV, θ_{cm}=90° (a), and θ_{cm}=37° (b). Photoprotons including pions are shown by the solid line. The pion distribution (hatched) is removed by the Čerenkov cut.

To estimate the amount of pion background, the π/p separation was determined at all momentum settings. The π/p ratio is defined as the ratio of the number of pions in the clean mass-squared distribution that fall within the E_γ-cut, and the number of protons that fall within the same cuts. At momentum settings where the Čerenkov provides separation, the number of pions is determined by their distribution in the mass-squared distribution for a Čerenkov cut >3 photoelectrons. The number of protons is determined by the number of protons falling within the standard m^2-cut in a mass-squared distribution with Čerenkov cut <3 photoelectrons. At lower momentum settings pions can be integrated directly in the total mass-squared distribution (without Čerenkov cuts), because they are separated from the protons. In the intermediate region, $2.3 < p < 2.7$ GeV/c, where pion and proton distributions overlap, an estimate of the pions was made assuming that the proton distribution is symmetric, so that the shape of the tail above the pions can be approximated by the proton tail on the high m^2 side of the proton distribution.

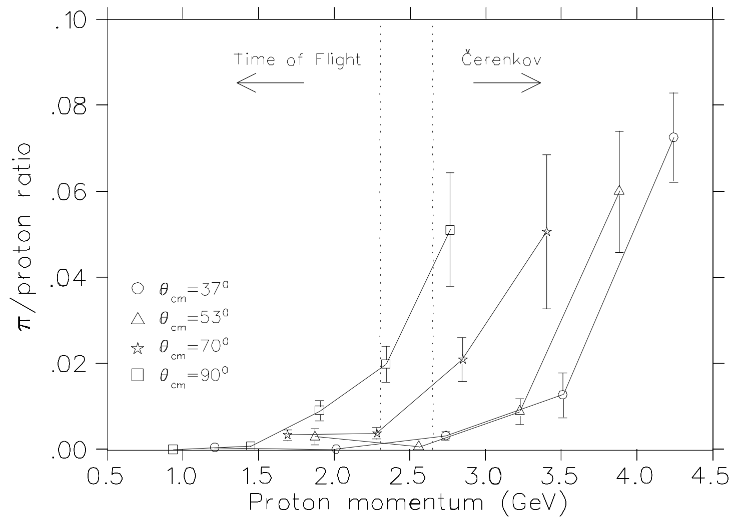

Figure 5.13: Measured π/p ratio for all momentum settings and scattering angles, at which data was taken in this experiment. The solid lines connect data points measured at the same angle, and have the sole purpose of showing the trend. The two vertical dashed lines mark the intermediate momentum region, where time-of-flight π/p separation is no longer possible and the Čerenkov rejection turns on.

Figure 5.13 shows the π/p ratio for the momentum settings at each of the angles measured. The π/p ratios shown were calculated using LD_2^{IN} runs, which had not been corrected for accidental background. The lines connecting the points have no significance and are merely added to guide the eye. The vertical dashed lines mark the momentum region where time-of-flight π/p separation is no longer possible and the Čerenkov rejection turns on. The figure shows that at the highest momentum, where the background is the largest, the π/p is less than 10%. The Čerenkov cut removes over 99% of the pions that fall within the E_γ-cut at settings above $\sim$2.7 GeV/c. At lower momentum settings all pions are successfully removed using time-of-flight. Since >99% of all pions are successfully rejected, no correction for pion contamination of the E_γ-yield was applied.

5.7.2 Accidental Background

In addition to the known backgrounds caused by the target end-caps and pions, which can be measured and corrected for, a source of background events remains. This remaining background, the so-called accidental background, is caused by particles that did not necessarily originate from deuteron photodisintegration, but entered the acceptance of the spectrometer after scattering off of materials in their path. Most accidentals have clean, valid tracks, but reconstruct back to vertices outside of the target volume, which makes it easy to remove them using software cuts. A small fraction of left-over accidentals falls within the software cuts and will be treated as if they are photoprotons, consequently biasing the true photoproton yield. In the photoproton energy distribution these events manifest themselves as events that show up above the beam energy, where, in theory, photoprotons are kinematically forbidden. The distribution of accidentals is not limited to the energy region above the endpoint, but continues underneath the photoproton energy distribution, where it is masked by the true photoproton distribution.

In order to correctly subtract the accidentals from the photoproton yield, the shape of the accidental background must be known and a method was developed to determine the shape of the background [82]. Since the accidentals are masked by the photoproton events within the HMS acceptance, the method is based on the distribution of events that reconstruct back to the area outside of the opening of the collimator of the HMS. Figure 5.14 shows the distribution of events over a plane at the location of the face of the collimator at the entrance of the HMS. The distribution is obtained by projecting the coordinate y_{tar}, and angles x'_{tar} and y'_{tar} of the vertex at the target to the collimator plane (located at z_{HMS}=126 cm) for all events that pass the software cuts (except the box cut). The data shown for illustration are LD_2^{in} data for E=4.045 GeV, θ_{cm}=53° from the 1997 run. The gate valve was not obstructing

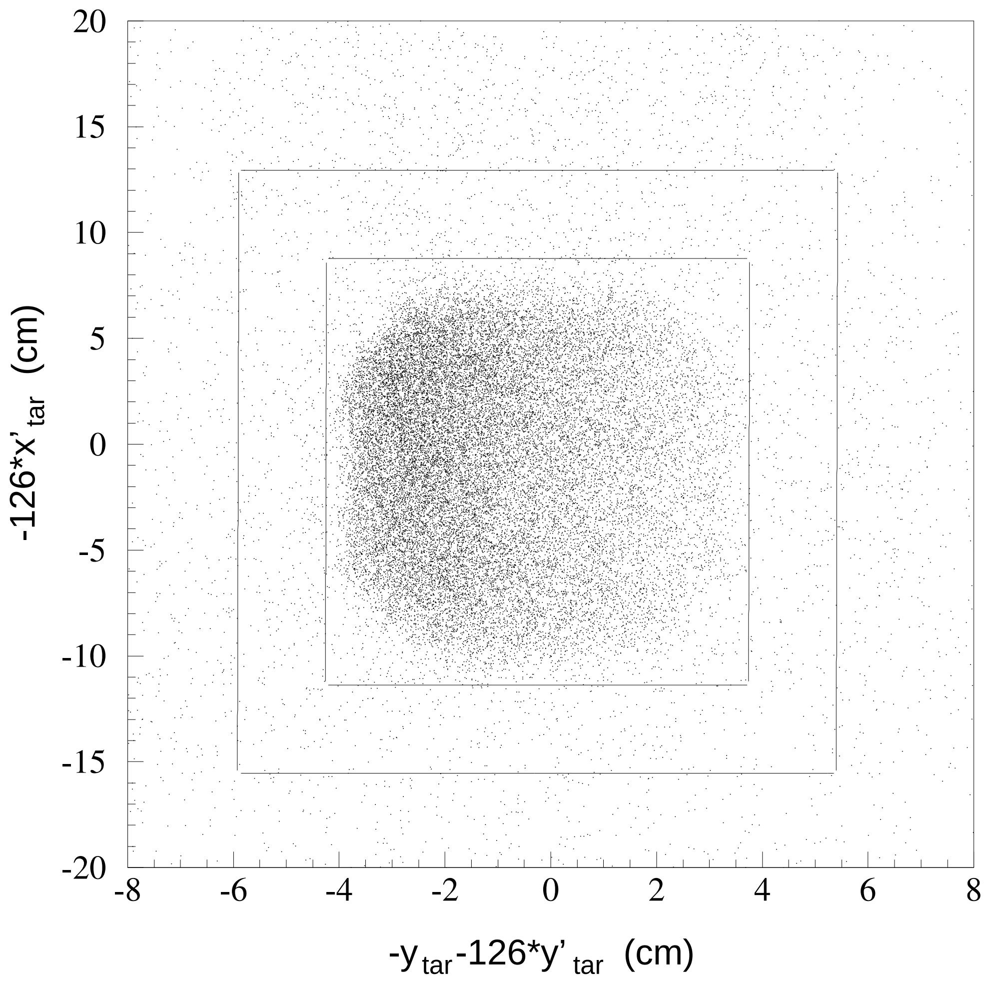

Figure 5.14: Proton events projected from the target vertex to the plane of the HMS collimator for E_{beam}=4.045 GeV, θ_{cm}=53°, LD_2^{in}. The inner box corresponds to the software box cut used in the data analysis. The accidental background is determined from the event distribution in the area between the inner and outer box, which is equal to the area of the inner box, and only includes accidental events.

the acceptance at that time, but the method is equally successful for data passing the good part of the acceptance at the other kinematics.

In the figure events distributed in the octagon shape correspond to particles that passed through the aperture of the collimator. Distributed throughout the entire area, and most visible outside the octagon are the accidental events. The inner box

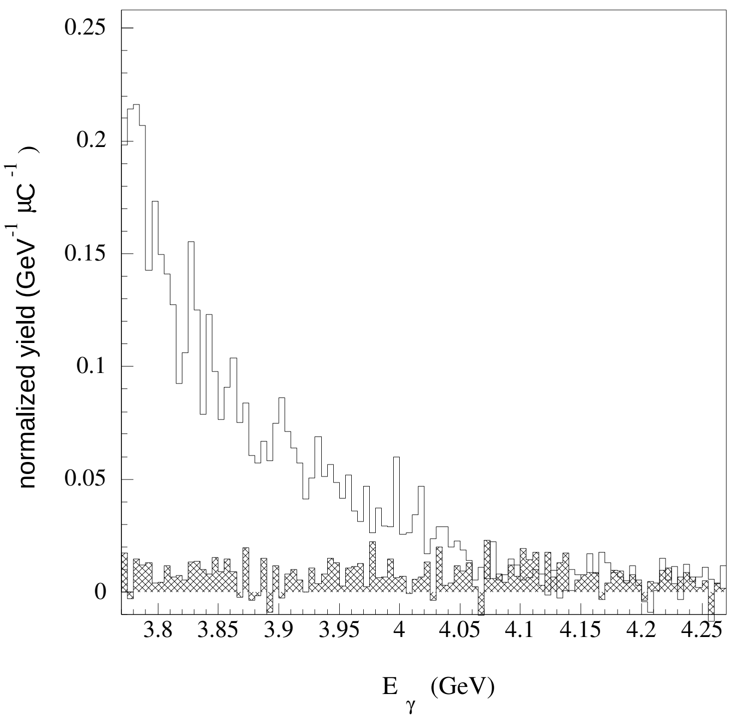

Figure 5.15: Normalized E_γ spectrum and estimated accidental background for E=4.045 GeV, θ_{cm}=37°. The accidental background distribution is calculated with the inner/outer box method outlined in the text and shown as cross hatched. The yield plotted on the vertical axis is for a 5 MeV bin, corrected for tracking efficiency, dead time and normalized to the integrated charge.

directly around the octagon marks the location of the software box cut which removes most of the accidentals. The outer box is constructed so that the area between the inner and outer box is equal to the area of the inner box. Assuming a uniform areal distribution of accidentals, the amount and shape of the accidental background in the inner box is determined from the events in the area between the outer and the inner box.

This method was applied to data taken at highest momentum setting and most forward scattering angle, E_{beam}=4.045 GeV, θ_{cm}=37°, where the rate of accidentals is the highest. Figure 5.15 shows the E_γ histogram for this setting. The normalized yield is represented by the solid line, and a non-zero background above the endpoint, caused by accidentals, is present. The normalized spectrum of accidentals from the area between the inner and outer box is represented by the cross-hatched distribution. In the energy region above the bremsstrahlung endpoint, where no events are expected, the distribution of accidentals shows good agreement with the observed distribution of E_γ events. Below the bremsstrahlung endpoint the background continues to be flat and small well beyond the energy region where the photoproton yield is extracted.

The observation of a small uniform background distribution in a 400 MeV energy region centered around the bremsstrahlung endpoint makes a well-defined background subtraction feasible. In the cross section calculation, the normalized yields are corrected for the background by subtracting the average flat accidental yield above the endpoint, scaled to the size of the E_γ–window.

Figure 5.15 represents the case at highest momentum setting and most forward scattering angle where the accidentals rate is expected to be the highest. Initially it was assumed that the accidentals rates would be correlated with scattering angle and momentum setting, expecting a higher background at more forward angles and higher momenta. However, as illustrated in Figure 5.16, there appears to be a correlation between the accidental background and the nominal beam energy. This could indicate that the background in Hall C was uniform for given beam energy, rather than the assumed forward (along the beam) peaked shape. The accidental background drops rapidly for lower beam energies and becomes almost negligible at the lowest beam energies. The rapid fall-off is also observed when comparing the accidental background above the endpoint for different settings in Figure 5.1.

Special care has to be taken in the analysis of the 1996 data, where the level of the accidental background could be affected by the presence of the gate valve shutter. Events that strike the shutter and undergo multiple scattering end up having the wrong reconstructed quantities, thereby making their appearance as accidentals. This process is best observed for events showing up in energy bins above the endpoint, which are ordinarily only filled with accidentals. Figure 5.17 illustrates the

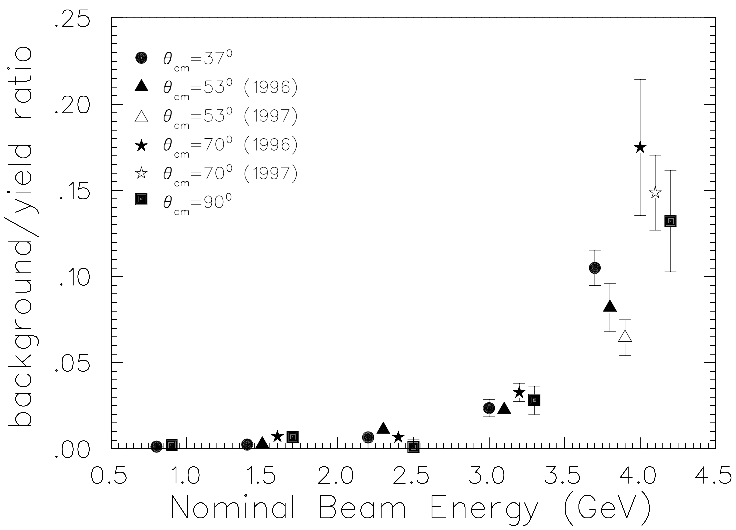

Figure 5.16: Ratio of the accidental background to the measured yield as function of the nominal beam energy for all center-of-mass angles. The data points include corrections for tracking efficiency and dead time. Only statistical error bars are shown.

result of this process in E_γ spectra for the good and bad side of the acceptance, for $E=$ 4.045 GeV, $\theta_{cm}=$ 37°. The difference in level and shape of the background above the endpoint for the bad and good side of the acceptance is evident. Fortunately most of the accidentals caused in this way are removed by the valve cut, and the remaining background above the endpoint has a flat appearance, for which the above described background subtraction procedure is valid.

In the flat background subtraction scheme, the average background in the E_γ energy interval is approximated by the flat background above endpoint. The approximated level of background has a systematic uncertainty associated with it. As an estimate of the systematic uncertainty of this method, the statistical error in the flat background estimation expressed as percentage of the corrected yield was taken. For the half-acceptance analysis, a systematic uncertainty of 0.02−4.0% was found, for the full-acceptance analysis the systematic uncertainty varied 0.08−1.5%.

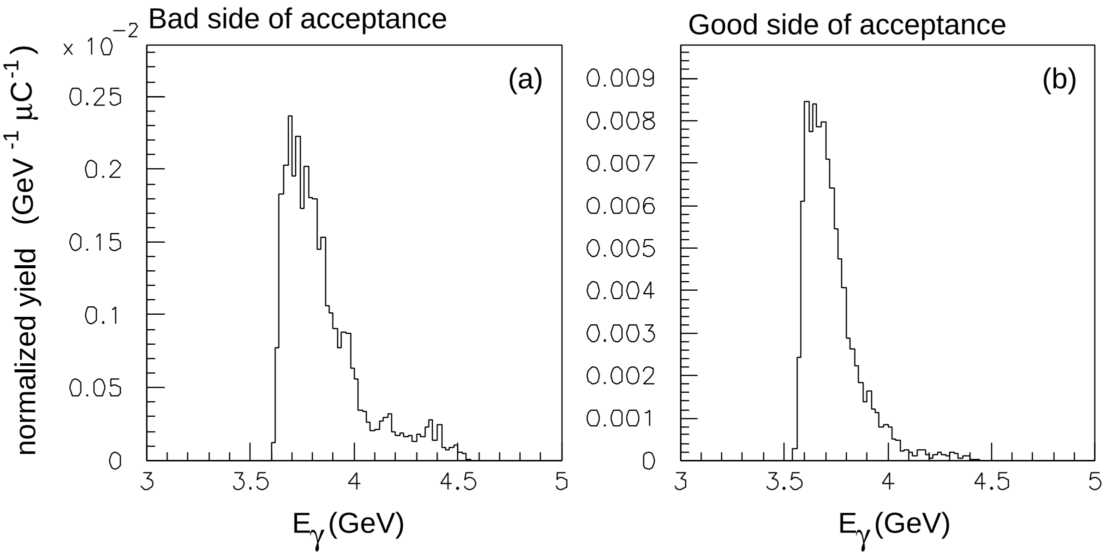

Figure 5.17: Photoproton distributions showing the accidental background above the endpoint in the worst case, E= 4.045 GeV, θ_{cm}= 37°. Figure a (b) shows the accidental background for events passing the bad (good) part of the acceptance. The figures illustrate that the "valve-cut" reduces the accidental background by a large amount. Moreover, the background for the good part of the acceptance appears to have a flat shape.

5.8 Target Thickness

The cross section depends on the amount of deuterium nuclei in the path of the beam, hence the target density and length must be well known. The number of deuterium nuclei per unit area in the target is defined as:

$$n_{nucl} = \frac{N_A \rho N_N L_{target}}{A}, \tag{5.28}$$

where N_A is Avogadro's number, ρ the density of the cryogen (g/cm^3), A the atomic mass (g/mole), N_N the number of nuclei per molecule (N_N=2 for D_2), and L_{target} the target length used in the analysis. The target length is calculated from the software target length cuts y_{tar} and the lab scattering angle θ_{lab}:

$$L_{target} = \frac{2|y_{tar}|}{\sin\theta_{lab}}. \tag{5.29}$$

In this section the major contributions to the uncertainty in n_{nucl} are discussed, which are the uncertainty introduced by the use of software cuts and the uncertainty in the correction to the reconstructed target length. The uncertainty in the determination of the target density is 0.5% (see Section 3.4).

5.8.1 Software Target Length Cuts

Photoprotons originating from processes in the entrance and exit windows of the target cell are a source of unwanted background and have to be excluded from the deuteron photodisintegration yield. Most of the unwanted photoprotons coming from the windows are removed using the customary subtraction method (Section 5.3, Equation 5.3). However, after the subtractions a photoproton signal from the cell windows usually remains because the subtractions are not perfect due to small target misalignments and the variation in width of the distributions.

To exclude the photoprotons coming from the windows a software cut on the reconstructed target length, y_{tar} is applied. This cut limits the events to photoprotons with a vertex starting in the bulk of the deuterium volume, therefore also removing accidental background events from outside the target cell. The y_{tar} cuts used in this experiment are listed in Table D.1. in Appendix D. Figure 5.18 shows y_{tar} distributions for all measured angles at 2.445 GeV beam energy. As the figure shows, the width of the distribution increases going to larger center-of-mass angles, because y_{tar} depends on the scattering angle according to $y_{tar} = z_{target}\sin(\theta_{lab})$. The rapid fall-off on both sides marks the location of the two cell windows. Negative y_{tar} corresponds to the upstream (entrance) cell window. The intensity peak of the larger gauge exit window is discernible at large scattering angles, and merges with the distribution at more forward angles where the resolution is worse.

To validate the procedure of applying a software cut to determine the “effective” target length it is necessary to verify that there is no dependence of the cross section on the size of the target length selected by the cut. The dependence is best studied at large scattering angle where $y_{tar} \simeq z_{target}$, so that a large range of y_{tar} is available.

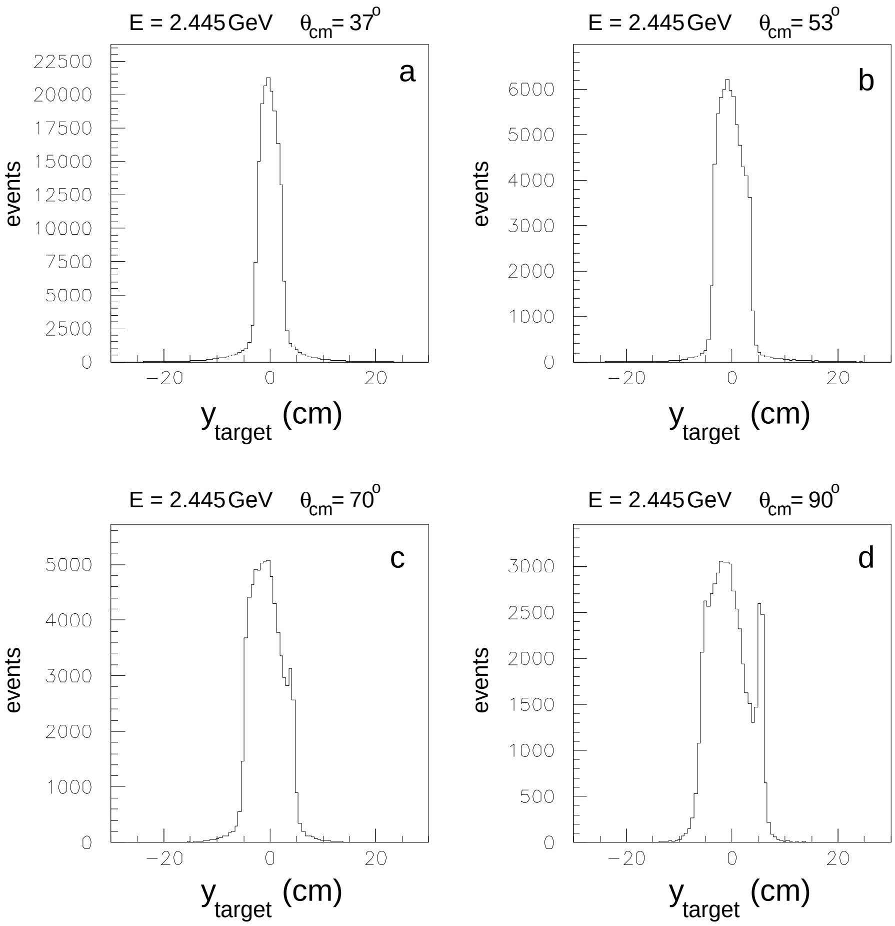

Figure 5.18: Event distributions for y_{target} at E_{beam} =2.445 GeV, for θ_{cm} =37°(a), 53°(b) 70°(c), and 90°(d). Negative y_{target} corresponds to a location upstream of the center of the target cell.

The dependence was studied at θ_{cm}=90°, E_{beam}=1.645, 2.445 GeV were the nominal y_{tar} cut is 4.0 cm. Laboratory cross sections for the "good" part of the acceptance were calculated from yields extracted with $\mid y_{tar} \mid$ =1.0, 2.0, 3.0, and 4.0 cm, and the results are shown in Table 5.4. The lab cross sections shown are intermediate results, which include corrections for dead time and tracking efficiency only. In addition, the cross sections are calculated with the correct solid angles, since there is a 15% increase in solid angle when $\mid y_{tar} \mid$ is reduced from 4.0 cm to 1.0 cm. The results show that for both settings, there is excellent agreement between lab cross sections

E_{beam}, θ_{cm}	$\mid y_{tar} \mid$ (cm)	$(\frac{d\sigma}{d\Omega}_{lab})$ (nb/sr)
1.645 GeV, 90°	1.0	5.681 ± 0.230
	2.0	5.530 ± 0.163
	3.0	5.433 ± 0.135
	4.0	5.402 ± 0.120
2.445 GeV, 90°	1.0	0.3953 ± 0.0360
	2.0	0.4005 ± 0.0219
	3.0	0.3961 ± 0.0213
	4.0	0.4004 ± 0.0188

Table 5.4: Laboratory cross sections for the "good" part of the acceptance as calculated from yields extracted with $\mid y_{tar} \mid$ =1.0, 2.0, 3.0, and 4.0 cm. Corrections for dead time and tracking efficiency are included. The errors are statistical errors only.

calculated with the four y_{tar} cuts. On average the cross sections are between 0.7% and 1.5% different from the weighted mean. To account for imprecision in the y_{tar} cuts, a systematic uncertainty of 1.5% was assigned to the cross section.

5.8.2 Target Length Correction

Figure 5.19 shows the distribution of events along z_{target} for an empty target run with radiator in at E_{beam}=1.645 GeV, $\theta_{cm} = 90°$. The two peaks indicate the location of the upstream and downstream windows of the target. The exit window of the target is at positive z and is made of thicker gauge aluminum, causing a larger intensity. To calculate the reconstructed target length the intensity distributions are assumed Gaussian, and Gaussians are fitted to the distributions at both window locations. The reconstructed z_{target} is the sum of the absolute value of the centroids of the fitted distributions. For E_{beam}= 2.445 GeV, $\theta_{cm} = 53°$ it was first observed that the reconstructed target length deviated significantly from the nominal 15.2 cm target length of the long cryo target cells. The figure shows the effect for E_{beam}= 1.645 GeV, $\theta = 90°$ since it is very pronounced at this kinematic setting.

The observed effect implies that in the reconstruction of target quantities the

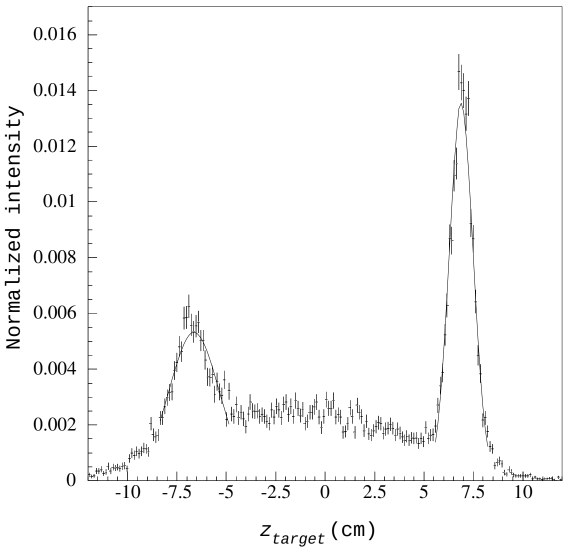

Figure 5.19: Event distribution along z_{target} for an empty target, radiator in run, taken at E_{beam}=1.645 GeV, θ_{cm} = 90°. The position of the two aluminum windows of the target is marked by the two peaks, with the large peak being the thicker downstream cell window.

COSY 5th order matrix elements do not map the events to their correct vertex z-coordinate. Since the target length used in the cross section calculation is not the surveyed target length, but rather a target length based on software cuts in which the cell windows are excluded, a correction to account for the mis-mapped yield has to be made.

Using the above described method of fitting the cell window intensity distributions, target lengths were calculated for all kinematic settings. Errors in the reconstructed target length are calculated by adding the error in the centroid of the each of the cell window fits in quadrature. A percentage correction was calculated by comparing the reconstructed target lengths to the target lengths obtained from survey of the cold target. The results are listed in Table 5.5. The table shows that there is indeed a disagreement between the physical target length and the software target length for all kinematics, and that the correction is not a constant. In fact, Figure 5.20 shows the dependence of the ratio of the surveyed over reconstructed target length as function

E_{beam} (GeV)	θ_{cm} (nominal)	L_{target} (Survey) (cm)	L_{target} (COSY) (cm)	Correction (%)	
0.845	37°	15.12 ± 0.04	13.57 ± 0.04	11.4 ± 0.4	
	90°	15.12 ± 0.04	13.42 ± 0.03	12.6 ± 0.4	
1.645	37°	15.12 ± 0.04	13.94 ± 0.07	8.5 ± 0.6	
	53°	15.12 ± 0.04	13.77 ± 0.08	9.8 ± 0.7	
	70°	15.12 ± 0.04	13.87 ± 0.07	9.0 ± 0.6	
	90°	15.12 ± 0.04	13.74 ± 0.04	10.0 ± 0.4	
2.445	37°	15.34 ± 0.04	14.61 ± 0.08	5.0 ± 0.6	
	53°	15.34 ± 0.04	14.70 ± 0.15	4.3 ± 1.1	
	70°	15.34 ± 0.04	14.51 ± 0.07	5.7 ± 0.6	
	90°	15.34 ± 0.04	14.23 ± 0.06	7.8 ± 0.6	
3.245	37°	15.34 ± 0.04	14.22 ± 0.13	7.9 ± 1.0	
	53°	15.34 ± 0.04	14.35 ± 0.10	6.9 ± 0.8	
	70°	15.34 ± 0.04	14.43 ± 0.07	6.3 ± 0.6	
	90°	15.34 ± 0.04	14.25 ± 0.04	7.7 ± 0.4	
4.045	37°	15.12 ± 0.04	14.13 ± 0.20	7.0 ± 1.6	
	53°	15.12 ± 0.04	14.10 ± 0.12	7.2 ± 0.9	
	53°	12.48 ± 0.04	11.76 ± 0.10	6.1 ± 1.0	1997 dataset
	70°	15.12 ± 0.04	14.25 ± 0.10	6.1 ± 0.8	
	70°	12.48 ± 0.04	11.66 ± 0.07	7.1 ± 0.7	1997 dataset
	90°	15.12 ± 0.04	14.19 ± 0.07	6.6 ± 0.6	

Table 5.5: Comparison of the target length obtained from survey of the cold target with the target length calculated from the centroids of fits to the target end-cap positions obtained by a software reconstruction with COSY 5th order matrix elements. During the 1997 runs a target with shorter cells was used. The 1996 runs made use of two different nominal 15 cm long empty target cells.

of the central momentum setting of the HMS. The ratio appears to saturate at higher momenta. The cause of this behavior is unknown. The cross section was corrected for the apparent target length reduction on a point-to-point basis. The systematic uncertainty in the correction was taken to be the systematic uncertainty for each setting.

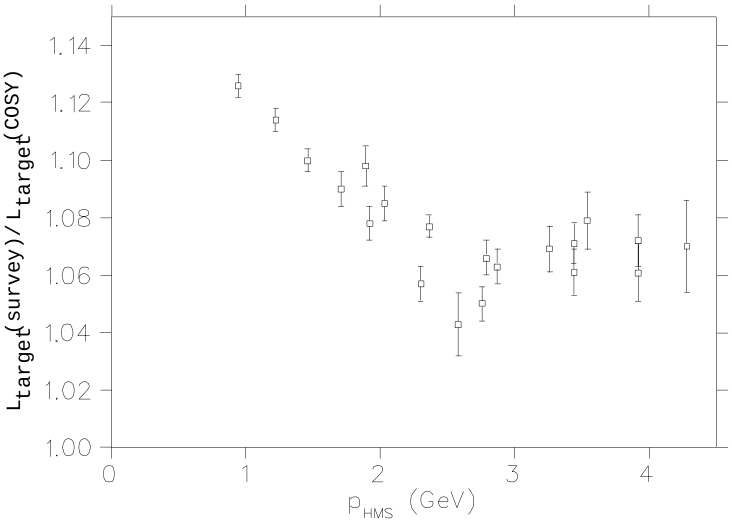

Figure 5.20: Ratio of surveyed over reconstructed target length as function of the HMS central momentum setting.

5.9 HMS Acceptance

For given angle and momentum settings, the HMS can only detect events that fall within a limited range around the central values. Events with parameters close to the limits of the accepted ranges have an increased probability to hit the collimator or magnet walls and scatter, so that they are unable to cause a valid trigger. The acceptance of the spectrometer is defined as the probability that an event coming from vertex (x, y, z) with kinematics given by δ, x', and y' will be detected by the spectrometer. The number of events, created in a process with scattering cross section σ, which are detected by the spectrometer depends on the vertex position and event kinematics:

$$N = \int d\delta dx'dy'dxdydz \cdot \sigma(\delta, x', y', x, y, z) \cdot A_6(\delta, x', y', x, y, z), \tag{5.30}$$

where $A_6(\delta, x', y', x, y, z)$ is the 6-dimensional acceptance function. Because of limited computation time, a high precision calculation of A_6 in all six dimensions is infeasible. Fortunately, for a target that is thin enough that energy loss and multiple scattering are negligible, the cross section becomes independent of the position, and the volume integration can be carried out, leaving a 3-dimensional acceptance function. To further simplify the calculation, a coordinate transformation from the vertex tangents x' and y' to the out-of-plane scattering angles θ and ϕ, is made, where θ is defined by Equation 5.2 and ϕ by the relationship:

$$\tan(\phi) = \frac{-x'}{\sin(\theta_c) - y'\cos(\theta_c)}. \tag{5.31}$$

Equation 5.30 then becomes:

$$N = \int d\delta d\theta d\phi \cdot \sigma(\delta, \theta, \phi) \cdot A_3(\delta, \theta, \phi). \tag{5.32}$$

To model the acceptance function in Equation 5.32 the HMS Monte Carlo model (introduced in Section 4.3.2) is used. Since an extended target is used in this experiment the target length z is also modeled in addition to δ, θ and ϕ. The modeled HMS acceptance in the variables z, δ, θ, and ϕ is shown in Figure 5.21. To determine the proper acceptance, the same cuts applied to the reconstructed data from the experiment, must be used in the Monte Carlo simulation. Figure 5.21 shows that the acceptance is roughly flat over the central region of the reconstructed quantities. Since the range of the reconstructed quantities used in the analysis of the experiment falls within the flat central region of the acceptance for the simulation, the acceptance becomes independent of θ and ϕ within these cuts, and the function can be taken out of the integral in Equation 5.32, giving:

$$N = A \int d\delta d\theta d\phi \cdot \sigma(\delta, \theta, \phi) = A \int d\delta d\theta \cdot \sigma(\delta, \theta), \tag{5.33}$$

where the ϕ integration was carried out because the cross section has no azimuthal dependence. The quantity A now corresponds to the total angular HMS acceptance for the cuts used in the data analysis, and can be interpreted as an effective solid angle. The effective solid angle $\Delta\Omega$ is calculated with the Monte Carlo model, using the correct target configuration and data analysis cuts as input:

$$\Delta\Omega = \frac{N_{pass}}{N_{gen}} \Delta\Omega_0, \tag{5.34}$$

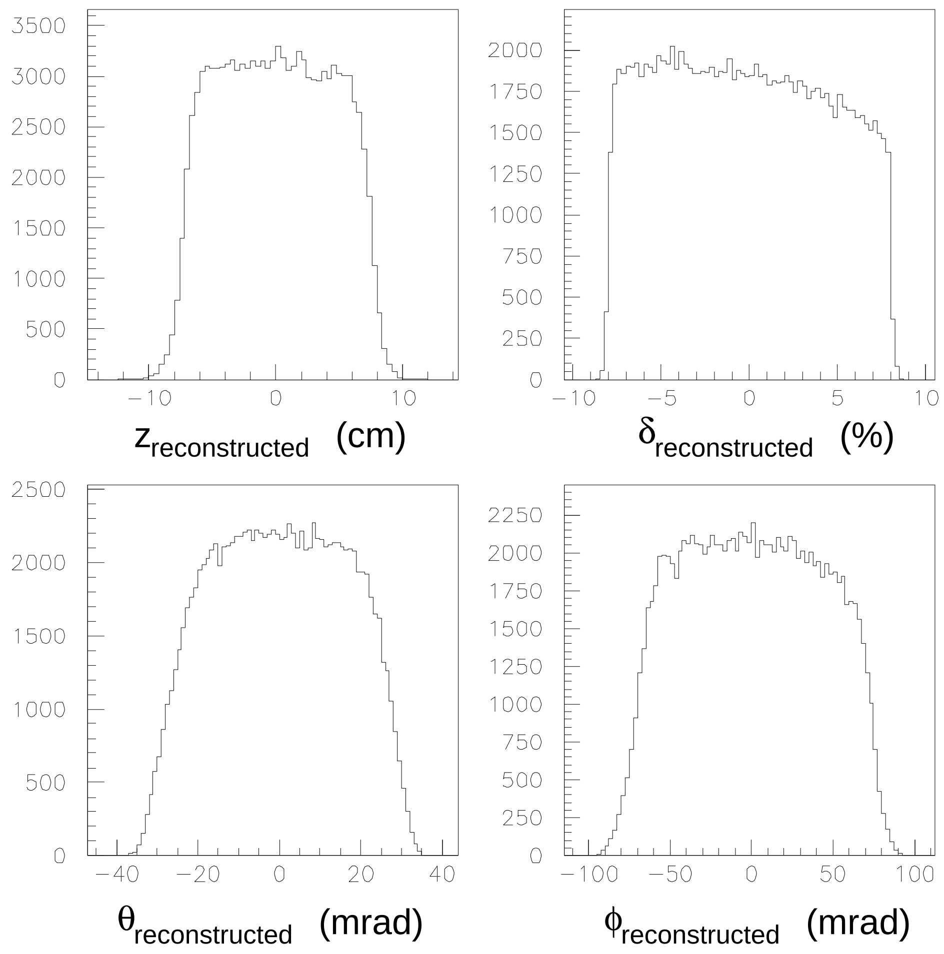

Figure 5.21: Reconstructed quantities z, δ, θ, and ϕ as determined from the HMS Monte Carlo model for a 15 cm target. The simulation was carried out at central momentum p_c=4.244 GeV/c and scattering angle $\theta_{c,lab}$=15.92°.

where N_{gen} is the number of events generated for the simulation, N_{pass} the number of events that made it to the detector stack and were successfully reconstructed to the target passing all cuts, and $\Delta\Omega_0 = \Delta\theta_0\Delta\phi_0$, with $\Delta\theta_0$=$\pm$55 mrad and $\Delta\phi_0$=$\pm$80 mrad, corresponding to the angular cuts used in the data analysis. For all kinematic settings in E89-012, the Monte Carlo was run with 1 million initial events having uniform illumination to calculate the solid angles.

Since the main analysis was carried out assuming that all data had a part that was obscured by the gate valve shutter, the solid angles were calculated for the unobscured half of the acceptance for all kinematics. The results are listed in Table D.1 in Appendix D. For the kinematics that were not influenced by the gate valve the full solid angle was calculated as well, so that the full acceptance cross section could be determined. Values for the full solid angles are listed in Table D.2. The results for the full acceptance are in good agreement with the nominal solid angle of 6.8 msr for HMS an extended target. The solid angles show a slight decrease for increasing angles and y_{tar} cuts, which can be attributed to the gradual increase in target length. Due to the extended length of the target it starts to behave more "unpointlike" at larger lab angles, so that events generated at the extremes of the target have a higher probability of failing to enter the spectrometer. Both the full solid angles and half-solid angle have a 0.5% statistical uncertainty. The systematic uncertainty was taken to be equal to this statistical uncertainty. The systematic uncertainty in the solid angle due to modeling the HMS with the COSY matrix element set, which is not ideal, is included in the systematic uncertainty in the reconstruction.

5.10 Reconstruction Uncertainties

The data analysis of most of the experiments performed in CEBAF Hall C, is carried out using fitted matrix elements (see Section 4.2) for the reconstruction. Fitted matrix elements are calculated to provide a better quality reconstruction of the angles at the target and at the edges of the acceptance. They are also used because the reconstruction using COSY matrix elements gives the wrong magnification.

Initially E89-012 data was analyzed with a set of 5th order fitted matrix elements, which were determined from calibration data taken before and immediately after the experiment. The E_γ spectra that are calculated from this analysis show an unusual shape of the photoproton distribution at the endpoint energy, and above. Towards higher beam energies and more forward angles, the observed effect becomes stronger, and at E_{beam}=4.045 GeV, θ_{cm}=37° an endpoint cannot be discerned. For comparison the same data were analyzed with COSY 5th order calculated matrix elements. The E_γ was calculated from the reconstructed quantities obtained with both sets of matrix elements, and histogrammed in the customary way. Figure 5.22.a(b) shows the histogram obtained using 5th order fitted (5th order COSY) matrix elements. An endpoint at the correct beam energy is only observed in the spectrum obtained with the COSY analysis. A miscalculation of energy loss causing the spread was singled out, and the effect was attributed to using the reconstructed quantities calculated with the fitted matrix elements.

Another illustration of the difference in reconstruction at the edges of the acceptance for 5th order fitted and COSY matrix elements is shown in Figure 5.23. The figure shows events projected forward from the target vertex to the plane of the collimator for the same kinematic setting as in Figure 5.22. The left figure shows the distribution that is obtained using 5th order fitted matrix elements for the reconstruction, and figure on the right the distribution for the same number of events, now reconstructed using COSY. The difference at the edge of the acceptance (which in fact falls outside the actual collimated acceptance) is evident. In the COSY analysis the events that are located outside the collimated acceptance are identified as accidental background (see Section 5.7.2). Unlike the COSY matrix elements, which can be calculated outside the acceptance, the fitted matrix elements are determined from experimental data and consequently cannot be fit for target quantities outside of the acceptance. For target quantities outside the acceptance the fitted matrix elements make use of an extrapolation instead. Since the total number of events is the

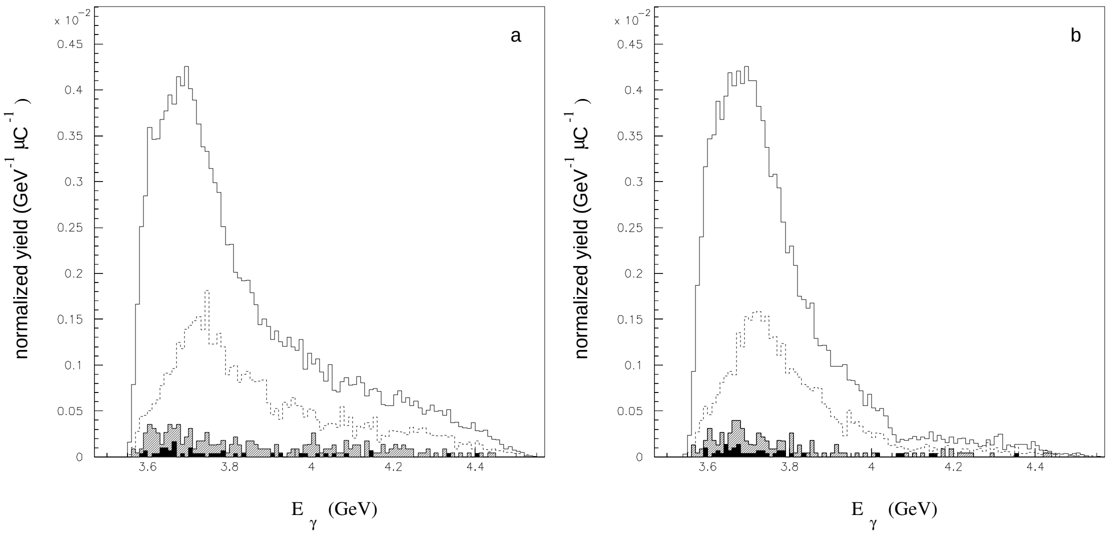

Figure 5.22: Photoproton distributions for E_{beam}=4.045 GeV, θ_{cm}=37°, where E_γ is calculated using reconstructed quantities obtained with 5th order fitted and 5th order calculated COSY matrix elements. Figure (a) shows the distribution obtained using the fitted matrix elements. Figure (b) shows the distribution for the same number of events, obtained using the COSY matrix elements. In both figures spectra are normalized to the integrated charge and corrected for dead time and tracking efficiency. Shown are the measurements for LD_2^{IN}(solid line), LD_2^{OUT}(dashed line), MT^{IN}(cross hatched), and MT^{OUT}(solid black).

same for both analyses shown in Figure 5.23 it appears that the extrapolation of the 5th order fitted matrix elements "squeezes" background events into the collimated acceptance. This mechanism accounts for the unusual large background above the endpoint observed in Figure 5.22.(a) .

Since the 5th order fitted matrix elements did not provide a reliable E_γ reconstruction, COSY matrix elements were considered as an alternative. It was realized that it is of no concern in this experiment that COSY calculates the wrong magnification, since the full acceptance of the spectrometer is used, thereby canceling the contribution of the magnification [110], except for the target length (see Section 5.8.2). It was also noted that COSY does have a coarser delta resolution in focal plane (see Figure 5.24), but no noticeable effect on the E89-012 data analysis due to the increased

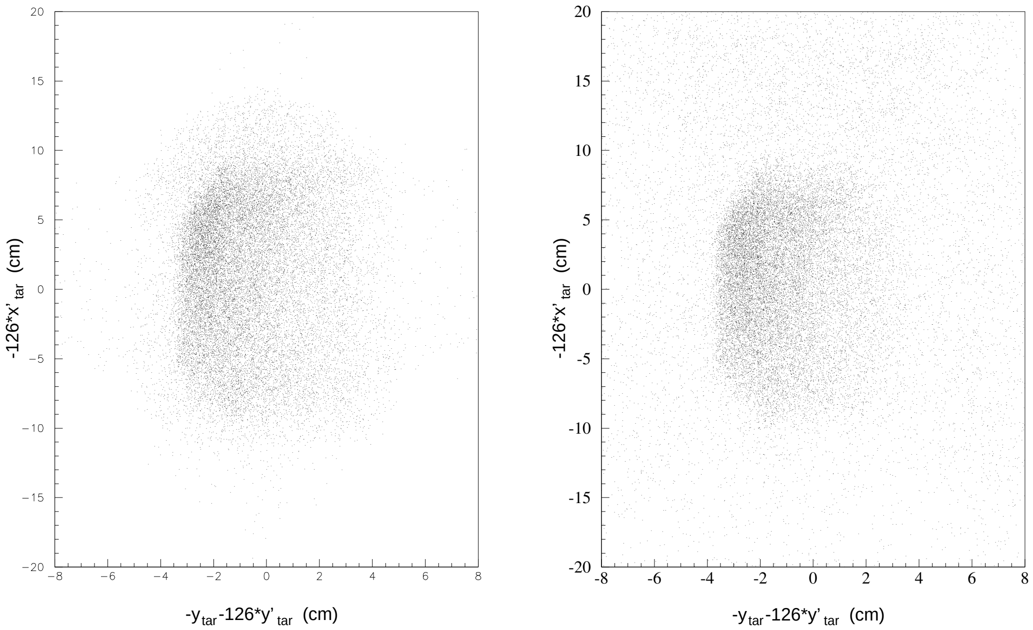

Figure 5.23: Proton events projected from the target vertex to the plane of the HMS collimator for E_{beam}=4.045 GeV, θ_{cm}=37°, as seen looking from the target to the spectrometer. The left figure shows the event distribution obtained when 5th order fitted matrix elements are used for the reconstruction. The right figure shows the distribution, obtained with COSY 5th order matrix elements, for the same number of events. The fitted matrix elements appear to "squeeze" background events into the acceptance.

delta resolution was observed. Therefore COSY seemed a viable alternative and the analysis was carried out with 5th order COSY matrix elements.

The COSY matrix elements still represent an approximation of the true spectrometer optics, and an estimate must be made of the systematic uncertainty incurred by their use. At the large angle and low energy kinematic settings where the fitted matrix elements provide a discernible endpoint, yields obtained from E_γ spectra were compared. A comparison between yields from the 5th order fitted, an older less accurate 4th order fitted, and the 5th order COSY matrix elements set was made for θ_{cm}=90° and 53° at E_{beam} = 1.645 GeV. On average a difference of 3.5% was found between yields obtained with the fitted sets on the one hand, and COSY on the other hand. The systematic uncertainty in the reconstruction and acceptance because of

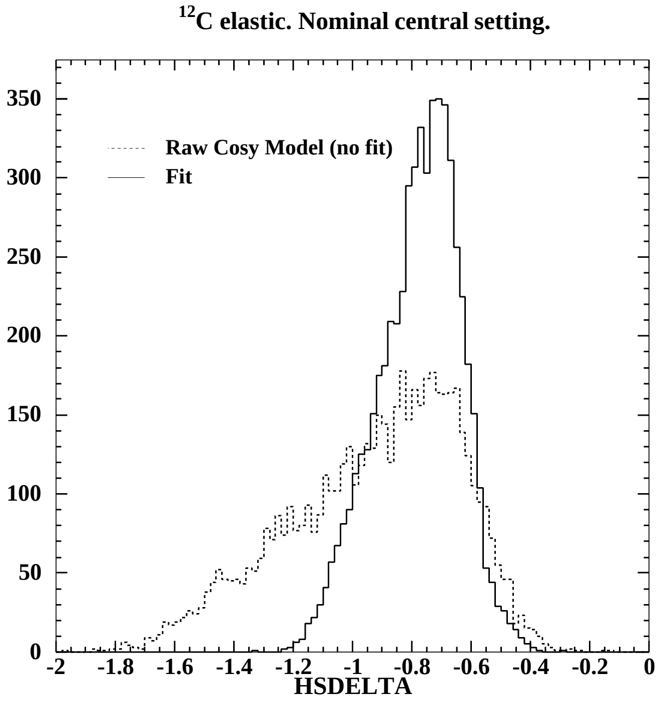

Figure 5.24: Reconstructed HMS spectrometer momentum (expressed as δ) for ^{12}C at the nominal momentum setting. The solid line shows the δ resolution obtained with 5th order fitted matrix elements. The dashed line corresponds to an analysis using 5th order COSY calculated matrix elements. In the COSY case the resolution is about a factor 2 larger. Figure courtesy of G. Niculescu.

the use of COSY is estimated at 4.6%. This estimate includes a 3% uncertainty in the solid angle calculation due to modeling the HMS Monte Carlo with the non-ideal COSY matrix elements, which was added in quadrature with the 3.5% reconstruction uncertainty.

5.11 Systematic Uncertainties

In addition to the statistical uncertainty in the cross section result, which is inherent to any measurement involving nuclear reactions and decay processes, the accuracy of the measured cross section is limited by systematic uncertainties as well. Systematic uncertainties can arise because of the limited knowledge of the experimental equipment, inaccuracies of calibration procedures and the inefficiencies of calculations and algorithms used for the analysis as described in preceding sections. The systematic uncertainties can be loosely grouped into two categories, point-to-point uncertainties and global uncertainties. Point-to-point uncertainties may vary for each run or kinematic setting, global uncertainties apply equally to all data points. A summary of the systematic uncertainties in the half-acceptance and full-acceptance cross sections is given in Table 5.6 The last column of Table 5.6 specifies which of the four quantities

	Global Uncertainty	Point-to-Point Uncertainty	Quantity affected
Beam Current	1.4%		Q
Bremsstrahlung formulae	3.0%		N_γ
Beam Energy	0.2%	0.2–2.1%	N_γ
Radiator Thickness	0.1%		N_γ
Radiator-Out Correction		1.0%	Y
Proton Absorption*	2.0%		Y
Tracking Efficiency*	3.4%		Y
Particle ID (TOF)		1–2.6%	Y
Dead Time correction	<0.1%		Y
Target length (y_{tar}) cuts		1.5%	n_{nucl}
Target length (reconstruction)*		0.4–1.6%	n_{nucl}
Target density	$< 0.5\%$		n_{nucl}
Reconstruction/Acceptance	4.6%		$Y, \Delta\Omega$
Solid Angle (calculation)	0.5%		$\Delta\Omega$
Valve Cut		3%	Y
Inscattering Correction*	0.5%		Y
Background Subtraction*		0.01–4%	Y

Table 5.6: Summary of systematic uncertainties. Entries marked with a '*' are items where a correction is made to the yield, with the uncertainty of the correction as listed in the table. Note that the valve cut uncertainty applies to half-acceptance cross sections only.

that make up the cross section is affected by the particular systematic error. In the paragraphs that follow, systematic errors that affect the same quantity are roughly discussed together.

The thick-target bremsstrahlung formulae have an expected accuracy of 3% [84], and give rise to the largest contribution to the uncertainty in the photon fluxes. Consequently, the radiator out correction function $f(E_\gamma)$, which is calculated using the same formulae, is also known to 3%. However, the effect of the accuracy of $f(E_\gamma)$ on the net yield is reduced to an uncertainty of the order of 1%, since the radiator-out yield is roughly one third of the photodisintegration yield. The copper radiator foils have thicknesses which were determined to better than 0.1% [42]. The small uncertainty in the foil-thickness has a minimal contribution to the error in the calculated bremsstrahlung flux.

The uncertainty in the electron beam energy gives rise to another contribution to the error in the photon flux, which is strongly dependent on the absolute beam energy. The electron beam energy is measured using the Hall C arc, and is known to 0.2% [77]. The error in the photon flux, due to the uncertainty in the beam energy is estimated by comparing the photon yield at the same nominal beam energies, where the integration interval is shifted in accordance with the beam energy error. A change in the photon flux of 0.2–2.1% was observed, dependent on the beam energy and the width of the integration interval. The error in the beam energy also determines the accuracy of the HMS momentum and thereby the reconstructed photon energy as well as that of the Jacobian which also has a momentum dependence. The extent of this effect will be discussed at the end of this section.

Of the corrections to the extracted yield, the contributions to the systematic error arising from the tracking efficiency correction are dominant. The largest contribution is due to the efficiency of the tracking algorithm. A comparison of endpoint yields generated with the 4-out-of-6 planes tracking algorithm, which was used in the analysis, with yields generated using the 5-out-of-6 planes tracking algorithm shows that they agree to 3.3%. A second smaller contribution arises from the tracking efficiency variation over the fiducial area size, which is of the order of 1% for fiducial areas adjacent to the fiducial area chosen in the tracking efficiency analysis for this experiment.

These contributions are added in quadrature to obtain the total systematic error due to particle tracking, which is 3.4%.

The integrated charge used for the yield-normalization has an absolute uncertainty 1.4% based on the electron beam current calibrations [82]. The absorption of protons traveling from the vertex to the detector stack is calculated using the materials in the path of the photoproton, and the associated uncertainty is based on the measured uncertainty of a proton absorption experiment with a comparable experimental set-up [105]. The systematic error in the absorption correction is 2%. The correction for computer dead time is calculated using the ratio of scalar trigger quantities and is assumed to be exact, so no systematic error was assigned. The electronic dead time correction is less than 0.1% for most kinematics, and the associated statistical error much less, hence the estimated systematic error in the total dead time correction is $<$0.1%. The trigger efficiency for the HMS hodoscopes was determined to be larger than $>$99.2%($>$99.5%) for triggers generated with 4/4 (3/4) hodoscope planes. The correction to the data is small compared to the other corrections, and the uncertainty in the cross section due to the trigger efficiency was assumed to be negligible.

The error in the time-of-flight particle identification is estimated from variations in measured yields extracted with different mass-squared cuts. For the data taken at beam energies 0.845–2.445 GeV, the uncertainty is estimated at $<$1%, for the data at E_{beam}=3.245 GeV the systematic error is 1.3% and at 4.045 GeV the contribution to the systematic error in the cross section is 2.6%. Accidental background events that were not removed from the acceptance by time-of-flight PID, reconstructed target length cuts and acceptance cuts, were subtracted using the flat-background subtraction scheme discussed in Section 5.7.2. The estimated systematic error in this method varies from 0.01–4%, with the smallest errors at the low momentum, large angle kinematics.

The uncertainty in the target thickness has contributions from the target density, target purity and reconstructed target length. Target density and purity have a combined 0.5% systematic uncertainty associated with them, as discussed in Section 3.4.

The physical target length used in the analysis is obtained by placing software cuts on the reconstructed target length. The cuts eliminate background from the upstream and downstream target cell windows as well as accidental background from outside the target volume. Variations in the measured yield with different cuts on the reconstructed target length, generate an estimated 1.5% systematic error in this method.

The use of COSY matrix elements in the event-reconstruction and modeling causes the largest contribution to the systematic uncertainty of the cross section. Three separate contributions can be identified. The correction to the measured target length because of reconstruction vertex mismapping described in Section 5.8.2 has a systematic uncertainty that varies from $0.4-1.6\%$, dependent on the kinematic setting. The largest systematic error is attributed to the reconstruction and acceptance modeling with COSY matrix elements. Based on a comparison of yields from analyses using fitted 4th and 5th order matrix element sets, with yields from the analysis with the 5th order COSY matrix elements a reconstruction uncertainty of 3.5% was found. When this uncertainty is added in quadrature with an estimated 3% systematic error in the solid angle due to modeling the HMS Monte Carlo with COSY, a total uncertainty of 4.6% for reconstruction/acceptance is found. A separate 0.5% systematic error in the solid angle is assigned due to inaccuracy of the actual solid angle calculation with the Monte Carlo.

The presence of the HMS gate valve in the acceptance of the spectrometer contributes to the systematic error in the half-acceptance cross sections at a noticeable level. A 3% error was assigned to placement of the valve cut, which separates the uncorrupted data from the full data set, as described in Section 5.6.2. The correction for the events passing through the gate valve shutter and scattering into the good part of the acceptance (the "inscattering correction") was calculated with a dedicated HMS Monte Carlo model and has an estimated accuracy of 0.5%.

The above discussed systematic errors are added in quadrature to estimate the total systematic error in the laboratory cross section, $d\sigma/d\Omega_{lab}$. The errors propagate linearly to the center-of-mass cross section $d\sigma/d\Omega_{cm}$ and invariant cross section $d\sigma/dt$. The latter two cross sections pick up an extra error due to the uncertainty in the boost parameters, the mean photon energy and scattering angle, where the main photon energy depends on both the scattering angle and the proton momentum. With the HMS momentum and scattering angle calibrated to 0.1% and 0.8 mrad respectively, the mean photon energy varies from 1.2 MeV to 8.7 MeV ($\sim 0.2\%$) over the the measured range of kinematics. The Jacobian for the transformation from the laboratory frame to the center-of-mass frame has an uncertainty <0.1%, whereas the transformation to the invariant cross section contributes a 0.3–0.4% systematic error to the cross section. The quantity $s^{11}d\sigma/dt$ has a 0.5–1.8% systematic uncertainty in addition to the systematic uncertainty in the laboratory cross section, due to a combination of the errors in the two boosts and the error in s which depends on the mean photon energy.

The center-of-mass cross sections calculated with the half-acceptance analysis, along with the statistical and systematic errors are listed in Table 5.7. The overall systematic error obtained by adding all contributions in quadrature varies between 8–10% dependent on the kinematic setting. The results for settings where a full-acceptance analysis was allowed, are listed in Table 5.8.

E_{beam} (GeV)	$\bar{E}_\gamma$ (GeV)	s (GeV^2)	θ_{cm}	$d\Omega_{cm}/dt$ ($\mathrm{nb/GeV}^2$)	$d\sigma/d\Omega_{cm}$ (nb/sr)
0.845	0.792	6.489	36.17°	6.26	177.9 ± 2.9 ± 15.6
	0.745	6.313	88.68°	6.77	221.8 ± 4.1 ± 19.5
	0.794	6.496	89.46°	6.24	147.0 ± 5.7 ± 12.9
1.645	1.592	9.490	35.82°	2.65	10.19 ± 0.23 ± 0.90
	1.587	9.471	51.90°	2.66	4.72 ± 0.23 ± 0.41
	1.579	9.441	68.87°	2.68	3.42 ± 0.16 ± 0.30
	1.563	9.379	88.97°	2.71	3.54 ± 0.08 ± 0.31
2.445	2.392	12.49	35.57°	1.65	1.27 ± 0.04 ± 0.11
	2.387	12.47	51.64°	1.66	0.482 ± 0.023 ± 0.043
	2.379	12.44	68.80°	1.66	0.332 ± 0.016 ± 0.029
	2.363	12.38	88.83°	1.68	0.222 ± 0.011 ± 0.019
3.245	3.192	15.49	35.46°	1.19	0.213 ± 0.018 ± 0.019
	3.187	15.47	51.64°	1.20	0.106 ± 0.005 ± 0.009
	3.179	15.44	68.68°	1.20	0.0407 ± 0.0028 ± 0.0036
	3.163	15.38	88.79°	1.21	0.0282 ± 0.0020 ± 0.0025
4.045	3.992	18.49	35.40°	0.93	0.0665 ± 0.0065 ± 0.0062
	3.987	18.47	51.50°	0.93	0.0212 ± 0.0027 ± 0.0020
	3.987	18.47	51.50°†	0.93	0.0236 ± 0.0018 ± 0.0022
	3.979	18.44	68.70°	0.94	0.00500 ± 0.00120 ± 0.00050
	3.979	18.44	68.70°†	0.94	0.00746 ± 0.00123 ± 0.00070
	3.963	18.38	88.77°	0.94	0.00573 ± 0.00090 ± 0.00055

Table 5.7: Center-of-mass cross sections for two-body deuteron photodisintegration, $\gamma d \rightarrow pn$, along with statistical and systematic errors. The cross sections are calculated using the half-acceptance analysis, where the valve cut is applied. Kinematics labeled with † were measured in 1997.

E_{beam} (GeV)	$\bar{E}_\gamma$ (GeV)	s (GeV^2)	θ_{cm}	$d\Omega_{cm}/dt$ (nb/GeV^2)	$d\sigma/d\Omega_{cm}$ (nb/sr)
2.445	2.392	12.49	37.08°	1.65	1.161 $\pm$ 0.031 $\pm$ 0.096
	2.387	12.47	53.05°	1.66	0.487 $\pm$ 0.017 $\pm$ 0.040
	2.379	12.44	70.07°	1.66	0.342 $\pm$ 0.011 $\pm$ 0.028
4.045	3.987	18.47	53.15°†	0.93	0.0233 $\pm$ 0.0013 $\pm$ 0.0020
	3.979	18.44	70.17°†	0.94	0.00887 $\pm$ 0.00093 $\pm$ 0.00071

Table 5.8: Center-of-mass cross sections for two-body deuteron photodisintegration, $\gamma d \to pn$, along with statistical and systematic errors. Results are shown for kinematics not affected by the gate valve, where a full-acceptance analysis is allowed. Kinematics labeled with † were measured in 1997.

Chapter 6

Results and Discussion

In this chapter the measured cross sections for the two-body deuteron photodisintegration reaction are presented. The energy and angular dependence of the new cross sections in combination with existing data are discussed in relation to the QCD- and conventional hadronic nuclear physics inspired models reviewed in Chapter 2.

6.1 Results

CEBAF experiment E89-012 was the third generation intermediate energy deuteron photodisintegration experiment, extending the data for the reaction $\gamma d \rightarrow pn$ at forward angles up to a photon energy of 4.0 GeV. With the data from this experiment the world's data on the forward $\gamma d \rightarrow pn$ reaction is almost doubled, as shown in the overview of kinematic settings presented in Figure 6.1. The previous experiments at SLAC (NE8 and NE17) [10, 11] provided the foundation for this experiment and their results, as well as results at lower energy, will be included in the theoretical discussion as they are important to understand the full energy and angular behavior of the $\gamma d \rightarrow pn$ cross section.

A table of the measured center-of-mass cross sections and their statistical and systematic errors was already presented at the end of Chapter 5. Inspection of the cross sections and their errors shows that for most settings statistical errors were obtained that are in good agreement with or better than the initial estimated statistical errors listed in Table 3.1, despite the fact that for all settings half of the data had to be

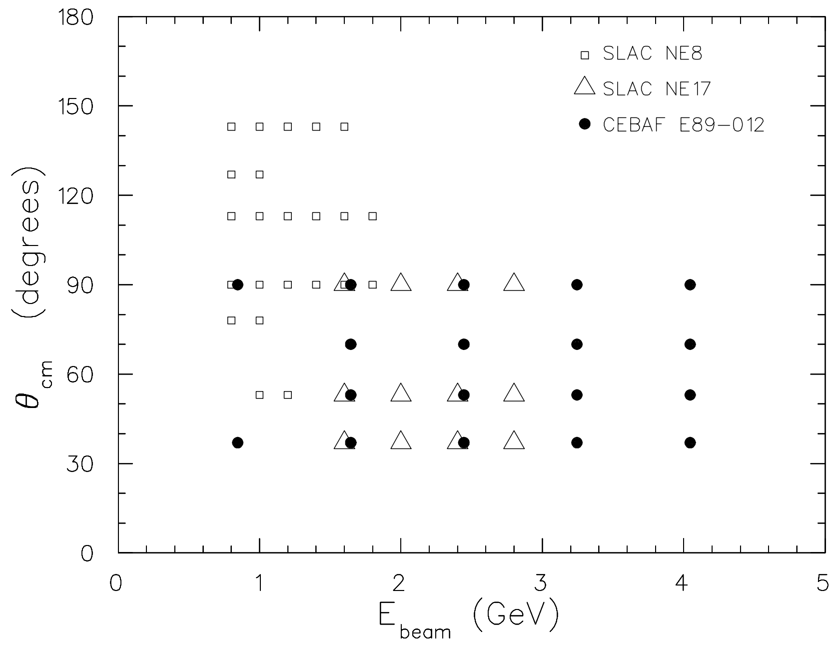

Figure 6.1: Kinematic coverage of intermediate energy $\gamma d \to pn$ experiments.

disregarded due to the gate valve acceptance problem which was not anticipated. In addition, the systematic error ranges from 8–10%, which includes contributions due to the gate valve modeling.

The energy dependence of the new center-of-mass cross sections is shown in Figure 6.2 for 90° and 70° and Figure 6.3 for 53° and 37°. It should be noted that here, and in the remainder of this chapter, references to the data will be made with the nominal angle settings, even though the actual center-of-mass angles for the different energy data points at each nominal angle setting vary, as listed in Table 6.1. In this table other kinematic quantities are listed as well, which are of importance when the data are compared with the theoretical models, in particular when the range of validity of a model is compared with the experimental data. In addition to the data measured here, the figures also show previous data from Dougan, *et al.* [36], Ching and Schaerf [37], Arend, *et al.* [39], and the SLAC experiments NE8 [10] and NE17 [11]. The curves are theoretical predictions, which are discussed in Section 6.2. The figures show that the new data are in reasonable agreement with the existing data, where overlap occurs, but a better comparison can be made when the data are plotted in terms of the scaled invariant cross section, $s^{11} d\sigma/dt$, which "eliminates" the many decades of s dependence from the data, and enables a comparison of the data on a linear scale over a large energy range.

θ_{cm} (nominal)	$\bar{E}_\gamma$ (GeV)	θ_{cm}	s (GeV^2)	t (GeV^2)	p_T^2 ((GeV/c)^2)	t_p (GeV^2)	t_n (GeV^2)
37°	0.792	36.17°	6.49	+0.21	0.26	−1.15	−0.33
	1.592	35.82°	9.49	−0.19	0.51	−2.46	−0.53
	2.392	35.57°	12.49	−0.51	0.76	−3.80	−0.69
	3.192	35.46°	15.49	−0.82	1.01	−5.15	−0.85
	3.992	35.40°	18.49	−1.12	1.26	−6.50	−0.99
53°	1.587	51.90°	9.47	−0.64	0.92	−2.22	−0.76
	2.387	51.64°	12.47	−1.24	1.38	−3.42	−1.06
	3.187	51.64°	15.47	−1.84	1.84	−4.63	−1.36
	3.987	51.50°	18.47	−2.41	2.29	−5.84	−1.64
70°	1.579	68.87°	9.44	−1.24	1.29	−1.90	−1.06
	2.379	68.80°	12.44	−2.22	1.94	−2.92	−1.55
	3.179	68.68°	15.44	−3.18	2.59	−3.94	−2.03
	3.979	68.70°	18.44	−4.14	3.24	−4.96	−2.51
90°	0.745	88.68°	6.313	−0.50	0.70	−0.71	−0.70
	0.794	89.46°	6.496	−0.60	0.75	−0.75	−0.74
	1.563	88.97°	9.38	−2.01	1.47	−1.49	−1.44
	2.363	88.83°	12.38	−3.74	2.22	−2.26	−2.18
	3.163	88.79°	15.38	−4.94	2.97	−3.02	−2.91
	3.963	88.77°	18.38	−6.41	3.71	−3.79	−3.65

Table 6.1: Kinematic settings corresponding to the experimental data points. Listed are the mean photon energy, $\bar{E}_\gamma$, the true center-of-mass scattering angle, θ_{cm}, Mandelstam s and t for the reaction $\gamma d \to pn$, the square of the transverse proton momentum, p_T^2, and t_p and t_n, the momentum transfer to the proton and neutron respectively.

Figures 6.4–6.7 show the invariant cross sections for the center of mass angles 90°, 70°, 53°, and 37°, respectively. For the E89-012 data points both statistical errors are shown (indicated by the error bar caps), and full error bars, which represent the statistical and systematic errors added in quadrature. At kinematics where two

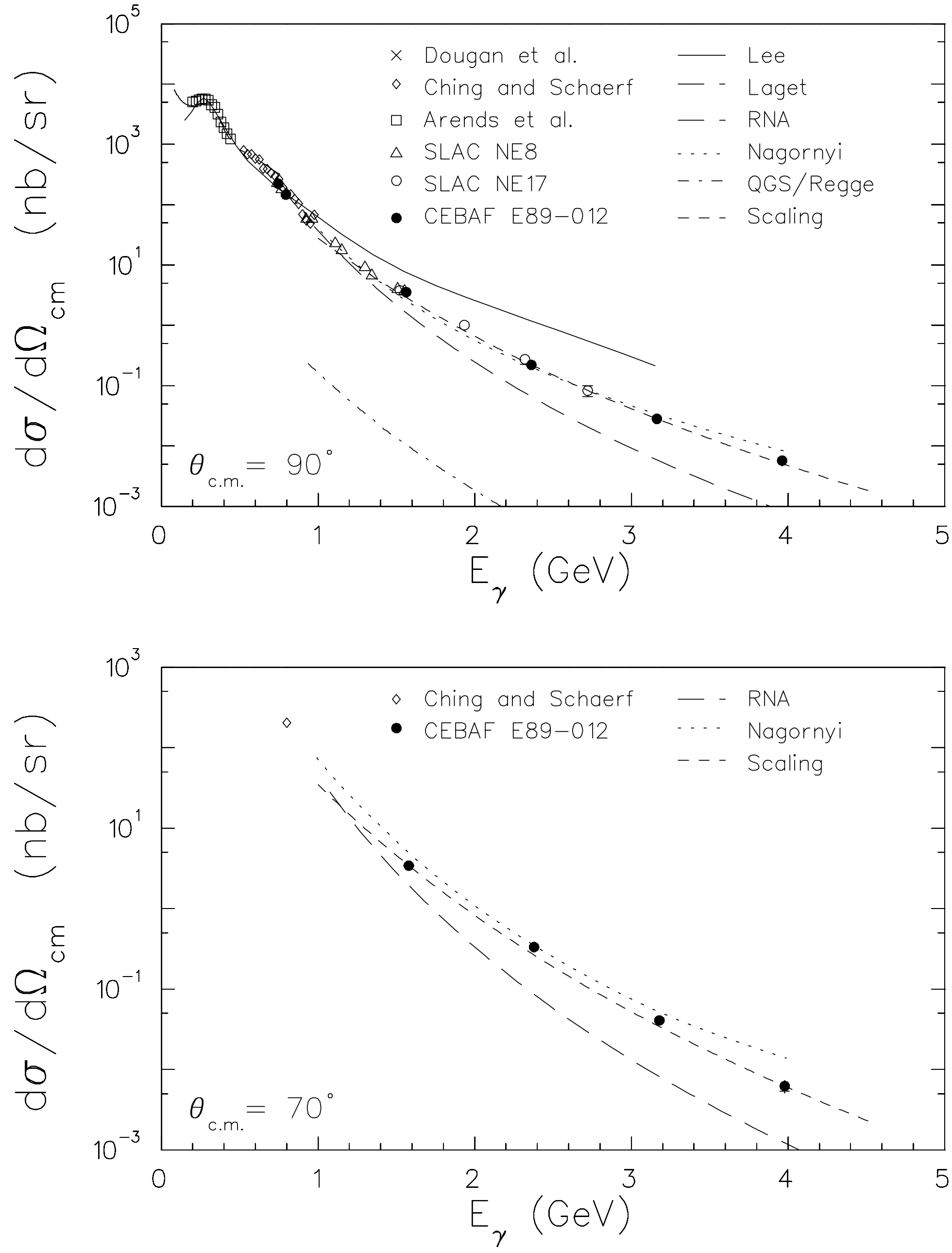

Figure 6.2: Energy dependence of the center-of-mass cross section measured at nominal angles 90°(top) and 70°(bottom). Note that the true angle range is 88.68–89-46° for the E89-012 90° data and 68.68–68.87° for the E89-012 70° data. Data from previous experiments [10,11,36,37,39] are also included. The curves represent the theoretical predictions of [21,24,26,27,28,71].

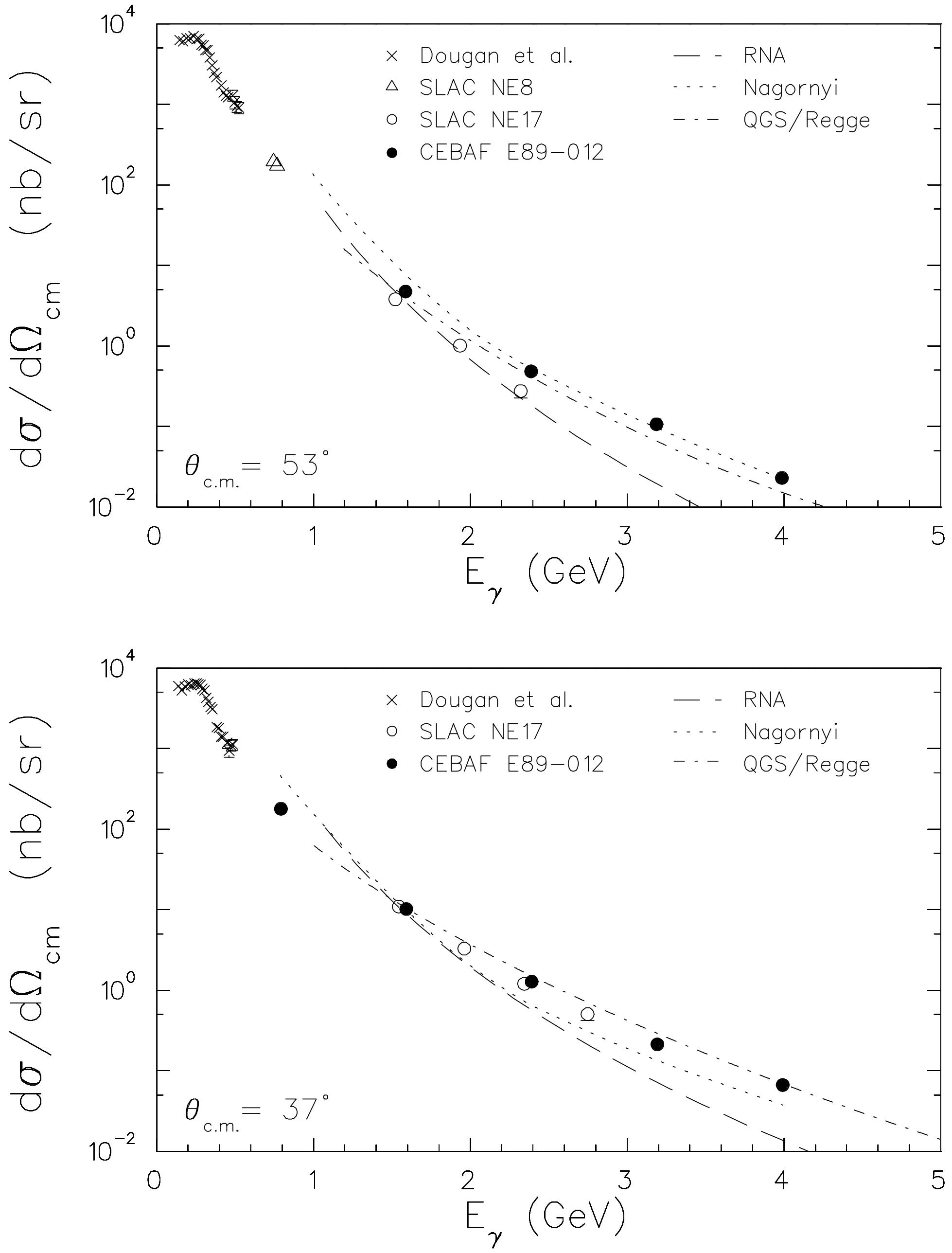

Figure 6.3: Energy dependence of the center-of-mass cross section measured at nominal angles 53°(top) and 37°(bottom). Note that the true angle range is 51.50–51.90° for the E89-012 53° data and 35.40–36.17° for the E89-012 37° data. Data from previous experiments [10,11,36] are also included. The curves represent the theoretical predictions of References [21,26,71].

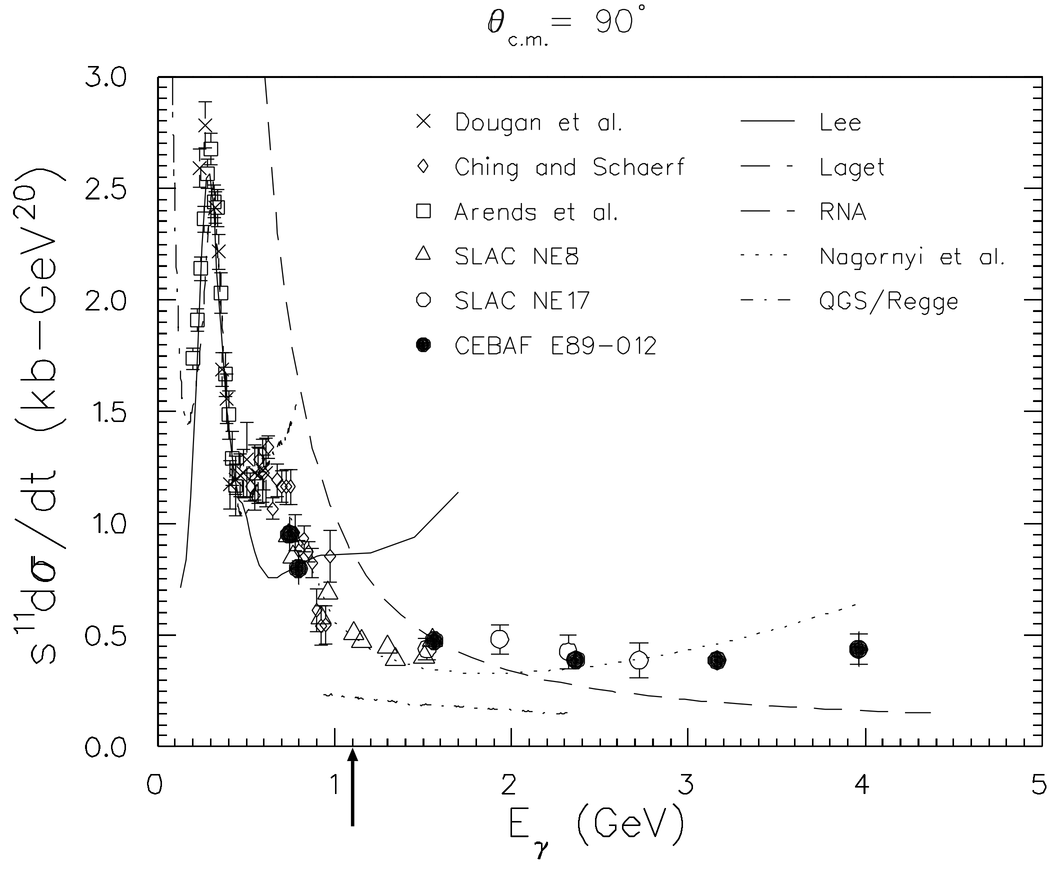

Figure 6.4: Energy dependence of the scaled invariant cross section $s^{11}d\sigma/dt$ for $\theta_{cm} = 90°$. Note that the true angle range is 88.68–89-46° for the E89-012 90° data. The curves represent theoretical predictions of References [21,24,26,27,28,71]. The solid arrow corresponds to the photon energy where the transverse proton momentum, $p_T^2 = 1$ (GeV/c)^2.

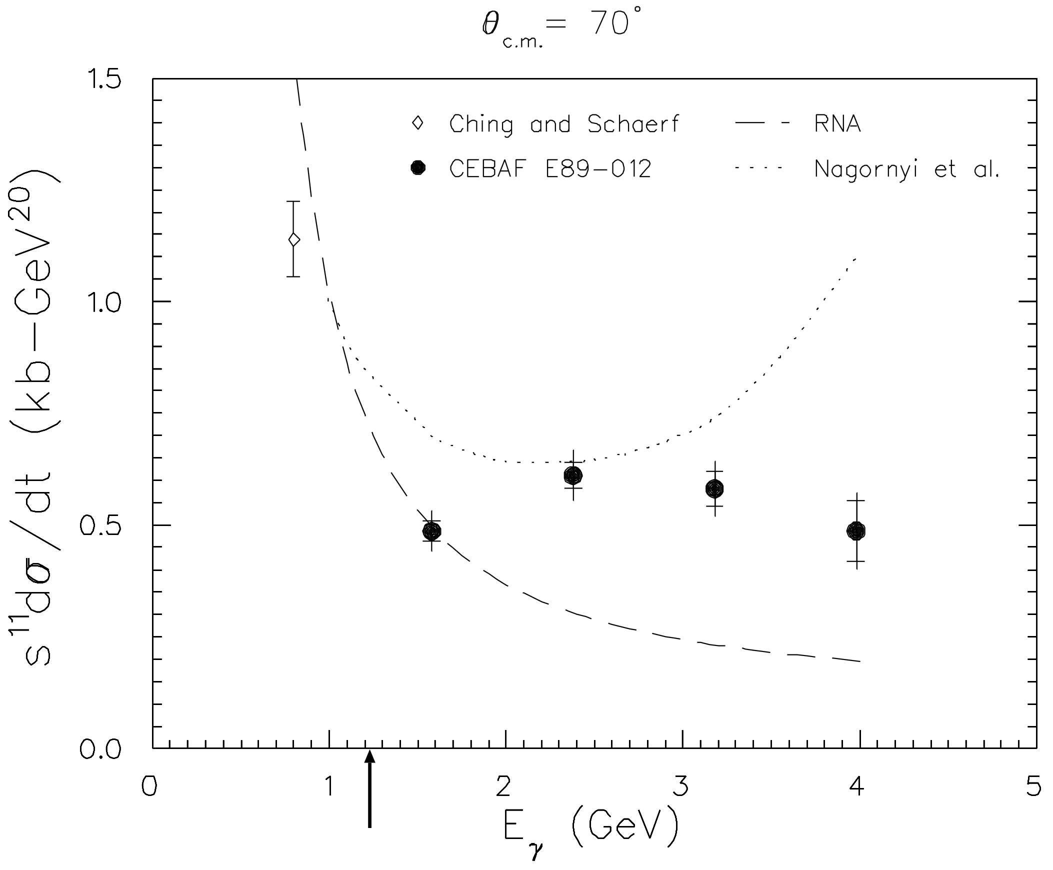

Figure 6.5: Energy dependence of the scaled invariant cross section $s^{11}d\sigma/dt$ for $\theta_{cm} = 70°$. Note that the true angle range is 68.68–68.87° for the E89-012 70° data. The curves represent theoretical predictions of [21,71]. The solid arrow corresponds to the photon energy where the transverse proton momentum, $p_T^2 = 1$ (GeV/c)^2.

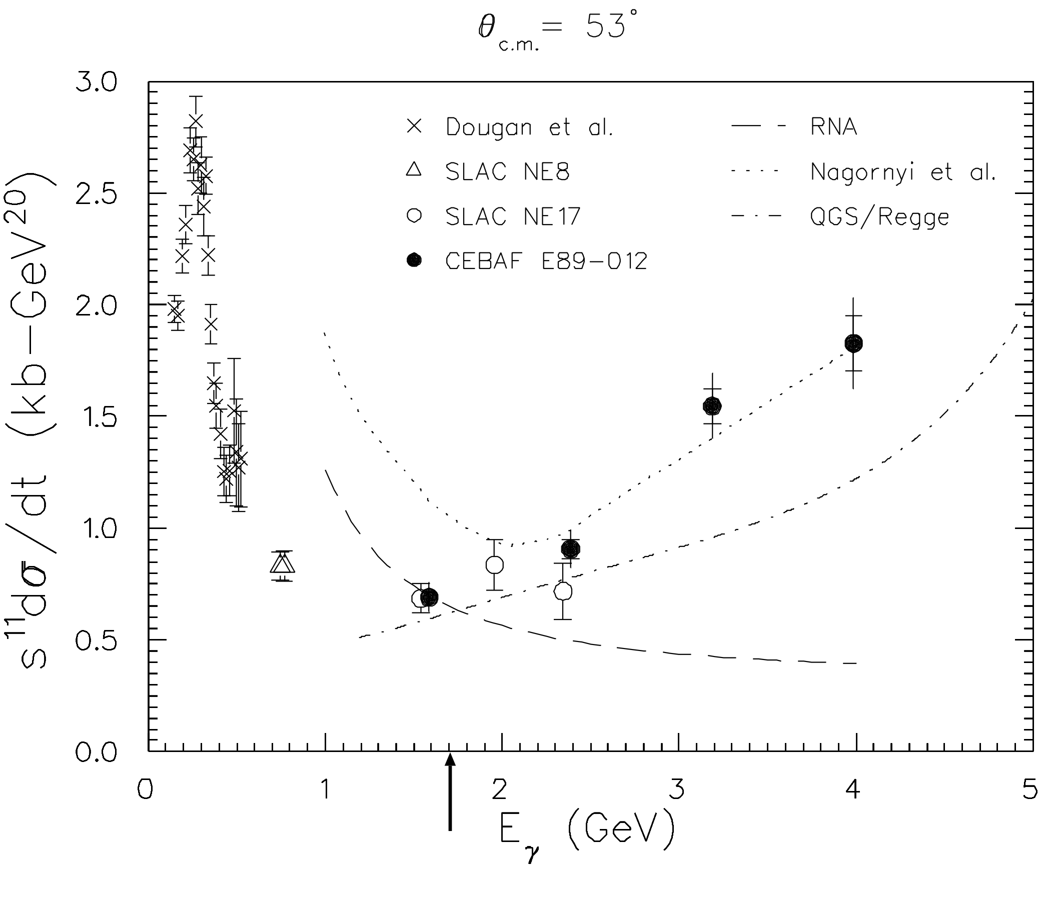

Figure 6.6: Energy dependence of the scaled invariant cross section $s^{11}d\sigma/dt$ for $\theta_{cm} = 53^\circ$. Note that the true angle range is 51.50–51.90° for the E89-012 53° data. The curves represent theoretical predictions of [21,26,71]. The solid arrow corresponds to the photon energy where the transverse proton momentum, $p_T^2 = 1$ (GeV/c)^2.

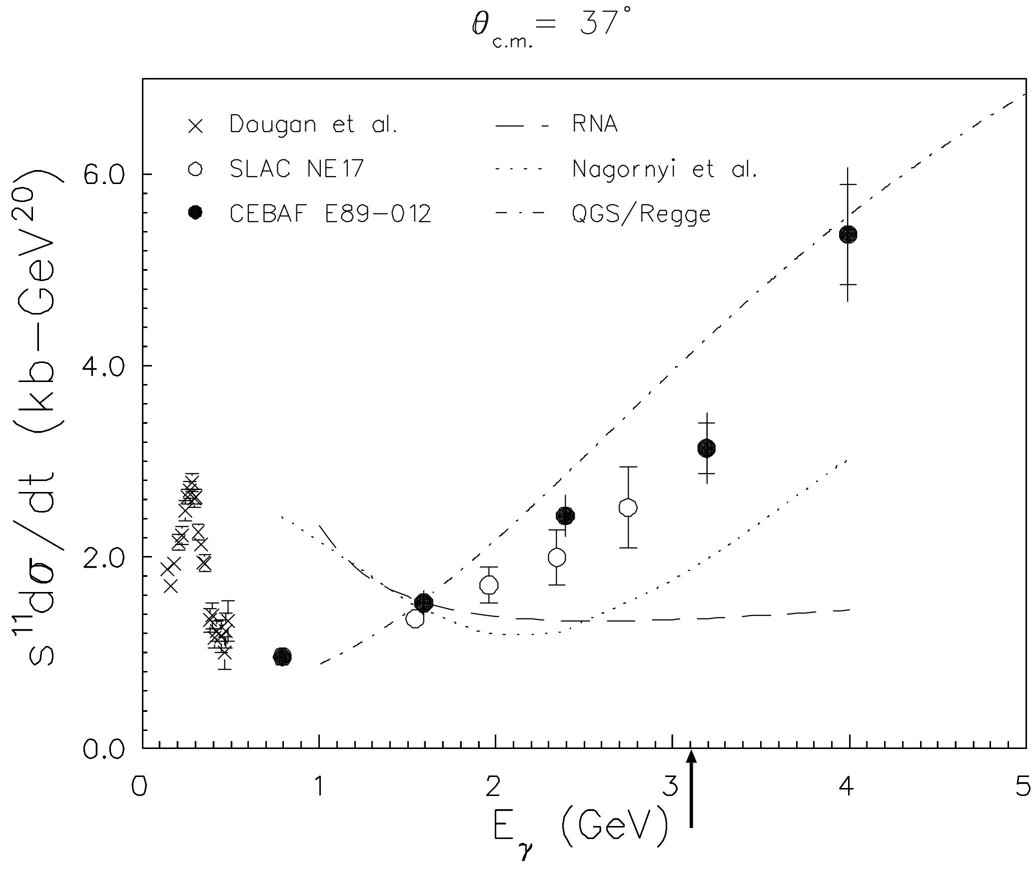

Figure 6.7: Energy dependence of the scaled invariant cross section $s^{11}d\sigma/dt$ for $\theta_{cm} = 37°$. Note that the true angle range is 35.40–36.17° for the E89-012 37° data. The curves represent theoretical predictions of [21,26,71]. The solid arrow corresponds to the photon energy where the transverse proton momentum, $p_T^2 = 1$ (GeV/c)^2.

different data sets exist, namely 53° and 70° for $E_{beam} = 4.045$ GeV, the cross section which is plotted is the weighted mean of the cross sections of the 1996 and 1997 runs, where the statistical errors were used as weights. The statistical error in the weighted cross section is the error in the weighted mean. For a determination of the error bar in quadrature, the systematic error in the weighted mean was taken to be the largest of the systematic errors for the 1996 and 1997 data points to provide a conservative estimate. For 90° the new data shown in Figure 6.4 are in excellent agreement with previous data over the range 1–2.5 GeV, but the most eye catching behavior is the continued scaling of cross section from the onset at 1 GeV observed in SLAC NE8, up to a photon energy of 4 GeV. No intermediate energy data at 70° existed prior to this experiment. Figure 6.5 shows the new 70° data up to 4 GeV which appear to exhibit a similar scaling behavior as the 90° data. The 53° and 37° data shown in Figures 6.6 and 6.7 are in reasonable agreement with data from the previous SLAC NE17 experiment, but any indication of scaling at these angles is absent. In the comparison of the new data with the SLAC NE17 data it should be noted that the NE17 data are shown at the true center-of-mass angles (~84–89.4°, ~52.5° and ~36.7°), and have not been corrected for differences in the angles.

In addition to the energy distribution of the cross section, the angular distribution can be studied. Angular distributions of center-of-mass cross sections from this experiment and SLAC NE8 and NE17 are plotted in Figure 6.8 for nominal photon energies 1.6 GeV, 2.4 GeV, 3.2 GeV and 4.0 GeV. The figure shows that the E89-012 data confirms the forward angular dependence of the NE17 data at 1.6 GeV and 2.4 GeV. Moreover, at all energies shown the center-of-mass cross section is strongly forward peaked, and the forward peaking appears to be stronger as the beam energy increases. If the cross section scales at each angle, an energy-independent angular distribution is expected. Therefore the observed stronger forward-peaking behavior for higher energies is consistent with the non-scaling behavior of the 53° and 37° data.

Before comparing the new data to the theoretical predictions a few remarks are in order with regard to final cross sections listed in Table 5.7 in comparison with

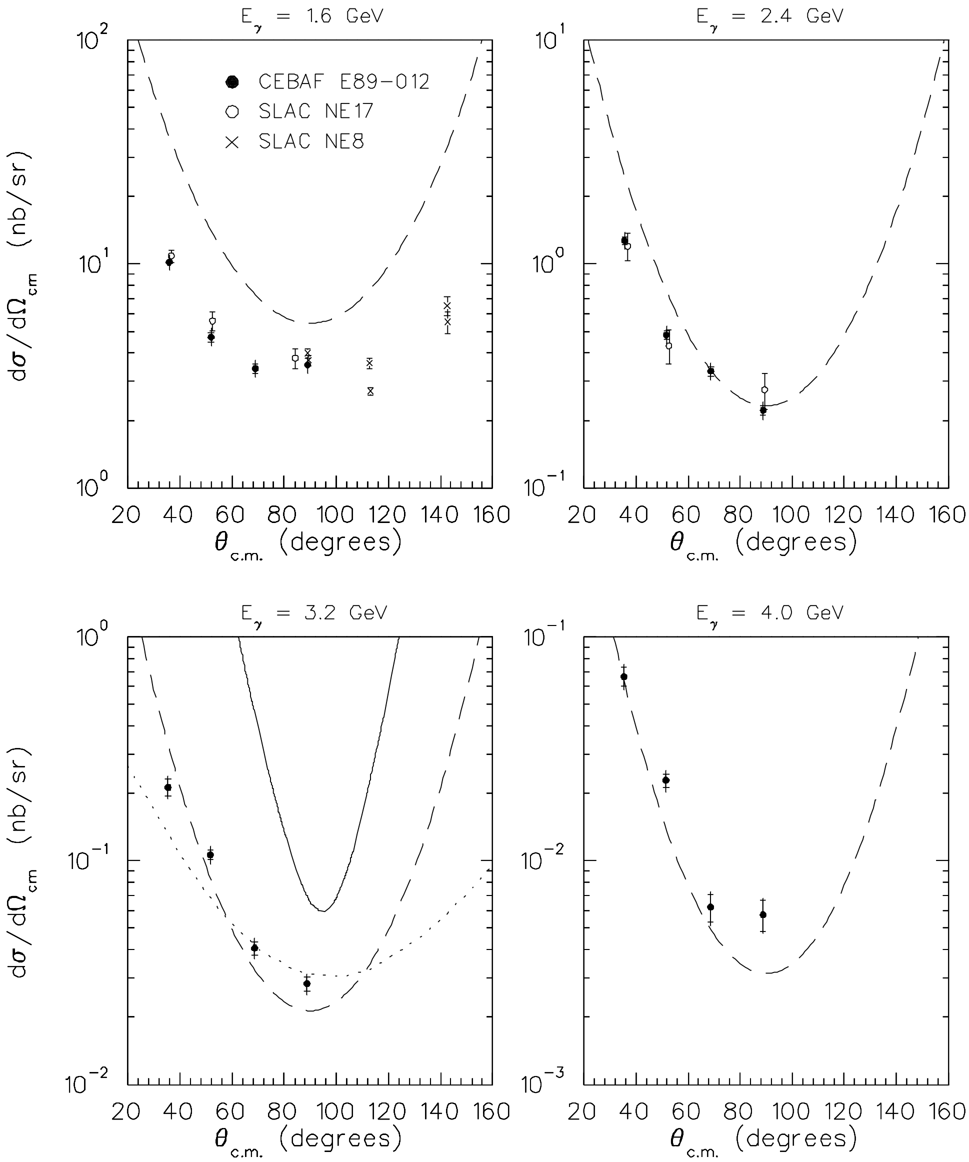

Figure 6.8: Angular distribution of the center-of-mass cross section at nominal photon energies of 1.6 GeV, 2.4 GeV, 3.2 GeV and 4.0 GeV. Data from this experiment and from SLAC NE8 [10] and SLAC NE17 [11] are shown. The curves are theoretical predictions of the angular behavior by the reduced nuclear amplitudes (RNA) model (dashed) and the asymptotic amplitudes model in covariant (solid) and light-front (dotted) formalism, with $g = 3$ and $\kappa = 1/2$. The latter two calculations are from Reference [71]. The RNA calculations included $f^2(\theta_{cm}) = 1$ and have a common normalization at the E89-012 2.4 GeV, 69° data point.

the ones graphed in the earlier publication [111]. A number of changes were made in the analysis, which could have potentially changed the cross sections in this work noticeably from the ones in the earlier publication, but ended up mostly canceling against each other. For completeness the changes are briefly discussed here. The cross sections in this work were calculated with a photon energy integration interval which was reduced by 5 MeV in comparison to the interval used in the analysis for the publication to be certain that the pion production threshold was excluded (see Section 5.3.1). Another change concerns the charge normalization, which was done exclusively with beam current monitor (BCM) #3 for the publication's results, whereas in this work the cross sections are normalized to the charge measured with BCM1, except for the $E_{beam} = 2.445$ GeV data and the 1997 data, which do use the BCM3 charge for their normalization. The last changes to mention concern correction factors, which change the value of the final cross section. For the publication an estimated 5.5% proton absorption correction, a 1% inscattering correction, and a global 7% target length correction were applied. In this work the proton absorption is estimated at 10.9%, the inscattering correction at 1.5% and a point-to-point target length correction was carried out. The large change in the absorption correction has it origin in the fact that earlier estimate was made for a hydrogen target. As mentioned before, the changes fortunately offset each other by and large, so that no significant change in behavior of the cross section energy dependence between the publication and the data in this work exists.

6.2 Comparison with Theoretical Models and Discussion

6.2.1 Dimensional Scaling Rules

The dimensional scaling laws predict that the $\gamma d \to pn$ invariant cross section for fixed center-of-mass angles starts showing a power law energy dependence according to

$$\frac{d\sigma}{dt} \sim s^{-11} , \tag{6.1}$$

at photon energies where $s \gg m_d^2 = 3.518$ GeV^2. This scaling behavior is best observed by studying the quantity $s^{11} d\sigma/dt$ which should be independent of energy when scaling sets in. The predicted scaling behavior had already been observed in the SLAC NE17 [11] 90° data starting at a photon energy of 1 GeV. The new CEBAF E89-012 data are in good agreement with the SLAC data in the overlap region, and continue to exhibit the scaling up to the highest photon energy of 4.0 GeV, as shown in Figure 6.4. In perturbative QCD descriptions the onset of scaling is governed by the momentum transfered to the constituents, and the transverse proton momentum p_T is often used as a parameter to indicate the scaling threshold. It is believed that scaling will set in around a p_T of about 1 GeV/c. The transverse proton momentum is calculated from $p_T^2 = \frac{1}{2} m_d E_\gamma \sin^2(\theta_{cm})$ and a value $\sim$ 1 GeV/c is obtained at photon energy 1 GeV, which coincides with the observed scaling behavior. However, it is surprising that the constituent counting rules works so well in the description of this data, especially when one considers that the momentum transfer to each individual quark in the deuteron is well below 1.0 (GeV/c)^2 for the photon energy range up to 4.0 GeV. A significant variation of the cross section due to the dependence of the strong coupling constant on the momentum transfer would be expected in addition to the energy dependence of the cross section, but this effect is not observed (see the discussion at the end of Section 2.4.1).

The 70° data in Figure 6.5 show a scaling behavior similar to the 90° data. A precise onset of scaling cannot be determined due to the lack of low-energy data, however the data appears to be scaling at the photon energy which corresponds to $p_T \sim$ 1 GeV/c . No scaling behavior is observed in the 53° and 37° data. For the 53° data this is remarkable if the $p_T \sim$ 1 GeV/c assumption is expected to hold, since the threshold for scaling coincides with $E_\gamma = 1.7$ GeV. If scaling still had to occur for the two most forward angles, one could argue that the lowest photon energy corresponding to possible onset of scaling is 3.2 GeV, since only one data point remains at higher energy. This photon energy corresponds to $p_T \sim$ 1.4 GeV/c for 53° and 1.0 GeV/c for 37°. Therefore, the onset of scaling is not yet ruled out for 37°, but in the case of

53°, the $p_T \sim 1$ GeV/c assumption is facing some difficulties.

The invariant cross sections for the four angles were fitted with a form A/s^n to determine the exponents n. Two fits were carried out, one where only the new E89-012 data with $E_\gamma > 1$ GeV were fitted, giving $n_{E89-012}$ and another where all data above 1 GeV are included in the fit, giving n_{all}. The fit results including the reduced χ^2 are listed in Table 6.2. The exponents at 90° and 70° are in good agreement with the constituent counting rule prediction. The exponents for 53° and 37° do not agree, which was already inferred from the energy dependence of the cross section in the figures. The table also shows the exponents fit in Reference [11], for the data set at that time, denoted by n_{NE17}. The exponents for the current data set at 37° and 90° are in good agreement with the NE17 exponents which suggests that the energy dependence for those angles in this experiment continues the trend observed in SLAC NE17.

θ_{cm} (nominal)	E_γ (GeV)	n_{NE17}	$n_{E89-012}$	$\chi^2_{E89-012}$	n_{all}	χ^2_{all}
37°	0.792–3.992	9.5 ± 0.4	9.31 ± 0.10	1.72	9.29 ± 0.10	1.48
53°	1.587–3.987	10.6 ± 0.6	9.44 ± 0.12	3.42	9.47 ± 0.11	2.56
70°	1.579–3.979	–	10.7 ± 0.13	4.49	10.7 ± 0.13	4.49
90°	0.745–3.963	11.2 ± 0.2	11.5 ± 0.12	2.01	11.3 ± 0.08	2.76

Table 6.2: Values of the exponent n from fits of the cross section data to the scaling prediction $\frac{d\sigma}{dt} \sim s^{-n}$. The exponent $n_{E89-012}$ is the result of a fit to the data with $E_\gamma > 1$ GeV from experiment E89-012 only. The exponent n_{all} is the result of a fit to all data with $E_\gamma > 1$ GeV. Only statistical uncertainties are included in the fit. The exponent n_{NE17} is the result from a fit performed in Reference [11]. For the "E89-012" and "all" fits the reduced χ^2 are also listed.

6.2.2 Reduced Nuclear Amplitudes

In their reduced nuclear amplitudes (RNA) model Brodsky and Hiller [21] construct the center-of-mass cross section in a form to obtain scaling at photon energies of 1 GeV. This is done by factoring out the known asymptotic scaling behavior of the nucleons, so that 4 "elementary" constituents remain, which are expected to obey a dimensional scaling behavior $\sim p_T^{-2}$. They arrive at a center-of-mass cross section of the form

$$\left(\frac{d\sigma}{d\Omega}\right)_{cm} \propto \frac{1}{\sqrt{s(s-m_d^2)}} F_p^2(\hat{t}_p) F_n^2(\hat{t}_n) \frac{1}{p_T^2} f^2(\theta_{cm}) \ , \tag{6.2}$$

where the function $f^2(\theta_{cm})$ is assumed to be independent of energy. In the asymptotic regime (i.e. large momentum transfers and $|t| \gg 0.71$ (GeV/c)^2) the dipole form factors start to exhibit a scaling behavior according to $F_N(\hat{t}_N) \sim |t|^{-2}$. Thus, in the large s and t limit (with s/t fixed), where $s \gg m_d^2$ and $p_T^2 \sim s$ the energy dependence of Equation 6.2 becomes

$$\frac{d\sigma}{d\Omega_{cm}} \sim s^{-10} \rightarrow \frac{d\sigma}{dt} \sim s^{-11} \ , \tag{6.3}$$

which is the form predicted by dimensional scaling rules. In Figures 6.2 and 6.3 the calculation obtained with Equation 6.2 for $f^2(\theta_{cm}) = 1$ is shown by the long–dashed line. At each of the four angles the curves have a common normalization to the 1 GeV data point from Reference [40]. The calculation is also shown as the long dashed line in the invariant cross section graphs in Figures 6.4–6.7. In the latter graphs, each curve is normalized to the E89-012 1.6 GeV data point at the corresponding angle. This is allowed, since any of the angles could provide the best agreement with the energy dependence, thereby determining the normalization constant for the other angles. However, the figures show that the RNA curve falls below the high E_γ data at all angles, and does not reach the expected asymptotic limit at these energies. The 37° RNA prediction shows an especially large deviation from the data.

The model in Equation 6.2 also allows for the calculation of the angular dependence of the center-of-mass cross section at fixed energy (with $f^2(\theta_{cm}) = 1$). The calculations are shown in Figure 6.8 for nominal photon energies 1.6 GeV, 2.4 GeV, 3.2 GeV and 4.0 GeV. The calculations have a common normalization at $E_\gamma = 2.4$ GeV and 69°. The new data at forward angles are in reasonable agreement with the RNA prediction. The calculations (data) show that the center-of-mass cross section is strongly forward-backward (forward) peaked. This behavior can be understood from the momentum dependence of the nucleon form factor. At forward (backward) angles the momentum transfer to the proton (neutron) is softer, which leads to a larger nucleon form factor, resulting in a larger cross section. Since the four-momentum transfer from the photon to the deuteron at fixed beam energy is a constant, the quantity $F_p^2 \cdot F_n^2 \cdot \frac{1}{p_T^2}$ has a minimum for $\hat{t}_p \simeq \hat{t}_n$, which occurs at 90°. The theory correctly predicts this minimum. As part of their model Brodsky and Hiller [21] derive an expression for $f^2(\theta_{cm})$ by modeling the photodisintegration of the reduced deuteron after the photodisintegration of a polarized meson by a virtual photon. When the average over the two possible helicities of a transverse photon is taken, they arrive at an angular distribution

$$f^2(\theta_{cm}) = N\frac{ue_1 + te_2}{tu} \ , \tag{6.4}$$

where the e_i represent the variable coupling strengths of the quark and antiquark in the meson, and N provides an arbitrary normalization. This function provides strong forward and backward peaking, but a comparison with the current data set is not made, because of the lack of backward angle data at high energies.

So far the function $f^2(\theta_{cm})$ has been taken equal to unity in the calculations at fixed θ_{cm}. A test of the assumption that the function is independent of energy at fixed angle and energies above 1 GeV can be made by calculating $f^2(\theta_{cm})$, using the model in Equation 6.2 and the existing experimental center-of-mass cross sections for $\theta_{cm} = 90°$. The calculated $f^2(\theta_{cm} = 90°)$ is shown in Figure 6.9 and clearly does not exhibit the expected energy independent behavior above $E_\gamma = 1$ GeV.

6.2.3 QCD Rescattering

In the QCD rescattering model with strong final state interactions from Frankfurt *et al.* [25] the invariant cross section is calculated from

$$\frac{d\sigma^{\gamma d \to pn}}{dt} = \frac{4\alpha}{9}\pi^4 \cdot \frac{1}{s'} C(t_N/s) \frac{d\sigma^{pn \to pn}(s, t_N)}{dt} \times \left| \int \Psi_d^{NR}(p_z = 0, p_\perp) \sqrt{m_N} \frac{d^2 p_\perp}{(2\pi)^2} \right|^2 . \tag{6.5}$$

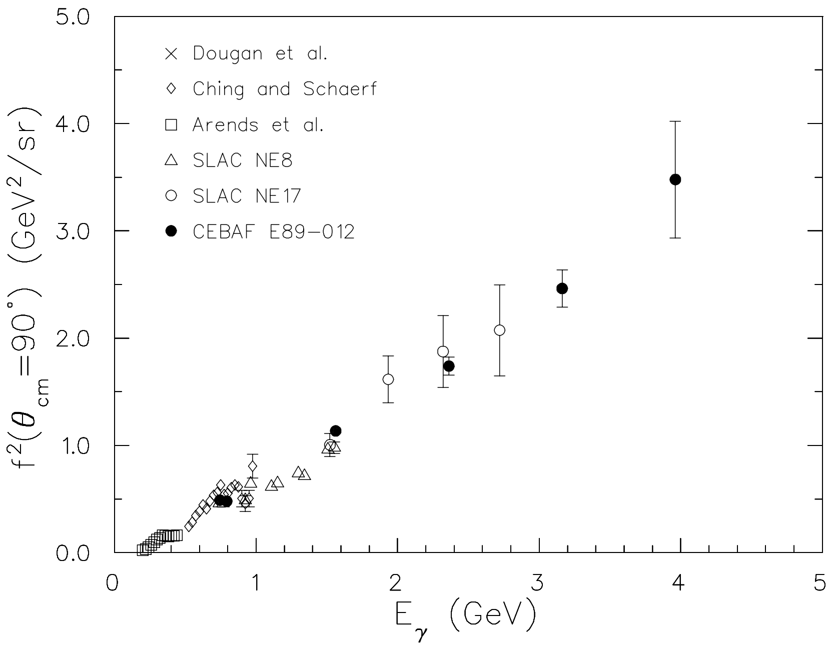

Figure 6.9: Energy dependence of the function $f^2(\theta_{cm})$ in the RNA cross section. The quantity $f^2(\theta_{cm} = 90°)$ was calculated using data from this experiment and previous experiments. In the RNA model $f^2(\theta_{cm})$ is expected to be independent of energy at photon energies above 1 GeV. The observed behavior clearly contradicts this expectation.

As outlined in Section 2.4.2, the cross section is computed using a Paris potential for the wave function, $pn \to pn$ scattering experimental data for the $\sigma(pn \to pn)$ cross section, and by taking a form for the scaling factor $C(\frac{t_n}{s})$, which is approximately 1 at 90° and assumed to be a slowly varying function of θ_{cm}. Because $pn \to pn$ data is not available at the exact t_N values required in the cross section, an extrapolation is made using existing pn data at $t_N^{min,max}$ with $-t_N^{min} < -t_N < -t_N^{max}$ creating a prediction band. In computation of the cross sections, the scaling function function $C(\frac{t_n}{s}) = 1$ at 90°, but at the other angles, the form $C(t_N/s) = \frac{-2t_N/s'}{1+2t_N/s'} \approx \frac{-t/s'}{1+t/s'}$ was used. This was done so that the 37° data could be included, which would otherwise fall outside the region of validity of the quark interchange mechanism ($-t \geq 2$ GeV^2) [25]. The region of validity of this model is dictated by kinematic conditions on the "hard-ness" of the gluon in the quark-exchange and the size of the transverse momentum of the outgoing nucleons, and requires that $E_\gamma \geq 2.4$–2.5 GeV and $-t \geq 2$ GeV^2. Figure 6.10 shows the computed bands that limit the energy dependence of the cross section for the four angles of this experiment. The prediction of the cross section within this range is in reasonable agreement with the data. The authors have pointed out that in the case of good agreement with the data, the magnitude of the photoproduction amplitude is determined by the high momentum transfer contained in the hard scattering NN amplitude. This would imply that the "infinite" number of quark interactions normally considered could be replaced by the hard amplitude of NN interactions.

6.2.4 The Quark Gluon String Model

The quark gluon string (QGS) model predicts an energy dependence of the invariant cross section according to $\frac{d\sigma}{dt} \sim F^2(t)s^{2\alpha-2}$. This is not of the form of a power law of energy but Kondratyuk *et al.* [26] make a dimensional scaling-like parameterization of the form $\frac{d\sigma}{dt} \sim s^{-n}$ for the limited energy region of interest in the intermediate energy $\gamma d \to pn$ experiments. In this parameterization the power n depends on the center-of-mass angle. This parameterization of the cross section is represented by the dot-dashed line in Figures 6.2–6.6, for θ_{cm}=37°,53°, and 90°. The parameterization is in reasonable agreement with the data at 37° and 53° for E_γ = 1–4 GeV. In this kinematic regime, $s \gg 1$ GeV^2 and $|t|$, $|u| \leq 1$ (GeV/c)^2, which corresponds to the predicted range of validity of the model. For the data at 90° $|t| = |u| \not\leq 1$ (GeV/c)^2, so that a deviation of the parameterization is expected, which is indeed reflected in the figures showing the 90° data. For the powers of s in the parameterization, Kondratyuk *et al.* find n=9.1 for 37°, n=10.3 for 53°, and n=11.8 for 90°. Comparison of these values with the values of the power fits to the current complete data set, listed in Table 6.2 confirm the observed agreement with the data at 37° and 53° and the disagreement at 90°.

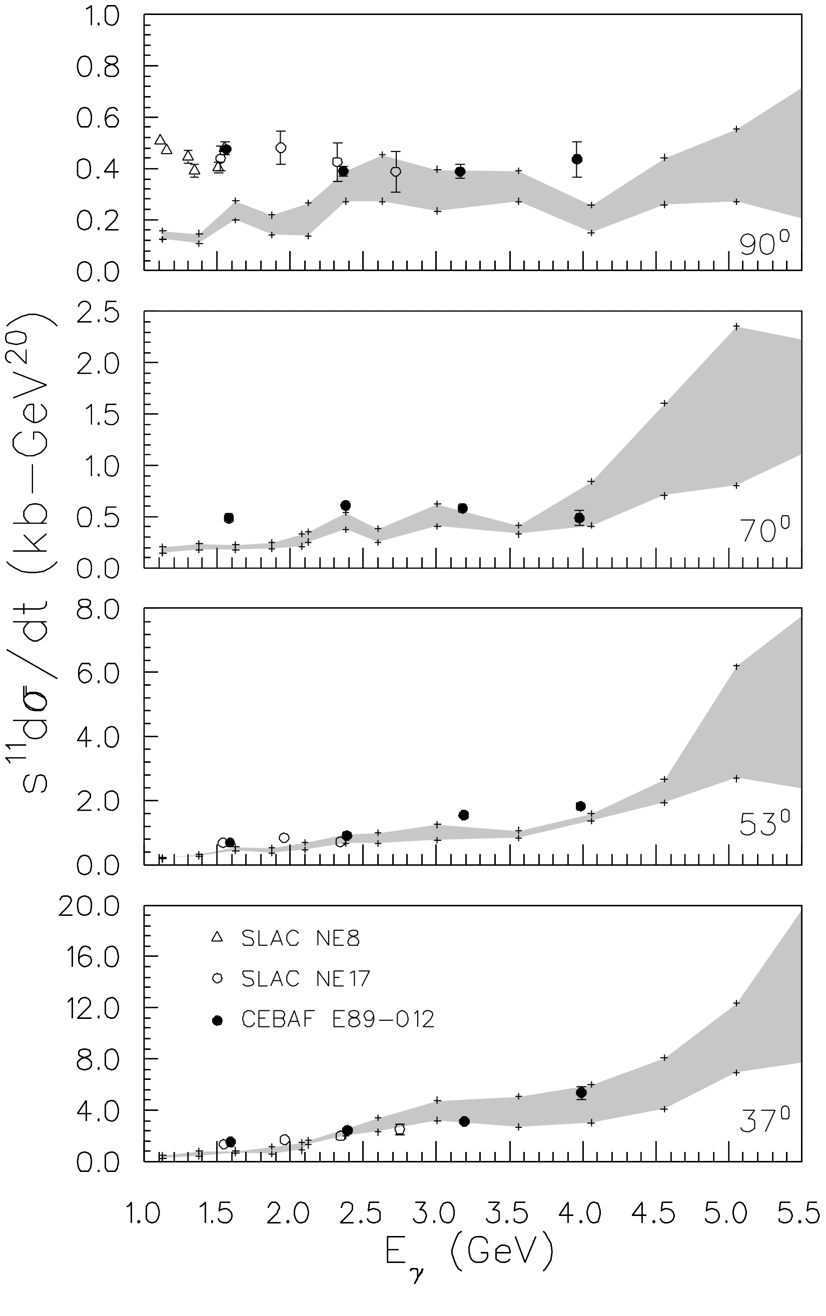

Figure 6.10: The invariant cross section as function of the photon energy for nominal center-of-mass angles θ_{cm} = 37°, 53°, 70°, and 90°. The data points are from this experiment and previous experiments [11,40]. The cross hatched bands correspond to the region over which the cross section has been computed in the QCD rescattering model, using the extrapolation of $pn \to pn$ data. In the 90° calculation $C(\theta_{cm})$= 1, for the other angles the scaling function as discussed in the text is used. The calculations are courtesy from [112].

6.2.5 Meson-Exchange Calculations

Results from previous intermediate energy $\gamma d \rightarrow pn$ measurements [10, 11] already showed that meson-exchange theories are most effective in describing the energy dependence of the cross section at 90° for energies below 1 GeV. Therefore it comes as no surprise that energy dependence of the new data in the 1–4 GeV range is not well described by the meson exchange models. Here the data are compared to the energy dependence of the cross section at θ_{cm}=90° as predicted by the coupled channel model by Lee [27] and by a meson-exchange calculation by Laget [28]. Figure 6.4 shows the coupled channel calculation as the solid line. Agreement with the data is very good in the low energy regime, below $E_\gamma = 0.5$ GeV, but for higher energies the model predicts a cross section which is below the data up to 1 GeV, followed by a behavior that deviates strongly from the data. The calculation by Laget, shown by the dot–long–dash curve is also in good agreement with the low energy data and extends farther than Lee's model, up to photon energy of 0.8 GeV, but starts to deviate strongly after that as well.

Upon closer examination of the meson-exchange approach, the failures of these calculations at high energies are not unexpected. The traditional approach involves the development of a model which is constrained by a large body of experimental data, for example nucleon-nucleon (NN) total cross sections, NN phase shifts and photomeson production. In the case of Lee's model, the NN phase shifts are reproduced up to 2.0 GeV [113]. Often low energy deuteron photodisintegration data provides additional constraints. The constraints are required to obtain values for the adjustable parameters in the model, like coupling constants and cut-off masses in form factors (see e.g. Equation 2.39). A data set like the one that currently exists at photon energies above 1 GeV is too limited to provide means of determining all the free parameters in a meson-exchange model. Consequently the meson-exchange models are more successful towards the lower end of the intermediate energy regime, where an abundance of experimental data is available.

6.2.6 Asymptotic Amplitudes

In recent work Nagornyĭ and Dieperink [71] build on the work of Reference [29] and arrive at an invariant cross section for $\gamma d \to pn$ in the large (but finite) s limit in the form of

$$\frac{d\sigma}{dt} = \frac{C m_d}{\sqrt{s}(s-m_d^2)^{2g-1}(s-m_d^2)^{3/2}} f(\theta_{cm}, s) \ . \tag{6.6}$$

Here g is the vertex parameter, and $f(\theta_{cm}, s)$ a function that depends on s and θ_{cm} through the light cone variable $\alpha(\theta_{cm}, s)$. They assume that in the measured s-range the deuteron mass m_d^2 in the denominator of Equation 6.6 cannot be neglected, so that an effective s dependence is obtained which deviates from the constituent scaling prediction.

At $\theta_{cm} = 90°$, where $\alpha = 1$ and $f(\theta_{cm}, s) = 1$, a "prescaling" behavior according to $\frac{d\sigma}{dt} \sim s^{-10}$ is found for a vertex parameter $g = 3$. The calculation at 90° is shown in Figure 6.4 by the dotted line. The observed energy dependence in the range 1.5 to 3.5 GeV is very close to $1/s^{11}$. At other angles the function $f(\theta_{cm}, s)$ becomes a function of s and effectively adds additional powers of s to the numerator of Equation 6.6. The fractions α and $2-\alpha$ in the t- and u-channel momentum transfers are independent of s only when $s \to \infty$, therefore angular independent scaling is only expected in this limit. In the energy regime under current investigation the energy dependence has an angle dependent exponent in the power law, and varies from $1/s^{10}$ at 90° to $1/s^{8}$ at 10°. For the other angles, the calculations are shown as a dotted line in Figures 6.5–6.6. Overall the agreement of the calculations with the data at these angles is not good, but there is reasonable agreement with the energy dependence of the 53° data above $E_\gamma = 2$ GeV.

The angular dependence of the cross section depends entirely on the the variable α which appears in the vertex form factor $G(\alpha, \vec{k}^2)$. The two different form factors which are used in Reference [71], the covariant (instant form) and the light front form factor, predict vastly different angular distributions. In the instant form description the form factor depends on α for the t and u channels, and correspondingly shows a strong angular dependence at forward and backward angles. Moreover, the vertex form factor depends on one covariant variable e.g. $k_t(s,\theta)$ so that the angle and s-dependence are coupled by the vertex parameter g which determines the s fall-off and the angular behavior. In the light-cone description the vertex depends on two (in principle) independent parameters, α and $\vec{k}^2$, so that the s- and θ-dependence are decoupled. In this description the two dependences are factorized (see Section 2.6), and a flat angular dependence can go together with a steep s-dependence. Reference [71] provides predictions for the center-of-mass cross section over an angular range 20°–160° at $E_\gamma = 3.2$ GeV. The cross sections are calculated for both the instant form and light front form of the vertex form factor. The resulting curves from [71] are shown in Figure 6.8 in the lower left panel. The cross section result with in the instant form approach is depicted by the solid line, and shows the steep forward-backward angular dependence. It is in poor agreement with the data. In the light-front formalism a κ dependence of 1/2 was chosen. For the forward data the light-front formalism provides a reasonable prediction of the angular dependence of the cross section at 3.2 GeV, as shown by the dotted line.

6.3 Summary

The main result of this experiment is the continuation of the scaling behavior of the 90° center-of-mass cross section from $E_\gamma \approx 1$ GeV up to the maximum photon energy of 4 GeV, and the first evidence of a similar scaling for 70°. In both data sets the onset of scaling is observed around the photon energy that corresponds to $p_T \sim 1$ (GeV/c)^2, which would suggest that the perturbative regime has started. However, the 53° data rule out that threshold of scaling is marked by $p_T = 1$ (GeV/c)^2, and the 37° data do not extend to high enough energies to draw a conclusion. The reduced nuclear amplitudes (RNA) analysis is unsuccessful in describing the energy dependence at all angles. RNA does provide the strong forward peaked angular dependence which is observed in the data. Other QCD-inspired models have modest success in describing the energy behavior of the data. The QGS model is in reasonable agreement with the data at the two most forward angles, 37° and 53°, but, as expected, does not agree with the large angle 90° data. The QCD rescattering approach is in fair agreement with the data at all angles. The conventional meson-exchange models exhibit large deviations from the data above photon energies of 1 GeV. However, the asymptotic amplitudes model, which also describes the dynamics of the cross section using hadronic degrees of freedom is remarkably successful in the prediction of the energy behavior at 90°. The model also generates an angular distribution at 3.2 GeV which is in reasonable agreement with the measured center-of-mass cross sections at forward angles.

It is evident that further theoretical efforts in combination with more experimental work are needed to understand the reaction dynamics which cause the observed scaling behavior. If perturbative QCD were indeed applicable in the energy range where scaling is observed, it is surprising that the running of the coupling constant is not observed as well.

Chapter 7

Summary and Conclusions

The differential cross section for the exclusive two-body deuteron photodisintegration reaction $\gamma d \rightarrow pn$ has been measured at a set of forward center-of-mass angles ($37^\circ < \theta_{cm} < 90^\circ$) at beam energies from 0.8 GeV to 4.0 GeV. Despite an unforeseen limitation of the spectrometer acceptance, which caused a significant reduction in the data set, the majority of the cross sections exceed the projected statistical accuracy. This can be attributed to the CEBAF high luminosity continuous-wave electron beam, which provides a high data rate and low accidental background.

The main result of this experiment is the observation of a continued energy dependence consistent with the dimensional scaling rules prediction $d\sigma/dt \sim s^{-11}$ for the 90° center-of-mass cross section, up to a photon energy of 4 GeV, and the first observation of a similar scaling for 70° in the same energy regime. This scaling is not observed for the 53° and 37° cross sections and their fall-off appears to be slower than s^{-11}. The prediction of the energy behavior from the reduced nuclear amplitudes (RNA) analysis is in disagreement with the data, however, the RNA model does predict the strong forward peaked angular dependence of the data. The QGS model makes a reasonable prediction of the energy dependence of the high energy (> 1 GeV) data at 37° and 53°, but its range of validity is too limited to describe 90° data. The QCD rescattering approach is in fair agreement with the data above 1 GeV at all angles. The conventional meson-exchange models fail to predict the s^{-11} fall-off of the invariant cross section with energy. The asymptotic amplitudes model, which also describes the dynamics of the cross section using hadronic degrees of freedom mimics the $1/s^{-11}$ constituent counting behavior of the cross section quite well at 90° for energies between 1.5 GeV and 3.5 GeV. The energy dependence of the cross section at the other angles is not quite as well reproduced by the model, but its prediction of the angular distribution at 3.2 GeV is in good agreement with the forward angle data.

It is widely believed that there is a relation between the size of the four-momentum transfer to the final state in an exclusive reaction and the observation of scaling in that reaction. For the search of scaling in exclusive reactions, photoreactions like $\gamma d \rightarrow pn$ are a pre-eminent tool since the photon transfers all of its energy and momentum to the nuclear system, thereby providing the largest attainable four-momentum transfer. The onset of scaling of the 90° and 70° cross sections coincides with a transverse proton momentum $p_T \sim 1$ GeV/c, which in QCD is often associated with the start of the perturbative regime. Therefore one could argue that the observed scaling is an indication that the perturbative regime has started although some claim that the application of perturbative QCD to the intermediate energy regime is not warranted [47, 48]. If the observed scaling of the cross sections at 90° and 70° is indeed attributed to pQCD, two problems arise. An explanation for the lack of scaling of the 37° and 53° cross sections must be found and the absence of scaling violations in the 90° and 70° cross sections must be explained as well. Apart from that, the success of Nagornyĭ *et al.* in obtaining the observed energy dependence at 90° using just hadronic degrees of freedom suggests that a description of the reaction dynamics in terms of the QCD quarks and gluons may not be a necessity.

It is clear that the role of QCD in nuclear reactions at these energies is not yet well understood. Further measurements at higher energies at the forward angles can test whether scaling has truly set in and whether p_T is the physical quantity governing the onset of scaling behavior. Experimental determination of the physical observable associated with the onset of scaling is essential for understanding the underlying mechanism for the scaling behavior in the exclusive two-body process. Perhaps then the large gaps in the current understanding of the transition from meson-baryon degrees of freedom to quark-gluon degrees of freedom in nuclear reactions can be filled in.

The new E89-012 data constitute a notable advance in the experimental study of photonuclear reactions involving the deuteron. CEBAF Experiment E96-003 [114] which was proposed as an extension of experiment E89-012 shortly after its preliminary results became available, has completed data taking in the spring of 1999. Its focus is on the most forward angle 37° and 53° cross sections, which were measured up to beam energies of 5.5 GeV, so that possible onset of scaling at these angles can be further investigated. Also recently, a new proposal [115] has been approved to measure the $\gamma d \to pn$ reaction at the backward center-of-mass angles 115°, 130°, and 145° at photon energies up to 3.2 GeV. These measurements are complementary to the angular range measured in this experiment and will provide a full angular data set so that a further check of the angular dependence predictions of the asymptotic amplitudes [71] model can be made. Thus far, the attention has been focused on cross section measurements testing the constituent counting rules of asymptotic scaling and no photodisintegration reaction detecting hadron polarization has been carried out at high energies. CEBAF experiment E89-019 [116] has been approved to measure proton polarization in the $^2\mathrm{H}(\gamma, \vec{\mathrm{p}})\mathrm{n}$ reaction, so that the other requirement of asymptotic QCD in exclusive nuclear reactions can be tested as well, namely that hadron helicity conservation is conserved.

References

[1] J. Chadwick, Nature **129**, 312 (1932); J. Chadwick, Proc. Roy. Soc. (London) **A136**, 692 (1932).

[2] H.C. Urey, F.G. Brickwedde, and G.M. Murphy Phys. Rev. **39**, 164 (1932); H.C. Urey, F.G. Brickwedde, and G.M. Murphy Phys. Rev. **40**, 1 (1932).

[3] J. Chadwick and M. Goldhaber, Nature **134**, 237 (1934).

[4] R.E. Bell and L.G. Elliott, Phys. Rev. **79**, 282 (1950).

[5] C.M.G. Lattes, H. Muirhead, G.P.S. Occialini, and C.F. Powell, Nature **159**, 694 (1947).

[6] H. Yukawa, Proc. Phys.-Math. Soc. Japan (3) **17**, 48 (1935); reproduced in *Foundations of Nuclear Physics*, R.T. Beyer (ed.), Dover, New York, (1949).

[7] W. Marciano and H. Pagels, Phys. Rep. **36**, 137 (1978).

[8] J.M. Laget, in *New Vistas in Electro-Nuclear Physics*, E.L. Tomusiak, H.S. Caplan and E.T. Dressler (eds.), Plenum Press, New York, (1986).

[9] J.J. Domingo, in *Beam up, running at CEBAF*, W.H. McMichael (ed.), Newport News Daily Press, November 18 1995, page C2 (1995).

[10] J. Napolitano *et al.*, Phys. Rev. Lett. **61**, 2530 (1988).

[11] J.E. Belz, *et al.*, Phys. Rev. Lett. **74**, 646 (1995).

[12] J.C. Collins and D.E. Soper, Ann. Rev. Nucl. Part. Sci. **37** 383 (1987).

[13] C.E. Carlson, J.R. Hiller, and R.J.Holt, Ann. Rev. Nucl. Part. Sci. **47** 395 (1997).

[14] D. Sivers, Ann. Rev. Part. Sci., **32**, 149 (1982).

[15] P.V. Landshoff and J.C. Polkinghorne, Phys. Lett. **44B**, 293 (1973).

[16] S.J. Brodsky and G.P. Lepage, in *Advanced Series on Directions in High Energy Physics - Vol. 5, Perturbative Quantum Chromodynamics*, A.H. Mueller (ed.), World Scientific, London, (1989).

[17] S.J. Brodksy and G.P. Lepage, Nucl. Phys. **A353**, 247c (1981).

[18] R.J. Holt, Phys. Rev. C. **41**, 2400 (1990).

[19] F. Halzen and A.D. Martin, *Quarks and Leptons*, Wiley, New York, (1984).

[20] R.M. Barnett, *et al.*, Phys. Rev. C. **D43**, 72 (1996).

[21] S.J. Brodksy and J.R. Hiller, Phys. Rev. C **28**, 475 (1983).

[22] F. Wang, *et al.*, Phys. Rev. Lett. **69**, 2901 (1992).

[23] S.J. Brodsky and C.-R. Ji, SLAC-PUB-3747, (1985), p.56 .

[24] S.J. Brodsky and G.R. Farrar, Phys. Rev. Lett. **31**, 1153 (1973).

[25] L.L. Frankfurt, *et al.* LANL preprint hep-ph/9904222 (1999).

[26] L.A. Kondratyuk *et al.*, Phys. Rev. C **48**, 2491 (1993).

[27] T.-S.H. Lee, Argonne National Laboratory Report ANLPHY-5253-TH-88 (1988).

[28] J.M. Laget, Nucl. Phys. **A312**, 265 (1978);
J.M. Laget, Rapport DPh-N Saclay n°2146, (1984).

[29] S.I. Nagornyĭ, Yu.A. Kasatkin, and I.K. Kirichenko, Sov. J. Nucl. Phys. **55**, 189 (1992).

[30] V.A. Matveev, R.M. Muradyan, and A.N. Tavkhelidze, Lett. Nuovo Cimento **7**, 719 (1973).

[31] P.V. Landshoff, Phys. Rev. D **10**, 1024 (1974).

[32] S.J. Brodsky and G.R. Farrar, Phys. Rev. D **11**, 1309 (1975).

[33] Yu.L. Dokshitzer, V.A. Khoze, A.H. Mueller, and S.I. Troyan, *Basics of Perturbative QCD*, Editions Frontières, Gif-sur-Yvette Cedex - France (1991).

[34] R.L. Anderson, *et al.*, Phys. Rev. D **14**, 679 (1976).

[35] D.G. Crabb, *et al.*, Phys. Rev. Lett. **65**, 3241 (1990).

[36] P. Dougan, *et al.*, Z. Phys. **A276**, 55 (1976).

[37] R. Ching and C. Schaerf, Phys. Rev **141**, 1320 (1966).

[38] H. Myers, *et al.*, Phys. Rev. **121**, 630 (1961).

[39] J. Arends, *et al.*, Nucl. Phys. **A412**, 509 (1984).

[40] S.J. Freedman *et al.* Phys. Rev. C **48**, 1864 (1993).

[41] J.E. Belz, Ph.D. thesis, California Institute of Technology, (1994), unpublished.

[42] D.G. Meekins, Ph.D. thesis, College of William and Mary, (1998), unpublished.

[43] S.J. Brodsky and B.T. Chertok, Phys. Rev. D **14**, 3003 (1976).

[44] S. Rock *et al.*, Phys. Rev. Lett. **49**, 1139 (1982).

[45] L.C. Alexa *et al.*, Phys. Rev. Lett. **82**, 1374 (1999).

[46] R.G. Arnold *et al.*, Phys. Rev. Lett. **35**, 776 (1975).

[47] N. Isgur and C.H. Llewellyn Smith, Phys. Rev. Lett. **52**, 1080 (1984).

[48] N. Isgur and C.H. Llewellyn Smith, Nuc. Phys. **B317**, 526 (1989).

[49] S.J. Brodsky and B.T. Chertok, Phys. Rev. Lett. **37**, 269 (1976).

[50] S.J. Brodksy and J.R. Hiller, Phys. Rev. D **46**, 2141 (1992).

[51] R.G. Arnold *et al.*, Phys. Rev. Lett. **35**, 776 (1975);
R.G. Arnold (private communication to S.J. Brodksy and J.R. Hiller);
R. Cramer *et al.* Z. Phys. C **29**, 513 (1985);
S. Platchkov *et al.*, Nucl. Phys. **A510**, 740 (1990).

[52] C.E. Carlson, Nuc. Phys. **A508**, 481c (1990).

[53] A.I. Vainshtein and V.I. Zakharov, Phys. Lett. **72B**, 368 (1978).

[54] C.E. Carlson and F. Gross, Phys. Rev. Lett. **53**, 127 (1984).

[55] G.R. Farrar, K. Huleihel, and H. Zhang, Phys. Rev. Lett. **74**, 650 (1995).

[56] S.J. Brodsky, private communication to R. Holt (1996).

[57] J.M. Cornwall, Phys. Rev. D **26**, 1453 (1982).

[58] S. Capstick and N. Isgur, Phys. Rev. D **34**, 2809 (1986).

[59] C. White *et al.*, Phys. Rev. D **49**, 58 (1994).

[60] M. Lacombe, *et al.* Phys. Lett. **B101**, 139 (1981)

[61] A.B. Kaidalov, Z. Phys. C **12**, 63 (1982).

[62] P.D.B. Collins, *An introduction to Regge Theory & High Energy Physics*, Cambridge University Press, Cambridge (1977).

[63] E. De Sanctis, A.B. Kaidalov, and L.A. Kondratyuk, Phys. Rev. C **42**, 1764 (1990).

[64] M. Lacombe *et al.*, Phys. Rev. C **21**, 861 (1980).

[65] W. Leidemann and H. Arenhövel, Phys. Lett. **139B**, 22 (1984).

[66] T.-S.H. Lee, Phys. Rev. C **29**, 195 (1984).

[67] C.R. Chen and T.-S.H. Lee, Phys. Rev. C **38**, 2187 (1988).

[68] T.-S.H. Lee and A. Matsuyama, Phys. Rev. C **36**, 1459 (1987).

[69] T.-S.H. Lee, Few-Body Systems, Suppl. 6, 526, (1992).

[70] R.V. Reid, Ann. Phys. (N.Y.) **50**, 411 (1968).

[71] A.E.L. Dieperink and S.I. Nagornyĭ, LANL preprint nucl-th/9904058 (1999).

[72] S.I. Nagornyĭ, *et al.*, Sov. J. Nucl. Phys. **49**, 465 (1989).

[73] F. Gross and B.D. Keister, Phys. Rev. C **28**, 823 (1983).

[74] C. Yan *et al.*, Nucl. Instrum. Meth. **A365**, 46 (1995).

[75] C. Yan *et al.*, Nucl. Instrum. Meth. **A365**, 261 (1995).

[76] P. Gueye, Status of the Actual Beam Position Monitors in the Hall C Beamline, CEBAF Internal Report (unpublished).

[77] P. Gueye, M. Tiefenback, and C. Yan, Hall C Beam Energy Measurement, CEBAF Internal Report (unpublished).

[78] K.B. Unser, The Parametric Current Transformer, a Beam Current Monitor Developed for LEP, CERN SL/91-42 (unpublished).

[79] G. Niculescu, Resonant Cavities used as Beam Current Monitors, CEBAF Internal Report (1995), unpublished.

[80] C. Armstrong, Beam Current Measurement in Hall C, CEBAF Internal Report (1996), unpublished.

[81] D.J. Mack, private communication (1999).

[82] C.W. Bochna, Ph.D. thesis, University of Illinois, (1999), unpublished.

[83] H. Bethe and W. Heitler, Proc. Roy. Soc. (London) **A146**, 83 (1934).

[84] J.L. Matthews and R.O. Owens, Nucl. Instr. and Meth. **111**, 157 (1973).

[85] J.H. Mitchell, Specifications for the Control System of the Hall C Cryogenic Targets, CEBAF Internal Report (1995), unpublished.

[86] J. Dunne, Cryo and Dummy Target Information, CEBAF Internal Report (1997), unpublished.

[87] J. Dunne, Cryo and Dummy Target Information, CEBAF Internal Report (1998), unpublished.

[88] K. Gustafsson, Cryotarget Density Dependence on Beam Current, CEBAF Internal Report (1996), unpublished.

[89] Experimental & Physics Industrial Control System (EPICS), Los Alamos National Laboratories, 1984.

[90] J.K. Oosterhout, *Tcl and the Tk toolkit*, Addison-Wesley, Reading, Mass., (1994).

[91] MI-TECH Metals Inc., Indianapolis, IN, USA.

[92] D.C. Carey, K.L. Brown, and F. Rothacker, TRANSPORT, A Computer Program for Designing Charged Particle Beam Transport Systems, SLAC-R-95-462, 1995.

[93] O.K. Baker *et al.*, Nucl. Instrum. Meth. **A367**, 92 (1995).

[94] W.R. Leo, *Techniques for Nuclear and Particle Physics Experiments*, Springer-Verlag, Berlin, (1994).

[95] J.R. Arrington, Ph.D. thesis, California Institute of Technology (1998)

[96] H. Mkrtchyan, CEBAF Internal Report, unpublished.

[97] D. Abbott *et al.*, in *Proc. of the IEEE Conference on Real-Time Computer Applications in Nuclear, Particle, and Plasma Physics,*, R. Fox (ed.), Michigan State University-NSCL, East Lansing, (1995), p. 147.

[98] C. Group, PAW (Physics Analysis Workstation) Users Guide, Program Library Q121, CERN.

[99] D.G. Meekins, private communication (1996).

[100] D.F. Geesaman, Tracking in the SOS Spectrometer, CEBAF Internal Document (1993), unpublished.

[101] D. van Westrum, Measurement of Tracking Errors in the Regular and "4 of 6" Tracking Algorithms, CEBAF Internal Report (1996), unpublished.

[102] M. Berz, COSY Infinity Version 7 Reference Manual, NSCL Technical Report MSUCL-977, Michigan University, 1995.

[103] K.A. Assamagan, D. Dutta, and P. Welch, Hall C Matrix Element Optimization Package, CEBAF Internal Report (1996), unpublished.

[104] C.S. Armstrong, Hall C Time-of-Flight Fitting Code, CEBAF Internal Report (1996), unpublished.

[105] D. van Westrum, Measurement and Estimate of Proton Absorption in the Hall C Spectrometers, CEBAF Internal Report (1997), unpublished.

[106] R.L. Lucke, Rev. Sci. Instrum., **47**, 766 (1976).

[107] L. Lions, *Statistics for Nuclear and Particle Physicists*, Cambridge, New York, (1986).

[108] L.E. Wright and L. Tiator, Phys. Rev. **C26**, 2349 (1982).

[109] Y.S. Tsai, Rev. Mod. Phys. **46**, 815 (1974).

[110] R.J. Holt, private communication (1997).

[111] C.W. Bochna and B.P. Terburg, *et al.*, Phys. Rev. Lett. **81**, 4576 (1998).

[112] M. Sargsian, private communication (1999).

[113] T. Sato and T.-S.H. Lee, Phys. Rev. C **54**, 2660 (1996).

[114] R.J. Holt, University of Illinois, TJNAF Proposal PR-96-003, 1997.

[115] R. Gilman, Rutgers University, TJNAF Proposal PR-99-008, 1999.

[116] R. Gilman, Rutgers University, CEBAF Proposal PR-89-019, 1989.

[117] C.B. Chiu, Ann. Rev. Nucl. SCi., **22**, 255 (1972).

[118] F. Duncan, Hall C Cryogenic Target User Manual, Version 1.51, CEBAF Internal Report (1997), unpublished.

[119] J.H. Mitchell, Safety Assessment Document for the Hall C Cryogenic Targets, CEBAF Internal Report (1995), unpublished.

[120] Coors Brewing Company, Golden, Colorado.

[121] B.P. Terburg, The Target Gas Analysis Vademecum, CEBAF Internal Report (1997), unpublished.

[122] Lawrence Livermore National Laboratory, publication UCRL TB–119663.

[123] J. Lindsey, Lawrence Livermore National Laboratory, private communication (1996).

[124] J.B. Anderson, M. Kraimer, Experimental Physics and Industrial Control System (EPICS) Input Output Controller (IOC) Record Reference Manual, Los Alamos National Laboratory, (1991).

[125] B.P. Terburg, CEBAF Hall C Cryogenic Target Documentation for the Expert, Volume 2: The Brain, CEBAF Internal Report (1996), unpublished.

[126] A. Kozubal, State Notation and Sequencer Users Guide Version 1.9, Los Alamos National Laboratory, (1995).

[127] B. Daly, EPICS TCL/TK Interface, Argonne National Laboratory APS (1995).

[128] J. Anderson, Alarm Handler User's Guide, Argonne National Laboratory, (1998).

[129] F. Duncan, CEBAF Hall C Cryogenic Target Control System Programmers Guide, Version 1.11 CEBAF Internal Report (1997), unpublished.

[130] Wolley *et al.*, *"Compilations of Thermal Properties of Hydrogen in its Various Isotopic and Ortho-Para Modifications"*, Journal of REsearch of National Bureau of Standards, **41**, 379 (1948).

[131] B.P. Terburg, CEBAF Hall C Cryogenic Target Documentation for the Expert, Volume 1: The Nervous System, CEBAF Internal Report (1996), unpublished.

Appendix A

Kinematics Quantities

This Appendix contains useful kinematics identities and a presentation of the derivations of the reconstructed photon energy and the maximum proton energy at threshold pion production in the deuteron photodisintegration reaction.

A.1 Scattering Kinematics

Consider a two-body process $A + B \to C + D$, where particles A and B with four-momenta p_A and p_B and masses m_A and m_B scatter to particles C and D with four-momenta p_C and p_D and masses m_C and m_D. A schematic representation of this process is given in Figure A.1. For this scattering process the Lorentz-invariant Mandelstam variables[1], s, t, and u are defined by

$$s = (p_A + p_B)^2, \tag{A.1}$$

$$t = (p_A - p_C)^2, \tag{A.2}$$

$$u = (p_A - p_D)^2. \tag{A.3}$$

They satisfy the relationship

$$s^2 + t^2 + u^2 = m_A^2 + m_B^2 + m_C^2 + m_D^2. \tag{A.4}$$

[1]Reference [19] is used as a starting point for many of the kinematic expressions obtained in this section.

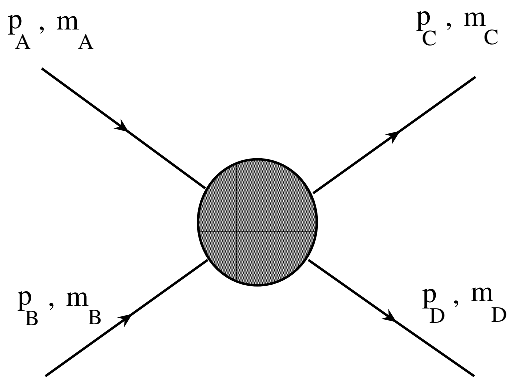

Figure A.1: Generic scattering reaction $AB \to CD$. The particles i ($i = A, B, C, D$) have masses m_i and four-momenta p_i.

An expression for the initial and final three-momenta in the center-of-mass, $\boldsymbol{p_i}$ and $\boldsymbol{p_f}$, is derived from the center-of-mass energy. For the reaction shown in Figure A.1 the center-of-mass energy is given by

$$\sqrt{s} = \sqrt{|\boldsymbol{p_A}|^2 + m_A^2} + \sqrt{|\boldsymbol{p_B}|^2 + m_B^2} \; . \tag{A.5}$$

After squaring this equation twice, making use of the definition of the center-of-mass, namely that $|\boldsymbol{p_A}| \equiv |\boldsymbol{p_B}| \equiv |\boldsymbol{p_i}|$, and rearranging the terms so that all $|\boldsymbol{p_i}|$ terms are on one side, one obtains

$$s^2 - 2s(m_A^2 + m_B^2) + (m_A^2 - m_B^2) = 4|\boldsymbol{p_i}|s \; . \tag{A.6}$$

This equation is readily solved for $|\boldsymbol{p_i}|$, giving the expression for the center-of-mass three-momentum of the incoming particles A and B,

$$|\boldsymbol{p_i}|^2 = \frac{[s - (m_A + m_B)^2)][s - (m_A - m_B)^2]}{4s} \; . \tag{A.7}$$

The expression for $|\boldsymbol{p_f}|$ is identical, except that m_A is replaced with m_C and m_B with m_D.

It is customary to express the results of the deuteron photodisintegration cross section measurements in terms of the invariant cross section $\frac{d\sigma}{dt}$. The invariant cross section is obtained from the standard differential cross section in the center-of-mass frame,

$$\frac{d\sigma}{d\Omega_{cm}} = \frac{1}{64\pi^2 s}\frac{|\boldsymbol{p_f}|}{|\boldsymbol{p_i}|}|M|^2 \tag{A.8}$$

by multiplication with the Jacobian for the coordinate transformation from center-of-mass to the invariant coordinates. The Jacobian for this transformation is given by

$$\frac{d\Omega_{cm}}{dt} = \frac{\pi}{|\boldsymbol{p_i}|\ |\boldsymbol{p_f}|} \approx \frac{\pi}{s}\ . \tag{A.9}$$

Thus the following form is obtained for the invariant cross section:

$$\frac{d\sigma}{dt} = \frac{|M|^2}{64\pi s|\boldsymbol{p_i}|^2}\ . \tag{A.10}$$

This relation is used in Chapter 2.

A.2 Reconstructed Photon Energy E_γ

In the two-body deuteron photodisintegration reaction, a beam of photons is incident on a target of deuteron nuclei, which are at rest in the laboratory frame. The scattered proton has momentum $\boldsymbol{p_p}$ and scattering angle θ_p. The energy of the incident photon can be reconstructed from the proton laboratory momentum and scattering angle. Figure A.2 defines the reaction kinematics for this process. The relationship between E_γ and ($\boldsymbol{p_p}$,θ_p) is determined with use of the the two-body scattering kinematics presented in Section A.1. For two-body deuteron photodisintegration, the Mandelstam variables become

$$\begin{aligned} s &= (p_\gamma + p_d)^2, & \text{(A.11)} \\ t &= (p_\gamma - p_p)^2, & \text{(A.12)} \\ u &= (p_d - p_p)^2. & \text{(A.13)} \end{aligned}$$

and relationship A.4 is expanded giving

$$p_d^2 + 2p_\gamma \cdot p_d + p_p^2 - 2p_\gamma \cdot p_p + p_d^2 + p_p^2 - 2p_d \cdot p_p = m_d^2 + m_p^2 + m_n^2\ , \tag{A.14}$$

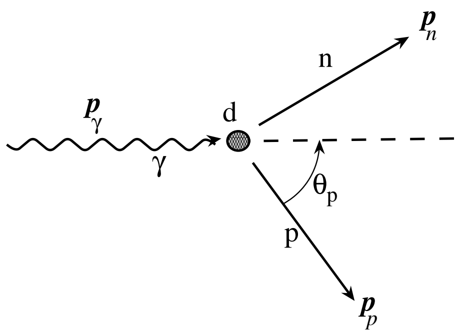

Figure A.2: Definition of the kinematics for the two-body deuteron photodisintegration reaction $\gamma d \to pn$ in the laboratory frame.

since $p_\gamma^2 = 0$. After substitution of the masses, energies and particle 3-momenta Equation A.14 becomes:

$$m_d^2 + 2E_\gamma m_d + m_p^2 - 2(E_\gamma E_p - \mid \boldsymbol{p_\gamma} \mid\mid \boldsymbol{p_p} \mid \cos\theta_p^{lab}) + m_d^2 + m_p^2 - 2m_d E_p = m_p^2 + m_n^2 + m_d^2. \tag{A.15}$$

The expression for the reconstructed photon energy in terms of the proton lab momentum and scattering angle is obtained by rearranging the terms in Equation A.15 and solving it for E_γ, realizing that $\mid \boldsymbol{p_\gamma} \mid = E_\gamma$:

$$E_\gamma = \frac{E_p m_d - \frac{1}{2}(m_d^2 + m_p^2 - m_n^2)}{m_d - E_p + \mid \boldsymbol{p_p} \mid cos\theta_p^{lab}}. \tag{A.16}$$

A.3 Proton Energy at Pion Production Threshold

In the first available pion production channel of deuteron photodisintegration, one pion is created in addition to the final state proton and neutron, $\gamma d \to pn\pi^o$.

Figure A.3 shows a diagram of the break-up in the center-of-mass (CM) frame. The proton energy has a maximum at threshold pion production and is calculated from conservation laws in the CM-frame. Conservation of energy, $E_{cm} = E_p + E_n + E_\pi$, gives:

$$E_{cm} = \sqrt{p_p^2 + m_p^2} + \sqrt{p_n^2 + m_n^2} + \sqrt{p_\pi^2 + m_\pi^2} \tag{A.17}$$

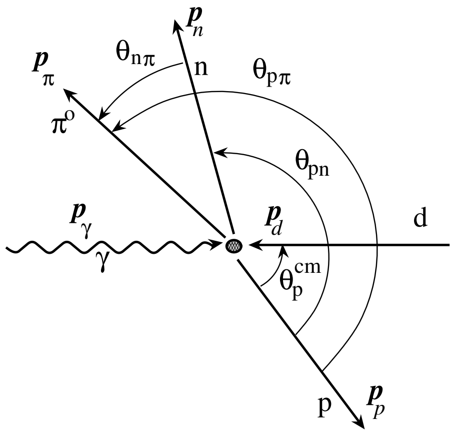

Figure A.3: Deuteron photodisintegration with a 3-body final state including a π^o. The figure shows the break-up in the center-of-mass frame. At threshold pion production the neutron and pion have parallel momenta and move in opposite direction of the proton.

and the sum of the particle momenta in the CM-frame is zero by definition:

$$\left(\sum_i \vec{p}_i\right)_{cm} \equiv 0 \qquad \Rightarrow \qquad \vec{p}_p + \vec{p}_n + \vec{p}_\pi = 0. \tag{A.18}$$

Using Equation A.18, the proton momentum can be rewritten as

$$p_p = \sqrt{p_n^2 + p_\pi^2 + 2p_n p_\pi \cos\theta_{n\pi}}, \tag{A.19}$$

where $\theta_{n\pi}$ is the angle between the neutron and pion as they depart. The extreme values of the proton momentum are obtained by differentiating Equation A.19 with respect to $\theta_{n\pi}$. Extreme values are found for $\theta_{n\pi} = 0°$, and $180°$, of which $\theta_{n\pi} = 0°$ corresponds to a maximum in proton momentum. As a consequence $\theta_{pn} = \theta_{p\pi} = 180°$. Since there are two unknowns in Equation A.17, an additional relationship between p_n and p_π is necessary to solve for the maximum proton energy E_p^{max}. Rewriting Equation A.18 as $\vec{p}_\pi = -\vec{p}_p - \vec{p}_n$, squaring the result, while using $\theta_{pn} = 180°$ gives

$$p_\pi = p_p - p_n. \tag{A.20}$$

After substituting this expression for p_π in Equation A.17 and differentiating the left hand side with respect to p_n one finds:

$$\frac{p_n}{E_n} - \frac{p_\pi}{E_\pi} = 0 \qquad \Rightarrow \qquad \beta_n = \beta_\pi \quad , \tag{A.21}$$

since E_p is a constant for maximum proton momentum.

Thus it is found that the maximum proton energy occurs when the neutron and pion travel in opposite direction of the proton with equal velocities. The maximum proton energy at pion threshold is then solved by makings substitutions in Equation A.17, using the relationships given in Equations A.20 and A.21. The result presented in Section 5.3.1 Equation 5.10 is obtained:

$$E_{p,max}^{cm} = \frac{E_{cm}^2 + m_p^2 - (m_n + m_{\pi^0})^2}{2E_{cm}}. \tag{A.22}$$

Appendix B

Fundamentals of Regge Theory

In this Appendix the fundamentals of Regge theory as pertaining to the discussion of the QGS model in Section 2.4.3 are presented. The discussion follows closely the material presented in Collins [62].

Regge theory is the theory of complex angular momentum plane, introduced by Regge in 1959 who showed that cases exist where it is useful to discuss the solution of the non-relativistic Schrödinger equation for potential scattering in terms of a complex angular momentum variable. Empirically, it has been observed that when hadrons are classified according to their quantum numbers (e.g. baryon number, charge, strangeness), that for a given set of quantum numbers sequences of particles (resonances) exist which have identical quantum numbers, except for their spin.

For a system of two pions, for instance, one could study the resonances as bound states, which are created by a potential $V(r)$ acting between the pions. In this case the radial Schrödinger equation has to be solved for an effective potential

$$V_{eff}(r) = V(r) + \frac{l(l+1)}{r^2} \ . \tag{B.1}$$

For increasing orbital angular momentum l of the pions the binding decreases, because of the presence of the second term in $V_{eff}(r)$ (the centrifugal barrier term). Therefore high-spin resonances have higher masses because of the decreased effectiveness of the potential. Regge observed that if the Schrödinger equation is solved for arbitrary complex values of l, that the eigenvalues vary continuously along a trajectory in the complex l-plane. The physical solutions occur at $l = n\hbar$, (n is integer) and are connected by the trajectory. Thus, in general, sequences of composite particles of mass m_i and spin σ_i will lie on a Regge trajectory $l = \alpha(s)$ (s is the center-of-mass energy) which provides the relationship between sets of resonances through $\alpha(m_i^2) = \sigma_i$. The Regge trajectory has an approximate linear form, given by

$$\alpha(t) = \alpha_0 + \alpha' t \ , \tag{B.2}$$

where t, the square of the momentum transfer, is the familiar Mandelstam variable. Figure B.1 shows some of the baryon Regge trajectories. The high energy behavior of a scattering amplitude $\mathcal{A}(s,t)$ is predicted by Regge theory to have the form

$$\mathcal{A}(s,t) \sim s^{\alpha(t)} \ . \tag{B.3}$$

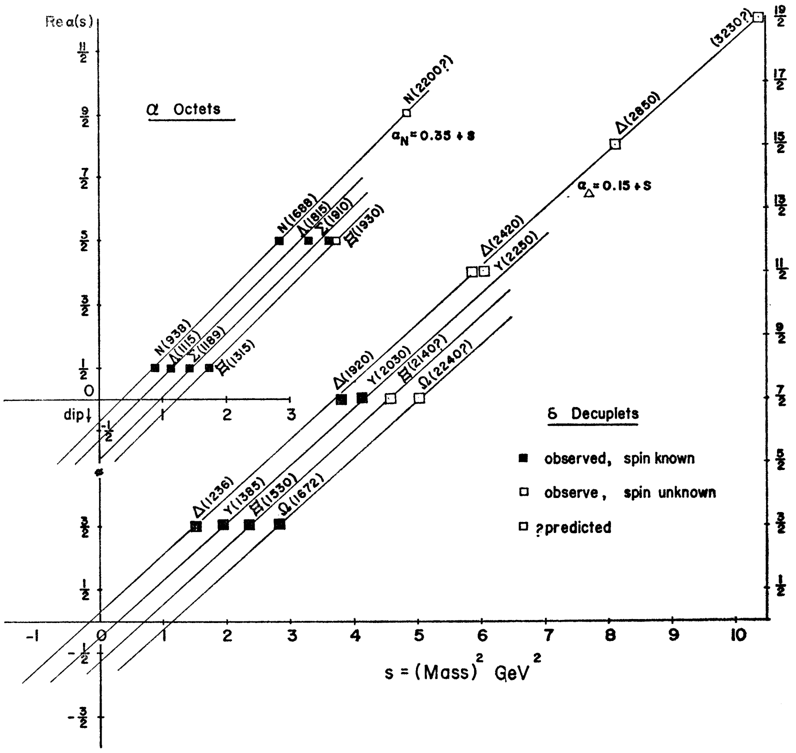

Figure B.1: Baryon Regge trajectories. Note the integer separation between the physical states. The figure is taken from Reference [117].

Appendix C

Hall C Cryogenic Target

The hall C cryogenic target provides hydrogen and deuterium targets for experiments in the end station. The cryotarget can be divided in three main subsystems. The hardware of the cryogenic target system is centered around the target cells filled with target materials, and consists of mechanical infrastructure to operate and position the cells in a cryogenic vacuum environment. A gas handling system, connected to the target hardware, controls storage of and manipulations with the target gases. The target hardware and gas handling system are instrumented to enable the cryotarget control system to monitor and control the target for operation in a safe way at settings desired by the experimental environment. Each of the three subsystems will be discussed in further detail in this Appendix. The target system has been well documented, and much information about the specifications, use and safety aspects of the cryotarget can be found in References [85, 118, 119].

C.1 Mechanical Construction and Parts

Figure C.1 shows the Hall C multiloop cryogenic target. The main mechanical part of the cryogenic target consists of three self contained target loops with target cells that contain the target fluid. The three target loops are suspended from the cryo tower, which rests on the scattering chamber top plate. The plumbing and electrical wiring which connect sensors and plumbing inside the cryotarget to the gas panels, refrigeration services and electrical instrumentation panels outside, enter the target

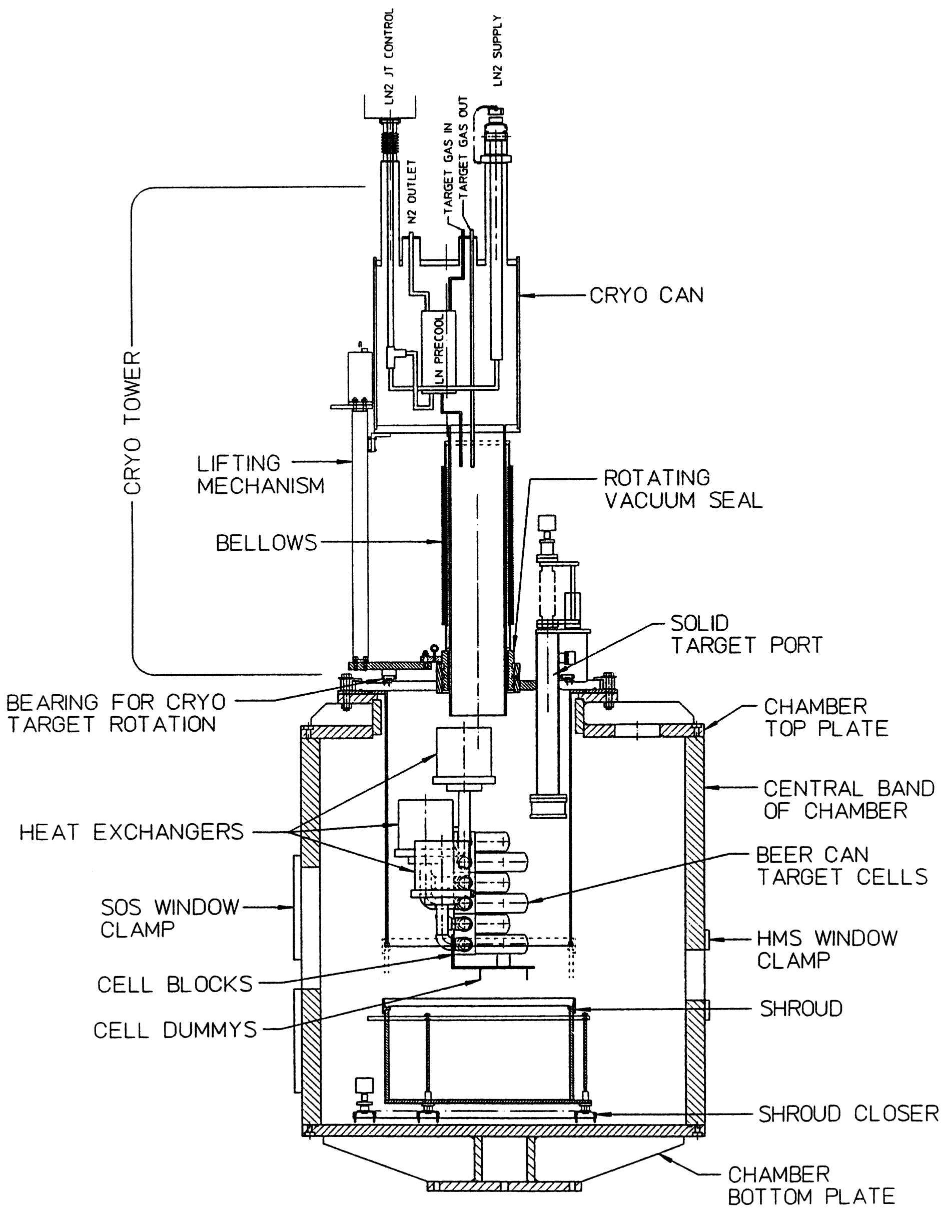

Figure C.1: The Hall C multiloop cryogenic target inside the scattering chamber.

through the cryo can at the top of the cryo tower. The cryo tower supports motion mechanisms to enable lifting and rotation of the targets. Since a cryogenic system cannot be maintained in air due to conductive and convective heat load, the cold parts of the target are kept under vacuum in the Hall C scattering chamber. Moreover, since hydrogen and deuterium are explosive gases, the vacuum also serves as an oxygen deprived environment in case of a cell failure. To reduce radiative heat load in the vacuum, the cold target parts are wrapped in super-insulation. The Hall C scattering chamber is not tall enough to allow for solid targets to be suspended from the cryo stack, therefore a separate solid target ladder is installed. The two different stacks also provide better means of doing separate maintenance. A discussion of the main mechanical components is presented below.

C.1.1 Scattering Chamber

The scattering chamber is made from a single forged ring of 6061-T6 aluminum (inner diameter 48.5 inch, wall thickness 2.5 inch, height 53.75 inch) which rests on a bottom plate, which has a pedestal that is bolted to the pivot point (common center of rotation of the Hall C spectrometers). A top plate seals the chamber off. The ring has cut-outs consistent with the angular acceptance and full angular ranges of the HMS and SOS. Thin aluminum vacuum windows are clamped over these openings. The opening for the SOS is 5 inches tall, and has a 0.008 inch thick 5052-H39 aluminum vacuum window. On the HMS side the opening is 8 inches tall, covered by a 0.016 inch thick 5052-H34 aluminum window. The ring has a beam entrance and beam exit port, as well as vacuum and view ports. A gate valve is installed in the beam entrance tube, so that the scattering chamber, which is part of the accelerator vacuum during data taking, can be isolated in the case of a target failure. The beam exit tube is sealed with 0.002 inch thick titanium foil.

The top plate has numerous openings, two of which serve as feed throughs for the solid target and cryotarget. The solid targets are mounted on a vertical ladder which can be moved remotely into the beam, or fully retracted in its own tubular

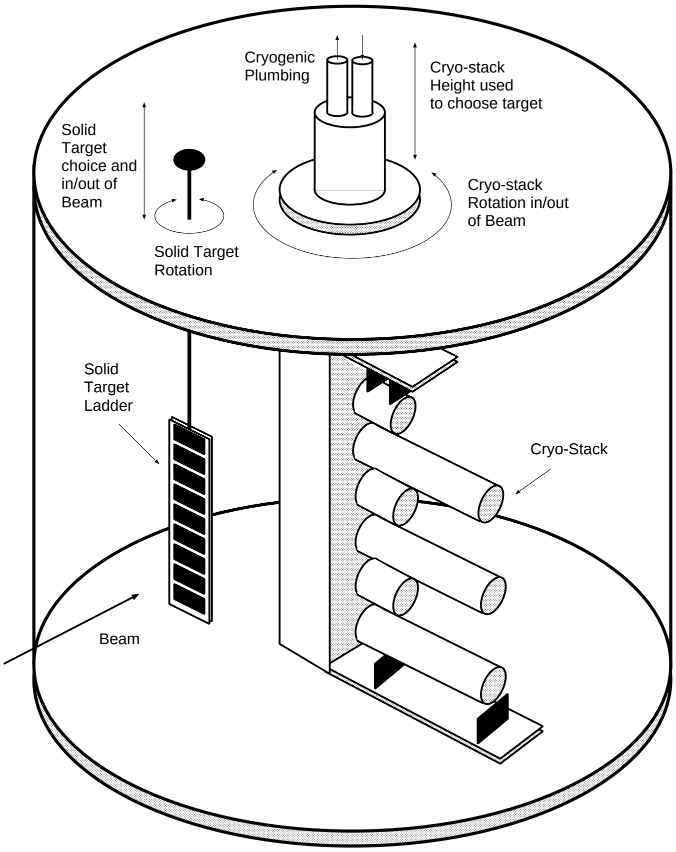

Figure C.2: Cut-away view of the Hall C scattering chamber. Figure courtesy of D. van Westrum.

vacuum chamber which can be sealed off from scattering chamber to facilitate solid target replacements or repairs. The cryotargets and attached plumbing are inserted through a large hole in the scattering chamber top plate. A transition spool piece supports the bottom plate of the cryo tower which in turn supports the cryotarget lifter and rotator. When measurements with solid targets are required, the cryotargets can be "parked" in a position outside of the HMS acceptance, by fully lifting them, followed by a 90° rotation. Figure C.2 shows an open view of the scattering chamber, with the cylindrical wall removed. Shown are the solid target ladder in inserted position, and the cryotarget stack which has been rotated 90° to its position out of the beam. Vacuum in the chamber is maintained by a Leybold 1000 liter per second turbomolecular pump at a level $\sim 10^{-6}$ torr. A Leybold Trivac roughing pump serves as the second stage.

C.1.2 Target Loop

A target loop consists of two target cells on a cell block, connected with plumbing to a heat exchanger, which has a circulation fan embedded in it. In the supply and return pipes to and from the cell block two heaters are installed which are used for temperature control. Target temperature control will be discussed in Section C.3. Figure C.3 is a scale drawing of a typical target loop. The various parts will be discussed below, except for the cell block with is the topic of the next section.

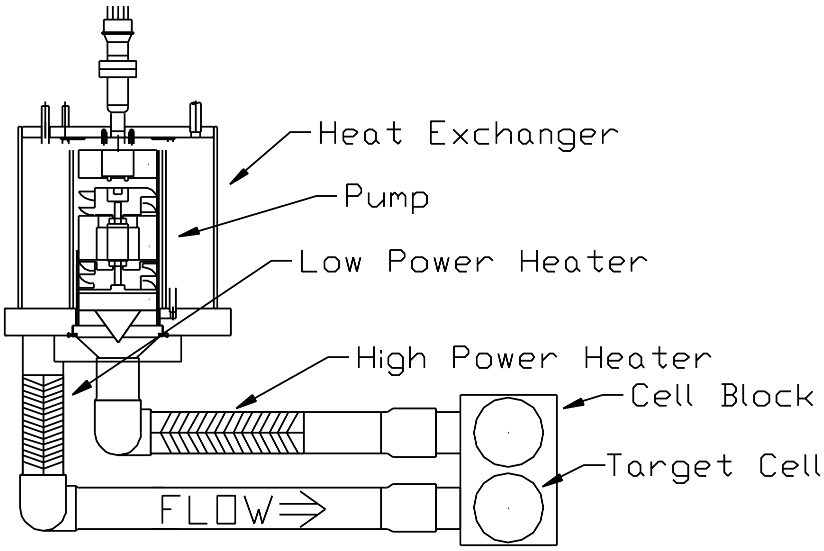

Figure C.3: Scale drawing of a cryogenic target loop. Figure courtesy of D. Meekins.

Figure C.4 shows a cross section of the target heat exchanger. The heat exchanger is fabricated from stainless steel cylinder shells (the largest has outer diameter $\sim$7.5 inch), which are arranged concentrically so that 4 partitions are created. The smallest inner partition houses the circulation fan. The outer three partitions each house 10 turns of copper fin tube (0.25 inch diameter, with fourteen 0.125 inch tall cooling fins per inch). Each wrapping of fin tube forms an "independent" coolant pass (see Section C.1.4).

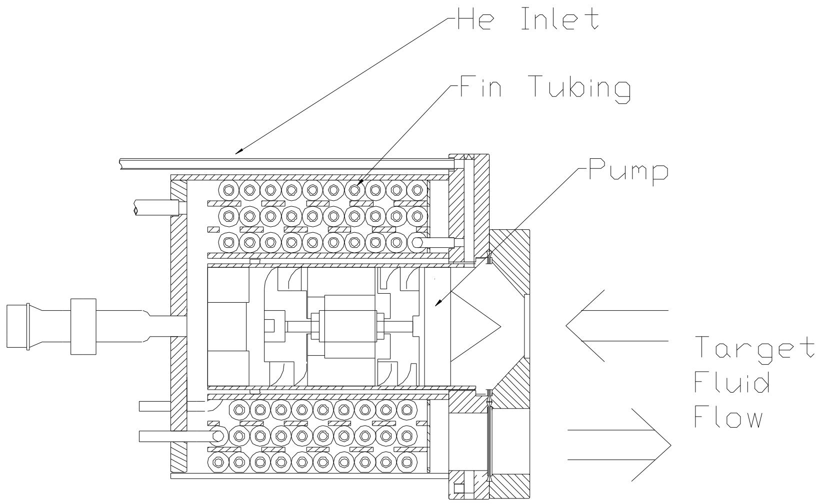

Figure C.4: Cross section of a target heat exchanger. Figure courtesy of D. Meekins.

The refrigeration fluid, 19 Atm. ^{4}He gas at $\sim$4 K from the CEBAF Central Helium Liquefier (CHL) flows through the fin tubes. A circulation fan immersed in the target fluid forces the target fluid to flow over the finned outer surface of the tubes, so that heat can be transfered to the fin tubes and helium refrigerant. The fans are built using three-phase AC induction motors from computer cooling fans (Globe Motors Vane-Axial Blower VAX-3-FC). Screw-like aluminum blades are attached to both sides of the rotor, creating a 2 stage axial fan. The motors were initially run asynchronously with a driver consisting of a stepdown transformer and a variac, which has maximum output of 30 V, 5 A. Currently a variable frequency drive controller is used. The fan has a tachometer, a pick-up coil that views the flux change of a permanent magnet attached to the rear blade (see Figure C.10), which is used to monitor the fan speed (see also Section C.3).

Both heaters are "hair dryer" style heaters (the heater element is similar to the heater core in a hair dryer). The low power heater is wound on a G10 carrier board from 0.0179 inch diameter Nichrome wire with a resistance of 1.993 Ω per foot. The low power heater is controlled by an Oxford ITC502 smart temperature controller.

The heater has a typical resistance of ~24 Ω, and maximum power output 80 W. The high power heater is wound on an anodized aluminum carrier board. This heater was wound with thicker Nichrome wire (0.051 inch diameter) with a resistance 0.2544 Ω per foot, and has total resistance ~2 Ω. The high power heater is fed by a 40 V 25 A power supply (Power Ten Inc, Series 3300 D, model 4025) and has a maximum output ~800 W.

C.1.3 Assembly and Testing of the Cell Blocks

Each cell block is assembled from 9 aluminum parts, the cell block base, two cells, two retainer rings, two upstream window tubes, and two upstream windows. Assembly of the cell block requires 6 solder joints. The parts which are soldered, are plated with copper at the surface where the solder joint is made. Figure 3.6 shows a drawing of a cell block used in the cryogenic target.

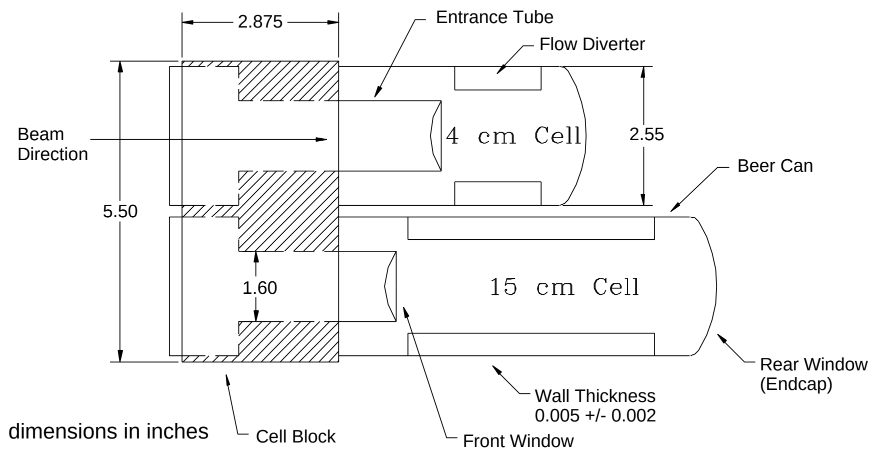

Figure C.5: Cross section of a target cell block. Figure courtesy of D. Meekins.

The cell block base is machined from a solid block of 6061 series aluminum. The side has two circular holes, where two bi-roll aluminum-stainless transition pieces are welded, so that the stainless steel supply and return plumbing from the heat exchanger can be welded to the block. The cell block is plated with copper at the front, where the cans are connected using the retainer rings, and at the rear, where the upstream window tubes are inserted.

Both cells are made from 3004 series aluminum beer can blanks (outer diameter 2.55 inch), supplied by Coors Brewing Company [120]. The beer can blanks are produced by extrusion and have thin walls (0.005 $\pm$ 0.002 inch) with uniform wall thickness, which is important to reduce absorption and energy loss of the detected final state particles. With a punch-die the cans, which are supplied by Coors with flat ends, are domed with a semi-ellipsoid surface. To further reduce the endcap wall thickness, the domes are chemically etched. The endcap wall thickness after etching are measured on a Coordinate Measuring Machine. The thicknesses are listed in Table C.1 and come from References [86, 86].

Each block has two cells, a short '4 cm' cell (outside length 11.4 cm), and a long '15 cm' cell (outside length 16.5 cm). At the open end the first 0.75 inch of the cell is plated with copper. The cells are secured to the block by slipping a 0.5 inch wide retainer ring over the cell. Then a solder joint is made with Duratec (or Alpha Metals) solder paste (63% Sn, 37% Pb melting point 360 deg F).

The upstream window tubes are machined from 6061 series aluminum, and have flow diverters welded to them. The flow diverters create a turbulent flow, and also ensure that the flow pattern is close to 100% transverse to the beam direction. Each upstream window tube is sealed with a convex upstream window (radius of curvature 3.25 inch) which is formed with a punch die from 0.0028 inch thick 5052-0MF aluminum foil. Both the upstream window tube and the window are plated with copper, and soldered together. This joint is made with Kester solder cream with RMA flux (62% Sn, 36% Pb, 2% Ag, eutectic blend which melting point of 360 deg F).

In the final assembly step, both upstream window tubes are soldered in place in the cell block. For this joint a indium solder paste (25% In, 37.5% Sn, 37.5% Pb) with NC-80 flux is used. The melting point of this paste is 300 deg F, in order to prevent that the solder joints to the cells and upstream windows melt. In addition to the solder connection, the upstream window tubes are held in place in the cell block by capscrews.

Year	Target cell	Nominal length (cm)	Cold Length (cm)	Endcap Thickness (cm)
1996	Loop 1	15	15.34 $\pm$ 0.04	0.0119 $\pm$ 0.0005
	Loop 2	15	15.19 $\pm$ 0.04	0.0130 $\pm$ 0.0005
	Loop 3	15	15.12 $\pm$ 0.04	0.0135 $\pm$ 0.0005
1997	Loop 1	12.5	12.48 $\pm$ 0.04	0.0105 $\pm$ 0.0005
	Loop 3	12.5	12.46 $\pm$ 0.04	0.0114 $\pm$ 0.0005

Table C.1: Cold cell lengths from survey. The front windows all have a thickness 0.0071 $\pm$ 0.0003 cm.

The actual target cell lengths are calculated from survey results of warm, and cold target, so that thermal contraction can be estimated. Table C.1 gives a listing of the cell lengths for the cells used in this experiment (see also Section 3.4). During a major target overhaul in the Spring of 1997 new cell blocks were installed, with nominal 12.5 cm cells, instead of the 15 cm cells. A summary of all survey results is given in References [86, 87].

For safe operation with explosive gases, the cell block has to withstand the target operating pressure and reasonable excursions therein. In addition, the block has to be vacuum leak tight. For a safe operation margin, the cells and upstream windows need to hold at least twice the target operating pressure under standard conditions (p_{op} ~25 psiA). The burst pressure of the target cells was determined by a destructive hydrotest with cells which were soldered to a test block. In a hydrotest, the object is pressurized with water instead of gas, to reduce the risk of violent failure. Both 4 cm and 15 cm cells were tested and burst pressures varied from 72 psiG to 156 psiG. The upstream windows subject to test were soldered to a tube, and hydrotested to determine the burst pressure. The window-tube solder joint was cold shocked three times in a liquid nitrogen bath, before the hydrotest took place. Burst pressures varying from 75 psiG to 120 psiG were measured. The test results show that the cells and upstream windows have burst pressures well in excess of the requirement.

Prior to assembly of the cell block, the upstream window tube–upstream window solder joint is leak tested using a helium mass spectrometer. The remaining four solder joints in the cell block assembly, which connect the two beer cans and two upstream window tubes to the block, are tested in a reverse leak test, where the block is pressurized with helium to 58 psiA (twice the operating pressure) in a vacuum chamber connected to the leak detector.

C.1.4 Refrigeration

The target is connected to the CEBAF on site refrigeration lines through the cryo can. At the cryo can, the main helium refrigerant supply and return enter the target plumbing. At the start of the experiment, the main supply was 4 K helium gas delivered by the CEBAF Central Helium Liquefier (CHL). Later a switch-over was made to 14 K helium (19 ATM) from the End Station Refrigerator (ESR), which also feeds the spectrometer magnets and the other end stations. In addition to the helium lines, the target is also connected to liquid nitrogen supply and return lines. The liquid nitrogen is used in the precooler heat exchanger, which is located in the cryo can. When the target gases enter the target at the cryo can they pass through the precooler before they flow to the heat exchanger, so that the temperature is $\sim$70 K prior to liquefication. In this way a smaller heat load on the helium refrigerant is accomplished.

The flow of the coolant in the target is controlled using 4 Joule-Thompson (J-T) valves. One of the J-T valves controls the nitrogen flow for precooler heat exchanger. There are three helium J-T's, one that controls the absolute helium supply, and two J-T's which control the relative flow through Loop 1 and Loop 3, by enabling bypass of fluid flow around the loops (the full coolant flow always passes through Loop 2). A flow schematic of the coolant in the target is presented in Figure C.6. The figure also shows how the heat exchangers are connected in series by "cross-connecting" the three separate coolant passes in each heat exchanger. Since the individual concentric fin tube coils have different lengths, coils of different length are connected, when the three heat exchangers are connected in series, to equalize the total pressure drop

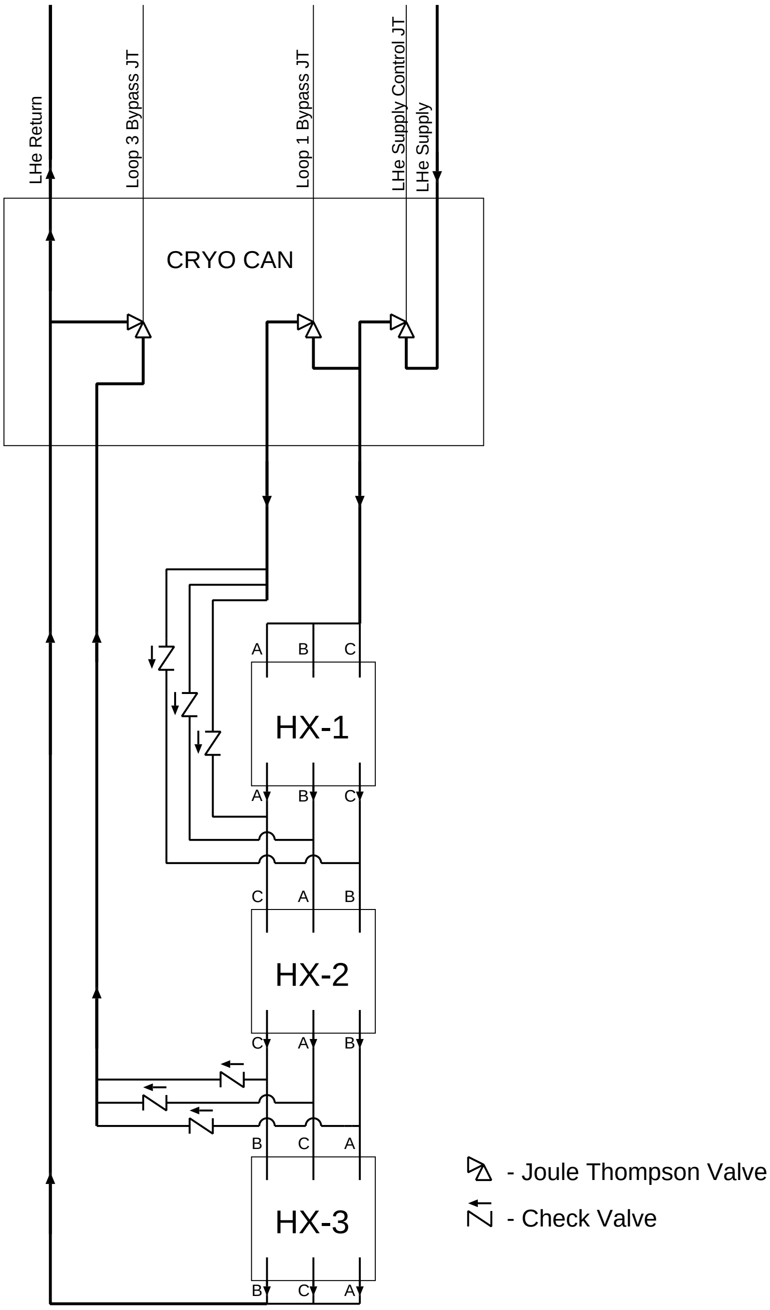

Figure C.6: Schematic of the coolant flow and JT-valve control in the cryotarget.

of the refrigerant over the 3 heat exchanger system. Check valves are installed in the bypass tubing, so that the refrigerant flow is unidirectional. The “main” helium supply J-T regulates the inlet of helium in the target, and is usually operated during target cool down, after which it is maintained at a fixed setting. Typical inlet flow of 4 K helium to provide enough refrigeration for a 200 W target was $\dot{m}$=14 g/s . Each bypass J-T can divert as much as 50% of the helium flow. The bypass J-T's are often re-adjusted during target operations, when the cooling requirements for a particular loop change. Each valve is set using a digital I/O line on the ADIO card (see Section C.3), which communicates the setting to a specially built J-T valve control box, that drives a stepper motor which moves the valve. The fluid flow has logarithmic dependence on the valve lift, i.e. the initial 20% lift creates the largest in flow of coolant. Position read-back from the valve is accomplished with a Linearly Variable Differential Transducer (LVDT). The LVDT has an analog output 0–10 V corresponding to 0–100% open. The output voltage is read with analog inputs on the ADIO card.

C.1.5 Target Motion

The multiloop target is created by a combination of three complete target loops, where the cell blocks are stacked together in a vertical stack (see Figure 3.7). The three loop system is suspended off of a stainless steel pipe, which is part of the cryo tower (see Figure C.1) and extends into the scattering chamber. Since the pipe is part of the scattering chamber vacuum, a vacuum bellows is installed around it. The cryo tower supports the vertical motion mechanism (the cryotarget lifter) which is used to lift the appropriate target cell to the location where the beam passes through. Since the solid targets are mounted on a separate ladder, their insertion is enabled by lifting the entire cryotarget including the cryo tower to the top position, after which it is rotated out of the beam line (with the cryotarget rotator) over a 90° angle, so that the cryotargets are in a position where they do not obstruct the HMS acceptance.

The mechanical lifting system consists of three carriages that move over vertical rails, equally spaced at 120° intervals around the cryo tower. The carriages are connected to the bottom of the cryo can. The rails are supported at the bottom by the rotator plate (see below), and by a common aluminum ring at the top. Each carriage moves through a ball screw, which is driven by an AC servo motor with 50 to 1 gear reducer. Each servo motor is equipped with a 12 bit resolution resolver. The three motors are run in a master-slave setup by a Koll-Morgan BDS5 control system. In the master-slave setup the resolver of one motor (the master) is used to determine the position and synchronize the motion of all three motors. The resolvers of the two slaves are idle. Communication with the control system is established over a RS-232 serial line.

The cryotarget and cryo tower are rotated by single mechanical arm, which has pivots on both ends. One pivot is connected to the scattering chamber top plate, the other to the rotator plate. The rotator plate is supported on the cryo target base plate with a "rail-type" bearing. At the center hole below the bellows, where the loop support pipe passes into the scattering chamber, the rotator plate and base plate are connected with a piston type rotating seal with dual O-rings. A port is connected to the volume between the O-rings, so that the seal can be differentially pumped. The mechanical arm is moved by a screw mechanism, driven by a DC stepping motor with is controlled using an IDC S5851 stepping motor controller with RS-232 serial interface. The position is determined by step counting. The arm allows for continuous positioning of the cryotarget over roughly a 0–90° angle range, but only two positions are used, 0° (target in beam) and 90° (target out of beam).

For accurate positioning as well as for safety reasons both the target lifter and rotator have home and limit switches installed. The limit switches are located at the allowed extreme positions of travel, and will terminate motion when activated. The home switch is located at a pre-defined location, so that the position read-out can be re-calibrated after a power failure. Each of the target lifter servo motors also has a fail safe brake, which is activated after the motion is completed. Target motion is interlocked with the accelerator fast shut-down (FSD) system to prevent a possible dangerous situation when the target is moved while it receives beam from the accelerator.

C.2 Gas Handling System

The cryotarget is connected to a gas handling system, which is used for all manipulations with target fluids, like the pump-purge cycles prior to the filling, and the filling and emptying of the target loops. The gas handling system consists of three separate systems (one for each loop), which have a common pump-purge gas system. The three systems are made up from valves, regulators and pressure gauges, mounted on panels close to the pivot in Hall C. Supply and return lines from each of the panels enter the cryotarget through the cryo can. At the time of the commissioning of the cryotarget two fully instrumented gas panels for use with explosive gases were present and connected to Loop 1 and Loop 3. Loop 2 was initially connected to the common ^{4}He pump-purge panel. Presently Loop 2 is connected to a complex system for handling of ^{3}He gas (inert, but extremely expensive). Figure C.7 shows the schematic layout of the deuterium gas handling system. The hydrogen system is identical.

Since the hydrogen and deuterium systems are intended for use with explosive gases, they are are constructed from stainless steel components, and connections are welded where possible. All valves, transducers etc. are approved for use in explosive (NEC class 1, division 1, group B) environments. The system makes use of manual (NUPRO) valves and solenoid (ASCO) valves. The solenoid valves are locally as well as remotely controllable and are used at locations were opening of a valve cannot introduce any contaminations (i.e. only between hydrogen lines). The solenoids are switched using AC power, and have an LED indicator placed next to them to show the valve status. Valve status is also read back using the target control computer (see Section C.3).

Gas pressures in the target loops and the gas system are measured with analog (dial) gauges and electronic pressure heads (transducers). The pressure transducers are Sensotec model 811 FMA, with range 0–100 PSI and a 0.25% full scale accuracy. The pressure heads are connected to a Sensotec SC200 read-out unit, which can read out up to four transducers. Communication between the computer and the SC200 read-out box is established using a RS-232 serial line. An Omega PX750-HDI differential pressure transducer is installed between the feed and return line to the target loop, to measure the pressure (pump head) generated by the circulation fan. The amount of head generated is a measure for the proper functioning of the fan and can also be used to ascertain whether the target loop has been filled. The Omega has its transducer in an explosion proof chamber. The transducer has a 4-20 mA output corresponding to 0–150 inches of water, with a 0.2% full scale accuracy. The output signal is read by an Omega DP41E read-out unit, which communicates its reading to the target computer through a single channel RS-232 connection.

Normal operating pressures for the hydrogen and deuterium targets are 24 psiA and 20 psiA respectively. In order to prevent damage to the target cells in case of unforeseen pressure surges, a triple redundant relief system is installed. A solenoid valve in the fill line relief assembly (SV 9084 for the deuterium gas panel) is slaved of a pressure transducer output in the return line (PT 9093 for deuterium). The solenoid valve opens at 15 psiG. In the event the solenoid cannot dampen the pressure surge fast enough, a mechanical relieve valve with crack pressure 20 psiG (RV 9086 for deuterium) opens. Should the pressure still rise, then a carbon composite rupture disk (RD 9097 for deuterium) will break at 40 psiG. All relief lines from the target are tied into the main vent line, which contains an inert nitrogen atmosphere that is vented to the outside environment through a stack outside the experimental hall. Both the solenoid valve and the mechanical relief valve close after the pressure surge has dampened, however the rupture disk creates a permanent opening to the main vent line.

The relief system was of great importance during the first months of target operation, when the cryotarget was filled directly from gas cylinders. No expansion volume had been connected to the gas system and the system proved to be very susceptible

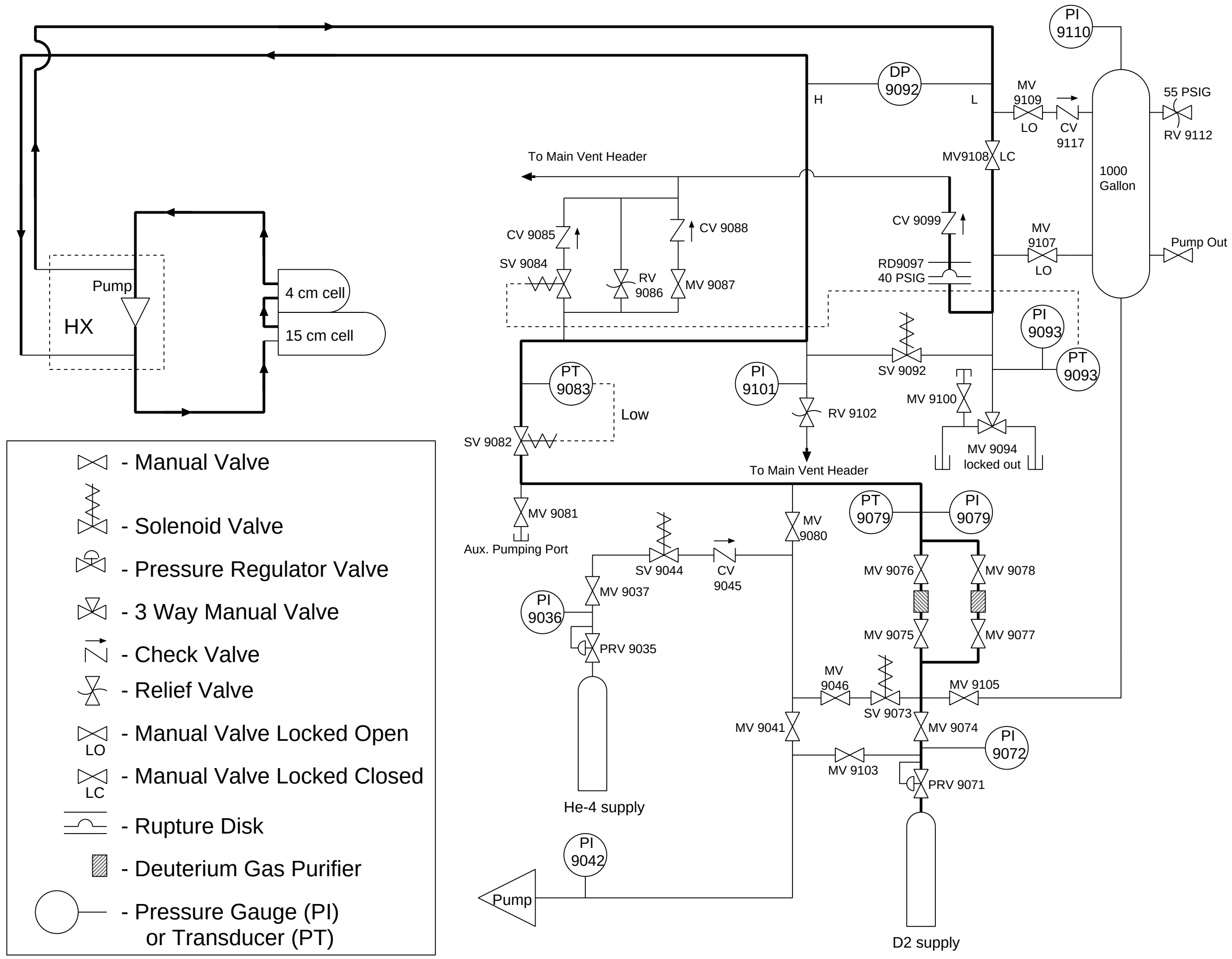

Figure C.7: Schematic of the deuterium gas handling system.

to pressure surges during filling. Because of the expense incurred with every fill of deuterium gas a 1000 gallon storage tank was installed. A similar tank was also installed in the hydrogen system, since the tank serves as a ballast/expansion volume as well, to dampen out pressure excursions. With the tank in place the relief header should technically only be necessary in unforeseen situations. The target loops have a volume of about 3 liter (the heat exchanger has a volume of about 2 liter, the plumbing and cell block combined another liter). Since 1 liter of liquid hydrogen is equivalent to roughly 800 STP liters of gaseous hydrogen, a total of roughly 2500 STP liters of gas is required to fill a target loop. The initial fill is done using gas from vendor-supplied cylinders. At warm-up the gas is collected in the 1000 gallon reservoir, which serves as the supply for subsequent fills.

C.2.1 Target Gas Analysis

After completion of the experiment, samples of the target gases were collected to determine their chemical composition. Prior to the installation of the recovery tank, which happened while the experiment was well underway, the target was filled directly from gas cylinders. Because the original expansion tank had a small volume, instabilities in the target pressure caused the deuterium to be vented and lost on three occasions. The three occasions included deuterium from two suppliers, and and a sample from a gas cylinder from each of the two lots was taken. Those samples are labeled deuterium sample 1 and sample 2. Deuterium sample 3 and the hydrogen sample were taken from their respective recovery tanks. The samples are collected in a 300 cm^3 flow-through stainless steel gas bottle (see Figure C.8) which has valves on both sides. The bottle is connected to a gas panel port on one side and to a roughing pump on the other side. Prior to the sample taking the bottle is evacuated, and baked out. Then a series of pump-purges is performed with the target gas flowing through the bottle, to dilute any remaining impurities from the evacuation. After that the final sample is taken and the bottle is sealed off. The complete sample taking procedure is described in [121].

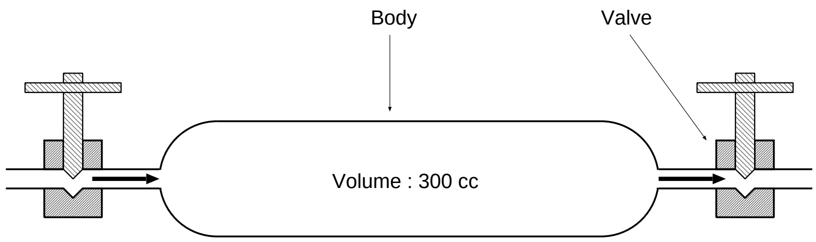

Figure C.8: Cross section of the flow-through gas analysis sample bottle.

The chemical composition of the samples was determined at Lawrence Livermore National Laboratory using Gas Mass Spectrometry [122]. A VG 30-01 Gas Mass Spectrometer was used for the analysis [123]. The sample molecules are brought in the vacuum of the gas mass spectrometer, where they are bombarded by an electron beam produced with a thorium iridium element. The electron beam breaks chemical bonds in the molecules, forming charged fragments, which are accelerated through a constant electrostatic field and a varying magnetic field after which they are detected on a collector. By varying the magnetic field an ion with a specific mass-to-charge (m/e) ratio can be directed to the collector. Quantitative analysis is achieved by comparing the measured mass spectrum with reference gas standards. Samples of approximately 5 cc were taken from each of the bottles, and each analyzed three times. The average and standard deviation of three analyses was calculated. The analysis results for the four samples are listed in Table C.2. The concentrations listed are in mole (volume) percent. The method is sensitive to gases present above 0.01%.

C.3 Cryotarget Control System

The many components that make up the complete cryogenic target have to be monitored and controlled to operate the target in a safe way at settings desired by the experimental environment. The core of the cryogenic target control system is a single board VME computer (Motorola MVME-162-12), the input/output controller (IOC),

Gas analysis				
Target Gas	Sample	Molecule	Concentration	Std. Deviation
D_2	1	D_2	99.59	0.01
		HD	0.301	0.002
		N_2	0.070	0.008
		O_2	0.037	0.004
D_2	2	D_2	99.54	0.013
		HD	0.220	0.001
		N_2	0.183	0.008
		O_2	0.060	0.004
D_2	3	D_2	99.28	0.01
		HD	0.616	0.003
		N_2	0.072	0.013
		O_2	0.037	0.004
H_2	1	H_2	99.81	0.01
		N_2	0.127	0.008
		O_2	0.061	0.004

Table C.2: Gas analysis results. The concentrations listed are in mole (volume) percent.

which interfaces with the target hardware.

EPICS [89] software in the form of a database is loaded on the IOC and used to monitor and control system parameters and variables of all the target subsystems using the database records [124]. Two types of databases exits, lower-level databases, which establish the direct communication with the target hardware through EPICS drivers, and higher level databases. The higher level database often uses records from lower level databases in order to perform calculations, or other manipulations with the records (e.g. feedback loops). In the cryotarget EPICS software the different subsystems have different lower level databases. One higher level database was developed [125]. In addition to the databases which only provide manipulation of cryotarget operation variables, "intelligence" is added to the control system using sequencers [126]. A sequencer or "Finite State Machine" is a computer code which looks for changes in certain parameters in the EPICS database and initiates an action based on the value of the monitored parameter. An example of a sequencer is the high power heater final state program discussed in Section C.3.2.

The IOC communicates with a personal computer and an HP 9000 workstation (located in the counting house) over the Hall C local ethernet. Communication between the user and the IOC is established through a Tcl/Tk [90] graphical user interface (GUI) that runs on the PC. A Tcl/Tk interface [127] enables communication with the EPICS database on the IOC. The GUI allows the user to inspect operating parameters, make interactive parameter changes and view strip charts of pressures and temperatures in the target system.

For a safe operation of the target, operating ranges and alarm set-points are defined for many critical system parameters like loop temperature, pressure, fan speed, and target vacuum. The alarm set-points are loaded in the EPICS Alarm Handler [128], which runs on the HP workstation. The alarm handler monitors all critical target parameters and provides a visible and audible warning when a variable makes an excursion outside of its operating range. A cryotarget data logger also runs on the HP workstation, which saves a predefined subset of target variables to a log-file on disk.

The software used in the target control system is described in great detail in Reference [129]. The hardware instrumentation of all target subsystems and related aspects of the target control is discussed in the following sections.

C.3.1 Instrumentation and Control of Target Subsystems

Figure C.9 shows a schematic layout of the control system and the communication lines between various components of the system. The Motorola MVME-162-12 single board computer which serves as the input/output controller (IOC) is located in a VME crate, located in electronics racks on the Hall C floor, behind the gas panels. The communication between the IOC and the target hardware components is predominantly through RS-232 serial connections. For this purpose, Industry Pack

(IP) serial cards are installed on the IOC motherboard through which serial communications are established using EPICS serial device drivers. All components that communicate with the IOC via serial lines are connected to a Green Spring serial break-out box. A ribbon cable from the break-out box is connected to the IP serial card on the IOC. The IOC and a separate IOC carrier board, which is also in the VME crate, also house a few other IP's which provide digital-to-analog (DAC) channels to provide output signals to drive hardware, analog-to digital (ADC) channels to read back signals, as well as digital I/O.

The control subsystems that communicate with the IOC through serial lines are the Sensotec SC200 pressure transducer and Omega differential pressure gauge readout units, cryotarget motion hardware and the Oxford ITC temperature controllers. All but the last type of controllers were discussed in previous sections. The Oxford ITC's play a major role in the target control system, since they provide the temperature readings that allow for loop temperature control. Since the relative fluctuation of target fluid density with temperature is much larger than with pressure (see Section 3.4), the target loops have to be maintained a constant and well-known temperature. The temperature instrumentation and control is discussed in Section C.3.2.

In the first year of cryotarget operation the circulation fans were run with a driver consisting of a stepdown transformer and a variac. This SLAC-style motor controller has a maximum output of $\sim$30 V, $\sim$5 A. A stepper motor is attached to the dial of the variac, to enable remote controlled setting of the voltage that drives the fans. The stepper motor is controlled through a CAMAC stepper motor controller. Communication between the CAMAC module and the IOC is established with a Kinetic Systems CAMAC Controller. Voltage and current setting of the fans are read back using ADC channels on the IP ADC on the IOC carrier board. The tachometer in the circulation fan gives off a frequency signal, which is read by the SLAC motor controller and displayed on the frequency meter in the front panel. The frequency signal is also read by the IP Quadrature card on the IOC carrier board. The tachometer frequency signal is intended to monitor the fan speed, but the tachometers

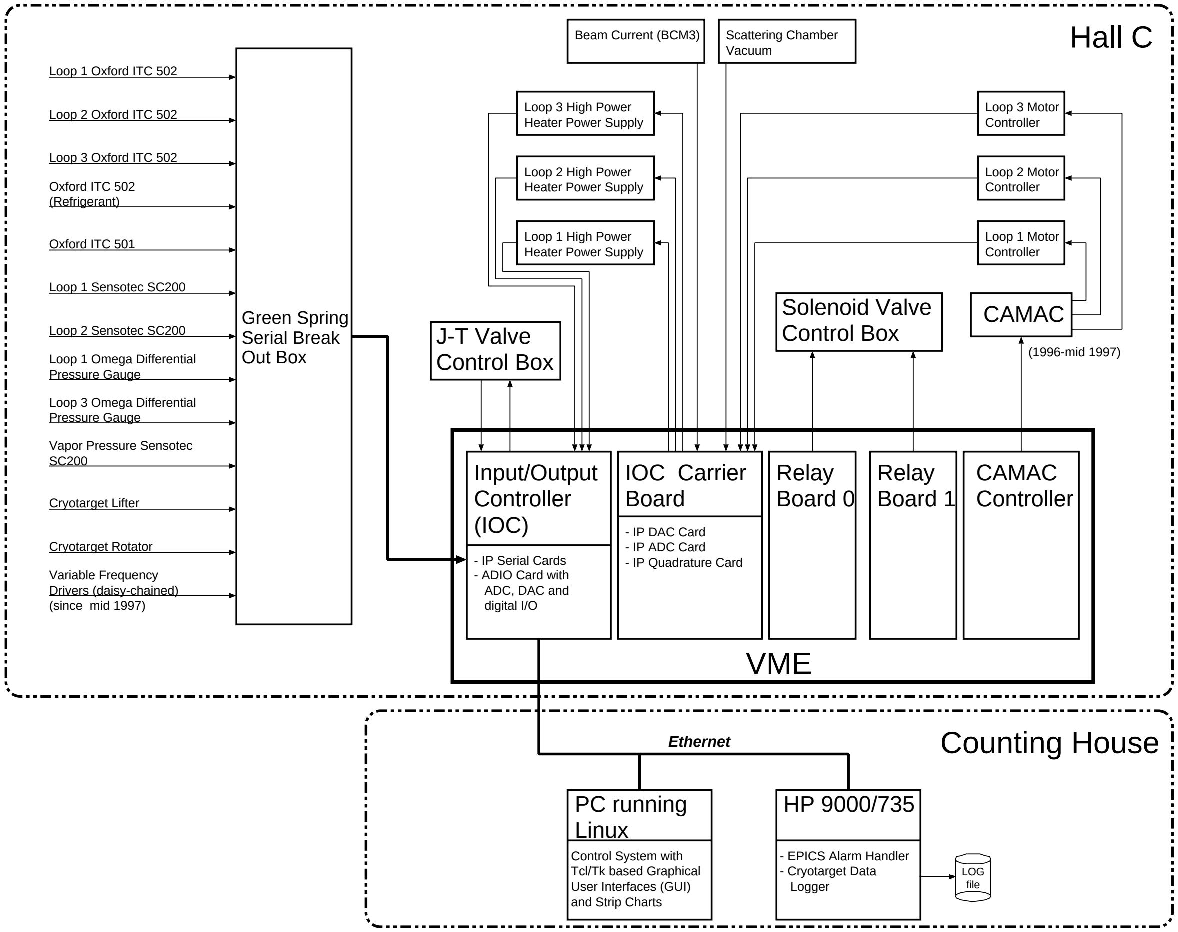

Figure C.9: Schematic of the cryotarget control system.

turned out to be fragile parts, and the pressure head across the fan as well as read-back of the fan operating voltage were determined to be a more reliable indicators of proper fan operation. Mid 1997 variable frequency drive controllers were installed to drive the circulation fans. The variable frequency drivers are daisy-chained and controlled by the IOC through one RS-232 serial line.

The high power heater power supplies are controlled by the IOC through use of the DAC Industry Pack, by supplying DAC signals to the voltage and current references on the unit. A 0–5 V DAC signal is applied to the voltage reference. The power supplies are operated in current limited mode, so that the DAC signal applied to the current reference (0–0.1 mV) determines the current through the load, and hence the output power. The unit has voltage and current monitors, which are read into ADC channels on the ADIO card. Since the voltage monitor gives a signal voltage equal to the voltage on the load (max. 40 V), the voltage monitor is read in the 0–10 V ADC through a 1:4 divider.

Two types of valves are controlled by the IOC, J-T valves, which are used to regulate the coolant flow, and solenoid valves in the gas panels. The J-T valves are set using the signal of digital IO lines on the ADIO card. The signal is sent to the J-T valve control box, which drives a stepper motor that moves the J-T valve. Position read-back from the valve is accomplished with a Linearly Variable Differential Transducer (LVDT), which has an analog output 0–10 V (corresponding to 0–100% open). The output voltage is read with ADC input lines on the ADIO card. The solenoids are controlled using a relay board in the VME crate. Two relay boards (VME Microsystems International Corporation, VMIVME-2232-100) are installed in the VME, that each have 32 channels with both normally closed (NC) and normally open (NO) contacts. Relay board 1 provides the relays used to switch the solenoid valves in the gas panels. The 24 V DC relays on the board switch 120 V AC relays that control the solenoids. Read-back of the relay (valve) status is done by reading the register on the relay board with a low level EPICS driver. The other relay board, relay board 0, provides the relays, which are connected to the accelerator fast shut down (FSD) system. The high level EPICS database is programmed to drive a relay on this board in case of a temperature, pressure or fan-speed emergency.

Several signals from other subsystems that relate to cryotarget operation are included in the control system. Cryogenics variables such as mass flows, temperatures and pressures in the refrigerant supply and return lines are monitored by an auxiliary Hall C IOC and communicated to the Tcl/Tk control interface over ethernet. The cryotarget IOC itself monitors the scattering chamber vacuum and beam current. The scattering chamber vacuum is measured with a cold cathode gauge connected to an MKS controller. An analog output of the controller is read into an ADC channel from the ADC card on the IOC carrier board, and used to display in the Tcl/Tk strip charts. Another output is connected to a relay, which, when closed, activates the accelerator fast shutdown system, and closes the gate valve in the beam pipe at the entrance of the scattering chamber. A beam current signal from the beam current monitor just in front of the target (BCM3) is read into a ADC channel of the IP ADC on the carrier board. The value of the beam current is used to calculate the power deposited in the target, which in turn is used in the finite state machine for heater operation (see Section C.3.2).

C.3.2 Temperature Instrumentation and Control

With the exception of coolant temperature diodes at the top of the cryo can, all temperature sensors of the target are located inside the scattering chamber. Each target loop is instrumented with sensors for resistive thermometry and vapor pressure thermometry. Figure C.10 shows the sensors for a typical loop. Two radiation resistant Lakeshore Cernox semiconductor resistors are mounted on the G10 low power heater board. Individual calibration of each Cernox resistor is performed at Lakeshore. Calibration curves from up to three Cernox's are loaded into an Oxford ITC502 temperature controller, which converts a resistance measurement to a temperature. The accuracy of absolute temperature is measurements is 100 mK. Temperature changes can be measured to 50 mK. The other resistive temperature measurement is carried

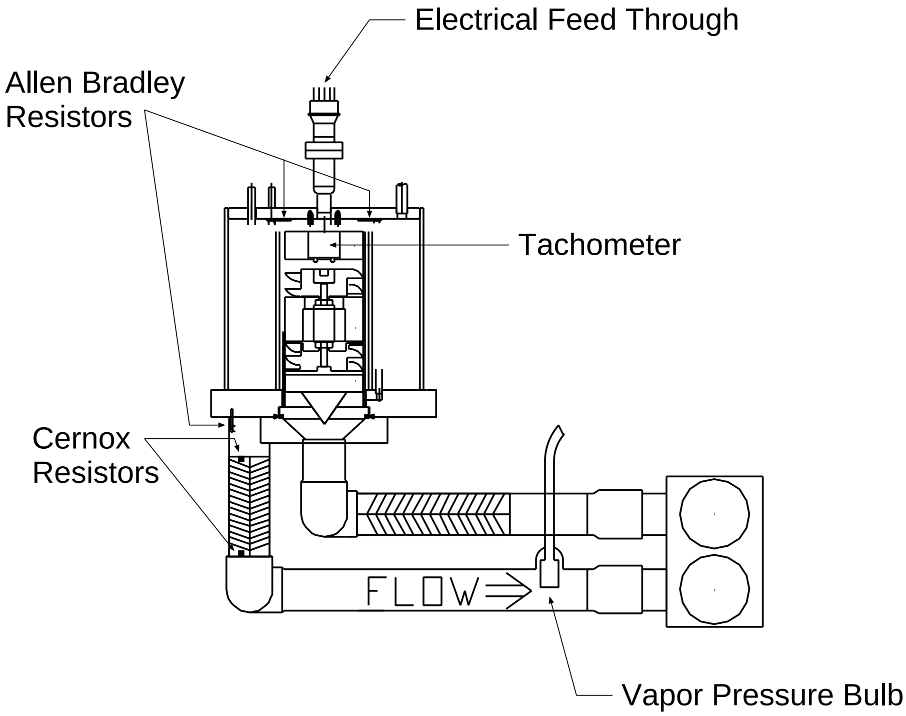

Figure C.10: Instrumentation of a typical target loop. The vapor pressure bulb at the top of the heat exchanger is not shown.

out using 270 Ω Allen-Bradley carbon resistors. The resistors were calibrated at CEBAF using liquid helium. The common calibration curve is loaded in an Oxford ITC 501 10-channel multiplexed temperature controller, which reads temperature from the 9 Allen-Bradleys of the three loops combined. Temperature measurement with a carbon resistor has limited accuracy and the sensors were only installed to determined the level of the liquid in the heat exchanger during filling.

Two hydrogen vapor pressure (VP) bulbs are submerged in the target fluid of the loop, one near the cell block, and one at the top of the heat exchanger (not shown in Figure C.10). The bulbs are charged with a small volume of hydrogen, and connected with capillary tubing to a high precision pressure gauge located outside the scattering chamber. The vapor pressure thermometry method makes use of the fact that the hydrogen vapor pressure as function of the temperature is well known. High precision Sensotec TJE-absolute pressure transducers (range 0–25 psi, accuracy

0.1% of full scale) are used to determine the bulb pressure, and the temperature is calculated using the vapor pressure–temperature relationship for hydrogen [130]. The TJE transducers are read by a Sensotec SC200 read-out controller, connected to the IOC with a RS-232 serial line. After charging of the bulbs, the pressure transducers are calibrated against an accurate dial gauge in the separate vapor pressure gas system mounted on the cryo can. The method provided accurate temperature measurements in a short period after the calibration, but proved to be unreliable after longer periods of time, possibly due to radiation damage to the transducer [42].

In addition to the temperature sensors which measure the target fluid temperature, Lakeshore DT-470 silicon diodes are installed in the coolant supply and return lines, to monitor the temperature of the refrigerant. The diodes have a standard temperature response curve, which is loaded in an Oxford ITC502 temperature controller. Signals from all resistive temperature sensors are brought out of the scattering chamber through a vacuum feed through in the cryo can, along with target fan control, tachometer and heater wiring. On the vacuum side of the feed through, the Cernox's, diodes and Allen-Bradleys are connected with phosphor-bronze Quad lead 36 AWG thermocouple wire. A detailed layout of the cryotarget control wiring is presented in [131].

Temperature control of the target loop is established using the Cernox sensors and the heaters. The Oxford ITC502 temperature controller monitors the temperature on both Cernox resistors in the loop. The low power heater is connected to the Oxford ITC502 and operated in a proportional-integral-differential (PID) feedback loop slaved off of one of the Cernox resistors. A set-point for the sensor is recorded in the ITC which can provide an output voltage to the heater, so that small temperature fluctuations can be smoothed out by changing the power deposit of the heater in the loop. The low power heater has a maximum power output of $\sim$80 W and is usually operated at half range in a target taking beam at temperature equilibrium.

When the electron beam passes through the target, power is deposited in the target liquid. The power deposited is calculated from

$$P = I_B \times \frac{dE}{dx} \times \rho \times t, \tag{C.1}$$

where I_B is the beam current, $\frac{dE}{dx}$ the electron energy loss, ρ the target density, and t the target length. Small fluctuations in the power deposited due to small fluctuations in beam current are generally compensated for with the low power heater. The high power heater is installed to replace the entire beam power deposit and has a maximum output of ~800 W. The control system allows four high power heater modes, which are implemented through a sequencer (final state machine) that runs on the target IOC. The first two modus operandi are heater "OFF" and "Manual" heater operation. In the latter mode, the user enters the desired heater power through the GUI. A "Constant Heat Load" mode is available, where the control system keeps the sum of the heat load of the beam and high power heater equal to a preset constant. The beam power deposited is calculated from the ADC reading of the beam current (BCM3) using Equation C.1, and the high power heater is controlled to match the constant power setting. The fourth mode is a "PID Control" mode. I this mode a software PID loop (programmed in the high level EPICS database) on the IOC controls the high power heater setting in a feedback loop using the temperature of a Cernox resistor in the target loop as reference.

Appendix D

Cross Section Quantities

This Appendix includes tables with quantities used for the cross section calculation. Tables D.1 and D.2 show the quantities used for the half-acceptance and full-acceptance cross sections, respectively. Each table shows entries for all kinematics for the limits of the E_γ integration interval, the mean photon energy, $\bar{E}_\gamma$, and the integrated photon flux, N_γ, the reconstructed target length cuts, y_{tar}, and the solid angle, $\Delta\Omega$.

The low and high limits on E_γ define the interval $[E_{\gamma,low}, E_{\gamma,high}]$ over which the photoproton yield and the photon flux is integrated. The mean photon energy is calculated using Equation 5.13 on this interval as well. For the E_{beam}=0.845 GeV, $\theta_{cm} = 90°$ data the integration interval was divided into two equal 50 MeV bins. The integrated photon yield is expressed per microCoulomb of electrons impinging on the copper radiator foil. The radiator thickness is 6.02% radiation lengths for all kinematics, except for the data taken at $E_{beam} = 0.845$, where a 3.49% r.l. radiator was used. The determination of the radiator thickness is described in Reference [42].

The cuts on the reconstructed target length, y_{tar}, are used in the extraction of the photoproton yield, and for the solid angle calculations. Solid angles were calculated with the HMS Monte Carlo model described in Section 4.3.2.

E_{beam} (GeV)	θ_{cm}	$E_{\gamma,high}$ (GeV)	$E_{\gamma,low}$ (GeV)	$\bar{E}_\gamma$ (GeV)	N_γ (10^9 γ's/μC)	y_{tar} (cm)	$\Delta\Omega$ (msr)
0.845	36.17°	0.820	0.765	0.792	12.13	2.0	3.184
	88.68°	0.820	0.770	0.745	12.18	4.0	2.875
	89.46°	0.770	0.720	0.794	10.96	4.0	2.875
1.645	35.82°	1.620	1.565	1.592	10.00	1.5	3.293
	51.90°	1.620	1.555	1.587	11.96	2.0	3.231
	68.87°	1.620	1.540	1.579	14.95	3.5	2.978
	88.97°	1.620	1.510	1.563	21.08	4.0	2.896
2.445	35.57°	2.420	2.365	2.392	6.61	1.5	3.288
	51.64°	2.420	2.355	2.387	7.89	2.0	3.230
	68.80°	2.420	2.340	2.379	9.85	3.5	2.983
	88.83°	2.420	2.310	2.363	13.86	4.0	2.896
3.245	35.46°	3.220	3.165	3.192	4.90	1.2	3.335
	51.64°	3.220	3.155	3.187	5.86	2.0	3.233
	68.68°	3.220	3.140	3.179	7.31	3.0	3.073
	88.79°	3.220	3.110	3.163	10.28	4.0	2.886
4.045	35.40°	4.020	3.965	3.992	3.90	1.2	3.338
	51.50°	4.020	3.955	3.987	4.66	2.0	3.227
	51.50°†	4.020	3.955	3.987	4.66	1.8	3.255
	68.70°	4.020	3.940	3.979	5.81	3.0	3.061
	68.70°†	4.020	3.940	3.979	5.81	2.2	3.181
	88.77°	4.020	3.910	3.963	8.16	4.0	2.877

Table D.1: Quantities used in the calculation of the half-acceptance cross sections. The kinematics labeled with '†' were measured in 1997.

E_{beam} (GeV)	θ_{cm}	$E_{\gamma,high}$ (GeV)	$E_{\gamma,low}$ (GeV)	$\bar{E}_\gamma$ (GeV)	N_γ (10^{13} γ's/μC)	y_{tar} (cm)	$\Delta\Omega$ (msr)
2.445	37.08°	2.420	2.365	2.392	6.61	1.5	6.556
	53.05°	2.420	2.355	2.387	7.89	2.0	6.421
	70.07°	2.420	2.340	2.379	9.85	3.5	5.926
4.045	53.15°†	4.020	3.955	3.987	4.66	1.8	6.491
	70.17°†	4.020	3.940	3.979	5.81	2.2	6.346

Table D.2: Quantities used in the calculation of the full-acceptance cross sections. The kinematics labeled with '†' were measured in 1997.

Vita

Bart Paul Terburg was born on July 6, 1969 in Leidschendam, The Netherlands. From 1987 to 1992 he attended the Delft University of Technology where he received the degree of Ingenieur in applied physics cum laude in the spring of 1992. He enrolled in the graduate program in physics at the University of Illinois at Urbana-Champaign in August 1992 and received his Ph.D. in physics from the University of Illinois in the summer of 1999. He was a recipient of a Fulbright Graduate Student Program Mutual Educational Exchange Grant in 1992 and the Felix T. Adler Fellowship in 1999.

Publications:

Inclusive Electron-Nucleus Scattering at Large Momentum Transfer, J. Arrington *et al.* (CEBAF E89-008 collaboration), Phys. Rev. Lett. **82**, 2056 (1999).

Measurements of Deuteron Photodisintegration up to 4.0 GeV, C. Bochna *et al.* (CEBAF E89-012 collaboration), Phys. Rev. Lett. **81**, 4576 (1998).

Quasifree $(e, e'p)$ Reactions and Proton Propagation in Nuclei, D. Abbott *et al.* (CEBAF E91-013 collaboration), Phys. Rev. Lett. **80**, 5072 (1998).

Measurement of the Proton's Neutral Weak Magnetic Form Factor, B. Mueller *et al.* (SAMPLE collaboration), Phys. Rev. Lett. **78**, 3824 (1997).

Coherent Scattering Length Measurements on Krypton with Neutron Interferometry at a Small Reactor, B.P. Terburg, P. Verkerk, E. Jericha, and M. Zawisky, Journal of Neutron Research, **1** 37 (1993).

The Coherent Scattering Length of ^{86}Kr Determined by Neutron Interferometry, B.P. Terburg, P. Verkerk, E. Jericha, and M. Zawisky, Nucl. Instrum. Meth. **A324** 247 (1993).

Evidence for Valence Quark-Hadron Duality, I. Niculescu *et al.*, in preparation.

Experimental Verification of Quark-Hadron Duality, I. Niculescu *et al.*, in preparation.

Coherent π^0 Photoproduction on the Deuteron up to 4 GeV, D.G. Meekins *et al.*, in preparation.

Talks Presented:

First Results from Deuteron Photodisintegration at CEBAF, Gordon Research Conference on Photonuclear Reactions, NH, July 1996.

Cryogenic Target Development at CEBAF, American Physical Society, Wash. D.C., April 1995.